# Novel design and development of high power with high brightness optical sources using a coherently coupled array of semiconductor lasers

Masanotti, Delia

*Award date:*
2005

*Awarding institution:*
University of Bath

# Novel Design and Development of High Power with High Brightness Optical Sources Using a Coherently Coupled Array of Semiconductor Lasers

Delia Masanotti

A thesis submitted for the degree of Doctor of Philosophy

University of Bath

Department of Electronic and Electrical Engineering

June 2005



**Delia Masanotti**





ProQuest LLC
789 East Eisenhower Parkway
P.O. Box 1346
Ann Arbor, MI 48106-1346

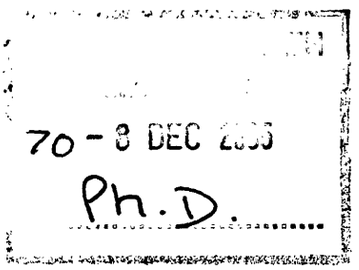
70 - 8 DEC 2005
Ph.D.

# Acknowledgements

*Special thanks must go to my supervisor Dr F. Causa for contributing to this research with helpful discussions and constructive criticism but also with continuous support and to Dr J. Sarma for his enormous availability.*

*My gratitude goes to the whole optoelectronics group of the University of Bath, in particular to my office 'mates' and friends N. Cinosi, A. Tarlis, L. Burrow and T. C. Woo for helpful discussions but also for continuous support and 'recharging laughs'; to Trevor Ryan for his patience and ability in interpreting my requirements for the fabrication of the devices and to Dave Hatten for his help in 'electronics matter'.*

*Thanks to Dr J. S. Roberts, University of Sheffield, for providing the required material for device fabrication.*

*Thanks also to the EPSRC for the financial support, to the University of Bath for the facilities provided throughout and the Max Born Institut fur Nichtlineare Optik und Kurzzeitspectroscopie, Berlin, for the use of their equipment for some of the measurements presented.*

*Last but not the least, many many thanks to my family, without which I would not be here, for continuous encouragement and support.*

*Special thanks go also to all my friends in Bath who have had to put up with me and have made my life here very special and enjoyable, and to my dearest friends Francesca, Monica e Silvia, whose continuous support has been invaluable.*

# Summary

This PhD thesis presents the design and the characterisation of a novel index-guided bow-tie laser array in which the emitters are coherently coupled to achieve high power operation in a diffraction-limited output beam and, therefore, high brightness.

Different aspects must be considered when designing arrays that emit in a diffraction limited beam, including the optimisation of the individual emitter radiated beam and the analysis of the coupling occurring between adjacent emitters. Importantly, the mutual coherence between array elements and the mechanism responsible for mode discrimination need to be studied to predict the performance of the devices and therefore the occurrence of in-phase-locking.

The novel feature of the device described here is that the (lateral) coupling between the elements in the array is longitudinally non-uniform, that is weak coupling along the length of the device and strong coupling at the output of the device, leading to in-phase locking of the arrays and, therefore, to diffraction-limited operation. Notably, the narrow output beam is achieved without the use of external lenses, thereby reducing the device complexity.

Comparisons of the operational characteristics measured from several in-house fabricated devices of different geometries show that Parabolic Bow-Tie Laser Arrays (PBTLAs) are the most suited to achieve high-power and high-brightness. Results from the experimental characterisation, interpreted by using the Coupled-Mode Theory, indicate that coherence is significant in the operation of PBTLAs. The devices described here are simple to fabricate and, thus, represent an attractive option for low-cost applications that require devices with high quality operational characteristics.

# Contents

# List of Symbols

$\alpha_i$ Distributed losses

$\alpha_m$ Mirror losses

$\alpha_{FC}$ Free carrier absorption losses

$\alpha_C$ Coupling losses

$\alpha_S$ Scattering losses

$\hat{\beta}$ Gain coefficient

$\beta_m$ Propagation constant for the m-th mode of a waveguide laser

$\gamma_{mn}$ Complex degree of coherence between the m-th and n-th elements of a laser array

$\varepsilon$ Dielectric constant for the material

$\eta_i$ Differential internal quantum efficiency

$\eta_e$ Differential external quantum efficiency

$\lambda$ Laser light (peak) emitting wavelength

$\theta$ Angular coordinate in the spherical coordinate system

$\theta_d$ Diffraction-limit angle

$\theta_x$ Horizontal divergence angle of the far-field pattern at FWHM

$\theta_y$ Vertical divergence angle of the far-field pattern at FWHM

$\sigma_x$ Lateral variance of a beam

$\sigma_s$ Angular variance of a beam

$\omega$ Laser light (peak) emitting angular frequency

$\hat{\nu}$ Laser light (peak) emitting frequency

$\Gamma_{mn}$ Mutual coherence between the m-th and n-th elements of a laser array

$\Gamma_{QW}$ Confinement factor of a waveguide mode in the active region

$\Gamma_{CL}$ Confinement factor of a waveguide mode in the cladding layers

$\Omega$ Solid divergence angle of an emitted beam at FWHM

$\Phi$ Complex field component associated to an optical source

$\Psi$ General field component associated to an optical source

| | |
|---|---|
| $a$ | Young Two Slit aperture |
| $c_{mn}$ | Coupling coefficient between the m-th and n-th elements of a laser array |
| $d$ | Vertical width of a laser emitting aperture |
| $d_A$ | Longitudinal astigmatism |
| $d_{QW}$ | Thickness of the active region |
| $f$ | Lens focal length |
| $g$ | Modal gain |
| $g_{th}$ | Threshold gain |
| $g_{mat}$ | Material gain |
| $h$ | Plank's constant |
| $h_{RIB}$ | Etch depth of the rib in a laser |
| $k$ | Wave number |
| $n$ | Refractive index for the material |
| $n_{eff}$ | Effective refractive index of a waveguide vertical mode |
| $\Delta n_{eff}$ | Lateral effective refractive index step |
| $q$ | Electronic charge |
| $r$ | Radial coordinate in the spherical coordinate system |
| $t_w$ | Thickness of the guide layers |
| $w$ | Width of the rib in a waveguide laser |
| $w_0$ | Gaussian Beam waist |
| $x$ | Horizontal coordinate in the rectangular coordinate system |
| $y$ | Vertical coordinate in the rectangular coordinate system |
| $z$ | Longitudinal coordinate in the rectangular coordinate system |
| $z_0$ | Rayleigh range |
| $A$ | Gain constant |
| $B$ | Brightness |
| $B_r$ | Bimolecular recombination constant |
| $D$ | Horizontal width of a laser emitting aperture |
| $D_c$ | Diffusion coefficient |
| $E$ | General component for the electric field |
| $F$ | General component for the electric or magnetic field |
| $F_{TOT}$ | Total field distribution in laser arrays |

| | |
|---|---|
| $I$ | Current |
| $I_{Gv}$ | Grating function of the v-th oscillating mode of a laser array |
| $I_{th}$ | Threshold current |
| $\hat{I}$ | Angular intensity profile of emitted beams |
| $J$ | Current density |
| $J_{th}$ | Threshold current density |
| $J_{tr}$ | Current density at transparency |
| $L$ | Length of a waveguide laser |
| $L_D$ | Carrier diffusion length |
| $M^2$ | $M^2$-factor |
| $N$ | Carrier density |
| $N_0$ | Doping density in the active region |
| $N_{tr}$ | Carrier density at transparency |
| $P$ | Total output power of a waveguide |
| $P_d$ | Photon density |
| $P_{sat}$ | Saturation power |
| $P_{stim}$ | Stimulated emission |
| $P_{COD}$ | Power density at the laser facet before COD |
| $R$ | Power reflectivity of the facets |
| $S$ | Inter-element spacing (at centreline) in laser arrays |
| $S_F$ | Inter-element spacing (between edges at the output facets) in laser arrays |
| $S_S$ | Equivalent spot size |
| $S_{sl}$ | Young Two Slit separation |
| $T_h$ | Temperature of the heatsink |
| $T_0$ | Temperature coefficient of $I_{th}$ |
| $T_1$ | Temperature coefficient of $\eta_e$ |
| $\Delta T$ | Temperature rise with respect to the heat sink |
| $V$ | Visibility of the interference pattern between optical sources |
| $W$ | Output facet width of a waveguide laser |
| $W_T$ | Output facet width of a laser array |
| $W_x$ | Lateral beam spot size |
| $W_s$ | Angular beam spot size |

# List of Abbreviations

| | |
|---|---|
| ARROW | Anti-Resonant Reflective Optical Waveguide |
| BPM | Beam propagating Method |
| BTL | Bow-Tie Laser |
| BTLA | Bow-Tie Laser Array |
| CM | Collocation Method |
| CMM | Cascaded Matrix Method |
| CMT | Coupled-Mode Theory |
| COD | Catastrophic Optical Damage |
| CW | Continuous Wave |
| DBR | Distributed Bragg Reflectors |
| DFB | Distributed Feedback Lasers |
| EDC | Effective Dielectric Constant |
| EBTL | Exponential Bow-Tie Laser |
| EBTLA | Exponential Bow-Tie Laser Array |
| FWHM | Full Width at Half Maximum |
| GG | Gain-Guiding |
| HG | Hermite-Gauss |
| HGCM | Hermite-Gauss Collocation Method |
| IG | Index-Guiding |
| LME | Local Mode Expansion |
| LBTL | Linear Bow-Tie Laser |
| LBTLA | Linear Bow-Tie Laser Array |
| LOC | Large Optical Cavity |
| MOPA | Master Oscillator Power Amplifier |
| MO | Master Oscillator |
| PA | Power Amplifier |
| PBTL | Parabolic Bow-Tie Laser |
| PBTLA | Parabolic Bow-Tie Laser Array |
| SDT | Simple Diffraction Theory |

| | |
|---|---|
| SG | Super Gaussian |
| SHB | Spatial Hole-Burning |
| SL | Stripe Laser |
| SLA | Stripe Laser Array |
| SR | Strehl Ratio |
| STM | Step Transition Method |
| S-5PBTLA0 | Short-cleaved 5-Parabolic Bow-Tie Laser Array, 10μm inter-element spacing |
| ROW | Resonant Optical Waveguide |
| TQW | Triple Quantum Well |
| 10PBTLA0 | 10-Parabolic Bow-Tie Laser Array, 10μm inter-element spacing |
| 20PBTLA0 | 20-Parabolic Bow-Tie Laser Array, 10μm inter-element spacing |
| 3LBTLA0 | 3-Linear Bow-Tie Laser Array, 10μm inter-element spacing |
| 3LBTLA10 | 3- Linear Bow-Tie Laser Array, 30μm inter-element spacing |
| 3PBTLA0 | 3-Parabolic Bow-Tie Laser Array, 10μm inter-element spacing |
| 3PBTLA10 | 3-Parabolic Bow-Tie Laser Array, 30μm inter-element spacing |
| 3SLA0 | 3-Stripe Laser Array, 10μm inter-element spacing |
| 3SLA10 | 3-Stripe Laser Array, 30μm inter-element spacing |
| 4LBTLA0 | 4-Linear Bow-Tie Laser Array, 10μm inter-element spacing |
| 4LBTLA10 | 4-Linear Bow-Tie Laser Array, 30μm inter-element spacing |
| 4PBTLA0 | 4-Parabolic Bow-Tie Laser Array, 10μm inter-element spacing |
| 4PBTLA10 | 4-Parabolic Bow-Tie Laser Array, 30μm inter-element spacing |
| 4SLA0 | 4-Stripe Laser Array, 10μm inter-element spacing |
| 4SLA10 | 4-Stripe Laser Array, 30μm inter-element spacing |
| 5LBTLA0 | 5-Linear Bow-Tie Laser Array, 10μm inter-element spacing |
| 5LBTLA10 | 5-Linear Bow-Tie Laser Array, 30μm inter-element spacing |
| 5PBTLA0 | 5-Parabolic Bow-Tie Laser Array, 10μm inter-element spacing |
| 5PBTLA10 | 5-Parabolic Bow-Tie Laser Array, 30μm inter-element spacing |
| 5SLA0 | 5-Stripe Laser Array, 10μm inter-element spacing |
| 5SLA10 | 5-Stripe Laser Array, 30μm inter-element spacing |

# Introduction

This PhD thesis presents the outcome of research investigations which were motivated by the need to develop a novel, compact and simple to fabricate, high power semiconductor optical source characterised also by high brightness.

Semiconductor laser diodes have raised increasing interest for various scientific and industrial applications where high power in a diffraction-limited beam is required.

The challenge in designing such optical sources resides in overcoming Catastrophic Optical Damage (COD), optical gain saturation, and filamentation of the optical field. In addition, the output beam profile should be optimised to achieve the desired high brightness.

A straightforward way of increasing the achievable output power is to operate many individual lasers into arrays, because the array total emitted power is the sum of the powers of the individual elements. However, even if the total output power increases, if high spatial beam quality is not achieved the laser might not be useful for many applications.

Arrays of mutually incoherent (i.e., optically uncoupled) otherwise identical emitters are well suited to achieve high output power, do not usually require sophisticated adjustment and are robust systems because of the redundancy afforded by the multiple sources. In addition, collimation optics, if needed, must be diffraction-limited only over the small region illuminated by the single-laser aperture and costs are lower than those associated to equivalent (in emitting aperture width) single-laser systems, where the collimating optics must be diffraction-limited over the entire aperture. However, even if the individual emitters do operate in fundamental mode, the output beam from such incoherent arrays is at best identical to that of an individual emitter. Thus, the obtained effect is only of multiplying the output power of a single element and no improvement is observed in the brightness.

To achieve the desired mode control and diffraction-limited beam over the entire array aperture, it is essential that the fields of the different emitting regions are

coherent: coherent (in-phase locked) array emission can, in fact, provide brightness comparable to that of a similar-sized broad area emitter operating in its lowest mode.

The lasing field of a phase-locked array is a combination of the array modes supported by the dielectric structure. Ideally the array should operate in the fundamental array-mode with constant phase across the facet and produce the desired single lobe, narrow far-field. However, due to the occurrence of multiple apertures, the array total field is greatly affected by the mutual coherence and by the optical field phase-shift from one emitter to another, sometimes yielding to undesirable multi-lobed far field profiles.

Effective designs have been proposed to achieve in-phase operation, such as Y-junction arrays or Antiresonant Reflecting Optical Waveguides (ARROWs), but such designs usually require sophisticated device fabrication to achieve effective mode selection and to sustain in-phase operation.

The aim of the research work presented in this PhD thesis was to develop arrays of index-guided parabolic bow-tie lasers to achieve high power and high brightness with an effective design that combines the desirable operational characteristics with a simple, low cost device fabrication.

Tapered geometry lasers diodes have attracted particular attention as simple, cost-effective devices to achieve high-power in a narrow-output beam. The key advantage in using a tapering rib is that the device (central) narrow section acts as mode filter and provides control on the field shape while the broad (output) facet allows for higher saturation output power as well as lower optical power density (therefore reducing the risk of COD). In particular, the proposed tapered arrays are a development of the index-guided Parabolic Bow-Tie Laser (PBTL) design that has been demonstrated to be effective for relatively high output power with good quality output beam.

Tapered laser arrays have already been reported in literature, but they are essentially of uncoupled, linear tapered elements and high output power is achieved in a non-diffraction limited output beam. The intention here was to achieve in-phase-locking between the emitters. The novelty of the Parabolic Bow-Tie Laser Arrays (PBTLAs) resides in the fact that the combination of the guiding strength and of the longitudinal non-uniform inter-element coupling (weak coupling along the length of

the device and strong coupling at the output of the device) provides much improved scopes to sustain in-phase (array) mode operation, thus enhancing high-power with high-brightness operation also. In fact, in the region near the output facets, where the elements merge in a single contact and there is no explicit lateral mode control, the optical gain in the inter-element regions is larger than that in the element regions, due to the effect of carriers on the refractive index and to the gain hole-burning. Thus, the modal gain associated to this mode is the highest.

In this context, the Parabolic Bow-Tie Laser Arrays (PBTLAs) are different also from the conventional (index-guided) stripe laser arrays where, because of the better field intensity overlap with the gain distribution (higher modal gain) the highest order (out-of-phase) mode is typically favoured.

To obtain the final device design, a detailed study has been necessary to optimise both the semiconductor material structure and the tapered laser geometry. Several arrays of different geometry, number of elements, inter-element spacing and guiding strength have been fabricated and characterised in-house to show that careful cavity design is essential to achieve, simultaneously, high power and high brightness.

The experimental results from in-house fabricated arrays of coupled Parabolic Bow-tie Lasers have been interpreted using models based on the coupled-mode theory and on function expansion methods. Both models take into account the interaction between the propagating optical field and the carriers, typical of active sources.

The thesis is structured as follows:

Chapter 1: Review of relevant device designs discussed in the literature to achieve high-power high-brightness operation. The aim of the chapter is to establish the research context.

Chapter 2: Discussion of the factors that mostly affect output power levels and beam quality, and definition of quantitative parameters to characterise the beam quality. The intention is to introduce and describe the aspect that will be addressed throughout the thesis to study the operational characteristics of the laser arrays.

Chapter 3: Introduction of theoretical and mathematical definition of coherence and discussion of its effect on laser array output power intensity and brightness.

Together with Chapter 3 this chapter constitutes the essential background to interpret the beam characteristics of parabolic bow-tie lasers.

Chapter 4: Overview of phase-locked arrays and description of the theoretical model based on the coupled-mode theory that has been used to interpret experimental results.

Chapter 5: Experimental results from the characterisation of individual PBTLs are discussed and compared with those measured from corresponding Linear Bow-Tie Lasers (LBTLs), Exponential Bow-Tie-Lasers (EBTLs) and Stripe Lasers (SLs). Comparisons are made also with results obtained from the theoretical models. The methodology used for the optimisation of both the material epitaxy and the device geometry is also discussed as the essential background for the development of the laser array.

Chapter 6: Experimental characterisation of the in-phase-locked PBTLAs and comparison with corresponding Linear Bow-Tie Laser Arrays and Stripe Laser Arrays with the same size. Results obtained from the theoretical models are also presented to interpret and validate the experimental ones. The study of the scalability to arrays of a larger number of elements is also presented.

Chapter 7: Robustness and effectiveness of the optimised PBTLA design are discussed. The operational characteristics of arrays of mutually incoherent and of gain-guided PBTLAs are discussed and compared with those from in-phase locked PBTLAs. The tolerance of the device to fabrication errors is also discussed.

Finally, some conclusions drawn from this PhD research work are presented along with suggestions for future work.

# Chapter 1

# *Review of Semiconductor Lasers for High-Power High-Brightness Operation*

High-power high-brightness diode lasers, due to their better efficiency, compactness and reliability, are gaining more and more interest for applications previously dominated by expensive and inefficient solid state lasers. Among others, fibre amplifier and solid state laser optical pumping, [1-1], [1-2], free space communications, [1-3], [1-4], second harmonic generation, [1-5], medicine, [1-6], laser printing, [1-7], lidar, [1-8], are fast growing fields where semiconductor lasers are going to play a major role, taking a considerable part also of the world laser market. In all of these applications, high output power together with diffraction-limited beam, i.e., high brightness, are either the key requirements or strongly improve the system performance.

To achieve simultaneously high power and high brightness, the device geometry must be carefully designed. The challenge is to develop optical sources with high beam quality, but that are also compact and simple to fabricate to reduce size and costs.

This Chapter gives an overview of the different designs proposed in literature to meet the requirements described above and of the work that has been carried out in order to enhance the output power as well as to improve the beam quality of these devices.

## 1.1 Stripe Lasers

Single lateral mode operation can be achieved by using appropriately designed narrow stripe semiconductor lasers, but the output power for such devices tends to be limited by optical gain saturation and the onset of Catastrophic Optical Damage (COD), [1-9], [1-10]. The schematic of a typical stripe laser is presented in Fig. 1.1.

The output power from stripe lasers can be increased by facet passivation, e.g., [1-9] and [1-10], where up to 60% increase in output power has been achieved after passivation, or by designing buried ridge lasers fabricated by selective area epitaxy, [1-11]. However, the above device designs require sophisticated material growth and device fabrication, with low tolerance, e.g., to small changes in the ridge thickness.

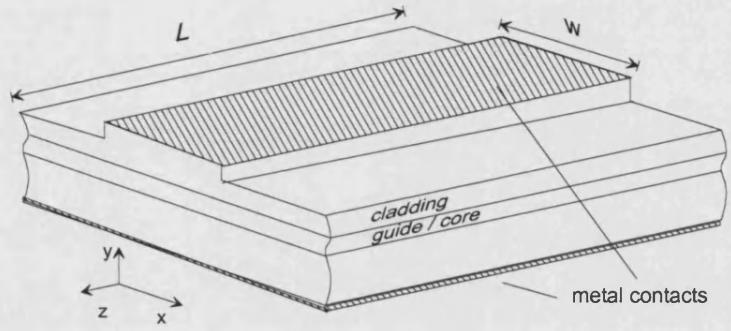


**Fig. 1.1: 3D schematic of a stripe laser. For narrow stripe lasers w~2-5μm; for broad area lasers w~50-200μm.**

It can be argued that a simple solution to the problems discussed above could be to increase the area of the gain region, i.e., to use broad area stripe lasers, [1-12], [1-13]. However, although large output powers can be achieved with such lasers, e.g., [1-13], the quality of the output beam is poor and difficult to control, [1-14], [1-15]. In fact, broad area lasers are subject to temporal and spatial instabilities (filamentation) of the optical field as well as unstable wavefront lensing due to non uniform lateral carrier distribution and non uniform lateral temperature profile, [1-16], [1-17]. As a consequence the output beam is generally multi-lobed and non-diffraction-limited.

Current profiling, [1-18], can be used to control the output beam quality in broad area lasers; however, this technique is generally effective only under pulsed operation, e.g., [1-18], since the large thermal gradients arising under CW operation degrade the beam by inducing filamentation. The output beam quality from broad area lasers can be significantly improved also by incorporating the large gain section into an unstable resonator cavity design, e.g., [1-19], [1-20]. In this case the optical field diverges in the gain area, therefore reducing the risk of saturation, filamentation and beam instability and thus providing high power as well as high brightness. The

mirrors, however, have to be designed and fabricated with extreme care, e.g., [1-20], and this is the main drawback of such devices. The other, inevitable, difficulty to be overcome with broad area unstable resonator lasers is that the astigmatism is typically current-dependent and, therefore, the adjustment of the external optics needed for focusing becomes cumbersome.

A completely different design has been adopted in [1-21]-[1-23], where the broad area gain section is combined with an underlying diffraction grating to achieve simultaneously high power and diffraction-limited operation. Such configuration is referred to as angled-grating distributed feedback (α-DFB) laser. A schematic of a typical α-DFB laser is presented in Fig. 1.2.

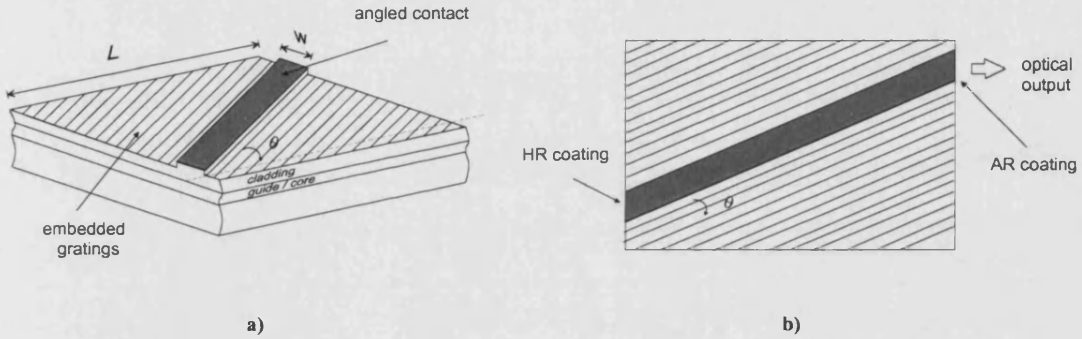


**Fig. 1.2: Schematic diagram of a α-DFB laser: a) 3-dimensional diagram and b) top view.**

The embedded diffraction grating and the contact stripe are angled with respect to the laser facets. The tilted-angle grating provides for spectral as well as spatial mode filtering but also for optical confinement for the light that propagates into the cavity. The optical output emerges at a normal incidence from the output facet in form of a broad, laterally collimated, diffraction-limited beam. Although high powers have been achieved with α-DFB lasers, the main disadvantage associated with such device structures originates from the weak lateral-mode confinement which facilitates local refractive index changes induced by thermal and carrier density gradients, therefore, causing beam instabilities. In addition, sophisticated material growth and device fabrication are required and complicated lens arrangements are needed to correct the field phase curvature.

An overview of recent, relevant results referring to the devices discussed in this Section is presented in Tab. 1.1.

**Tab. 1.1: Summary of results from stripe lasers.**

| Device | Characteristics | References |
|---|---|---|
| Narrow stripe lasers | 350mW @ 2A (pulsed), w=3µm<br>460mW @ 2A (pulsed), w=4µm | G. Beister et al., 1996, [1-9] |
| | 264mW @ 1.3A (pulsed) | J. S. Yoo et al., 1991, [1-10] |
| Narrow stripe lasers with facet passivation | 420mW @ 2A (pulsed), w=3µm<br>>550mW @ >2A (pulsed), w=4µm | G. Beister et al., 1996, [1-9] |
| | 420mW @ 1.8A (pulsed) | J. S. Yoo et al., 1991, [1-10] |
| Buried ridge lasers | 1W @ 1.5A (CW), w=2µm<br>diffraction-limited up to 450mW | R. B. Swint et al., 2002, [1-11] |
| Broad stripe lasers | 11.3W @ 13A (CW), w=100µm<br>Not diffraction-limited<br>Brightness: 16MWcm$^{-2}$sr$^{-1}$ @ 4W | S. O'Brien et al., 1998, [1-13] |
| | 16.5W @ 23A (CW), w=200µm<br>Not diffraction-limited | S. O'Brien et al., 1998, [1-13] |
| α-DFB lasers | 1.2W @ 3.5A (CW), w=2µm<br>diffraction-limited | V. V. Wong et al., 1998, [1-22] |
| | 3W @ 10A (CW), w=160µm, L=4mm<br>diffraction-limited up to 1.2W | K. Paschke et al., 2003, [1-23] |

## 1.2 Tapered Devices

In the quest for high power and high brightness, taper geometry devices are promising because they provide an effective design to combine the desirable operational characteristics of high power and narrow output beam with simple, low cost device fabrication. Tapered devices have several advantages over other high power sources. While the narrow section acts as mode filter, the longitudinally broadening gain region permits to achieve higher saturation output power and, at the same time, to reduce the optical power density and, therefore, the risk of COD at the (wide) output facet.

Tapered devices presented in the literature can be usefully classified in two broad categories on the basis of the guiding properties of the structure: *i*) gain-guided (or diffraction-type) tapered devices, where the beam freely diffracts in the homogeneous gain medium under the gain region defined by a flared metal contact – these devices are strongly astigmatic and require the use of external lenses to focus the beam to a small spot and ii) index-guided tapered devices, where a tapered etched rib provides an explicit lateral (effective) refractive index step that weakly guides the optical field within the device – the output beam quality in this case depends on the device geometry and no additional optics is needed to focus the beam.

### 1.2.1 Gain-Guided Tapered Devices

Diffraction-type tapered devices include semiconductor power amplifiers, [1-16], [1-24]-[1-26], consisting essentially of a gain region where both facets are anti reflection (AR) coated in order to prevent the device from lasing, Fig. 1.3. Large output powers in a single-spatial mode and near-diffraction-limited beam can be achieved with tapered amplifiers. However, the device operation is strongly affected by temporal and spatial instabilities (filamentation) of the optical field due to non-uniform gain saturation, [1-16], and by feedback due to external reflections that can lead to lasing, [1-25]. A further problem is that additional external optics must be used to effectively inject the source beam at the input of the amplifier and to correct the strong astigmatism and the phase curvature of the output beam. The effective far-field pattern is, in fact, measured by imaging the virtual source point in the far-field plane. In addition, very high quality facet coatings are required.

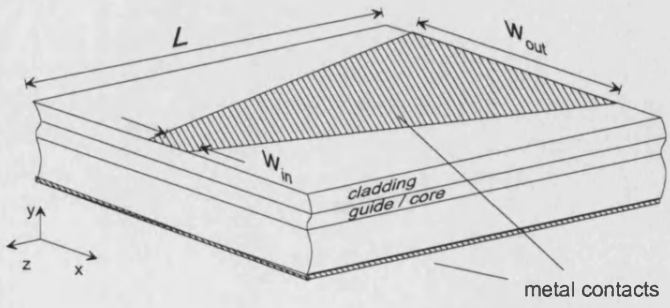


**Fig. 1.3: Schematic of a tapered amplifier. Typically $w_{out}$=200μm, L=2mm.**

High diffraction-limited output powers have been achieved also with tapered amplifiers operated in the Master Oscillator Power Amplifier (MOPA) configuration. The MOPA geometry, that offers also the advantages of single-frequency operation, is one of the most successful designs for high-power high-brightness operation. In the earliest designs the Master Oscillator (MO) and the Power Amplifier (PA) were separated, discrete devices coupled together via bulk optics, [1-27]. More recent is the development of monolithically integrated tapered MOPAs, [1-28], where the Master Oscillator laser is monolithically integrated with the amplifier on a single chip, Fig. 1.4. The monolithically integrated MOPA devices permit the available power from the master oscillator laser to be efficiently coupled into the amplifier section. Hence, even a small power is sufficient to achieve saturation intensity; importantly, differently from tapered amplifiers, uniform gain saturation is obtained, that prevents from non-linear effects typically associated to a non-uniform distribution of the carriers, [1-16]. The main disadvantage of the MOPA-type devices is, however, that, similarly to the tapered amplifiers, in order to characterise the output beam, a system of optics is needed to correct the beam phase front divergence and to subsequently form the far-field image.

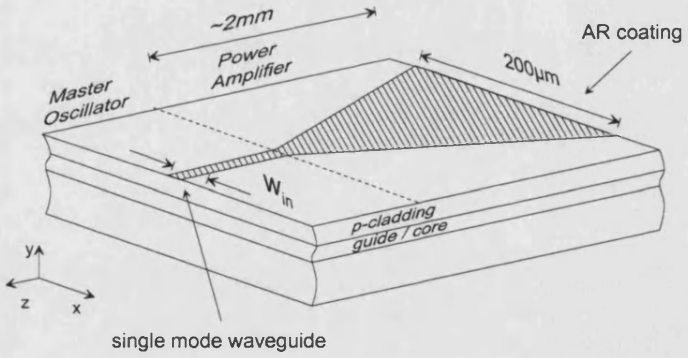


**Fig. 1.4: Monolithically integrated MOPA with separate oscillator and amplifier contacts.**

Lasers with a tapered gain region can also be used to achieve high power, [1-25], [1-29], [1-30]. However, in some cases, grooves are etched on either sides of the narrow end facet of the taper to reduce the feedback to the mode-selective narrow

aperture, [1-29]. In addition, similarly to taper amplifiers and MOPA type devices, these structures are highly astigmatic and prone to filamentation, [1-29].

**Tab. 1.2: Summary of results reported in literature for gain-guided tapered devices. External optics is needed to correct astigmatism and image the far-field pattern.**

| Device | Characteristics | References |
|---|---|---|
| Tapered amplifiers | 5.25W @ 8A (CW), $P_{in}$=200mW<br>$w_{in}$=250μm, $w_{out}$=500μm, L=1.5mm<br>near-diffraction-limited | D. Mehuys et al., 1993, [1-24] |
| | 3.5W @ 5.4A (CW), $P_{in}$=90mW<br>$w_{out}$=215μm, L=2mm<br>near-diffraction-limited | E. S. Kintzer et al., 1993, [1-25] |
| | 4.5W @ 7A (CW), $P_{in}$=100-150mW<br>$w_{in}$=215μm, $w_{out}$=450μm, L=1.5mm<br>near-diffraction-limited | D. Mehuys et al., 1993, [1-26] |
| MOPAs | 5W @ 7A (CW), $P_{in}$=90-165mW<br>$w_{in}$=180μm, $w_{out}$=500μm, L=2mm<br>diffraction-limited | S. O'Brien et al., 1997, [1-27] |
| Integrated MOPAs | 2W @ 3.5A (CW),<br>$w_{out}$=250μm, L=2mm<br>diffraction-limited | S. O'Brien et al., 1993, [1-28] |
| Tapered lasers | 4.2W @ 10A (CW),<br>$w_{out}$=215μm, L=3mm<br>diffraction-limited up to 3.5W | E. S. Kintzer et al., 1993, [1-25] |
| | 1W @ 3.8A (CW),<br>$w_{in}$=2.5μm, $w_{out}$=210μm, L=2mm<br>near-diffraction-limited | J. P. Donnelly, 1998, [1-29] |
| | 2W @ 5A (CW),<br>$w_{in}$=3μm, $w_{out}$=200μm, L=2.5mm<br>diffraction-limited up to 0.5W | B. Sumpf et al., 2002, [1-30] |

High output power in a diffraction-limited beam has been achieved with configurations that combine the mode-selective properties of unstable resonators with the high output power obtained with tapered structures. Recently, a tapered unstable resonator has been demonstrated with distributed Bragg reflectors integrated at both device ends to provide the feedback necessary to support lasing, [1-31]. Due

to the presence of the Bragg reflectors this resonator operates in a single longitudinal mode. However, similarly to the gain-guided tapered structures described above, additional optics is needed to correct astigmatism and to image the far-field beam. More recent is the development of asymmetric tapered unstable resonators with one curved and one flat facet and that can produce high output beams of good quality, [1-32]. Important feature of these devices is that, differently from the other gain-guided tapered structures described in this Section, the position of the beam virtual source, i.e. the longitudinal astigmatism, is not strongly dependent on carrier density or temperature changes at high power operation.

Recent relevant results from the devices discussed in this Section are summarised in Tab. 1.2.

### 1.2.2 Index-Guided Tapered Devices

Compared to the gain-guided (MOPA-type) devices, relatively small lateral dimensions are essential in index-guided tapered lasers to maintain adiabatic conditions, [1-33], [1-34]. Two conditions have to be satisfied in this case: broadening of the rib width to achieve high power and minimisation of the coupling of the field to higher order local modes to maintain most of the power in the fundamental mode and, therefore, to achieve diffraction-limited operation, [1-33].

Tapered lasers of different geometries (linear, parabolic, and exponential) and sizes have been modelled to predict and improve their performance for high power diffraction-limited operation, [1-33], [1-34]-[1-39]. Experimental results, [1-34], [1-35], [1-38]-[1-42], have confirmed that with a careful design of both the semiconductor material epitaxy and the device geometry, index-guided tapered structures are well suited for relatively high-power with high-brightness operation.

The tapered devices of interest here consist of a twin-tapered structure and have a characteristic 'Bow-Tie' configuration, [1-34], [1-35], [1-38], [1-39]. Such devices, where the narrow central stripe acts as a mode filter, have the added advantage, over single-tapered lasers, that the risk of COD is reduced at both output facets. Schematic diagrams of an index-guided tapered laser and a Bow-Tie laser are presented in Fig. 1.5.

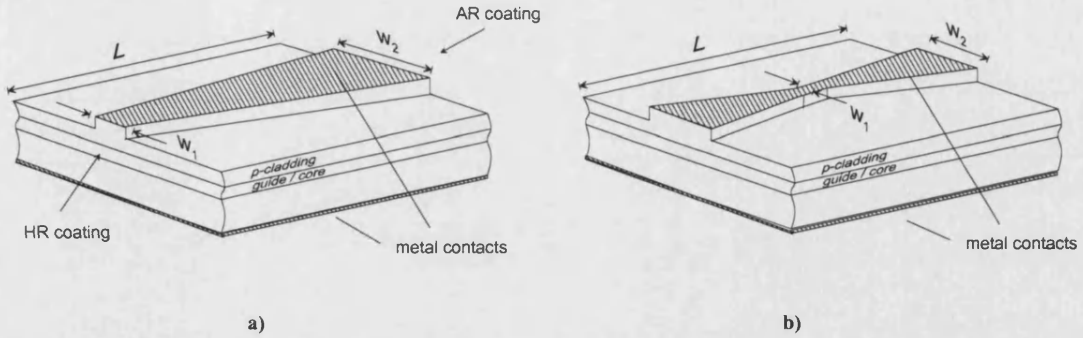


**Fig. 1.5: Schematic diagram of a) a linear taper laser and b) a linear bow-tie laser. Typically, $w_1$=2-3µm, $w_2$=20-30µm, L=1-2mm.**

Relatively high power outputs in a diffraction-limited output beam, measured without the use of external optics, have been achieved with Parabolic Bow-Tie Lasers fabricated in house, [1-38], [1-39], as discussed in Chapter 5 of this thesis.

The most relevant results obtained with the devices described in this Section are summarised in Tab. 1.3

**Tab. 1.3: Summary of results from index-guided tapered devices. The device geometry provides good beam quality and no additional optics is needed to focus the beam.**

| Device | Characteristics | References |
|---|---|---|
| Tapered lasers | 1W @ 1.4A (CW)<br>$w_2$=20-30µm, L=2.5mm<br>not diffraction-limited | M. Krakowski et al., 2003, [1-42] |
| Parabolic Bow-Tie Lasers | 0.1W @ 0.4A (pulsed),<br>$w_1$=3µm, $w_2$=20µm, L=1mm<br>diffraction-limited | N. S. Brooks et al., 1998, [1-34], 1996, [1-35] |
| | 0.2W @ 0.8A (CW),<br>$w_1$=3µm, $w_2$=30µm, L=2mm | N. S. Brooks et al., 1998, [1-34], 1996, [1-35] |
| | 0.64W @ 1A (pulsed)<br>0.3W @ 0.6A (CW)<br>$w_1$=3µm, $w_2$=20µm, L=1.05mm<br>diffraction-limited | D. Masanotti et al., 2003, [1-38], 2004, [1-39] |

## 1.3 Stripe Laser Arrays

In the quest for high output power with high brightness, arrays of a large number of conventional stripe lasers, Fig. 1.6, has been studied in great detail, as discussed also in Chapter 4.

Incoherent combination of individual stripe lasers, [1-43]-[1-45], is a straightforward way to achieve higher output power without COD failure, as the power of the resulting array is the sum of the powers of the individual lasers and the array emitting area is the sum of the emitting areas of the individual elements. However, the increase in output power does not result in the increase of brightness as the output beam of an incoherent laser array is identical to that of the individual array emitters, and if broad area laser arrays are used, e.g. in [1-44], the radiated beams can present multilobed far-fields patterns. In addition, the necessity to work with a large number of individual elements may lead to a considerable increase of the volume of the system as well as to growing expenses.

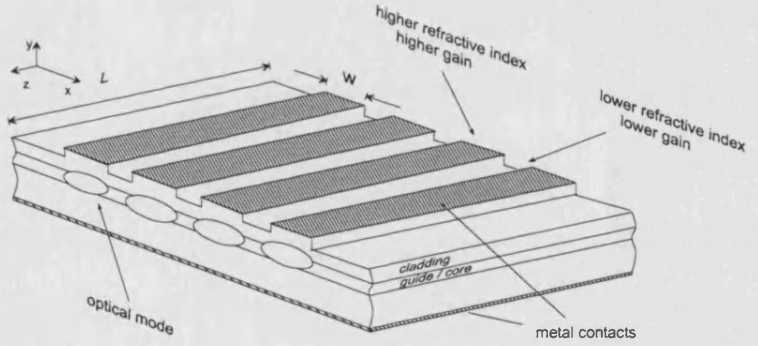


**Fig. 1.6: Schematic of a typical array of semiconductor stripe lasers. The gain (and the optical field intensity) is higher in the regions where also the refractive index is higher.**

High power has been achieved with 1D and 2D incoherent arrays of α-DFB, [1-46]-[1-48], that emit in a single spectral mode, single-lobe radiated pattern, although not diffraction-limited, as the output beam of the laser array is identical to that of an individual device. However, α-DFB arrays retain the same disadvantages as the individual α-DFBs, since elaborated and expensive fabrication process is required, and collimation of the beam is possible only with the use of lenses appropriately integrated with the laser device.

The development of laser arrays with high optical beam quality requires a high degree of coherence so that the individual devices are in-phase-locked, thus emitting in a diffraction-limited far-field pattern and having a peak intensity proportional to the square of the number of beams, [1-46], [1-49]. The lasing field of a phase-locked array is a combination of the array modes (supermodes) supported by the dielectric structure, [1-43], [1-50]. Ideally the array should operate in the fundamental array-mode with constant phase across the facet and produce the desired single-lobe, narrow far-field, [1-43]. However, especially in typical index-guided arrays, Fig. 1.6, because of the better overlap with the gain distribution, the out-of-phase mode is typically favoured thus producing an undesirable multi-lobed far field profile.

Hence, a careful design is required to achieve effective mode selection in a laser array. In fact, to have coherent combination of a large number of beams, sophisticated adjustments, which increase with the degree of beam quality required, are necessary. Various designs have been proposed to achieve effective mode selection in a laser array, including varying the inter-element spacing, [1-51], and current profiling, [1-52]. However, the efficiency of these devices was substantially improved only after realising that global-coupling (each element equally coupled to all others) could lead to higher overall coherence as well as to improved inter-modal discrimination compared to series-coupling (nearest-neighbour coupling), [1-43]. Global-coupling, also called parallel coupling, is the most suitable to obtain the desired in-phase mode operation: it can be effectively achieved in structures that provide strong optical mode confinement although is quite difficult to be controlled.

'Y-junction' laser arrays, Fig. 1.7, have been proposed to achieve strong coupling, [1-43], [1-53]. At each Y-junction, fields from adjacent waveguides couple efficiently only if they are in phase with each other (constructive interference). The combination of out-of-phase fields would be lost as a radiative mode (destructive interference). Thus such devices are very effective in suppressing out-of-phase mode operation.

However, the practical implementation of such devices is very complicated, because of the difficulty in fabricating low-loss symmetric Y-junctions. In addition the divergence of the emitted single-lobed beams is in most of the cases several times the diffraction limit: this is due to the fact that the coupling is nearest-neighbour

coupling, and there is poor discrimination against adjacent modes, [1-53], [1-54]. Another drawback of such configuration is the stability: as the operation current increases, variations in carrier profile, and therefore refractive index, change the optical path length of the different emitters. Constructive interference is no longer obtained and the device begins to operate in multiple spatial modes.

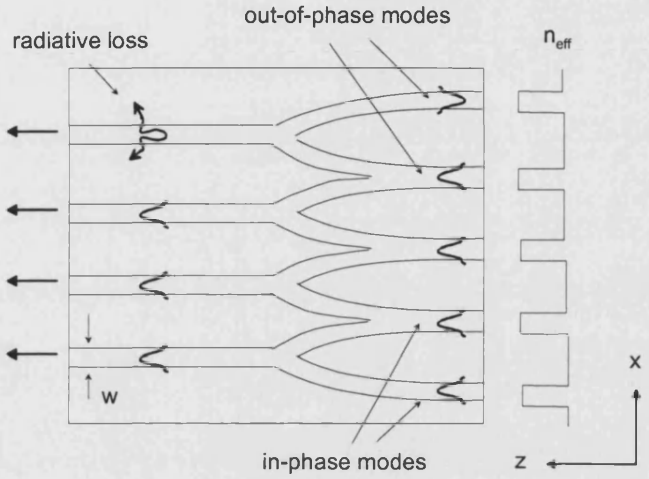


**Fig. 1.7: Top view schematic representation of a Y-junction laser array.**

Phase-locking can be obtained with resonant arrays of antiguides, also called resonant optical-waveguide (ROW) antiguided arrays, [1-55], [1-56], in which parallel coupling is achieved. Differently from the conventional arrays of stripes described at the beginning of this section, where the gain (and the optical field intensity) is higher in the regions where also the refractive index is higher, in ROWs the gain is higher in the regions where the refractive index is lower. Optical mode peaks, also, reside in these regions.

A schematic of the ROW structure is presented in Fig. 1.8. Carriers are injected into the low index regions and the light is generated into leaky modes, which resonantly couple between the high gain regions. However, antiguide arrays must meet a certain (lateral) optical resonance condition to provide strong discrimination against the out-of-phase mode, [1-43], and the fabrication tolerances on their structural parameters have been experimentally and theoretically determined to be very tight, especially if the number of elements increases, [1-57].

A similar device that employs antiguided structures is the three-core-antiresonant-reflective-optical waveguide (ARROW), [1-58], [1-59]. Arrays of ARROW waveguides can be considered complementary to ROW arrays in meeting resonance conditions. In such arrays effective parallel coupling and mode discrimination is obtained also by means of so called ARROW reflectors, placed in the high index region, that reduce the losses of the fundamental mode relatively to the loss of the first higher order mode.

Similarly to ROW arrays, in ARROW arrays the strong built-in refractive index step makes these devices immune to gain spatial hole-burning and other carrier- and thermal-induced index variations that degrade performance and reliability of broad area devices. In addition, the relatively small number of elements considerably eases fabrication tolerances, [1-57].

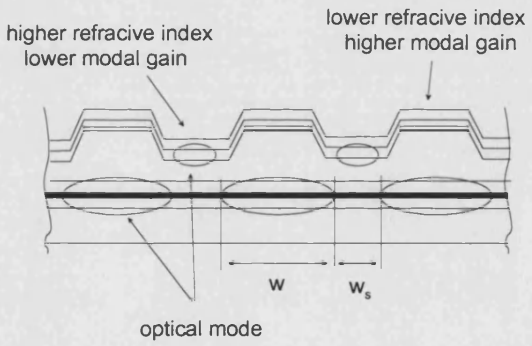


**Fig. 1.8: Schematic diagram of an array of closely spaced antiguides. The gain (and the optical field intensity) is higher in the regions where the refractive index is lower.**

The most relevant results from arrays of stripe lasers and phase-locked arrays described in this section are presented in Tab. 1.4.

**Tab. 1.4: Summary of results from arrays of stripe lasers. Sophisticated device fabrication is required to obtain coherent, in-phase, operation.**

| Device | Characteristics | References |
|---|---|---|
| Incoherent stripe laser arrays | 8W @ 12A (CW)<br>emitting aperture: 200μm<br>not diffraction-limited | D. F. Welch et al.,1998, [1-44] |
| | 72W @ 90A (CW)<br>emitting aperture:1600μm<br>not diffraction-limited | X. He et al.,1997, [1-45] |
| Incoherent α-DFB laser arrays | 20W @ 75A (CW), 14 elements<br>not diffraction-limited<br>Brightness: 1.4MWcm$^{-2}$sr$^{-1}$ @ 20W | A. Shoenfelder et al., 1997, [1-47] |
| Phase-locked Y-junction arrays | 0.2W (CW), 0.4W (pulsed)<br>10 elements, w=1.5μm<br>not diffraction-limited | D. F. Welch et al., 1987, [1-53] |
| Phase-locked ROW-arrays | 5W (pulsed), 0.3W (CW)<br>20 elements<br>near-diffraction-limited up to 1.6W (pulsed) | D. Botez et al., 1991, [1-55] |
| | 1W (CW)<br>20 elements, w=5μm<br>near-diffraction-limited | D. Zmundzinski et al., 1993, [1-56] |
| Phase-locked ARROW arrays | 0.4W @ 0.7A (CW)<br>3 elements, w=5μm<br>diffraction-limited | A. Bhattacharya et al., 1996, [1-58] |
| | 10W @ 0.7A (pulsed)<br>20 elements, w=4μm<br>near-diffraction-limited | H. Yang et al., 1996, [1-59] |

## 1.4 Arrays of Tapered Lasers

Arrays of tapered lasers have been demonstrated to be effective in achieving high power and good quality output beam. The first proposed array of tapered lasers consisted of incoherently coupled MOPAs similar to those depicted in Fig. 1.4, with a common Distributed Bragg Reflector (DBR) laser as Master Oscillator, [1-60]. Narrow output beam, although non diffraction-limited, was achieved; external optics was used to correct the field wavefront curvature and subsequently image the far-field pattern.

Arrays of incoherently combined gain-guided tapered lasers were also fabricated, [1-61], [1-62]. Diffraction-limit was not achieved and microlens arrays were used to collimate the beam of each emitter and correct them from astigmatism. Similarly to the MOPA array described above, after collimation the beams were combined with standard optics.

Incoherent arrays of index-guided linearly tapered lasers similar to those depicted in Fig. 1.5 a), were also demonstrated, [1-63]. Similarly to the arrays described above, in such arrays the separation between adjacent elements is such that the individual lasers are optically decoupled to achieve high output power and controllable output beam quality. In this case in fact, the output beam of the laser array is identical to that of an individual device and the advantage of the incoherent array configuration is mainly in the increase of output power.

In the context of index-guided tapered arrays for high power operation, Parabolic Bow-Tie Laser Arrays (PBTLAs), Fig. 1.9, have been developed, [1-64], [1-65], as the main aim of this PhD thesis, with the intention to achieve high power and simultaneously high brightness with a compact, low-cost device. The novelty of the PBTLAs relies on the fact that the individual tapered bow-tie lasers are coherently coupled with longitudinally non-uniform inter-element coupling (weak coupling along the length of the device and strong coupling at the output of the device). The longitudinally non-uniform coupling, combined with the mode-filtering effect of the central narrow sections, provides much improved scope to sustain in-phase operation, as discussed in details in Chapter 4 and in Chapter 6. A key advantage of the compact PBTLAs is that the narrow output beam is achieved without the use of external lenses.

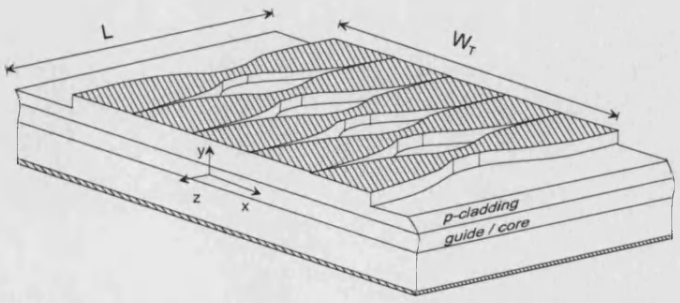


**Fig. 1.9: Schematic of a five-element Parabolic Bow-Tie Laser Array.**

The most relevant results from the tapered arrays described in this Section are presented in Tab. 1.5.

**Tab. 1.5: Summary of results from arrays of tapered devices.**

| Device | Characteristics | References |
|---|---|---|
| Incoherent MOPA arrays | 60W @ 80A (pulsed)<br>8 elements, $w_{out}$=315μm<br>not diffraction-limited | J. S. Osinski et al., [1-60] |
| | 25W @ 50A (CW)<br>25 elements, , $w_{out}$=200μm<br>not diffraction-limited | M. Mikulla et al., [1-61] |
| | 1.7W @ 18.5A (pulsed)<br>9 elements, $w_{out}$=140μm<br>not diffraction-limited | J. N. Walpole et al., [1-62] |
| Incoherent tapered laser arrays | 9W @ 14.5A (CW)<br>7 elements, $w_2$=30μm<br>not diffraction-limited | F. J. Wilson et al., [1-63] |
| Phase-locked Parabolic Bow-Tie laser arrays | 2.8W @ 3.6A (pulsed)<br>0.6W @1.2A (CW)<br>5 elements, $w_2$=20μm<br>near-diffraction-limited | F.Causa et al., [1-64]<br>D. Masanotti et al., [1-65] |

## Summary

Different categories of semiconductor lasers, proposed in literature for high power high brightness operation, have been reviewed. The intention has been to discuss the physical concepts behind the design of optical structures that support only one spatial mode but can produce high power output, and to describe their operational characteristics.

The challenges in designing high power semiconductor sources with high brightness reside in overcoming Catastrophic Optical Damage (COD), optical gain saturation, filamentation of the optical field and at the same time achieving the desired narrow output beam for high brightness. Narrow stripe laser diodes may be designed for high brightness, but the output power attainable with such sources is

limited by the device dimensions required to achieve single mode operation. Broad area lasers on the other hand produce high output powers but without high brightness and with the added inconvenience of being subject to temporal and spatial instabilities which further degrade the quality of the output beam.

Tapered geometry devices seem to be the most promising candidates when a reproducible and low-cost fabrication is a further requirement. Devices based on tapered gain-section, have demonstrated high beam quality at high power levels, but their performance is limited by beam filamentation. In addition systems of optics are needed to correct the beam divergence and to measure the emitted beam pattern. On the other hand mode stability can be achieved with index-guided tapered geometry: smaller devices dimensions are required to optimise the output beam characteristics, and therefore not very high powers can be achieved, but the added advantage is that no external lenses are needed to focus the beam as the output beam quality in this case depends on the device geometry.

Most high power diode lasers have been designed also as diode arrays, where the increase of the emitting area results in an increase of the achievable output power and at the same time in a further reduction of COD. However, the disadvantage of the increased transverse size of the active region is that in general it enables the simultaneous oscillation of multiple lateral modes, with a consequent decrease of the quality of the emitted beam. Single spatial mode operation can be obtained with phase-locked arrays of stripe lasers, although such devices generally require sophisticated device fabrication to sustain in-phase operation.

Recently, arrays of tapered devices have been proposed that allow for high power scaling and high quality beam. In particular, arrays of coherently coupled bow-tie lasers have been developed, that are also the main aim of the research work presented in this PhD thesis, that operate in a diffraction-limited beam and allow for higher powers as well as higher brightness.

# References

[1-1] B. Pederson, B. A. Thompson, S. Zemon, W. J. Miniscalco, T. Wei, *'Power requirements for Erbium-doped fibre amplifiers pumped in the 800, 980, 1480nm bands'*, IEEE Photon. Technol. Lett., vol. 4, n. 1, 1992, p. 46

[1-2] D. P. Bour, N. A. Dinkel, D. B. Gilbert, K. B. Fabian, M. G. Harvey, *'980nm diode laser for pumping $Er^{3+}$-doped fibre amplifiers'*, IEEE Photonics Technol. Lett., vol. 2, n. 153, 1990

[1-3] S. B. Alexander, E. S. Kintzer, J. C. Livas, J. N. Walpole, C. A. Wang, L. J. Missaggia, S. R. Chinn, *'1 Gbit/s coherent optical communication system Using a 1W optical power amplifier'*, Electron. Lett., vol. 29, 1993, p. 114

[1-4] P. Chazan, J. M. Mayor, S. Morgott, M. Mikulla, R. Kiefer, S. Müller, M. Whalter, J. Braunstein, G. Weimann, *'High-power near-diffraction-limited tapered amplifier at 1064nm for optical inter-satellite communications'*, IEEE Photon. Technol. Lett., vol. 10, 1998, p. 1542

[1-5] L. Goldberg, L. Busse, D. Meyus, *'Blue Light Generation by Frequency Doubling of AlGaAs Broad Area Amplifier Emission'*, Appl. Phys. Lett., vol. 60, 1992, p. 1037

[1-6] P. J. Williams, J. J. Lewandowski, D. J. Robbins, A. K. Wood, F. O. Robson, B. K. Nayar, *'Tapered laser arrays for high power operation (>1.4W CW) at 1.59μm for application in surgery'*, Electron. Lett., vol. 35, 1998, p. 993

[1-7] D. B. Carlin, Y. Tsunoda, *'Diode Lasers for Mass Marked Applications: Optical Recording and Printing'*, Proceedings of the IEEE , vol. 82, n. 4, 1994, p. 469

[1-8] S. M. Lord, G. W. Switzer, M. A. Krainak, *'Using Fibre Gratings to stabilise laser diode wavelength under modulation for atmospheric lidar transmitters'*, Electron. Letters, vol. 32, n. 6, 1996, p.561

[1-9] G. Beister, J. Maege, G. Erbert, L. Weixelbaum, M Weyers, J. Wurfl, O. P. Daga, *'Stability of Sulfur-Passivated Facets of InGaAs-AlGaAs Laser Diodes'*, IEEE Photon. Technol. Lett., vol. 8, n. 9, 1996, pp. 1124-1126.

[1-10] J. S. Yoo, H. H. Lee, P. Zory, *'Enhancement of Output Intensity Limit of Semiconductor Lasers by Chemical Passivation or Mirror Facets'*, IEEE Photon. Technol. Lett., vol. 3, n. 3, 1991, pp. 202-203.

[1-11] R. B. Swint, A. E. Huber, T. S. Yeoh, C. Y. Woo, J. J. Coleman, B. O. Faircloth, M. S. Zediker *'900-mW High Brightness Buried Ridge Lasers by Selective Area Epitaxy'*, IEEE Photon. Technol. Lett., vol. 3, n. 3, 1991, pp. 202-203.

[1-12] S. O'Brien, H. Zhao, A. Shoenfelder, R. Lang, *'9.3CW (In)AlGaAs 100μm wide lasers at 970nm'*, Electron. Lett., vol. 33, n. 22, 1997, pp. 1869-1870

[1-13] S. O'Brien, H. Zhao, R. Lang, *'High Power Wide Aperture AlGaAs-based lasers at 870nm'*, Electron. Lett., vol. 34, n. 2, 1998, pp. 184-186

[1-14] J. Guthrie, G. L. Tan, M. Ohkubo, T. Fukushima, Y. Ikegami, T.Ijichi, M. Irikawa, R. S. Mand, J. M. Xu, *'Beam instability in 980nm power lasers: experiment and analysis'*, IEEE Photon. Technol. Lett., vol. 6, n. 12, 1994, pp. 1409-1411

[1-15] R. J. Lang, A. G. Larsson, J. G. Cody, *'Lateral Modes of Broad Area Semiconductor Lasers: Theory and Experiments'*, IEEE J. Quantum Electron., vol. 27, n. 3, 1991, pp. 312-320

[1-16] D. C. Hall, M. R. Surette, L. Goldberg, D. Mehuys, *'Carrier-Induced Lensing in Broad-Area and Tapered Semiconductor Amplifiers'*, IEEE Photon. Technol. Lett., vol. 6, n. 2, 1994, pp. 186-188

[1-17] J. K. Lee, K. H. Park, D. H. Yang, H. S. Cho, E. S. Nam, K. E. P. Yun, J. Jeong *'Improvement of Kink and Beam Steering Characteristics of 0.98-μm GaInAs-GaInP High-Power Lasers Utilizing Channel Ion Implantation'*, IEEE Photon. Technol. Lett., vol. 12, n. 12, 2000, pp. 140-142.

[1-18] J. R. O'Callaghan, J. Houlihan, V. Voignier, G. H. Wu, E. O'Neill, J. G. McInerney, G. Huyet, *'Spatial Coherence and Thermal Lensing in Broad-Area Semiconductor Lasers'*, IEEE J. Quantum Electron., vol. 40, n. 1, 2004, pp. 1-9.

[1-19] G. C. Dente, *'Unstable resonator semiconductor lasers'* Lasers and Electro-Optics Society Annual Meeting, LEOS '93 Conference Proceedings. IEEE, 1993, pp. 596-597

[1-20] S. A. Biellak, C. Geoff, Y. Sun, S. S. Wong, A. E. Siegman, *'Reactive-Ion-Etched Diffraction-Limited Unstable Resonator Semiconductor Lasers'*, IEEE J. Quantum. Electron., vol. 33, n. 2, 1997, pp. 219-230.

[1-21] S. D. DeMars, K. M. Dzurko, R. J. Lang, D. F. Welch, D. R. Scifres, A. Hardy, *'Angled-grating distributed feedback laser with 1W CW single-mode diffraction-limited output at 980 nm'*, Summaries of Papers Presented at the Conference on Lasers and Electro-Optics, CLEO '96, 1996, pp. 77-78

[1-22] V. V. Wong, S. D. DeMars, A. Schoenfelder, R. J. Lang, *'Angle-grating distributed-feedback lasers with 1.2W CW single-mode diffraction-limited output at 1.06μm'* Summaries of Papers Presented at the Conference on Lasers and Electro-Optics, CLEO '99, 1999, pp. 46-47

[1-23] K. Paschke, R. Guther, J. Fricke, F. Bugge, G. Erbert, G. Trankle, *'High power and high spectral brightness in 1060nm α-DFB lasers with long resonators'*, Electron. Lett., vol. 39, n. 4, 2003, pp. 369-370

[1-24] D. Mehuys, L. Goldberg, D. F. Welch, *'5.23W CW Near-Diffraction-Limited Tapered-Stripe Semiconductor Optical Amplifier*, IEEE Photon. Technol. Lett., vol. 5, n. 10, 1993, pp. 1179-1182

[1-25] E. S. Kintzer, J. N. Walpole, S. R. Chinn, C. A. Wang, L. J. Missaggia, *'High-Power Strained-Layer Amplifiers and Lasers with Tapered Gain Regions'*, IEEE Photon. Technol. Lett., vol. 5, n. 6, 1993, pp. 605-608

[1-26] D. Mehuys, L. Goldberg, R. Waarts, D. F. Welch, *'4.5W CW, Near-Diffraction-Limited Tapered-Stripe Semiconductor Amplifier'*, Electron. Lett., vol. 29, n. 2, 1999, pp. 219-221

[1-27] S. O'Brien, A. Shoenfelder, R. J. Lang, *'5W CW Diffraction-Limited InGaAs Broad-Area Flared Amplifier at 970nm'*, IEEE Photon. Technol. Lett., vol. 9, n. 9, 1997, pp. 1217-1219

[1-28] S. O'Brien, D. F. Welch, R. Parke, D. Mehuys, K. Dzurko, R. Lang, R. Waarts, D. Scifres *'Operating Characteristics of a High-Power Monolitically Integrated Flared Amplifier Master Oscillator power Amplifier'*, IEEE Photon. Technol. Lett., vol. 29, n. 6, 1993, pp. 2052-2057

[1-29] J. P. Donnelly, J. N. Walpole, S. H. Groves, R. J. Bailey, L. J. Missaggia, A. Napoleone, R. E. Reeder, C. C. Cook, *'1.5-μm tapered-gain-region lasers*

*with high-CW output powers'*, IEEE Photon. Technol. Lett., vol. 10, n. 10, 1998, p. 1377-1379

[1-30] B. Sumpf, R. Hulsewede, G. Erbert, C. Dzionk, J. Fricke, A. Knauer, W. Pittroff, P. Ressel, J. Sebastian, H. Wenzel, G. Trankle, *'High-brightness 735 nm tapered diode lasers'*, Electron. Lett., vol. 38, n.4, 2001, pp. 183-184

[1-31] S. O'Brien, D. Mehuys, R. Lang, D. F. Welch, *'1W CW single frequency, diffraction-limited unstable resonator semiconductor laser with distributed Bragg reflector mirrors'*, Electron. Lett., vol. 31, n.3, 1995, pp. 203-205

[1-32] Y. Tanguy, V. Voignier, E. O'Neill, J. G. McInerney, G. Huyet, B. Corbett, *'Focusing properties of Semiconductor Lasers with Broad-Area and Shaped Unstable Resonators'*, IEEE Photon. Technol. Lett., vol. 15, n. 10, 2003, p. 637-639

[1-33] A. F. Milton, W. K. Burns, *'Mode Coupling in Optical Waveguide Horns'*, IEEE J. Quantum Electronics, vol. QE-13, n. 10, 1997, pp. 828-835.

[1-34] N. S. Brooks, *'Design and Development of Tapered Lasers'*, PhD Thesis, University of Bath, December 1998.

[1-35] N. S. Brooks, J. Sarma, I. Middlemast, *'A new design for tapered-geometry high-power semiconductor optical sources'*, Proceedings of the Conference on Laser and Electro-Optics Society, IEEE-LEOS'96, vol. 2, 1996, p. 207-208

[1-36] G. Bendelli, K. Komori, S. Arai, Y. Suematsu, *'A New structure for High Power TW-SLA'*, IEEE Photon. Technol. Lett., vol. 3, n. 1, 1991, pp. 42-44

[1-37] P. G. Suchosky Jr, R. V. Ramaswamy, *'Design of Single-Mode Step-Tapered Waeguide Sections'*, IEEE J. Quantum Electron., vol. QE-23, n. 2, 1992, pp. 205-211

[1-38] D. Masanotti, F. Causa, J. Sarma, *'Design optimisation of high power high brightness parabolic bow-tie laser diodes'*, IEE Proceedings - Circuits, Devices and Systems, vol. 150, n. 6, 2003, pp. 537-541

[1-39] D. Masanotti, F. Causa, J. Sarma, *'High brightness, index-guided Parabolic Bow-Tie laser diodes'*, IEE Proceedings Optoelectronics, vol. 151, n. 2, p. 123, 2004

[1-40] G. Bendelli, K. Komori, S. Arai, *'Gain saturation and propagation characteristics of index-guided tapered-waveguide travelling-wave semiconductor laser amplifiers (TTW-SLA's)'*, IEEE J. Quantum Electron., vol. 28, n. 2, pp. 447-458, 1992

[1-41] I. Middlemast, J. Sarma, P. S. Spencer, *'Output Characteristics of high power GaAs/GaAlAs Double Heterostructure Rib-Waveguide Bow-Tie Lasers'*, Integrated Photonic Research, vol. 6, OSA technical Digest Series, 1996, p. 534

[1-42] M. Krakowski S. C. Auzanneau, F. Berlie, M. Calligaro, Y. Robert, O. Parillaud, M. Lecomte, *'1W high brightness index guided tapered laser at 980nm using Al-free active region materials'*, Electronics Letters, vol. 39, n. 15, p. 1122, 2003

[1-43] D. Botez, D. Scifres, *Diode Laser Arrays*, Cambridge University Press (1994).

[1-44] D. F. Welch, B. Chan, W. Streifer, D. R. Scifres, *'8W CW, Single-Quantum-Well Laser Diode Array'*, Electron. Lett., vol. 24, n. 2, 1998, pp. 113-115

[1-45] X. He, M. Ung, S. Srinivasan, R. Patel, *'155W CW Optical Power from 1cm monolithic AlGaAs/InGaAs Laser Diode Array'*, Electron. Lett., vol. 23, n. 14, 1997, pp. 1221-1222

[1-46] V. V. Wong, A. Schoenfelder, S. O'Brien, S. D. DeMars, R. J. Lang, *'High-Brightness αDBF Arrays at 915nm and 1.06μm'*, Summaries of Papers Presented at the Conference on Lasers and Electro-Optics, CLEO '96, 1996, pp. 46-47

[1-47] A. Schoenfelder, S. D. DeMars, S. O'Brien, R. J. Lang, *'20W high-brightness angled-grating DFB laser array'*, Summaries of Papers Presented at the Conference on Lasers and Electro-Optics, CLEO '97, 1997, pp. 1

[1-48] A. Schoenfelder, M. Staksus, M.Carico, S. D. DeMars, R. J. Lang, *'2D High-Brightness Laser Diode Array'*, Summaries of Papers Presented at the Conference on Lasers and Electro-Optics, CLEO '97, 1997, pp. 480-481

[1-49] G. A. Evans, J. M. Hammer, *Surface Emitting Semiconductor Lasers and Arrays*, New York Academic Press (1993).

[1-50] G. H. B. Thompson, J. E. A. Whiteaway, *'Analysis of the Stability of the Highest-Order Supermode in Semiconductor Laser Arrays'*, Electronics Letters, vol. 23, n. 9, Apr. 1987, pp. 444-446.

[1-51] E. Kapon, *'Non-Uniform Phased-Arrays of Diode lasers'*, Electronics Letters, vol. 23, No. 17, Aug 1987, pp. 879-881.

[1-52] W. Streifer, A. Hardy, R. D. Burnham, R. L. Thornton, D. R. Scifres, *'Criteria for Design of Single-Lobe Phased-Array Diode Lasers'*, Electronics Letters, vol. 21, n. 11, 1985, pp. 505-506.

[1-53] D. F. Welch, W. Streifer, P. S. Cross, D. R. Scifres, *'Y-Junction Semiconductor Laser Arrays: Part II - Experiments'*, IEEE J. Quantum Electronics, vol. 23, 1987, pp. 752-756.

[1-54] W. Streifer, A. Hardy, D. F. Welch, D. R. Scifres, P. S. Cross, *'Improved Y-X Junction Laser Array'*, Electronics Letters, vol. 26, n. 20, 1990, pp. 1730-1731.

[1-55] D. Botez, M. Jansen, L. J. Mawst, G. Peterson, T. Roth, *'Watt-range, coherent, uniphase powers from phase-locked arrays of antiguided diode lasers'*, Appl. Phys. Lett, vol. 58, n. 19, 1991, pp. 2070-2072

[1-56] C. Zmundzinski, D. Botez, L. J. Mawst, C. Tu, L. Frantz, *'Coherent 1W continuous wave operation of large-aperture resonant arrays of antiguided lasers'*, Appl. Phys. Lett, vol. 63, n. 23, 1993, pp. 2914-2916

[1-57] D. Botez, A. Napartovich, C. Zmudzinski, *'Phase-Locked Arrays of Antiguides: Analytical Theory II'*, IEEE J. Quantum Electronics, vol. 31, 1995, pp. 244-253.

[1-58] A. Bhattacharya, l. J. Mawst, M. P. Nesnidal, J. Lopez, D. Botez, *'0.4W CW diffraction limited beam Al free 0.98μm wavelength three core ARROW-type diode lasers'*, Electronics Letters, vol. 32, n. 7, 1996, pp. 657-658.

[1-59] H. Yang, L. J. Mawst, M. P. Nesnidal, J. Lopez, A. Bhattacharya, D. Botez, *'10 W near-diffraction-limited peak pulsed power from Al-free, 0.98μm-emitting phase-locked antiguided arrays'*, Electronics Letters, vol. 33, n. 2, 1996, pp. 136-137

[1-60] J. S. Osinski, D. Mehuys, D. F. Welch, K. M. Dzurko, R. J. Lang, *'High-power, spectrally coherent arrays of monolithic flared amplifier-Master*

*Oscillator Power Amplifiers (MFA-MOPAs)'*, IEEE Photonics Technology Letters, vol. 6, n. 10, 1994, pp. 1185-1187

[1-61] M. Mikulla, A. Schmitt, M. Walther, R. Kiefer, W. Pletschen, J. Braunstein, G. Weimann, *'25-W CW high-brightness tapered semiconductor laser-array'*, IEEE Photonics Technology Letters, vol. 11, n. 4, 1999, pp. 412-414

[1-62] J. N. Walpole, H. K. Choi, L. J. Missaggia, Z. L. Liau, M. K. Connors, G. W. Turner, M. J. Manfra, *'High-Power High-Brightness GaInAsSb-AlGaAsSb Tapered Laser Arrays with Anamorphic Collimating Lenses Emitting at 2.05μm'*, IEEE Photonics Technology Letters, vol. 11, n. 10, 1999, pp. 1223-1225

[1-63] F. J. Wilson, J. J. Lewandowski, B. K. Nayar, D. J. Robbins, P. J. Williams, N. Carr, F. O. Robson, *'9.5W CW output power from high brightness 980nm InGaAs/AlGaAs tapered laser arrays'*, Electronics Letters, vol. 35, n. 1, 1999, pp. 43-44

[1-64] F. Causa, D. Masanotti, *'High brightness index-guided Parabolic Bow-Tie Laser Arrays'*, IEEE Photon. Technol. Lett., vol. 16, n. 9, 2004, pp. 2000-2002

[1-65] D. Masanotti, F. Causa, *'Optical guiding properties of high brightness Parabolic Bow-Tie Laser Arrays'*, IEEE J. Quantum Electron., vol. 41, n. 7, July 2005, pp. 909-916

# Chapter 2

# *Beam Quality*

Semiconductor laser diodes, for their small size, robustness, low-cost, high electrical-to-optical power (Wall-Plug) efficiency and lifetime have the potential to become integrated within optoelectronic and telecommunication subsystems, and therefore to replace other bulkier lasers in many scientific and industrial applications. However, stable power output and beam quality are required for most of the applications. In summary, high power laser beams with high spatial quality and stability are essential.

It is therefore important to be able to identify and analyse the possible factors that can limit obtainable power output and that can affect the beam quality of high-power semiconductor lasers. In addition, it is useful to define rigorous parameters, independent from the source under test, that can describe the quality of the laser emitted beam and that can be used to compare the performances of systems with different characteristics.

## 2.1 Factors Responsible for Output Beam Degradation

Mainly in broad area semiconductor diode lasers, the non-linear interaction between the carrier density in the device active region and the amplified optical wave has a strong impact on laser output power, efficiency and reliability, and is one of the main reasons for the deterioration of the beam quality. The factors that determine the laser beam quality are discussed in detail in this Section.

### 2.1.1 Multimode Operation

Multimode operation is the onset of higher-order spatial modes that causes a distortion of the far-field radiation pattern of the laser, but also one of the main limitations on the effective optical output power achievable. Broad area lasers are

naturally prone to multimode operation as the number of allowed modes generally depends on the laser size. However another physical phenomenon that gives rise to the simultaneous oscillation of two or more spatial modes is the perturbation of the waveguide refractive index or gain profile caused by inhomogeneities in the local carrier population or temperature, [2-1]-[2-3].

The simultaneous oscillation of several transverse modes, and in particularly the transition from the fundamental to the higher ones, usually yields to discontinuities (the so called "kinks") in output power or slope of the light-current curve and to distortion of the far-field profile that looses the typical single-lobed shape, [2-3], [2-4]. For most lasers, operating through these modal kinks is typically a non-catastrophic event and changes are reversible. However decrease in the lasers efficiency, and therefore in the achievable output power, is possible.

### 2.1.2 Gain Saturation and Filamentation

The performance of lasers diodes can be limited also because of the maximum gain achievable in the semiconductor medium and because of the spontaneous deterioration of the beam into narrow filaments. Both phenomena are a consequence of the coupling of gain and refractive index within the semiconductor, typical of active optical sources, and have enormous implications at high power operation especially in broad area gain-guided lasers, [2-1], [2-2], [2-5].

Gain saturation is the process whereby stimulated emission decreases the carrier population, and in turn the laser gain, from its unsaturated value. The unsaturated modal gain is the gain when no photons are present, i.e., when lasing has not occurred yet, and can approximated, near threshold, by the equation, [2-5]-[2-7]:

$$g(x) = \Gamma_{QW}\hat{\beta}(J(x) - J_{tr}) \qquad (2.1)$$

where $\Gamma_{QW}$ is the optical confinement factor in the active region, $\hat{\beta}$ the differential gain, J(x) the current density profile and $J_{tr}$ the current density at transparency, [Appendix A].

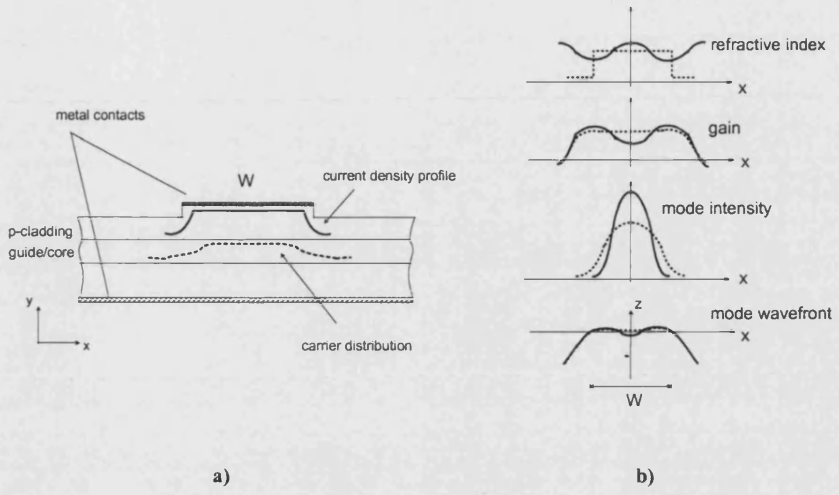


**Fig. 2.1: Stripe laser: a) schematic diagram showing current density profile and carrier distribution at threshold, and b) self-focusing resulting from gain saturation above threshold. Refractive index profile, gain, mode intensity and wavefront are shown below (dashed line) and above (solid line) threshold, [2-8].**

As laser threshold is surpassed, the modal gain becomes clamped at the level of the resonator losses, as is required for the steady-state carrier population. The dependence of modal gain (and carrier density) on field intensity is manifest in the reduction of modal gain due to gain saturation when photons are present. In particular, where the optical intensity is higher, the carrier density has a local minimum, implying locally decreased gain. The spatially varying gain profile can be described as, [2-5]:

$$g(x) = \frac{\Gamma_{QW}\hat{\beta}(J - J_{tr})}{(1 + P(x)/P_{sat})} \tag{2.2}$$

where $P(x)$ is the optical power density along the lateral dimension and $P_{sat}$ is the saturation power density, given by:

$$P_{sat} = \frac{hc}{\lambda q}\frac{\eta_i}{\Gamma_{QW}\hat{\beta}} \tag{2.3}$$

where h is the Plank's constant, q the electronic charge, $\lambda$ the laser emitting wavelength and $\eta_i$ the internal quantum efficiency, [Appendix A].

The effect of gain saturation in the case of fundamental mode propagation within a stripe-geometry laser is depicted in Fig. 2.1. The spatially varying gain profile yields to a spatially varying refractive index profile: the refractive index increases, in fact, where the carrier depletion is higher. This is the essence of the non-linear interaction between the laser optical field and the semiconductor material that determines the laser beam quality, [2-8]. The increase of the refractive index, above threshold, where the optical intensity is highest, creates a local refractive index waveguide: the mode is further narrowed and its peak intensity increases. This 'self-focusing' mechanism, combined with the local further decrease of the gain, referred to as Spatial Hole Burning (SHB), are collectively termed 'filamentation' because of their tendency to focus broader beams down into narrow filament like propagating streams of light, [2-8].

### 2.1.3 Beam Steering

Another fundamental problem that frequently limits the usable output power from high power laser diodes is the lateral steering of the radiated beam. Lateral beam steering is the peak shift of the lateral far-field pattern from side to side. Even when the total power emitted by the laser is free of other non-linearities due to high injection current, beam steering can eventually compromise the efficiency with which the laser emission can be coupled to an optical fibre, for example in optical pumping applications resulting in kinks in the (fibre) coupled power characteristic.

One of the mechanisms responsible for emission non-linearities such as beam steering is, in general, the lateral spatial hole burning (SHB), [2-9]. As the injection current increases, to compensate for the effect of localised gain saturation by the fundamental lateral mode, the local gain increases away from the cavity axis, turning into a double peaked profile which favours higher order lateral modes to be excited.

Support for the hypothesis that beam steering of the far-field pattern can be a result of the co-excitation of multiple lateral modes is obtained from numerical simulations, [2-9], and experimental observations, [2-4], that as the higher modes begin to lase, changes in the slope efficiency of the device and the fibre coupled L-I characteristic appear.

It has generally been recognised in literature that maintaining truly single (lateral) mode operation is important to avoid beam steering problems, [2-9]. Hence, the occurrence of beam steering and kinks is more serious in most high power lasers as the ridge width is increased to avoid catastrophic optical damage (COD). In fact, as described in the preceding section, at higher currents broad waveguides become inherently more sensitive to the effect of significant perturbations by injected carriers and to lateral SHB, and eventually lase on multiple lateral modes.

### 2.1.4 Thermal Rollover

Thermal roll-over consists of a slow decrease in the laser efficiency, with increased current injection, caused by the increased fraction of ohmic loss incurred at high drive levels. This increase in ohmic loss results in increased heat dissipated near the p-n junction, raising the temperature of the active region and lowering its conversion efficiency, [2-8].

The variation of the differential external quantum efficiency $\eta_e$ and the threshold current $I_{th}$ for a specific rise $\Delta T$ of the junction temperature, with respect to the temperature $T_h$ of the heatsink, are given respectively by, [2-8], [2-10], [2-11]:

$$\eta_e(T_h + \Delta T) = \eta_e(T_h)\exp\left(-\frac{\Delta T}{T_1}\right) \tag{2.4}$$

and

$$I_{th}(T_h + \Delta T) = I_{th}(T_h)\exp\left(\frac{\Delta T}{T_0}\right) \tag{2.5}$$

where $T_1$ and $T_0$ are the characteristic temperature coefficients for $\eta_e$ e $I_{th}$, respectively. The measured $T_0$ for (InGa)As/AlGaAs quantum well lasers, that are of interest in this PhD work, is in the range from 100°C to 200°C, [2-8]. The values for $T_1$ are usually a factor of three to five higher than $T_0$, [2-12], [2-13].

The increase of temperature eventually results in the saturation of the optical output that even decreases with increasing current. From equations (2.4) and (2.5), the expression for the corresponding maximum optical power achievable, $P_{max}$, is:

$$P_{max}(T_h + \Delta T) = \eta_e(T_h)\exp\left(-\frac{\Delta T}{T_1}\right)\left[I - I_{th}(T)\exp\left(\frac{\Delta T}{T_0}\right)\right] \quad (2.6)$$

A principal reason for the decreased optical output after saturation is the increased spillage of charge carriers out the active region, [2-13], into the barriers or cladding layers, where they cannot contribute to recombination. As the temperature rise becomes dramatic, the laser gain decreases at fixed current density eventually causing the optical output to diminish to near zero. Thermal rollover, like multimode operation, is usually not a catastrophic event but is reversible.

### 2.1.5 Astigmatism

Astigmatism is an inherent property of the output beam of gain-guided diode lasers. It is the difference between the guiding mechanisms in the direction parallel and perpendicular to the junction plane that determines how much astigmatism will be present at the output facet of a diode laser, [2-12].

In applications requiring collimation or transformation of beams, the astigmatism must be corrected by additional optics, if the final wavefront is to approach the diffraction-limit, [2-14], [2-15].

In index-guided diode lasers index-guiding is the principal guiding mechanism in both directions parallel and perpendicular to the junction plane. In these lasers the phase front of the optical wave is flat in both directions, and the emitted beam has its origins (waists) located at the output facet of the waveguide.

In gain-guided diode lasers, index-guiding is the mechanism perpendicular to the junction plane whereas gain-guiding is the mechanism parallel to the junction plane. In this type of lasers the effect of the gain on the guided mode yields to a divergent phase front imposed on the beam as it propagates in the longitudinal direction along the cavity.

In gain guided-lasers, Fig. 2.2, the beam waist (or virtual source point) perpendicular to the junction is located at the output facet of the diode laser, but the waist parallel to the junction plane is placed, from Snell's law, at a distance $d_A=L/n_{eff}$

inside the device, with L the device length and $n_{eff}$ the effective refractive index. The distance between the two waists is the longitudinal astigmatism, [2-15].

The longitudinal position of this virtual source point can be affected to a small degree by lensing due to thermal gradients and carrier density gradients from non-uniform gain saturation across the width of the device.

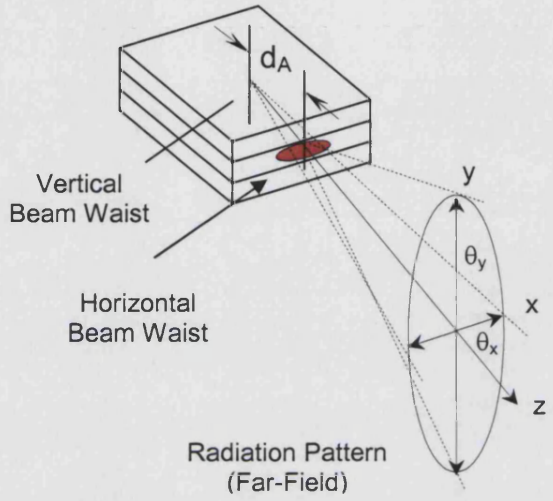


**Fig. 2.2: Diagram showing the amount of astigmatism $d_A$ in a semiconductor laser diode.**

For gain-guided devices the effective far-field pattern can be measured only after correcting the astigmatism by using additional optics, [2-8], [2-14], [2-15], that have to be chosen depending on the amount of astigmatism. Hence, it is very important that that astigmatism is stable against changes in the device operation conditions.

Astigmatism can sometimes occur also in index-guided devices, at high-power operation, in presence of non-uniform gain profile due to gain saturation.

### 2.1.6 Catastrophic Optical Damage

Catastrophic Optical Damage (COD) is the main failure mode of high-power semiconductor lasers and refers to irreversible damage of the laser facets caused by heating due to high optical density, [2-8].

The semiconductor crystal terminates at the cleaved laser facet and dangling bonds of surface layer atoms give rise to defect states. Surface recombination of

electrons and holes via these states reflects in emission of heat instead of light, this causing the active region near the facet to become absorbing at the lasing wavelength. Also simple impurities present on the laser facet, that usually do not interact chemically with the semiconductor, may still absorb laser radiation and give rise to localized heating.

In either cases, facet heating and the increase of the local temperature result in a decrease of the bandgap energy. Consequently, the optical absorption increases leading to further non-radiative recombination-induced heating. Eventually, such cycle undergoes thermal run-away, and as the temperature reaches the material melting point, the facet is mechanically damaged, its reflectivity drops, and the laser output is diminished irreversibly. In AlGaAs lasers with uncoated facets the optical power density achievable before COD, [Appendix D], is approximately 1-5MWcm$^{-2}$. However, facet coating and passivation techniques can increase this critical value to approximately 10-20MWcm$^{-2}$, [2-8].

### 2.1.7 Aging

One final limitation to the output power of a semiconductor laser is aging. All semiconductor lasers exhibit some degradation in optical output if operated at constant current and temperature for extended periods of time. Aging behaviour and the associated reliability of a given semiconductor laser are highly dependent upon its structure and operating conditions.

Semiconductor laser reliability is usually limited by thermal dissipation, high current density or COD. Thermal and current density induced degradation mechanisms are associated with the formation of point defects, which can migrate into and along the active region, degrading the laser output over time. Often, the lifetime of a laser is specified as the number of hours at which a specified output power can be maintained with the operating current being increased only by some defined percentage of the initial value, [2-12].

## 2.2 Beam Quality Characterisation

Of highest importance for high power diode laser designed to achieve also high brightness are the spatial properties of the output beam. An ideal laser would generate a laser beam with Gaussian intensity distribution in both transverse dimensions at any point along the beam. Such distribution is in fact characterised by the highest possible spatial beam quality as focusing of the beam generates the smallest beam cross section in the focus; in addition, with a given focal cross section a Gaussian beam possesses the lowest divergence upon propagation.

A complete characterisation of a laser beam involves the measurement of the two-dimensional field intensity and phase distribution across the plane through which the laser emits, as well as the measurement of the radiated beam pattern.

An overview of the different parameters and definitions that should be used to fully characterise and define the quality of a laser beam is given in this Section.

### 2.2.1 Far-Field Pattern

The intensity pattern of the laser emitted beam, or far-field, $I(x,y,z)$, Fig. 2.3, is the diffraction of the laser optical field from the laser aperture and corresponds to the Fourier transform of the near-field distribution. Considering a general 2-dimensional near-field complex amplitude distribution $E(x',y')$ at the laser output facet, the far-field intensity profile is given by, [2-8]:

$$I(x,y,z)=\left(\frac{1}{\lambda z}\right)^2\left|\int_{-\infty}^{+\infty}\int_{-\infty}^{+\infty}E(x',y')\exp\left[j\frac{2\pi}{\lambda z}(xx'+yy')\right]dx'dy'\right|^2 \qquad (2.7)$$

The far-field intensity profile is the most commonly used 'reference' to measure experimentally the quality of the output beam and it is very important to characterise it in both directions, parallel (or lateral, along the x-direction) and perpendicular (or vertical, along the y-direction) to the semiconductor junction plane.

The lateral and vertical widths of the far-field beam at Full Width Half Maximum (FWHM), i.e., where the output power is half of its maximum, are expressed by the quantities $\theta_x$ and $\theta_y$. The laser active region height $d_{QW}$ is usually

very small compared to its lateral width W, thus the vertical divergence is bigger than the lateral one.

It is important to note that the far-field profile can be optimised by properly designing both the multilayer semiconductor structure (which determines the vertical far-field profile) and the device geometry (which determines the lateral far-field profile).

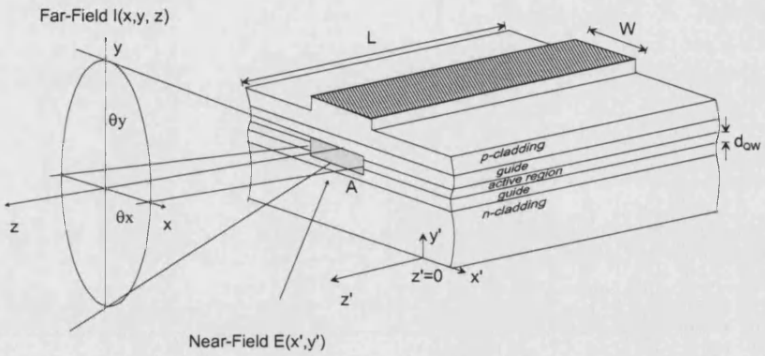


**Fig. 2.3: Schematic diagram of a semiconductor laser showing the definition of the active region width W and height $d_{QW}$, and the far-field divergences at FWHM, $\theta_x$ and $\theta_y$.**

Assuming that the total near-field spatial distribution at the output facet can be described as a function of the transverse coordinates x and y separately, the near-field variation along, for example, the lateral (x) direction can be expressed by E(x'). In spherical coordinates, substituting $z = r\cos\theta$ and $x = r\sin\theta$ in equation (2.7), the far-field profile in the horizontal plane can be then expressed as, [2-11]:

$$\hat{I}_x(\theta) \propto \cos^2(\theta)\left|\int_{-\infty}^{+\infty} E(x')\exp[jk_0 x'\sin(\theta)]dx'\right|^2 \qquad (2.8)$$

Similarly for the vertical (y) direction.

The importance of the profile described from equation (2.8) resides in the fact that, since it does not depend on the specific distance z, it is simpler to be evaluated or measured. Such profile has been considered in this PhD thesis for both the theoretical analysis and the experimental characterisation of the laser radiated beam.

### 2.2.2 Beam Divergence

The beam divergence, also called directionality, of any light source, corresponds to the degree of beam diffraction at a very large distance from the source, [2-16].

Sources with perfect spatial coherence, which are characterised by constant amplitude and uniform phase, are characterised by minimum diffraction (i.e. by the smallest beam divergence) and therefore commonly referred to as *diffraction-limited*, [2-16]. The corresponding divergence angle is defined as the diffraction-limit angle $\theta_d$.

Diffraction of Gaussian beams

Gaussian beams are ideal, coherent beams and their intensity profile, in a plane normal to the direction (z) of propagation, Fig. 2.4, has the form, [2-17]:

$$I_G(x,y,z) = I_{G0} \exp\left[-2\frac{(x^2+y^2)}{w}\right] \tag{2.9}$$

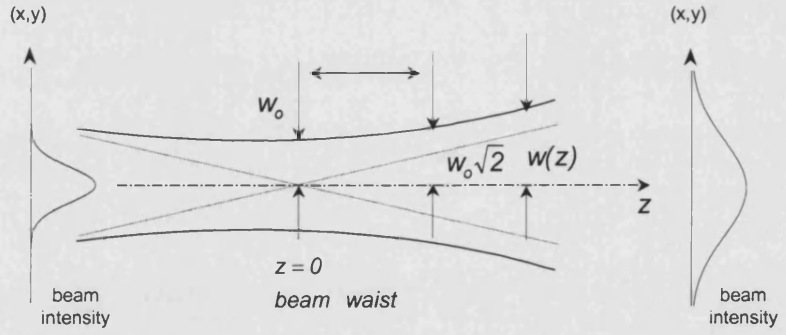


**Fig. 2.4: Propagation and variation of the spot size of a gaussian beam, [2-17].**

At a lateral distance w from the propagation axis, the intensity is a factor $e^2 = 7.389$ smaller than its value on axis, $I_{G0}$. If the beam is projected on a screen at a specific distance $\bar{z}$ a spot of radius $\bar{w}$ can be seen, corresponding to the spot size of the Gaussian beam in that position.

The beam spot size $w(z)$ has a minimum value $w_0$, called beam waist, at $z = 0$ and grows with distance z from this plane according to, [2-17]:

$$w(z) = w_0\sqrt{1+\frac{z^2}{z_0^2}} \tag{2.10}$$

where $z_0$, defined as:

$$z_0 = \frac{\pi w_0^2}{\lambda} \tag{2.11}$$

is known as the Rayleigh range and is a measure of the length of the so-called waist region, where the spot size is the smallest, being $w(z) \leq w_0\sqrt{2}$. The smaller the spot size $w_0$ at the beam waist, the smaller the Rayleigh range $z_0$, and thus the greater the rate of growth with z of the spot size from the waist. This is similar to what happens when a plane wave is diffracted by an aperture: the smaller the aperture diameter, the greater the diffracted beam.

Substitution of equation (2.11) in equation (2.10) gives the free-space propagation equation for a Gaussian beam, [2-16]:

$$w^2(z) = w_0^2 + \frac{\lambda^2}{\pi^2 w_0^2}(z - z_0)^2 \tag{2.12}$$

From equation (2.10) it follows that the divergence of a gaussian beam, corresponding to its diffraction-limit angle, at large distance z from the waist (i.e., for $\lambda z/\pi w_0^2 >> 1$, so that $w \cong \lambda z/\pi w_0$) is given by:

$$\theta_{Gd} = \frac{w}{z} = \frac{\lambda}{\pi w_0} \tag{2.13}$$

It is interesting to compare the result of equation (2.13) with the lateral divergence, or diffraction-limit angle, of a coherent source irradiated from a circular aperture (equivalently defined as diffraction from a uniformly illuminated circular aperture), [2-18]:

$$\theta_{Cd} = 1.22\frac{\lambda}{D} \tag{2.14}$$

where D is the diameter of the aperture, corresponding to the width of the beam. Following the convention of identifying the radius of the Gaussian beam with its spot size, and assuming $D = 2w_0$ then a comparison of equation (2.14) with equation (2.13) indicates that a Gaussian beam has divergence about half of that of a plane wave.

Diffraction of a uniformly illuminated rectangular aperture

With reference to equation (2.7), the diffraction of coherent beam from a rectangular aperture (equivalently defined as diffraction from a uniformly illuminated rectangular aperture) with lateral (x) dimension D and vertical (y) dimension d (corresponding to the lateral and vertical width of the beam), at a distance z from the aperture, is given by, [2-18]:

$$I_R(x,y,z) = \left(\frac{1}{\lambda z}\right)^2 \left[\frac{\sin(kDx/2z)}{kDx/2z}\frac{\sin(kdy/2z)}{kdy/2z}\right]^2 I_0 \tag{2.15}$$

The diffraction pattern described by equation (2.15), projected on a screen positioned in $z = \bar{z}$, consists of an elliptical central zone of maximum (on axis) intensity $I_0$ and surrounded by a series of ellipses of decreasing intensity, Fig. 2.5. The lateral and vertical divergence angles of the original beam can be defined as corresponding to the radius of the first nulls, in the x- and y-direction respectively, [2-16]. Considering only the profile in lateral direction, the first null is in

$$\theta_{Rx} \approx \arcsin\left(\frac{x}{\bar{z}}\right) = \arcsin\left(\frac{\lambda}{D}\right) \tag{2.16}$$

The first null in the y plane is of the same form as (2.16) by replacing D with d:

$$\theta_{Ry} \approx \arcsin\left(\frac{y}{\bar{z}}\right) = \arcsin\left(\frac{\lambda}{d}\right) \tag{2.17}$$

Using the same notation as in equations (2.13) and (2.14), $\theta_{Rx}$ and $\theta_{Ry}$ correspond to the diffraction-limit angles $\theta_{Rdx}$ and $\theta_{Rdy}$.

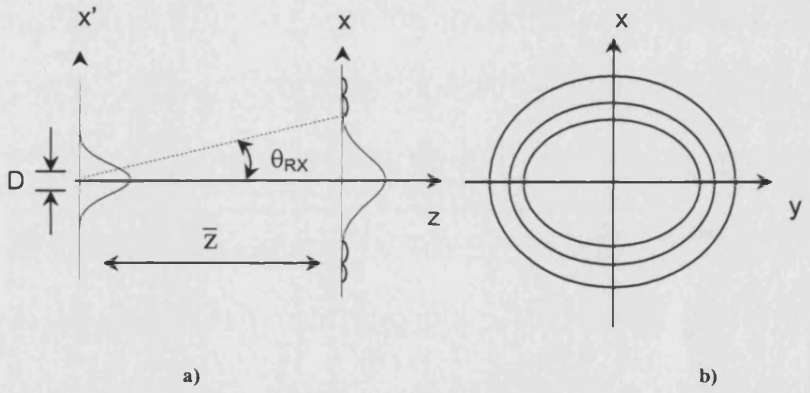


**Fig. 2.5: Diffraction from a uniformly illuminated rectangular aperture, a) top view, b) diffraction intensity pattern in the far-field, consisting of elliptic concentring spots.**

Directionality of laser radiation

The directionality of laser beams is related to their spatial coherence. Consider lasers with rectangular emission aperture, which are of interest in this PhD thesis, Fig. 2.3. From the theory of diffraction, for a spatially coherent beam diffracting from a rectangular aperture with lateral (x) dimension D, the lateral divergence angle would be expressed by equation (2.16) and would be diffraction-limited. However, if the laser beam is characterised by only partial spatial coherence, i.e., is coherent only over distances $D_c < D$ across the beam, then the divergence angle is:

$$\theta_{Lx} \sim \frac{\lambda}{D_c} > \frac{\lambda}{D} = \theta_{Rdx} \tag{2.18}$$

greater than in the totally spatially coherent case with the same intensity distribution.

Because of diffraction, a laser beam can never have divergence angle of zero. However, the beam divergence is minimised if the beam is spatially coherent. In this case, since the diffraction sets the ultimate lower limit on the beam spread, it can be said that the diffraction-limit has been reached, [2-16].

### 2.2.3 Brightness

Consider a laser source similar to that depicted in Fig. 2.3. The brightness, or radiance, B of such optical source is defined as the emitted power per unit area per solid angle, [2-8]:

$$B = \frac{P}{w_{NF} W_{NF} \theta_x \theta_y} \tag{2.19}$$

where P is total output power, and $w_{NF}$ and $W_{NF}$ are the near-field vertical and lateral widths respectively. When such values are not available, the dimensions $d_{QW}$ and W of the emitting aperture can be considered. $\theta_x$ and $\theta_y$ are, respectively, the far-field lateral and vertical divergence at FWHM.

The highest brightness is achieved when the divergence of the radiation pattern at FWHM is diffraction-limited. From equation (2.16) with $d=w_{NF}$ and $D=W_{NF}$, and from equation (2.19) it follows that:

$$B = \frac{P}{\lambda^2} \tag{2.20}$$

A fundamental theorem in optics states that the brightness of a source is an invariant quantity, unchangeable by a lens or any other passive optical system, [2-17]. The intensity of the beam can be increased by focusing, but the brightness

cannot. This concept is useful in practical applications, especially in systems where additional optics needs to be used to characterise the radiated beam, [2-14], [2-15].

To demonstrate the above concept, consider a Gaussian beams. From equation (2.13), the solid angle $\Omega$ of the Gaussian beam, corresponding to the product $\theta_x\theta_y$ is:

$$\Omega = \pi\theta_{Gd}^2 = \frac{\lambda^2}{\pi w_0^2} \tag{2.21}$$

Considering that the beam area, corresponding to the product dD, is $\pi w_0^2$, from equation (2.19) and (2.21) it follows that the brightness for a Gaussian beam is:

$$B = \frac{P}{\lambda^2} \tag{2.22}$$

where P is the total power transported by the beam. Equation (2.22) confirms the result in equation (2.20) and states that the brightness of a Gaussian beam does not change as it propagates.

In addition, importantly, the intensity that can be obtained in the focal plane of the lens is proportional to the brightness of the beam. To explain such statement, consider the peak intensity of a (lowest-order) Gaussian beam at its waist, [2-17]:

$$I_{max} = \frac{2P}{\pi w_0^2} \tag{2.23}$$

With a lens of focal length f we can focus the beam down to a spot size $w_f$, in the focal plane of the lens, [2-17]:

$$w_f = \frac{\lambda f}{\pi w_0} \tag{2.24}$$

The focused beam is still Gaussian, and so its peak intensity is given by equation (2.23) with $w_0$ replaced by $w_f$:

$$I_{max}(f) = \frac{2P}{\pi w_f^2} = \frac{2P}{f^2}\frac{\pi w_0^2}{\lambda^2} = \frac{2P}{f^2\Omega} \tag{2.25}$$

where $\Omega$, from equation (2.21), is the solid-angle divergence of the unfocused beam.

From the combination of equation (2.25) and equation (2.22) it follows that:

$$I_{max}(f) = \frac{2P}{\pi w_f^2} = 2\frac{B}{f^2}\frac{\lambda^2}{\Omega} \tag{2.26}$$

This result indicates that, for a beam of given power and area, the intensity that can be obtained by focusing is directly proportional to the beam brightness.

It also shows explicitly that a small divergence (i.e., directionality) is required for laser beams for obtaining high intensities by beam focusing.

### 2.2.4 $M^2$-factor

The aim of this section is to introduce a new parameter characterising the radiated beam quality, the so called $M^2$-factor, that can be used to describe beam propagation not only for diffraction-limited beams with an arbitrary transverse profile but also for more general non-diffraction-limited or only partially coherent laser beams, [2-8], [2-25].

The $M^2$-factor can be interpreted as the measure of the diffraction of a 'real' beam compared to that of an ideal diffraction-limited Gaussian beam and is widely used because it gives the possibility to rigorously characterise laser beams both theoretically and experimentally, in terms of a simple number. The importance of the $M^2$-factor resides also in the fact that it does not involve details related to the specific radiation aperture.

Let $I_{NF}(x', y')$ be the beam intensity profile at its waist (e.g., the near-field intensity profile at the laser aperture in Fig. 2.3 for index-guided lasers). The beam standard deviation $\sigma_{x'}(z)$ along, for example, the lateral direction, is then defined as [2-8]:

$$\sigma_{x'}^2(z) = \frac{\int_{-\infty}^{+\infty}\int_{-\infty}^{+\infty}(x'-\bar{x}')^2 I_{NF}(x',y')dx'dy'}{\int_{-\infty}^{+\infty}\int_{-\infty}^{+\infty} I_{NF}(x',y')dx'dy'} \tag{2.27}$$

where

$$\bar{x}' = \frac{\int_{-\infty}^{+\infty}\int_{-\infty}^{+\infty} x' I_{NF}(x',y')dx'dy'}{\int_{-\infty}^{+\infty}\int_{-\infty}^{+\infty} I_{NF}(x',y')dx'dy'} \tag{2.28}$$

is the mean position in the lateral direction. Similarly for the vertical coordinate.

For a Gaussian beam, the beam spot size can be defined as $w_{x'}(z) = 2\sigma_{x'}(z)$, with its minimum value $w_{x'0}(z) = 2\sigma_{x'0}(z)$ at the beam waist. Consequently, for an arbitrary laser beam of general transverse profile, the relation between the spot size parameters $W_{x'}(z)$ and $W_{x'0}$ can be expressed by:

$$W_{x'}(z) = 2\sigma_{x'}(z) \tag{2.29}$$

and

$$W_{x'0} = 2\sigma_{x'0} \tag{2.30}$$

In gain-guided devices the lateral beam waist is located at a specific longitudinal position within the devices cavity that coincides with the device astigmatism. For index-guiding devices, of interest in this work, it is located at the output facet, as previously explained.

A similar notation to equation (2.27) can be used for the beam divergence, that can obtained by considering the beam intensity I(x,y,z), equation (2.7), at a large

distance z from the source. The corresponding angular intensity profile, $\hat{I}(s_x, s_y)$, is then obtained using the relations:

$$x' = \theta_x z = s_x \lambda z \qquad \text{and} \qquad y' = \theta_y z = s_y \lambda z \tag{2.31}$$

where $s_x = \theta_x / \lambda$ and $s_y = \theta_y / \lambda$ are the normalised angular coordinates and are usually referred to as the spatial frequency coordinates of the wave, [2-16]. Having defined the intensity $\hat{I}(s_x, s_y)$, the variance of the spatial frequency $s_x$ can now be readily defined as:

$$\sigma_{sx}^2(z) = \frac{\int_{-\infty-\infty}^{+\infty+\infty} (s_x - \bar{s}_x)^2 \hat{I}(s_x, s_y) ds_x ds_y}{\int_{-\infty-\infty}^{+\infty+\infty} \hat{I}(s_x, s_y) ds_x ds_y} \tag{2.32}$$

where

$$\bar{s}_x = \frac{\int_{-\infty-\infty}^{+\infty+\infty} s_x \hat{I}(s_x, s_y) ds_x ds_y}{\int_{-\infty-\infty}^{+\infty+\infty} \hat{I}(s_x, s_y) ds_x ds_y} \tag{2.33}$$

is the mean position in the lateral direction. Similarly for the y-coordinate. It can be shown, [2-8], that:

$$\sigma_{x'0} \sigma_{sx} \geq \frac{1}{4\pi} \tag{2.34}$$

where the equality holds only for a coherent Gaussian beam.

The $M_x^2$-factor is defined as the ratio of the product $(\sigma_{x'0}\sigma_{sx})$ of the laser beam to the corresponding product $(\sigma_{x'0}\sigma_{sx})_G$ for the Gaussian beam, i.e.:

$$M_x^2 = \frac{(\sigma_{x'0}\sigma_{sx})}{(\sigma_{x'0}\sigma_{sx})_G} = 4\pi(\sigma_{x'0}\sigma_{sx}) \tag{2.35}$$

and similarly for the $y$-coordinate. Note that, according to equation (2.34), $M_x^2 \geq 1$.

The main result of the theory is expressed in a more generalised free-space propagation equation for laser beams, derived from the free-space propagation equation (2.12) for Gaussian beams:

$$W_{x'}^2(z) = W_{x'0}^2 + M_x^4\left(\frac{\lambda^2}{\pi^2 W_{x'0}^2}\right)(z - z_{x'0})^2 \tag{2.36}$$

Equation (2.36) expresses the propagation of a laser beam as a function of a precisely defined spot size parameter $W_{x'0}(z)$. At large distance from the waist position, here referred to as $z_{x'0}$, equation (2.36) takes the form:

$$W_{x'}(z) \cong M_x^2 \frac{\lambda}{\pi W_{x'0}}(z - z_{x'0}) \tag{2.37}$$

For a laser beam the lateral beam divergence can be expressed as:

$$\theta_{dx} = \frac{W_{x'}(z)}{(z - z_{x'0})} = M_x^2\left(\frac{\lambda}{\pi W_{x'0}}\right) \tag{2.38}$$

The beam divergence of a laser beam is thus $M_x^2$ times that of a Gaussian beam of the same spot size (i.e., such that $w_{x'0} = W_{x'0}$).

### 2.2.5 Strehl Ratio

The Strehl Ratio is defined as the ratio between the on-axis far-field intensity of an arbitrary laser beam and the on-axis far-field intensity of a uniformly illuminated

aperture (i.e., diffraction of a beam with constant intensity and uniform phase) with the same size and with the same total power P, [2-8].

With reference to Fig. 2.3, consider the general near-field complex amplitude distribution $E(x',y')$, defined on the region A of area dD, and rewrite it as $E(x',y') = \tilde{E}(x',y')\phi(x',y')$, where $\tilde{E}(x',y')$ and $\phi(x',y')$ are the magnitude and phase of $E(x',y')$. The total power associated to such laser distribution is given by:

$$P = \iint_A |E(x',y')|^2 dx'dy' \tag{2.39}$$

With reference to equation (2.7), the on-axis far-field intensity is given by:

$$\begin{aligned} I(0,0,z) &= \frac{1}{(\lambda z)^2}\left|\iint_A E(x',y')dx'dy'\right|^2 \\ &= \frac{1}{(\lambda z)^2}\left|\iint_A \tilde{E}(x',y')\phi(x',y')dx'dy'\right|^2 \end{aligned} \tag{2.40}$$

From equation (2.15), the on-axis far-field intensity of a uniformly illuminated rectangular aperture of the same dimensions is:

$$I_{ui}(0,0,z) = dD\left(\frac{1}{\lambda z}\right)^2 I_0 \tag{2.41}$$

where $I_0$ is the intensity of the beam.

With reference to equation (2.39), for the uniformly illuminated aperture to have the same power P as the laser beam, the constant amplitude $\bar{i} = \sqrt{I_0}$ must be:

$$\bar{i} = \sqrt{\frac{1}{dD}\iint_A |E(x',y')|^2 dx'dy'} \tag{2.42}$$

Consequently, its on-axis far-field intensity, $I_{ui}$, is given by:

$$I_{ui}(0,0,z) = \frac{1}{(\lambda z)^2}\left|\iint_A \left\{\sqrt{\frac{1}{dD}\iint_A |E(x',y')|^2 dx'dy'}\right\} d\tilde{x}d\tilde{y}\right|^2 = \frac{1}{(\lambda z)^2}(dD)\iint_A |E(x',y')|^2 dx'dy' \tag{2.43}$$

The Strehl Ratio, which is the ratio between (2.40) and (2.42), is therefore given by:

$$S_R = \frac{I\ (0,0,z)}{I_{ui}(0.0,z)} = \frac{\left|\iint_A \tilde{E}(x',y')\phi(x',y')dx'dy'\right|^2}{(dD)\iint_A |E(x',y')|^2 dx'dy'} \tag{2.44}$$

The conditions that maximise the Strehl Ratio can be understood by considering the following integral form of the Cauchy-Schwarz inequality, [2-19]:

$$\left|\iint_A E(x',y')\hat{b}(x',y')dx'dy'\right|^2 \le \iint_A |E(x',y')|^2 dx'dy' \iint_A \left|\hat{b}(x',y')\right|^2 dx'dy' \tag{2.45}$$

where the equality holds only when $E(x',y') = K\hat{b}(x',y')$ and K is a complex constant. If $\hat{b}(x',y') = 1$, then a modified inequality results:

$$\left|\iint_A E(x',y')dx'dy'\right|^2 \le dD\iint_A |E(x',y')|^2 dx'dy' \tag{2.46}$$

where the equality holds only when $E(x',y')$ equals a complex constant.

Comparing the inequality of (2.46) to the Strehl Ratio of (2.44), it is clear that the Strehl Ratio $S \le 1$, and that the unity Strehl Ratio is achieved only when the magnitude $\tilde{E}(x',y')$ and phase $\phi(x',y')$ are constant.

## Summary

Most of the applications for which diode lasers are increasingly used require stable high output power and high beam quality over long periods.

In this chapter the physics behind high power laser performance and the beam quality parameters are introduced, as useful background to study and characterise the performance of the devices of interest in this PhD thesis.

In the first part of the chapter the key factors that limit the useful output power and that determine the quality of the emitted beam of high power lasers, such as, for example, COD, gain saturation and thermal rollover have been discussed in details, and the concept of beam steering and astigmatism have been introduced.

In the second part, methods and parameters to fully characterise the quality of the radiated beam have been presented. Importantly, the characteristics of laser beams have been compared to those of Gaussian beams, ideally non-diffracting, and of beam diffracted by the so called 'uniformly illuminated apertures', that are coherent and show uniform amplitude and constant phase over an emitting aperture of size corresponding to the that of the laser emitting aperture.

The definition of diffraction-limit angle has been introduced to characterise the far-field width of laser beams compared to that of coherent beams, whereas the $M^2$-factor has been derived to analyse the diffracting properties of the laser beam as it propagates. Finally, the Strehl Ratio has been introduced to analyse the intensity profile of the beam and its on-axis (peak) value.

# References

[2-1] R. J. Lang, A. G. Larsson, J. G. Cody, *'Lateral Modes of Broad Area Semiconductor Lasers: Theory and Experiments'*, IEEE J. Quantum Electron., vol. 27, n. 3, 1991, pp. 312-320

[2-2] D. C. Hall, M. R. Surette, L. .Goldberg, D. Mehuys, *'Carrier-Induced Lensing in Broad-Area and Tapered Semiconductor Amplifiers'*, IEEE Photon. Technol. Lett., vol. 6, n. 2, 1994, pp. 186-188

[2-3] J. K. Lee, K. H. Park, D. H. Yang, H. S. Cho, E. S. Nam, K. E. P. Yun, J. Jeong *'Improvement of Kink and Beam Steering Characteristics of 0.98-μm GaInAs-GaInP High-Power Lasers Utilizing Channel Ion Implantation'*, IEEE Photon. Technol. Lett., vol. 12, n. 12, 2000, pp. 140-142.

[2-4] W. D. Herzog, B. B. Goldberg, M. S. Ünli, *'Beam Steering in Narrow-Stripe High-Power 980-nm Laser Diodes'*, IEEE Photon. Technol. Lett., vol. 12, n. 12, 2000, pp. 1604-1606

[2-5] R. J. Lang, A. Hardy, R. Parke, D. Mehuys, S. O'Brien, J. Major, D. Welch, *'Numerical Analysis of Flared Semiconductor Amplifiers'*, IEEE J. Quantum Electron., vol. 29, n. 6, 1993, pp. 2044-2051

[2-6] H. C. Casey, Jr., M. B. Panish, *Heterostructure Lasers, Part A: Fundamental Principles*, ed. by H. C. Casey, Jr. and M. B. Panish, Academic Press, London, 1978.

[2-7] H. C. Casey, Jr., M. B. Panish, *Heterostructure Lasers, Part B: Materials and Operating Characteristics*, ed. by H. C. Casey, Jr. and M. B. Panish Academic Press, London, 1978.

[2-8] E. Kapon, *Semiconductor Lasers II*, Academic Press (1999).

[2-9] J. Guthrie, G. L. Tan, M. Ohkubo, T. Fukushima, Y. Ikegami, T. Ijichi, M. Irikawa, R. S. Mand, J. M. Xu, *'Beam instability in 980nm power lasers: experiment and analysis'*, IEEE Photon. Technol. Lett., vol. 6, n. 12, 1994, pp. 1409-1411

[2-10] G. W. Yang, R. J. Hwu, Z. T. Xu, X. Y. Ma, *'Design Consideration and Performance of High-Power and High-Brightness InGaAs-InGaAsP-*

*AlGaAs Quantum-Well Diode Lasers ($\lambda$=0.98$\mu$m)'*, IEEE J. Selected Topics in Quantum Electronics, vol. 6, n. 4, 2000, pp. 577-584.

[2-11] B. Mroziewicz, M. Bugajski, W. Nakwaski, *Physics of Semiconductor Lasers*, Polish Scientific Publishers (1991).

[2-12] S. O'Brien, H. Zhao, A. Shoenfelder, R. Lang, *'9.3CW (In)AlGaAs 100$\mu$m wide lasers at 970nm'*, Electron. Lett., vol. 33, n. 22, 1997, pp. 1869-1870

[2-13] R. Diehl, *High-Power Diode Lasers – Fundamentals, Technology, Applications*, Springer-Verlag, Berlin, 2000

[2-14] D. Mehuys, L. Goldberg, D. F. Welch, *'5.23W CW Near-Diffraction-Limited Tapered-Stripe Semiconductor Optical Amplifier*, IEEE Photon. Technol. Lett., vol. 5, n. 10, 1993, pp. 1179-1182

[2-15] E. S. Kintzer, J. N. Walpole, S. R. Chinn, C. A. Wang, L. J. Missaggia, *'High-Power Strained-Layer Amplifiers and Lasers with Tapered Gain Regions'*, IEEE Photon. Technol. Lett., vol. 5, n. 6, 1993, pp. 605-608

[2-16] O. Svelto, *Principles of Lasers*, Plenum Press, 1998

[2-17] W. Milonni, J. H. Eberly, *Lasers*, Whiley & Sons, 1988

[2-18] S. Ramo, J. R. Winnery, T. Van Duzer, *Fields and Waves in Communication Electronics*, Whiley & Sons, 1993

[2-19] G. A. Evans, J. M. Hammer, *Surface Emitting Semiconductor Lasers and Arrays*, New York Academic Press (1993).

# Chapter 3

# *Coherence in Arrays of Lasers*

Spatial coherence is the most important requirement for individual laser sources to reach the maximum output power in a diffraction-limited radiated beam. It is particularly important for the performance of laser arrays, as it strongly affects the array field distribution. Coherence within each emitter but also in-phase-locking between emitters is required in high power lasers if also high brightness operation is desired.

Under the assumption that each individual element is spatially coherent, arrays of lasers can be seen as partially coherent sources, reaching overall perfect coherence when phase-locking is achieved. In Chapter 2 it was shown that if only partial coherence is observed, then the divergence of the emitted beam is greater than the diffraction-limit. However the effect of partial coherence on the output beam intensity was not described.

In this Chapter two approaches are followed to define coherence specifically in arrays of lasers and to describe its effect on the beam intensity. For an immediate understanding of the phenomenon, a more elementary approach is followed, in the first Section, that relies on the principle of superposition of waves and that makes use of the Young Two Slit interference experiment to describe the combination of two sources. A more general and rigorous treatment is presented in the second part of this Chapter, where several sources are considered and a general form for the array far-field intensity distribution is derived. In the last part of this Chapter some general considerations are made to further explain the difference between coherent and incoherent laser array operation.

## 3.1 Young Two Slit Experiment: Combination of Two Sources

The essential features of the Young Two Slit interference experiment are displayed in Fig. 3.1 a).

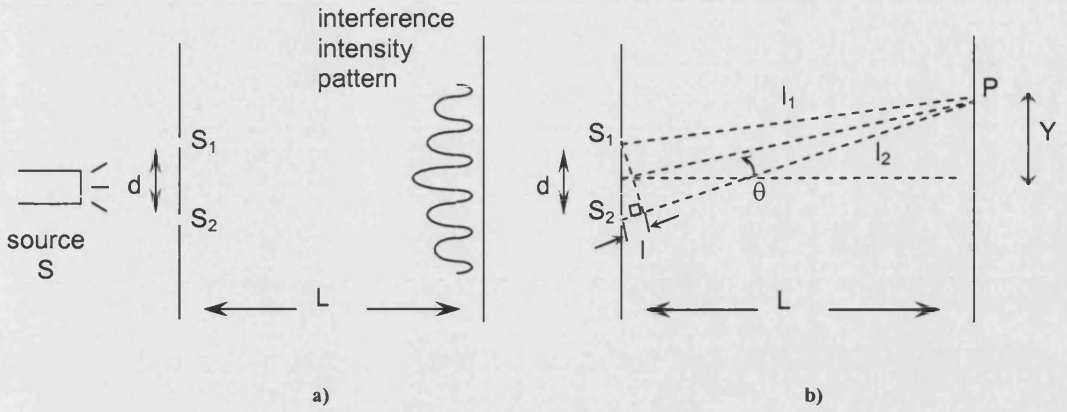


**Fig. 3.1: The Young Two Slit interference experiment, [3-1].**

The light from a source S is incident upon a screen containing two narrow slits, $S_1$ and $S_2$. The intensity distribution of the light emerging from the two slits can be observed at a second screen positioned at a distance L away from the first screen, [3-1], [3-2], and can be calculated using the principle of superposition of waves. It will be shown later in the section, that if sources with a certain degree of coherence are considered, fringes of intensity are observed. On the other hand, for incoherent sources, the intensity is simply the sum of the intensities associated to the individual sources.

The generic optical field components associated to the light emerging from the two slits, travelling the different distances $l_1$ and $l_2$, and arriving on the second screen at the specific point P at the same time t, Fig. 3.1 b), can be represented respectively by:

$$\Psi_1 = A_1 \sin(\omega t - kl_1)$$
$$\Psi_2 = A_2 \sin(\omega t - kl_2) \qquad (3.1)$$

where $A_1$ and $A_2$ are the amplitudes of the waves, $\omega = 2\pi\hat{\nu}$ the angular frequency, with $\hat{\nu}$ the frequency of the signal; $k = \frac{2\pi}{\lambda}$ is the wave number, with $\lambda$

the source wavelength. Applying the principle of superposition the resultant field amplitude is, [3-2]:

$$\Psi = A\sin(\omega t - kl) \tag{3.2}$$

where

$$\begin{aligned} A\cos(kl) &= A_1\cos(kl_1) + A_2\cos(kl_2) \\ A\sin(kl) &= A_1\sin(kl_1) + A_2\sin(kl_2) \end{aligned} \tag{3.3}$$

Therefore the total optical intensity I at a point P of the screen is:

$$I = I_1 + I_2 + 2\sqrt{I_1 I_2}\cos(kl_1 - kl_2) \tag{3.4}$$

where $I_1$ and $I_2$ are the intensities corresponding to the waves $\psi_1$ and $\psi_2$. The phase difference depends on the path difference $l = l_1 - l_2$, Fig. 3.1 b), that can be written as:

$$l = d\sin\theta \approx d\frac{Y}{L} \tag{3.5}$$

if the two slits subtend a small angle $\theta$ at P.

Constructive interference occurs when the optical path difference is an integer number of wavelengths, i.e., $k(l_2 - l_1) = 2\pi n$, which is when the two waves are in-phase. In terms of the position on the screen, the bright fringes are located at:

$$Y^{(max)} = n\frac{\lambda L}{d}, \quad n = 0,1,2,... \tag{3.6}$$

Destructive interference occurs when the path difference is an odd integer number of half wavelengths, i.e., $k(l_2 - l_1) = 2\pi\left(n + \frac{1}{2}\right)$, which is when the waves are out-of-phase; the dark fringes are located on the screen at:

$$Y^{(min)} = \left(n + \frac{1}{2}\right)\frac{\lambda L}{d}, \quad n = 0,1,2,... \tag{3.7}$$

From the above analysis it follows that to observe interference fringes the following conditions must be satisfied, [3-1]:

(i) d<<L

(ii) the two waves must have a constant phase difference $(kl_1 - kl_2)$ at any point, i.e. the two waves must be *spatially coherent*

(iii) the two sources $S_1$ and $S_2$ must be monochromatic

(iv) $A_1 = A_2$

For the special case of $I_1 = I_2 = I_s$ equation (3.4) becomes:

$$I = 4I_s \cos^2\left(\frac{kl_1 - kl_2}{2}\right) \tag{3.8}$$

When the waves are in-phase, then equation (3.8) becomes:

$$I = 4I_s \tag{3.9}$$

that is with constructive interference the total intensity at P is proportional to the intensity of the individual source multiplied the square of the number of sources $(2^2)$.

It is convenient to characterise the sharpness of the interference fringes by defining the visibility V, [3-1], [3-2]:

$$V = \frac{I_{max} - I_{min}}{I_{max} + I_{min}} \tag{3.10}$$

where $I_{max}$ and $I_{min}$ are, respectively, the maximum and minimum intensities on the observation screen. The maximum value for the visibility, $V = 1$, is obtained when constructive interference occurs. On the other hand, if the two waves add incoherently, there is no interference pattern and $V = 0$. The visibility thus provides a quantitative measure of the coherence of light.

## 3.2 The Mutual Coherence Function

A more general analysis of the coherence of a monochromatic source can be carried out using the complex scalar $\Phi(P_1, t)$ to represent the source amplitude and phase at a point $P_1$, [3-3], [3-4]:

$$\Phi(P_1, t) = A(P_1)\exp(i\omega t) \tag{3.11}$$

where $A(P_1)$ is a complex amplitude. The corresponding intensity $I_1^{\Phi}$ at $P_1$ is just the time average of the amplitude squared, therefore given by, [3-3], [3-4]:

$$\begin{aligned} I_1^{\Phi} &= \left\langle \Phi(P_1, t)\Phi^*(P_1, t) \right\rangle \\ &= \lim_{T\to\infty} \frac{1}{T} \int_0^T \left|\Phi(P_1, t)\right|^2 dt \end{aligned} \tag{3.12}$$

where the angle brackets denote the time average.

The mutual coherence function, $\Gamma_{12}(\tau)$, is defined as the time average correlation between the electromagnetic field at that point and time $\Phi(P_1, t)$, and the same field but at a different point and time, $\Phi(P_2, t + \tau)$. That is

$$\begin{aligned}\Gamma_{12}(\tau) &= \left\langle \Phi(P_1,t)\Phi^*(P_2,t+\tau)\right\rangle \\ &= \lim_{T\to\infty}\frac{1}{T}\int_0^T \Phi(P_1,t)\Phi^*(P_2,t+\tau)dt\end{aligned} \tag{3.13}$$

If the two point and the two times are the same in the mutual coherence function, i.e., if $P_1 = P_2$, and $\tau = 0$, then $\Gamma_{11}(0) = I_1^{\Phi}$. Therefore the mutual coherence can be seen as a generalisation of intensity defined in equation (3.12). The mutual coherence function is, in fact, included in the expression for the intensity $I^{\Phi}$ associated to the interference between the two fields $\Phi(P_1,t)$ and $\Phi(P_2,t+\tau)$, [3-3], [3-5]:

$$\begin{aligned}I^{\Phi} &= \left\langle [\Phi(P_1,t)+\Phi(P_2,t+\tau)][\Phi(P_1,t)+\Phi(P_2,t+\tau)]^*\right\rangle \\ &= \left\langle |\Phi(P_1,t)|^2\right\rangle + \left\langle |\Phi(P_2,t+\tau)|^2\right\rangle + 2\left\langle \Phi(P_1,t)\Phi^*(P_2,t+\tau)\right\rangle \\ &= I_1^{\Phi} + I_2^{\Phi} + 2\,\mathrm{Re}[\Gamma_{12}(\tau)]\end{aligned} \tag{3.14}$$

In general, $\Gamma_{12}(\tau)$ depends on the choice of points and times and on the time-dependent behaviour of the radiation. It is convenient to normalise $\Gamma_{12}(\tau)$ to obtain the *complex degree of coherence*, $\gamma_{12}$, defined as:

$$\gamma_{12}(\tau) = \frac{\Gamma_{12}(\tau)}{\sqrt{\Gamma_{11}(0)\Gamma_{22}(0)}} = \frac{\Gamma_{12}(\tau)}{\sqrt{I_1^{\Phi} I_2^{\Phi}}} \tag{3.15}$$

The magnitude $|\gamma_{12}(\tau)|$ is the measure of the coherence of the source: when $|\gamma_{12}(\tau)| = 1$ the radiation is coherent; when $|\gamma_{12}(\tau)| = 0$ it is incoherent; in between it is partially coherent.

At this stage it might be convenient to distinguish between spatial and temporal dependence of the considered electromagnetic field, and between spatial and temporal coherence. Spatial coherence is the time average correlation between two fields at separate points in space but measured at the same time and corresponds to

$\Gamma_{12}(0)$. Temporal coherence is the time average correlation between fields measured at the same point but at different times, and corresponds to $\Gamma_{11}(\tau)$, [3-5].

Temporal coherence is closely related to the spectral width of the source, whereas spatial coherence is related to the phase characteristics of the electromagnetic field. Using the definitions given above, the spatial coherence is $|\gamma_{12}(0)|$ and temporal coherence is $|\gamma_{11}(\tau)|$, [3-3], [3-5].

## 3.3 Coherent and Incoherent Light: the Limiting Cases

The limiting cases, of totally coherent and totally incoherent sources, are the most important to illustrate. A simple example of completely coherent radiation is a plane monochromatic wave, with constant amplitude and uniform phase at all times. The field at one point and time, $\Phi(P_1,t)$, is completely correlated with that at any other point and time, $\Phi(P_2,t+\tau)$. Then, since the amplitudes are independent of time, from equation (3.13), [3-2]:

$$\begin{aligned}\Gamma_{12}(\tau) &= \left\langle \Phi(P_1,t)\Phi^*(P_2,t+\tau)\right\rangle \\ &= |\Phi(P_1,t)||\Phi^*(P_2,t+\tau)|\left\langle \arg\Phi(P_1,t)\arg\Phi^*(P_2,t+\tau)\right\rangle \\ &= \sqrt{\Gamma_{11}(0)\Gamma_{22}(0)}\cdot\exp(-j\phi_\tau)\end{aligned} \tag{3.16}$$

where $\phi_\tau$ is a constant phase term depending only on the time delay. The complex degree of coherence in this case is:

$$\gamma_{12}(\tau) = \frac{\Gamma_{12}(\tau)}{\sqrt{\Gamma_{11}(0)\Gamma_{22}(0)}} = \exp(-j\phi_\tau) \tag{3.17}$$

and $|\gamma_{12}(\tau)| = 1$

Under these conditions equation (3.14) takes the form:

$$I^{\Phi} = I_1^{\Phi} + I_2^{\Phi} + 2\sqrt{\Gamma_{11}(0)\Gamma_{22}(0)} \cdot \cos(\phi_\tau) \tag{3.18}$$

Under the assumptions that $I_1^{\Phi} = I_2^{\Phi} = I_S^{\Phi}$ and $\cos(\phi_\tau) = 1$, then equation (3.18) takes the form:

$$I^{\Phi} = 4I_S^{\Phi} \tag{3.19}$$

On the other hand, considering an incoherent signal with randomly, temporally and spatially, varying phase, then $\Phi(P_1, t)$ and $\Phi(P_2, t+\tau)$ are completely uncorrelated, [3-3], [3-5]; therefore, for any choice of $P_1$, $P_2$ and $\tau$ the mutual coherence function is null:

$$\Gamma_{12}(\tau) = \left\langle \Phi(P_1, t)\Phi^*(P_2, t+\tau) \right\rangle = 0 \tag{3.20}$$

It follows that $|\gamma_{12}(\tau)| = 0$. Since the radiation is incoherent, from equation (3.14), the intensity associated to the interference of the two signals is equal to the sum of the individual intensities at $P_1$ and $P_2$ and at times t and $t+\tau$:

$$I^{\Phi} = I_1^{\Phi} + I_2^{\Phi} \tag{3.21}$$

## 3.4 Interference between Two Partially Coherent Point Sources

The intensity of the interference pattern resulting using two partially coherent signals is, [3-2]:

$$I^{\Phi} = I_1^{\Phi} + I_2^{\Phi} + 2\sqrt{I_1^{\Phi} I_2^{\Phi}} |\gamma_{12}(\tau)| \cos[k(l_1 - l_2) - \alpha_{12}(\tau)] \tag{3.22}$$

where $\tau = (l_1 - l_2)/c$. The term $\alpha_{12}(\tau)$ is the phase of $\gamma_{12}(\tau)$ and corresponds to the phase difference between the two signals. $\alpha_{12}(\tau)$ varies slowly with $\tau$, therefore it

can be considered as a constant: $\alpha_{12}(\tau) = \alpha_{12}$. The effect of $k(l_1 - l_2)$ is to produce a set of cosinusoidal fringes with varying $(l_1 - l_2)$, while the effect of $\alpha_{12}$ is to shift the fringe pattern.

If $\gamma_{12}(\tau) = 1$ then equation (3.22) becomes the elementary expression for the interference between two points radiating with constant phase difference $\alpha_{12}$:

$$I^{\Phi} = I_1^{\Phi} + I_2^{\Phi} + 2\sqrt{I_1^{\Phi} I_2^{\Phi}} \cos[(kl_1 - kl_2) - \alpha_{12}] \tag{3.23}$$

which shows the cosinusoidal variation as the path difference changes. The fringe visibility V, equation (3.10), can be rewritten as, [3-1], [3-3]:

$$V = 2|\gamma_{12}(\tau)| \frac{\sqrt{I_1^{\Phi} I_2^{\Phi}}}{I_1^{\Phi} + I_2^{\Phi}} \tag{3.24}$$

And the complex degree of coherence assumes the form:

$$|\gamma_{12}(\tau)| = V \frac{I_1^{\Phi} + I_2^{\Phi}}{2\sqrt{I_1^{\Phi} I_2^{\Phi}}} \tag{3.25}$$

If $I_1^{\Phi} = I_2^{\Phi}$, then:

$$|\gamma_{12}(\tau)| = V \tag{3.26}$$

It follows that the degree of coherence of a beam can be estimated by measuring the visibility V of the fringes produced by interfering just pair of points across its wavefront.

## 3.5 Arrays of Emitters Having Arbitrary Coherence

The analysis presented in the previous section can be generalised further, [3-5], to explain how coherence influences the beam pattern of (one-dimensional) arrays of N emitters, Fig. 3.2.

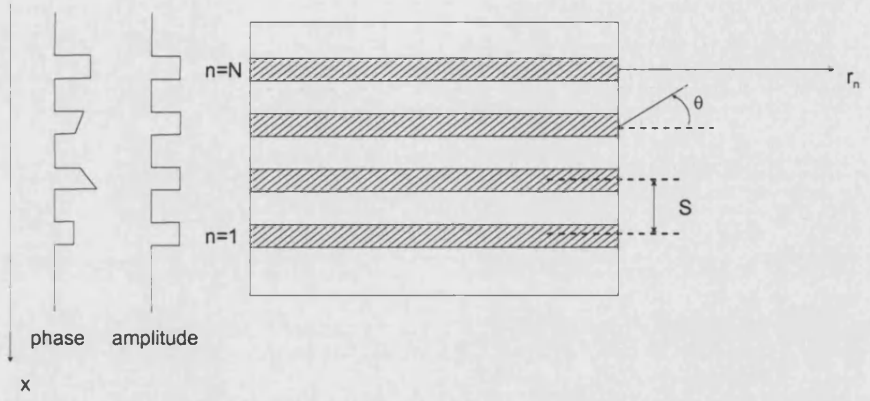


**Fig. 3.2: A linear array of N emitters with constant amplitudes and either constant or linear phase within each emitter, [3-5].**

The assumptions are:

1) any number of spatially coherent emitters
2) any degree of coherence $\gamma_{mn}$ between emitter pairs
3) constant intensity across each emitter, but it can vary from one emitter to another (not rigorous since the far-field distribution is not highly sensitive to intensity variations)
4) arbitrary phases across the array, but either constant or linear phase across each emitter

Using the complex scalar notation, the amplitude of the angular diffraction pattern of the individual, nth emitter alone, at a radial distance $r_n$ from the emitting aperture, can be written as, [3-5]:

$$\hat{\Phi}_n(\theta) = (I_n^{\Phi})^{1/2} F_n(\theta - \rho_n, r_n) U_n\left(t - \frac{r_n}{c}, \phi_n\right) \tag{3.27}$$

where $I_n^{\Phi}$ is the intensity of the n-th -emitter. The function $F_n(\theta-\rho_n, r_n)$ contains the information on the diffraction pattern as a function of the angle $\theta$ and the $1/r_n$ amplitude dependence; $F_n(\theta-\rho_n, r_n)$ is centred at an angle $\rho_n$ due to the angle tilt of the n-th source. $U_n$ contains the time dependence and the phase $\phi_n$ of the radiation source. The total far-field amplitude due to the N emitters is given by the superposition of the individual far-fields, [3-5]:

$$\hat{\Phi}(\theta) = \sum_{n=1}^{N} (I_n)^{1/2} F_n(\theta-\rho_n, r_n) U_n\left(t - \frac{r_n}{c}, \phi_n\right) \tag{3.28}$$

and the corresponding far-field, $I_{acoh}(\theta)$, is:

$$\begin{aligned} I_{acoh}(\theta) &= \left\langle \hat{\Phi}(\theta)\hat{\Phi}^*(\theta) \right\rangle \\ &= \sum_{n=1}^{N} F_n^2 I_n + 2\sum_{n=1}^{N}\sum_{m=n+1}^{N} (I_n I_m)^{1/2} F_n F_m \gamma_{mn} \\ &\quad \cdot \cos[kS(m-n)\sin(\theta+\phi_m-\phi_n)] \end{aligned} \tag{3.29}$$

where S is the centre to centre distance between emitters, Fig. 3.2.

The first term in equation (3.29) is the far-field of an incoherent array of N emitters: in fact, if $\gamma_{mn} = 0$ for all $m, n$, then the second term is null.

## 3.6 Laser Array Coherence and Brightness

The occurrence of multiple apertures in laser arrays presents additional and more significant design considerations, compared to those for simple, individual lasers, that must be take carefully into account if high power with high brightness is desired. In laser arrays, in fact, as seen in the previous sections, the mutual coherence from one laser to another strongly affects the field distribution that results from the combination of the beam radiated from the individual laser apertures.

Such considerations are summarised in this Section, where the differences, in terms of beam quality, between coherent and incoherent laser arrays are further discussed.

An array, Fig. 3.3 a), of N stripe lasers, each with emitting aperture w, Fig. 3.3 d), is considered. Each laser is assumed to be spatially coherent, emitting in the fundamental mode and therefore characterised by a diffraction-limited far-field divergence $\theta_x=\lambda/w$. It is assumed that such elements are totally incoherent with each other.

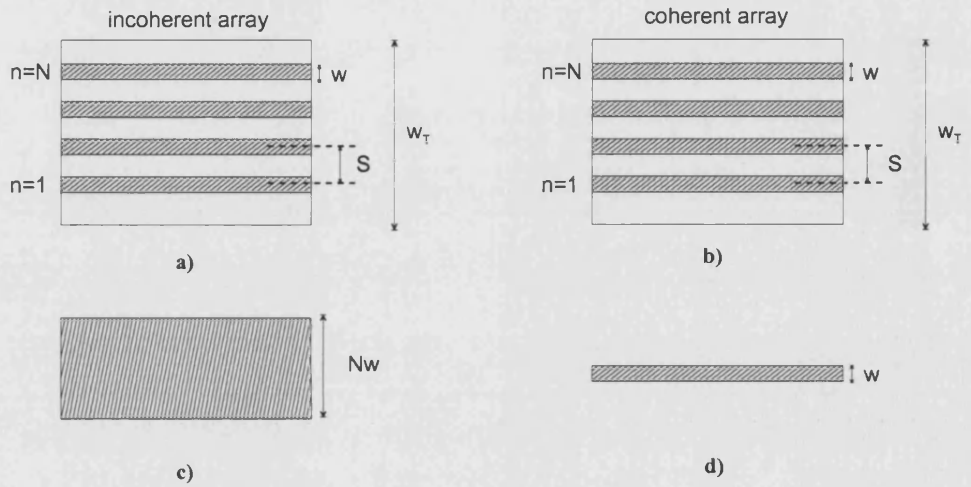


**Fig. 3.3: Schematic of a) an incoherent and b) a coherent array of lasers, compared to c) a coherent source with comparable emitting aperture and to d) the array individual element. Arbitrary spacing between the array elements has been considered for simplicity.**

Results from this Chapter show that using multiple incoherent sources increases the far-field peak intensity proportionally to the number of sources itself (N); however, also the total emitting area[1] is increased of the same amount. In addition, the far-field divergence would be exactly the same as the individual element, being the field coherent only across its emitting aperture w and not across the whole array aperture, Nw, resulting therefore in the same brightness.

The fact that the brightness of a mutually incoherent (but otherwise identical) laser array does not increase to a level greater than the brightness of the single brightest

[1] The emitting area is expressed here as the laser emitting aperture width in the lateral (x) direction only, because it is assumed that the laser emitting aperture width in the vertical (y) direction is the same for all types of devices considered. Similarly for the far-field pattern: the far-field lateral divergence, only, is considered.

source has direct consequences for many applications. For example, if high intensity at the centre of the far-field is required, the above considerations suggest that there is no benefit in using more than one laser in the array. In fact, by using a coherent source with aperture size Nw, Fig. 3.3 c), the same total output power as for an array of N elements with aperture size w could be achieved and, most importantly, the brightness would be enhanced N times because of the N-fold decrease in the far-field divergence. On the other hand, in this case, the challenge would be in designing a broad area laser operating in the fundamental mode.

There are two practical reasons, however, for using more than one incoherent source. First, the system is more robust because of the redundancy given by the multiple emitters: failure of a laser diode in the array would yield only to a small decrease of the power, rather than the catastrophic breakdown associated to the use of a single source or a coherent array. Second, the collimation optics (when needed) in the incoherent case must be diffraction-limited only over the small region illuminated by a single-laser aperture; the collimating optics for the equivalent single-laser system must be diffraction-limited over an aperture of the same size as the entire incoherent array, [3-6]. The cost and complexity associated with this more precise optic element can easily offset the advantages of using a single laser.

For applications that require high peak intensity at the centre of the focused spot, array of coherent emitters should be used. If mutual coherence is established across the laser array, Fig. 3.3 b), the source operates in a single (fundamental) spatial mode, characterised by constant phase; adding mutually coherent lasers would reflect, although the total emitting aperture area increases proportionally to N, into an increase of the on-axis intensity by $N^2$, as demonstrated in the previous Sections, and of the brightness by N. Such increase in the brightness results from the simultaneous increase in the total power by a factor of N and decrease (being the field coherent over the whole array aperture) in the far-field divergence by and additional factor of N compared to a single source.

Results from the above discussion are summarised in Table 3.1.

**Tab. 3.1: Comparison of the performances of coherent and incoherent arrays of lasers, compared to those of the array individual elements.**

| | individual laser | incoherent array | coherent array |
|---|---|---|---|
| Emitting aperture | w | Nw | Nw |
| Total aperture | w | $w_T > Nw$ | $w_T \geq Nw$ |
| N. of elements | 1 | N | N |
| Power | P | NP | NP |
| Divergence | $\theta_x$ | $\theta_x$ | $\theta_x/N$ |
| Brightness | B | B | NB |

### 3.6.1 Fill-factor considerations

The array fill factor is defined as the fraction of the array aperture occupied by the lasing apertures, [3-6], that is the ratio between the emitting aperture and the array aperture. It is particularly used to characterise arrays where the individual elements are not positioned close to each other. This is the particular case of most of the incoherent systems, where, to avoid optical coupling, the emitters are positioned far from each other.

Arrays of mutually incoherent lasers can be seen as partially coherent sources, [Chapter 2], i.e., sources coherent only over apertures $w<w_T$, Fig. 3.3 a). From the discussion above, it follows that the brightness from an incoherent array, fixed the total aperture $w_T$, can be maximised when the emitting area of the individual element is maximised, as its far-field divergence is minimised, or, equivalently, when the fill factor is maximised. For a coherent array, the Strehl Ratio, [Chapter 2] gives a better description of the array performance. However, the Strehl Ratio of a coherent array is proportional to the array fill factor: in most of the coherent arrays, the laser apertures are usually placed close to each other to improve the coupling, and a fill factor equal to 1 is obtained. However, to reduce the heat load, high power arrays are sometimes designed to contain significant non-lasing regions, resulting in a decrease of the output power emitted in the diffraction-limited beam. In such cases an estimation of the fill factor is essential if a comprehensive characterisation of the device performance is desired.

## Summary

In this chapter a rigorous, theoretical, approach has been followed to define coherence in laser sources, and in particular in laser arrays. The effect of mutual coherence between array elements on the intensity of the laser array emitted beam has been described; a general expression for the far-field of an array of N emitters, each characterised by spatial coherence but having any degree of coherence with the other emitters, has also been derived.

Importantly, it was shown that in arrays the mutual coherence function from one laser to another is the parameter that mainly affects the field distribution resulting from the combination of the beams emitted from the individual lasers.

The presented analysis also demonstrated that an important motivation for producing arrays having high degree of coherence is to obtain higher peak intensity and higher brightness. In fact, for arrays of N emitters each producing an intensity I, the on axis intensity is NI if the array is incoherent, and no improvement is observed in the brightness; on the other hand the on axis intensity is $N^2I$ if the array is coherent, reflecting also in a brightness that is N times the brightness of the individual element.

In the last part of the chapter some general considerations have been made to further explain the difference between coherent and incoherent laser array operation, and to compare it to that of the individual emitters. A new parameter, called fill factor, which is of particular importance for incoherent arrays, has also been introduced to further characterise the beam quality of laser arrays.

# References

[3-1] W. Milonni, J. H. Eberly, *Lasers*, Whiley & Sons, 1988

[3-2] E. Hecht, *Optics*, Addison-Wesley, 1998

[3-3] O. Svelto, *Principles of Lasers*, Plenum Press, 1998

[3-4] R. G. Driggers, *Encyclopedia of Optical Engineering*, vol. 1, Marcel Dekker Inc., 2003

[3-5] G. A. Evans, J. M. Hammer, *Surface Emitting Semiconductor Lasers and Arrays*, New York Academic Press (1993).

[3-6] D. Botez, D. R. Scifres, *Diode Laser Arrays*, Cambridge University Press (1994).

# Chapter 4

# *Modes of Phase-Locked Laser Arrays*

The aim of this chapter is to give an overview of the fundamental principles and features of semiconductor phase-locked arrays, which have attracted enormous attention as high-power arrays exhibiting also good spatial mode control.

Focusing the attention on arrays of positive-index guides, which are of particular interest in this PhD thesis, the description of the major types of arrays and the mechanism of coupling between emitters in the different configuration is presented.

Since the primary issue with arrays, and in particular with tapered arrays, is the lateral-mode selectivity, the emphasis of the chapter is on the calculation of the array modes and on the effect of lateral refractive index and gain profile on their discrimination.

The interest here is, also, in providing an overview of the modelling techniques, together with their regimes of validity, that have been successfully utilised to describe array behaviour. Importantly, the formulation of the Coupled-Mode Theory (CMT) is presented, together with the description of the steady-state, CMT-based analytic model used to analyse the Parabolic Bow-Tie Lasers Arrays.

## 4.1 Array Modes

A monolithic array of phase-coupled diode lasers can be described simply as a periodic variation of the real part of the lateral refractive index. Phase-coupled arrays can be organised in two main classes: 1) evanescent-wave-coupled arrays, also called positive-index-guided arrays, where field intensity peaks reside in the high-index array regions, and 2) leaky-wave-coupled arrays, also called antiguided arrays, where the lasing modes have the major field-intensity peaks in the low-index array regions, [4-1].

Another major distinction of phase-locked arrays can be made specifying the type of coupling between emitters: nearest-neighbour coupling, also called 'series' coupling, with each element coupling only to the adjacent ones, and strong overall inter-element coupling, also called parallel coupling, with each element coupling equally to each others.

The lasing field of a phase-locked array is a combination of the array modes (so called supermodes) supported by the dielectric structure, [4-1]-[4-3]. Ideally the array should operate in the fundamental array-mode with constant phase across the facet and produce the desired single-lobed, narrow far field, [4-1].

It has been demonstrated, [4-1], that if parallel coupling is achieved, then inter-modal discrimination is optimised and lowest-order mode (coherent, in-phase) operation is achieved. In addition, parallel-coupled systems have uniform (i.e. constant amplitude and phase) near-field intensity profiles, immune to the onset of higher-order-mode oscillation at high drive levels above threshold.

However, in positive-index devices, of interest in the work presented in this PhD thesis, the highest order (out-of-phase) mode is typically favoured because of the better field intensity overlap with the gain distribution (higher modal gain). Parallel coupling could be obtained in evanescent-wave-coupled devices, but only by weakening the optical-mode confinement, and thus making the devices vulnerable to thermal- and/or injected-carrier-induced variations in the dielectric constant.

The goal of achieving single-mode operation in positive-index arrays can be pursued by varying the gain and/or index (lateral) profile in longitudinally uniform devices to increase the modal gain associated to the lowest-order mode, or creating longitudinally non-uniform geometry devices for which the inter-element coupling mechanism (not evanescent waves) forces in-phase-mode operation, as seen for the Y-junction arrays, [4-4], [4-5]. A more detailed analysis of mode discrimination in positive-index guided arrays will be discussed in detail later in the Chapter.

The novelty of the index-guided Parabolic Bow-Tie Laser Arrays presented in this PhD thesis, compared to other phase-locked devices proposed in the literature, resides essentially in the fact that the inter-element coupling is longitudinally non-uniform; the inter-element coupling is weak along the length of the device but strong at the device output facets, Fig. 4.1.

In the region near the output facets, where the elements merge in a single contact and there is no explicit lateral mode control, the optical gain in the inter-element regions is larger than that in the element regions, due to the effect of carriers on the refractive index and to the gain hole-burning. Thus, the modal gain associated to this mode is the highest. The important, additional aspect to be considered is that the above effect is associated to the mode filtering effect of the central narrow stripe sections, thus providing much improved scope to sustain in-phase (array) mode operation.

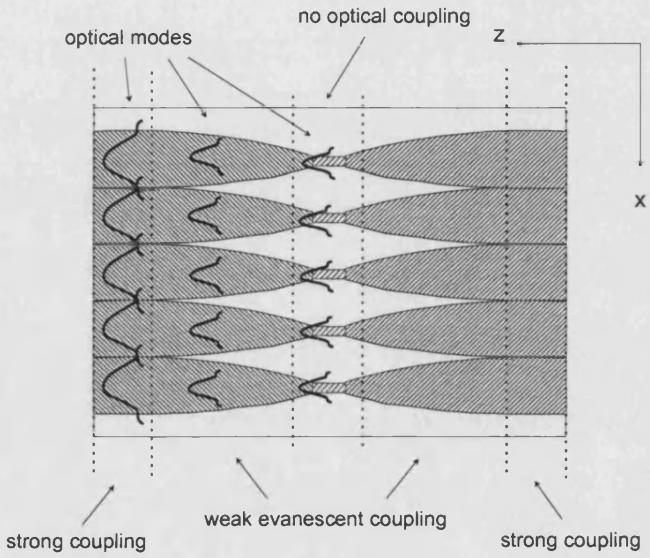


**Fig. 4.1: Top view schematic of a 5-element Parabolic Bow-Tie Laser Array (PBTLA). The longitudinally non-uniform rib design induces longitudinally non-uniform optical coupling, weak at the centre of the device, increasing as the mode propagates towards the device output ends.**

## 4.2 Modelling of Diode Laser Arrays

Initially, phase locked arrays of diode lasers were mainly of narrow, index-guided or gain-guided straight stripes (i.e., longitudinally uniform devices) that could be described simply by specifying the periodic variation of the lateral refractive index profile of the device, and could therefore be easily modelled, [4-1].

The first simple analysis of the behaviour and selectivity of phase-locked array modes was based on simple diffraction theory (SDT), [4-2], to predict the diffraction pattern from a uniformly illuminated grating with equally spaced slits corresponding to individual laser array elements. The SDT method proved to be useful in interpreting some experimental results, [4-2]. However, it could not describe all the allowed modes of the array, [4-1], [4-2], [4-6], [4-7], as only in-phase and out-of-phase modes could be analysed.

Shortly after, the first work on coupled-mode formalism applied to arrays was presented, that showed that coupled-mode analysis better described phase-locked arrays, [4-6], [4-7]. The Coupled-Mode Theory (CMT), [4-6]-[4-8], was used to study arrays of single-mode lasers with nearest-neighbour coupling. The array field is calculated by superimposing the individual element optical fields. The simplicity of the model allowed for a deeper insight into the problem and for better first understanding of phase-locking in such type of arrays, as it was possible to characterise all the supermodes individually.

However, in the present formulation, the coupled-mode theory did not apply to strongly coupled systems, and therefore did not cover leaky-type array modes, that seemed to be the key for high-power phase-locked operation. In addition it neglected carrier diffusion and the effect of gain, which are significant in arrays with optical coupling between elements.

In the recent years several, more complex phase-locked array designs have been proposed, [4-1], [4-9]-[4-13]. The capability to successfully model such new devices has become a crucial need and a comprehensive model would involve the calculation of carrier diffusion in multiple quantum wells as well as current and heat flow throw the multilayer semiconductor structure.

With this respect several models have been proposed, based on the exact theory, [4-14], the Bloch-function method, [4-15], or on steady-state, [4-16]-[4-18], as well as space-time dynamics, [4-19], [4-20], analysis of the coupled diffraction-diffusion partial differential equation for the optical field and the carriers in the structure. Such models are effective in describing phase-locked array behaviour as they can predict practical situations where the coupling due to the exchange of injected carriers between adjacent guides can be relatively significant, [4-19], [4-20].

However, the above procedures are numerically complicated and can require long computational time. Importantly, they are not easily applicable to tapered structures where not only the longitudinally non-uniform mutual interaction between emitters but also the longitudinally non-uniform distribution of carriers, have to simultaneously be addressed.

Recently, a computationally efficient, quasi-analytic model, based on the Hermite-Gauss (HG) expansion method using the Collocation numerical Method (CM), and referred to as HGCM, [4-21]-[4-23], has been developed and demonstrated to be suitable for the self-consistent field analysis of tapered lasers, [4-24]. The HGCM has been used to interpret some of the experimental results presented in this thesis. Details of the HGCM model are given in Appendix B.

However, in order to better understand the phase-locking phenomenon in tapered arrays, PBTLAs are here analysed also using the CMT.

Under the assumption that significant coupling between emitters occurs only at the device output facet, then the CMT theory is readily applicable to the PBTLAs and solutions for the allowed array modes can be found.

Importantly, in the present formulation of the CMT applied to tapered laser arrays the effect of carriers and gain profile is also included since the optical field for each emitter is calculated self-consistently using the HGCM model.

## 4.3 Coupled-Mode Theory

To introduce the main concepts of the coupled-mode analysis, an index-guided array of N adjacent stripe lasers is considered for simplicity, Fig. 4.2 for N=4.

It is assumed that each emitter supports the fundamental mode only, and that only weak nearest-neighbour coupling occurs between emitters.

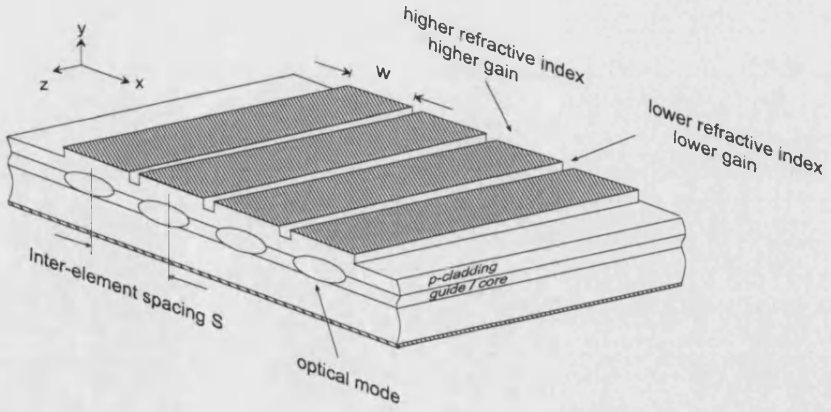


**Fig. 4.2: Schematic of a stripe laser arrays of N=4 single-mode identical emitter with inter-element spacing S. Only nearest-neighbour coupling occurs between emitters.**

With the CMT the field distribution of the array is described as the superposition of the fields of the N individual emitters, [4-8]:

$$F_{TOT}(x,z) = \sum_{m=1}^{N} \hat{A}_m(z)\hat{F}_m(x,z) \tag{4.1}$$

where $\hat{F}_m(x,z)$ is the normalised optical field in the m-th isolated waveguide laser and $\hat{A}_m(z)$ is a complex coefficient that determines the amplitude and phase of the individual emitter fields in the modes of the array.

Assuming propagation along the longitudinal (z) direction, the lateral fundamental mode in each stripe can be rewritten as $\hat{F}_m(x,z) = F_m(x)e^{-i\beta_m z}$, where $\beta_m$ is the propagation constant associated to $F_m(x)$. Therefore,

$$F_{TOT}(x,z) = \sum_{m=1}^{N} \hat{A}_m(z)F_m(x)e^{-i\beta_m z} \tag{4.2}$$

To calculate the array modes it is necessary to solve the wave equation, [Appendix B],

$$\frac{\partial^2 F(x,z)}{\partial z^2} + \frac{\partial^2 F(x,z)}{\partial x^2} + k_o^2 \varepsilon(x,z,N)F(x,z) = 0 \tag{4.3}$$

for the collection of N emitters, [4-8]. $\varepsilon(x,z,N) = n^2(x,z,N)$ is the complex dielectric profile distribution (with $n(x,z,N)$ the corresponding refractive index profile) that takes into account the non-linear interaction between photons and injected carriers (N(x,z) is the carrier density distribution in the active layer).

By substituting the assumed field solution of equation (4.2) in equation (4.3) a set of equations describing the N modes of the array is obtained, [4-8].

To obtain the eigenvalue equation for the allowed mode, the condition of orthonormality of the modes is applied; it follows that:

$$\sum_{m=1}^{N} k_0^2 c_{mn} \hat{A}_m(z) - 2i\beta_m \frac{\partial \hat{A}_m}{\partial z} = 0 \qquad (4.4)$$

where $c_{mn}$ are the coupling coefficients between emitters. Under the assumption that the emitters are identical and that only nearest neighbour coupling occurs, the only non-zero coefficients are $c_{m-1,m}=c_{m,m+1}=c$ and the eigenvalue problem of equation (4.4) reduces to a simple bidiagonal matrix equation in c. Under the assumption that the emitters are identical, then also $\beta_1 = \beta_2 .. = \beta_N = \beta$; by writing $\hat{A}_m(z) = \hat{a}_m e^{-i(\partial\beta)z}$ the equation (4.4) can be solved in terms of eigenvalues $\partial\beta$ and eigenvectors $\hat{a}_m$. For the $\nu$-th array mode it follows, [4-6]:

$$\begin{aligned} \partial\beta^{\nu} &= 2c\cos\theta_{\nu} \\ a_m^{\nu} &= \sin(m\theta_{\nu}) \end{aligned} \quad ; \quad \begin{aligned} m &= 1,...,N \\ \nu &= 1,...,N \end{aligned} \qquad (4.5)$$

where $\theta_{\nu} = \nu\pi/(N+1)$.

The v-th array mode can then be described as a linear superposition of the fields of the individual emitters with a fixed relative phase between them, [4-8]:

$$F^{\nu}(x,z) = \left[\sum_{m=1}^{N} a_m^{\nu} F_m(x)\right] e^{-i\gamma_{\nu} z} \qquad (4.6)$$

where $\gamma_\nu = \beta + \partial\beta^\nu$. Thus, the combination of modes originating the ν-th array mode described by equation (4.6) propagates together with a single phase factor $e^{-i\gamma_\nu z}$ that takes into account the propagation constant of the modes of the individual lasers and the coupling between emitters, [4-8]. From equations (4.5) and (4.6) it follows that:

$$F^\nu(x,z) = \left[\sum_{m=1}^{N} \sin(m\theta_\nu) F_m(x)\right] e^{-i\gamma_\nu z} \tag{4.7}$$

The corresponding far-field distribution can be calculated, [4-8], by summing the field contributions of the emitters including the phase variation across the array, as described below.

The far-field intensity associated to the ν-th array mode can be calculated by Fourier transform of the near-field distribution of the same array mode. From equation (4.7) it follows that the far-field intensity associated to the ν-th supermode is:

$$\hat{I}^\nu(\theta) = \sum_{m=1}^{N} \sin(m\theta_\nu) I_m(\theta) \tag{4.8}$$

where $I_m(\theta)$ is the far-field of the m-th emitter, and $\theta$ the angle with respect to the normal to the laser facet; For an array of N coupled, identical emitters, [4-8]:

$$I_m(\theta) = I_{m+1}(\theta) e^{-ikS\sin\theta} = I_0(\theta) e^{-ikmS\sin\theta} \tag{4.9}$$

where $I_0(\theta)$ is the far-field amplitude distribution for one of the individual element, S, Fig. 4.2, is the inter-element spacing and $kmS\sin\theta$, with $k = 2\pi/\lambda$ ($\lambda$ is the wavelength), is the extra phase delay, in the array far-field, between the far-field associated to adjacent channels.

By substituting equation (4.9) into equation (4.8), the ν-th supermode far-field intensity distribution is given by, [4-8]:

$$\hat{I}^{\nu}(\theta) = I_0(\theta)\hat{I}_{G\nu}(\theta) \tag{4.10}$$

where $\hat{I}_{G\nu}(\theta)$, called 'grating' function, represents the interference effect of the coupled emitters in the array.

For the coupled-mode theory the analytic expression for the grating function is, [4-7]:

$$\hat{I}_{G\nu}(\theta) = I_{G\nu}(u) = \frac{\sin^2\left[\frac{(N+1)u}{2} + \frac{\nu\pi}{2}\right]}{\left[\sin^2\left(\frac{u}{2}\right) - \sin^2\left(\frac{\nu\pi}{2(N+1)}\right)\right]^2}, \qquad \nu = 1,2,...,N \tag{4.11}$$

with $u = kS\sin\theta$. Using the notation already used in equation (4.5), equation (4.11) becomes:

$$I_{G\nu}(u) = \frac{\sin^2\left[\frac{(N+1)}{2}(u+\theta_\nu)\right]}{\left[\sin^2\left(\frac{u}{2}\right) - \sin^2\left(\frac{\theta_\nu}{2}\right)\right]^2}, \qquad \nu = 1,2,...,N \tag{4.12}$$

Equation (4.12) describes the far-fields of all N array modes of a N-element array. The grating function $I_{G\nu}(u)$, Fig. 4.3 c), accounts for the number of elements and the inter-element spacing S and is a periodic function in u with period $2\pi$, [4-8]. This is more obvious in the particular case of $\nu = 1$ and $\nu = N$ : the distance between the major, periodic, lobes is $\Delta\theta = \sin^{-1}(\lambda/S)$.

Near-field amplitudes profiles computed for all the array modes of an index-guided array of N=10 elements, each of rib width $w = 3\mu m$, with inter-element spacing $S = 5\mu m$, are depicted in Fig. 4.3 a). The working wavelength is $\lambda$=0.83μm.

The far-field profiles and the grating functions of all modes of the 10-element array described above are presented in Fig. 4.4 b) and c).

It can be observed, equation (4.10), that the far-field associated to the ν-th array mode corresponds to the 'convolution' between the individual emitter far-field distribution and the ν-th grating function. The array lowest ($\nu = 1$) and highest ($\nu = N$) order modes correspond respectively to the in-phase (no-phase shift between adjacent elements) and out-of-phase (π-phase shift between adjacent elements) modes of operation. The other eight additional/intermediate allowed modes have shapes that reflect more complex phase relationship between adjacent emitters. In the particular case $\nu = 1$ radiation pattern is centrally peaked whereas for $\nu = N$ the emission is into two lobes, with peak distance $\Delta\theta = \sin^{-1}(\lambda / S) = 9.5\,\text{deg}$. The results shown here match those presented in the literature, [4-6].

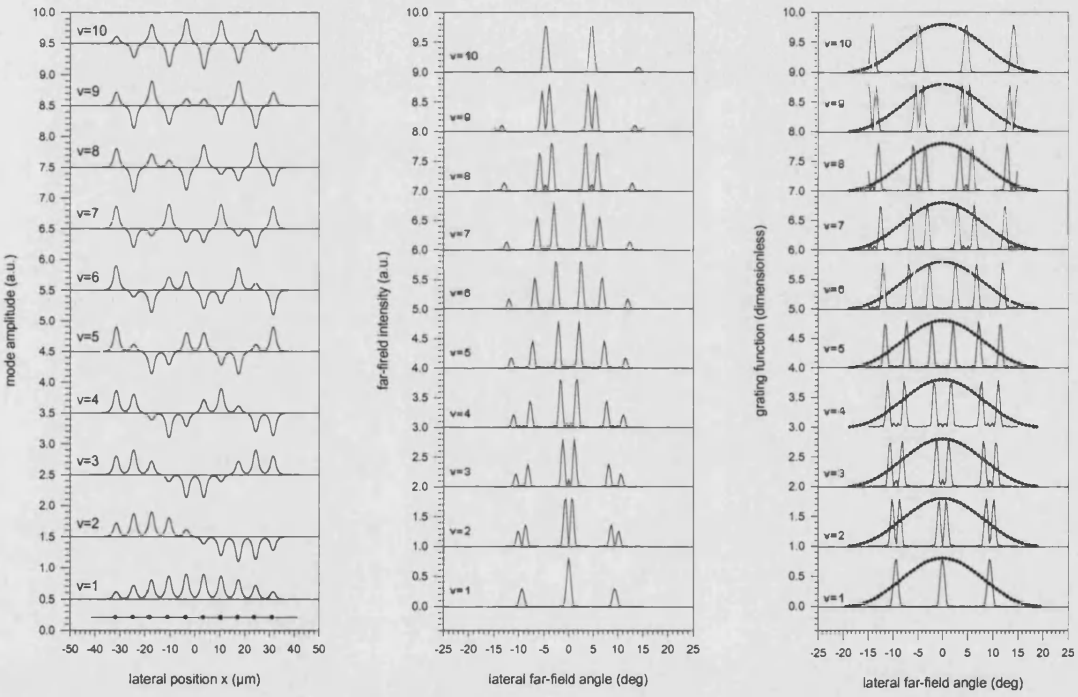


a) b) c)

**Fig. 4.3: CMT results for a 10-element array of single-mode stripe lasers, with w=3μm, S=5μm and λ=0.83μm. a) normalised amplitudes of the array modes. The solid circles show the position of the elements, corresponding to the regions where the refractive index is higher. The far-field profiles, b), result from c) the convolution between the grating functions (solid line) and the individual element far-field profile (solid line with circles). As presented in [4-6].**

To understand the effect of the grating function on the array far-field profile, computation results for an array of w=5μm wide single-mode emitters, similar to

those described above, but with N=5 elements and spacing $S = 20\mu m$, are also presented, Fig. 4.5. It can be observed that the change in the value of the inter-element spacing has a significant influence on the profile of the grating function and therefore on the far-field profiles: for S=20μm the distance between peaks in the grating function has decreased to a value $\Delta\theta = 2.3\,deg$ and more lobes are intercepted by the unchanged profile of the individual emitter.

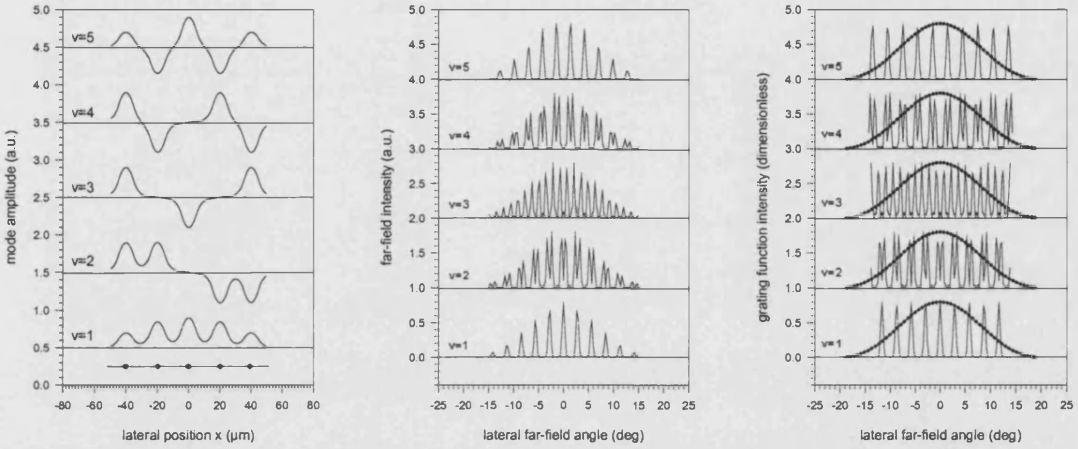


a) b) c)

**Fig. 4.4: CMT analysis for a N=5 element single-mode stripe laser array. The stripe width is w=3μm, the inter-element spacing is S=20μm and the working wavelength is λ=0.83μm. a) normalised amplitudes of the allowed modes. Corresponding b) far-field profiles and c) grating functions. The individual element far-field profile (solid line with circles) is also plot.**

The case presented above is of particular interest in this PhD thesis because the grating functions coincide with those computed also for the 5-element PBTLAs, as shown later in Chapter 6.

It is important to explain, at this stage, that although the general formulation of the problem presented in this chapter has been done for a stripe laser array structure, the CMT method is readily applicable to arrays of bow-tie lasers by substituting, in the far-field intensity profile of equation (4.10), the fields calculated for the individual tapered emitter.

## 4.4 Comparison between the CMT and the SDT

Phase-locked arrays of diode lasers were first studied by considering the diffraction pattern from a uniformly illuminated grating with equally spaced slits corresponding to individual laser-arrays elements, [4-2]. This so-called 'simple diffraction theory' had proved useful in interpreting some experimental results, but provides no method to describe all the modes of an array of coupled emitters, [4-7].

In simple diffraction theory, the grating function $\hat{I}_{Gv}(\theta)$ for an array of N coupled emitters is:

$$\hat{I}_{Gv}(\theta) = I_{Gv}(u) = \frac{\sin^2\left[\frac{N}{2}(u + \Delta\phi_v)\right]}{\sin^2\left(\frac{u + \Delta\phi_v}{2}\right)} \tag{4.13}$$

The main difference between the function grating $I_{Gv}(u)$ for the simple-diffraction theory and that of equation (4.12) is the presence of the term $\Delta\phi_v$ that corresponds to the phase-shift between adjacent elements and must be specified to calculate the array mode far-field patterns. For $\Delta\phi_v = 0$, equation (4.13) gives the profile of the in-phase array mode previously seen also in the coupled-mode analysis. However, a phase-shift $\Delta\phi_v = \pi$ must be introduced to obtain the out-of-phase-array mode that, in the coupled-mode analysis, is simply the solution of equations (4.10) for $v = N$.

Thus, to compare the two models, only the far-fields of the modes for $\Delta\phi_v = 0$ and $\Delta\phi_v = \pi$ (from simple-diffraction theory) and for $v = 1$ and $v = N$ (from coupled mode theory) can be considered.

Theoretical results obtained for the 5-element array described in Section 4.3, are presented and compared with the ones obtained with the CMT model in Fig. 4.5.

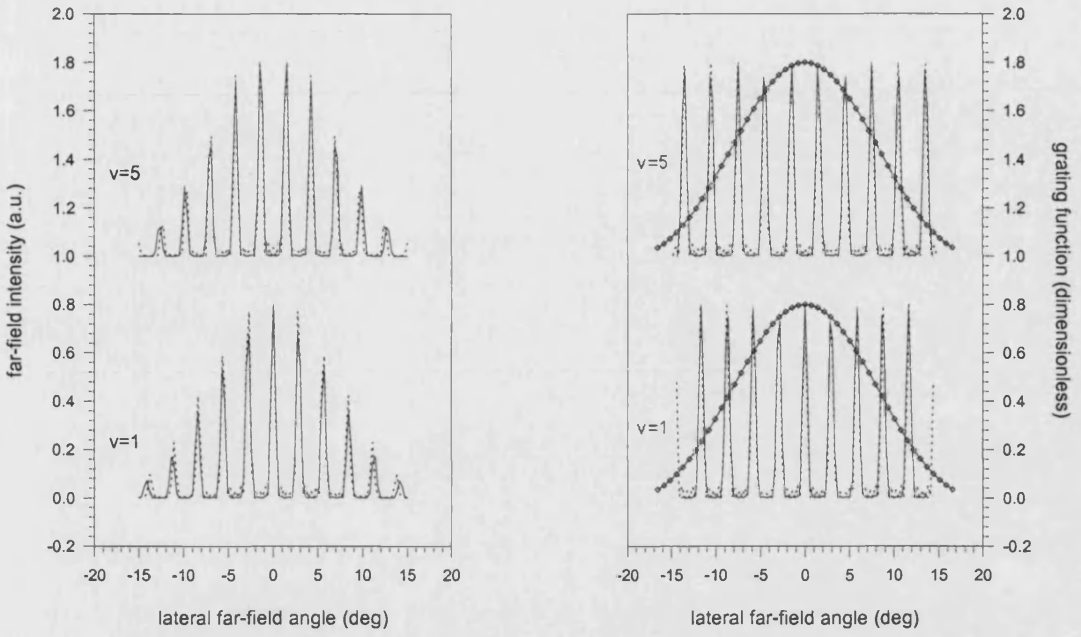


a) b)

**Fig. 4.5: Comparison between results computed with the CMT (solid line) and SDT (dotted line) method for a 5-element array with S=20μm, w=3μm and λ=0.83μm. The far-field profiles of the in-phase and out-of-phase modes, a), are the convolution of the corresponding grating functions with the individual element far-field profile (solid line with circles), b).**

## 4.5 Effect of Gain Profile and Losses on Mode Discrimination in Positive-Index Arrays

The most important aspect to be considered when studying phase-locked lasers is the effect of gain and losses on the lasing mode discrimination. Arrays similar to that in Fig. 4.2, as well as the arrays of interest in this work, are referred to as 'positive-index arrays' and are characterised by a built-in distribution of the refractive index (and the gain) with higher value under the emitter contacts and lower values in the inter-element regions.

In the vast majority of the cases, [4-14], [4-25], [4-26], positive-index arrays operate in the out-of-phase conditions because the out-of-phase evanescent mode having field nulls in the lossy inter-element regions, Fig. 4.3 and Fig. 4.4, has better field overlap with the gain profile than not does the in-phase mode. Under the assumption of higher gain where the refractive index is higher (i.e. under the laser contacts ridges) and lower gain where the refractive index is lower (i.e. between

adjacent elements), the modal gain (overlap of the optical field intensity with the gain distribution) is in fact highest for the out-of-phase mode.

Following the criteria of the maximum overlap between optical field and gain distribution, the next favoured mode would be the $\nu = N-1$ mode because the field goes through nulls between all the emitters but the two central ones, where the field amplitude is relatively low anyway. A combination of these two modes would give a two-lobed far-field pattern with a width in the range of two to three times the simple diffraction limit.

On the other hand in-phase operation can be favoured in situation in which the interchannel regions are less lossy than the adjacent channels, [4-14], [4-17], [4-25], [4-26], with the fundamental supermode having the highest modal gain.

Several calculations have been presented in literature to make these arguments more quantitative, where various spatial gain distribution were considered and the supermode modal gains were calculated by overlap integral between the supermode field intensity and the gain distribution itself.

However, promising results seemed to occur only in structures having no inter-element loss and relatively few elements (up to seven), [4-1], [4-14]. In addition, even for those lasers which appear to lase primarily in a single far-field lobe, the radiation pattern peak is often displaced or beam width is bigger than the diffraction limit, implying more complicated behaviour than single $\nu = 1$ supermode oscillation, and suggesting that self-focusing of the in-phase mode due to spatial hole burning, [4-3], and simultaneous excitation of higher order modes occurs, [4-2].

The above statement can be explained observing that, due to the raised-cosine-shaped envelope of the in-phase evanescent mode near-field intensity profile, Fig. 4.3 and Fig. 4.4, with increasing current above threshold, gain saturation due to the local photon density is stronger in the central array elements. Gain saturation and the decrease of carrier density, in turn yields an increase of the refractive index in the same region. The ultimate effect on the in-phase mode is self-focusing of the near-field and an increase of the far-field beam width. At the same time, since the array area is uniformly pumped, more gain is available for higher-order modes, which reach threshold and cause further broadening of the emitted beam.

The effect of carriers on the refractive index profile and of spatial hole-burning, combined with the longitudinally non-uniform coupling, is particularly important, as explained at the beginning of the chapter, for the mode discrimination in arrays of tapered laser. The criteria of the maximum overlap between optical field and gain distribution will be followed to investigate and explain the in-phase mode selection in PBTLAs, and to demonstrate that, differently from more conventional positive-index arrays of stripe lasers, scalability is in principle possible. However, also in this case changes in the lateral gain profile due to hole-burning can significantly increase the modal gain of higher order modes and, therefore, strongly influence the optical output profile.

## Summary

Lateral refractive index profile and gain distribution are responsible for mode selection in phase-locked arrays of positive-index guided and mainly in the Parabolic Bow Tie Laser arrays of interest in this PhD thesis.

The longitudinal tapering of the laser contact ridges reflects in a longitudinally non-uniform coupling between the array elements, with weak coupling along the device and strong coupling at the devices ends.

In the region near the output facets, where the elements merge in a single contact and there is no explicit lateral mode control, due to the effect of carriers on the effective refractive index and to spatial hole-burning, the optical gain in the inter-element regions is larger than that in the element regions, resulting in a higher modal gain for the in-phase (array) mode operation.

Under the assumption than each emitted operates in a single lateral mode and that strong nearest-neighbour coupling occurs only at the device output facet, the array behaviour can be analysed using the Coupled-Mode Theory. Importantly, in the presented formulation, the coupled-mode theory is applied to the optical field of each emitter, calculated self-consistently, to determine the far-field profiles of the oscillating modes supported by the array.

An analytic expression has been derived for the array far-field patterns that are calculated from the convolution between the individual element far-field intensity

profile and the so-called grating function, which accounts for the element number and inter-element spacing.

The presented model, which for a general formalisation has been used to analyse the propagation characteristics of conventional stripe laser arrays, is readily applicable to arrays of tapered lasers.

# References

[4-1] D. Botez, D. R. Scifres, *Diode Laser Arrays*, Cambridge University Press (1994).

[4-2] D. R. Scifres, W. Streifer, R. D. Burnham, *Experimental and analytical studies of coupled multiple stripe diode lasers*, IEEE J. Quantum Electron., QE-15(9), 1979, pp. 917-922

[4-3] G. H. B.Thompson, J. E. A.Whiteaway, *'Analysis of the Stability of the Highest-Order Supermode in Semiconductor Laser Arrays'*, Electronics Letters, vol. 23, n. 9, Apr. 1987, pp. 444-446.

[4-4] D. F. Welch, W. Streifer, P. S. Cross, D. R. Scifres, *'Y-Junction Semiconductor Laser Arrays: Part II - Experiments'*, IEEE J. Quantum Electronics, vol. 23, 1987, pp. 752-756.

[4-5] W. Streifer, A. Hardy, D. F. Welch, D. R. Scifres, P. S. Cross, *'Improved Y-X Junction Laser Array'*, Electronics Letters, vol. 26, n. 20, 1990, pp. 1730-1731.

[4-6] J. K. Butler, D. E. Ackley, D. Botez, *Coupled-mode analysis of phase-locked injection laser arrays*, Applied Physics Letters, 44(3), 1984, pp. 293-295

[4-7] D. Botez, *Array-mode far field patterns for phase-locked diode-laser arrays: coupled-mode theory versus simple diffraction theory*, IEEE Journal of Quantum Electronics, QE-21(11), 1985, pp. 1752-1755

[4-8] A. Yariv, *Optical Electronics in Modern Communications*, Oxford University Press 91997)

[4-9] D. F. Welch, W. Streifer, P. S. Cross, D. R. Scifres, *'Y-Junction Semiconductor Laser Arrays: Part II - Experiments'*, IEEE J. Quantum Electronics, vol. 23, 19875, pp. 752-756.

[4-10] D. Botez, M. Jansen, L. J. Mawst, G. Peterson, T. Roth, *'Watt-range, coherent, uniphase powers from phase-locked arrays of antiguided diode lasers'*, Appl. Phys. Lett, vol. 58, n. 19, 1991, pp. 2070-2072

[4-11] C. Zmundzinski, D. Botez, L. J. Mawst, C. Tu, L. Frantz, *'Coherent 1W continuous wave operation of lasrge-aperture resonant arrays of antiguided lasers'*, Appl. Phys. Lett, vol. 63, n. 23, 1993, pp. 2914-2916

[4-12] D. Botez, A. Napartovich, C. Zmudzinski, *'Phase-Locked Arrays of Antiguides: Analytical Theory II'*, IEEE J. Quantum Electronics, vol. 31, 1995, pp. 244-253.

[4-13] G. A. Evans, J. M. Hammer, *Surface Emitting Semiconductor Lasers and Arrays*, New York Academic Press (1993).

[4-14] H. Fujii, I. Suemune, M. Yamanishi, *Analysis of transverse modes of phased-locked multi-stripe lasers*, IEE Electronics Letters, vol. 21, n.16, 1985, pp. 713-714

[4-15] R. F. Nabiev, A. I. Onishenko, *'Laterally Coupled Periodic Semiconductor Laser Structures: Bloch Functions Analysis'*, IEEE J. Quantum Electron., vol. 28, 1992, pp. 2024-2032

[4-16] G. P. Aggrawal, N. K. Dutta, *Long-Wavelength Semiconductor Lasers*, Van Nostrand Reinhold, 1986

[4-17] S. R. Chinn, R. J. Spiers, *'Modal Gain in Coupled-stripe Lasers'*, IEEE J. Quantum Electron., vol. QE-29, n. 4, 1984, pp. 358-363

[4-18] W. K. Marshall, J. Katz, *'Direct Analysis of Gain-Guided phase-Locked Semiconductor Laser Arrays'*, IEEE J. Quantum Electron., vol. QE-22, n. 6, 1986, pp. 2024-2032

[4-19] L. Rahman, H. G. Winful, *'Nonlinear Dynamics of Semiconductor Laser Arrays: a Mean Field Model'*, IEEE J. Quantum Electron., vol. 30, n. 6, 1994, pp. 14051415

[4-20] H. Adachidara, O. Hess, R. Indik, J. V. Moloney, *'Semiconductor Laser Arrays Dynamics: Numerical Simulations on Multistripe Index-Guided Lasers'*, J. Opt. Soc. Am. B, vol. 10, n. 3, 1993, pp. 496-506

[4-21] F. Causa, *'Hermite-Gauss Functions in the Analysis of a Category of Semiconductor Optical Devices'*, PhD Thesis, University of Bath, 1998.

[4-22] F. Causa, J. Sarma, *'A quasi-analytic model for longitudinally non-uniform semiconductor optical sources'*, Optics Communications, Vol. 183, 2000, p. 149-157

[4-23] F. Causa, J. Sarma, *'A versatile method for analysing paraxial optical propagation in dielectric structures'*, Journal of Lightwave Technology, Vol. 18, p. 1445, 2000

[4-24] F. Causa, Model implemented in Fortran 77

[4-25] E. Kapon, *'The Supermode Structure of Phase-Locked Diode Laser Arrays with Variable Channel Spacing'*, IEEE J. Quantum Electron., vol. QE-23, n. 1, 1987, pp. 89-93

[4-26] W. Streifer, A. Hardy, R. D. Burnham, D. R. Scifres, *'Single-Lobe Phased-Array Diode Lasers'*, Eletron. Lett., vol. 21, n. 3, 1985, pp. 118-120

# Chapter 5

# *Parabolic Bow-Tie Lasers*

The aim of this chapter is to illustrate the operational characteristics of the Parabolic Bow-Tie Laser (PBTL) designed to achieve simultaneously high output power and a narrow output beam. The high brightness PBTL is the building block of the novel (high brightness) tapered array presented in Chapter 6 of this PhD thesis.

The specific PBTL structure discussed in this Chapter is the outcome of a systematic study on index-guided semiconductor Bow-Tie Lasers (BTLs) of different geometries and sizes, to show that with suitable design of the material structure and of the laser cavity it is possible to achieve the desired operational characteristics, [Appendix C].

The optical propagation in the dielectric structures was solved using an analytic model based on the Step Transition Method (STM), [5-1]-[5-3], in conjunction with the Local Mode Expansion (LME) method, [5-4], but making use of only the bound modes to simplify the computational scheme, [5-5]. In the present formulation the method is valid only for passive dielectric structures, but it can be considered to be sufficiently accurate to describe the laser optical field profile at threshold. This 'passive' model has been used for the optimisation of the device geometry because it produces a fast computational procedure. However, to ascertain that the device design optimisation with the analytic model is satisfactory, computed results have been compared with corresponding results from the HGCM model for active devices, [Appendix C], [5-6]-[5-8].

The device operational characteristics presented in this chapter have been systematically measured with emphasis on the characterisation of the output beam quality.

## 5.1 Semiconductor Material Characteristics

The lasers of interest in this PhD have been fabricated in-house from an InGaAs/GaAs/AlGaAs Large Optical Cavity (LOC) Triple Quantum Well (TQW)

Double Heterostrucure semiconductor material, for 980nm wavelength, [5-9]. The layer epitaxy, Tab. 5.1, was grown by low pressure Metal Organic Vapour Phase Epitaxy (MOVPE) on n-GaAs substrate.

**Tab. 5.1: Semiconductor material structure.**

| Layer | Composition | Thickness (μm) | Doping density ($cm^{-3}$) | Dopant |
|---|---|---|---|---|
| Contact | GaAs | 0.2 | $3.0\ 10^{19}$ | Zn |
| Cladding | $Al_{0.42}$ | 0.77 | $8.0\ 10^{17}$ | C |
| Guide | $Al_{0.20}$ | 0.24 | undoped | -- |
| QW | $In_{0.2}Ga_{0.8}As$ | 7nm | undoped | -- |
| Barrier | GaAs | 10nm | undoped | -- |
| QW | $In_{0.2}Ga_{0.8}As$ | 7nm | undoped | -- |
| Barrier | GaAs | 10nm | undoped | -- |
| QW | $In_{0.2}Ga_{0.8}As$ | 7nm | undoped | -- |
| Guide | $Al_{0.20}$ | 0.24 | undoped | -- |
| Cladding | $Al_{0.42}$ | 1.77 | $1.4\ 10^{18}$ | Si |
| Buffer | GaAs | 0.5 | $1.4\ 10^{18}$ | Si |

The semiconductor epitaxy has been specially designed, [5-9], to satisfy the contradictory requirements of low optical confinement to reduce the power density at the facet, and therefore increase the lever of optical output power density achievable before COD, and an adequate confinement to achieve sufficient gain, [Appendix D]. Importantly, the semiconductor material structure has been designed for index-guided operation. The device etched ridge had to provide the lateral effective refractive index step $\Delta n_{eff}$ required to effectively reduce current spreading and for lateral optical mode control, [Appendix C]. In addition it was essential to design also for a relatively small vertical beam divergence, $\theta_y$, to achieve high brightness. The thickness of the guide layers, $t_w$, was found to be the critical parameter to be adjusted to simultaneously satisfy all the above requirements, [5-9]. More details on the material design are given in Appendix D.

The modal properties of the semiconductor material used for device fabrication were solved with the Effective Dielectric Constant (EDC) method, [5-2], by using the Cascaded Matrix Method (CMM), [5-10], to analyse the multi-layer structure. The vertical layer structure supports only three (bound) modes of which the two higher order modes are mainly confined in the lossy, cladding layers, Fig. 5.1.

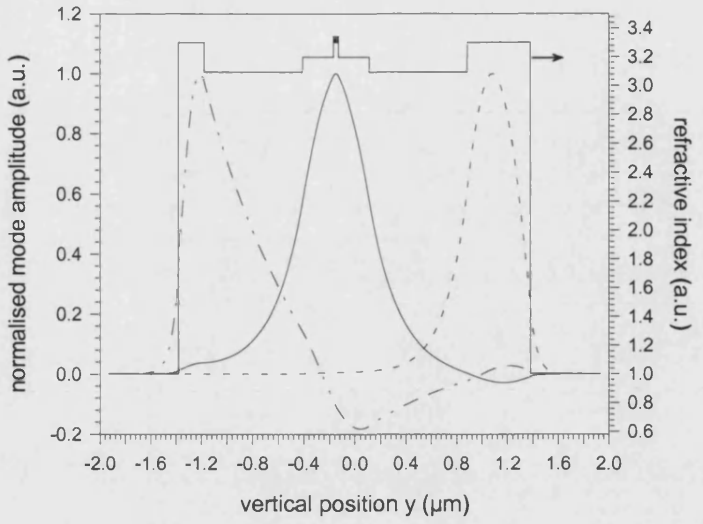


**Fig. 5.1: Refractive index profile of the designed semiconductor material and calculated mode distribution for the fundamental (solid line) and higher order modes (dashed, dashed-dotted line).**

The fundamental mode has the largest confinement factor in the active region, $\Gamma_{QW} = 0.045$, with a corresponding equivalent spot size $S_S = 0.46\mu m$, which is desirable for high power operation, [5-11]. The TQW structure ensures a sufficiently high gain to overcome the small confinement of the fundamental mode in the gain layers; the estimated free carrier absorption and propagation losses are $\alpha_{FC} = 0.6cm^{-1}$ and $\alpha = 3cm^{-1}$ respectively.

The experimental vertical far-field intensity profile measured from in-house fabricated devices matches with that predicted from the theory, giving a Full Width at Half Maximum (FWHM) far-field divergence angle of $\theta_y = 58deg$. The maximum (output) optical power density before COD for this material has been measured to be $P_{COD} \sim 12MWcm^{-2}$.

For the devices described here, the $h_{RIB} = 0.9\mu m$ deep rib waveguide etched in the top cladding layer not only is sufficient to guarantee suitable current confinement and the required explicit lateral effective index step, but also ensures that the device narrow central straight section is single moded, [Appendix C]. The variation of the effective refractive index with cladding layer thickness for the designed material and the corresponding value for $\Gamma_{QW}$ are shown in Fig. 5.2.

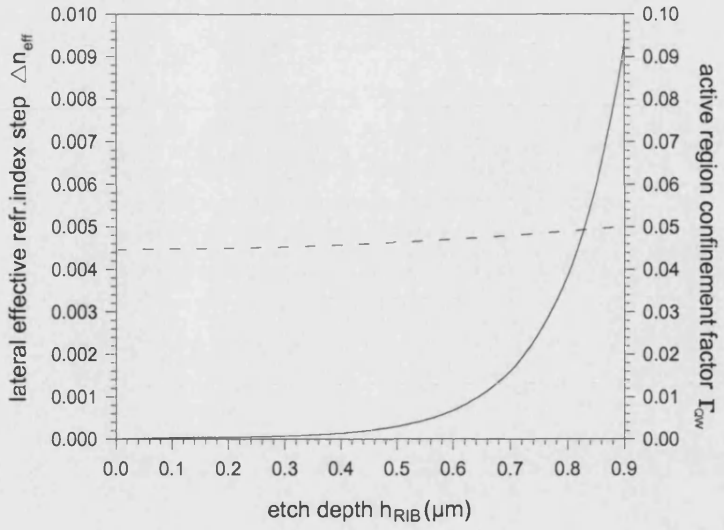


**Fig. 5.2: Effective refractive index step (solid line) and optical confinement factor in the active region (dashed line) as functions of the rib height ($h_{RIB}$) for the LOC material used for device fabrication.**

The fabrication of the devices is based on a photolithographic process in which the photoresist is exposed to UV light through a specially designed mask to reproduce the desired pattern on the material surface. The tapered ridge waveguide is formed by Ion Beam Etching (IBE).

The metallisation on the p-side contact is formed by vacuum thermal evaporation of Ti-Au. After thinning and AuGeNi n-metallisation, the wafer was cleaved to obtain the required total cavity length.

The lasers were successively mounted p-side down on Cu submounts, in order to have access to both facets and, finally, contacted by wire bonding. The heat sinking properties of the mount have not been optimised, therefore the devices have been typically tested under pulsed operation (5μs pulse width, duty cycle of 0.1%) and using a Temperature Controller for stabilised room temperature, $T = 20^{\circ}C$.

## 5.2 Bow-Tie Design Optimisation

To maximise device brightness it is necessary to achieve diffraction-limited operation. In the ideal case the desired narrow output beam would be achieved by restricting the number of modes propagating in the structure to just the fundamental mode, [5-1]. However, for high-power operation the above condition is restrictive and would enhance the risk of COD. Therefore, the output width of the tapered

structures of interest is broad, so that the corresponding local waveguide section is typically multimoded. The 'optimised' PBTL design, depicted in Fig. 5.3, [5-12], is therefore the outcome of a procedure, [Appendix C], entailed to find the optimum taper geometry that would minimise the coupling from the fundamental to the higher order modes and yield the narrowest possible, single-lobed far-field intensity profile, [5-3].

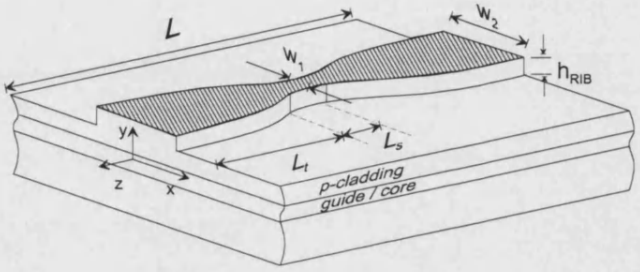


**Fig. 5.3: Schematic of the parabolic bow-tie laser geometry with definition of relevant parameters.**

The parameter of interest was the beam lateral divergence at Full Width Half Maximum (FWHM). The beam vertical divergence is not considered in the optimisation process because it depends on the semiconductor material multilayer structure and not on the device geometry. For the optimisation of the taper geometry, linear, parabolic and exponential taper profiles have been considered, whose rib width longitudinal variation is described by:

$$w_{Lin}(z) = w_1 + z\frac{(w_2 - w_1)}{L_t} \quad \text{, linear taper} \tag{5.1}$$

$$w_{Par}(z) = \left[ w_1^2 + z\frac{(w_2^2 - w_1^2)}{L_t} \right]^{1/2} \quad \text{, parabolic taper} \tag{5.2}$$

$$w_{Exp}(z) = w_1 \exp\left[ z\frac{1}{L_t} \ln\left( \frac{w_2}{w_1} \right) \right] \quad \text{, exponential taper} \tag{5.3}$$

A set of calculations varying first the length, $L_t$, and then the output width, $w_2$, of the taper were performed to study the effect of the device geometry on the far-field pattern. The range of variation of both parameters was dictated by the

contradictory requirements to achieve high power and high brightness: the device z-dependent width had to be small to restrict the number of guided modes but at the same time the output width had to be sufficiently wide to reduce the risk of COD. In addition the overall device dimensions had to be compact to favour integration, increase mechanical strength and reduce the occurrence of instability. To complete device optimisation the effect of $\Delta n_{eff}$ on the FWHM far-field divergence was analysed: the optimum value was found to be $\Delta n_{eff}$=0.007. More details on the device design are given in Appendix C.

The main results are presented in Fig. 5.4. It can be observed that the smallest values for the far-field lateral divergence are obtained with the parabolic geometry.

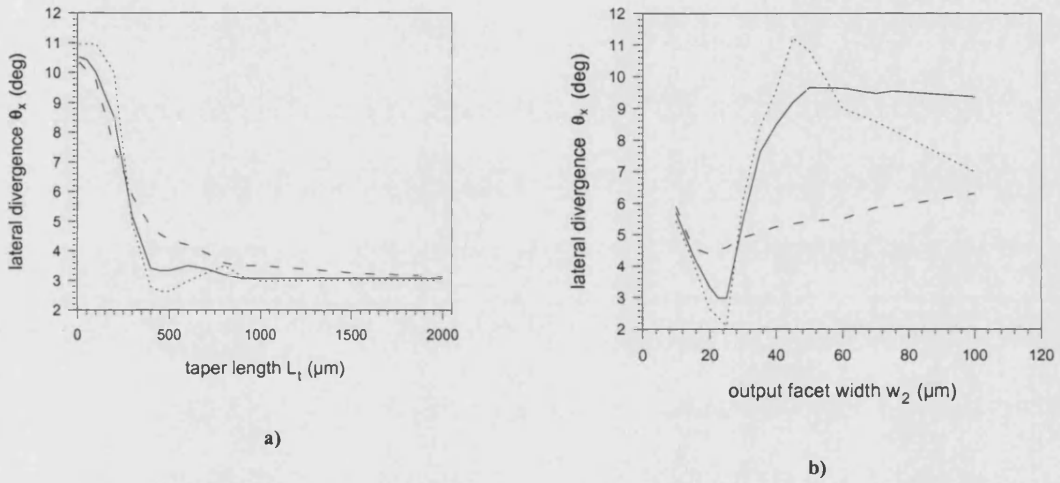


**Fig. 5.4: Computed far-field lateral divergence at FWHM, $\theta_x$, for linear (solid line), parabolic (dotted line) and exponential (dashed-dotted line) BTLs as a function of the a) length $L_t$ when $w_2$=20μm and b) output width $w_2$ when $L_t$=500μm. For all the devices $L_s$=50μm, $w_1$=3μm and $\Delta n_{eff}$=0.007.**

From the results obtained with the LME method the 'optimised' device parameters were chosen to be those summarised in Tab. 5.2

**Tab. 5.2: Relevant parameters for the parabolic bow-tie laser of Fig. 5.3.**

| Parameter | Value |
|---|---|
| Taper narrow end width | $w_1$=3μm |
| Taper broad end width | $w_2$=20μm |
| Taper length | $L_t$=500μm |

| Parameter | Value |
|---|---|
| Narrow section length | $L_S$=50μm |
| Rib height | $h_{RIB}$=0.9μm |
| Lateral effective index step | $\Delta n_{eff}$=0.007 |

## 5.3 Parabolic Bow-Tie Lasers: Experimental Results

Detailed optical and electrical measurements results for the optimised PBTLs are shown in Fig. 5.5. A representative characteristic curve of the laser (light) output power as a function of the injected current (L-I curve), is presented together with the corresponding voltage across the diode and the electrical-to-optical power conversion efficiency (Wall-Plug efficiency, W-P) curves measured under pulsed operation.

Typical threshold currents are $I_{th} = 50mA$, corresponding to a threshold current density $J_{th} = 0.4kA/cm^2$. The slope efficiency has been measured to be $\eta_e$=0.7W/A.

In pulsed operation output powers up to 640mW per facet, corresponding to a maximum Wall-Plug efficiency of 45%, have been measured from PBTLs without COD at an operating current $I = 1A = 20I_{th}$, [5-9], [5-12]. The junction voltage and the series resistance are measured to be $V_j$~0.9V and $R_S$~0.25Ω, respectively, and are in good agreement with the expected values, [Appendix A]. No kinks can be observed in the range of operating current (restricted because of the limitations in the thermal management of the experimental set-up, not to damage the devices).

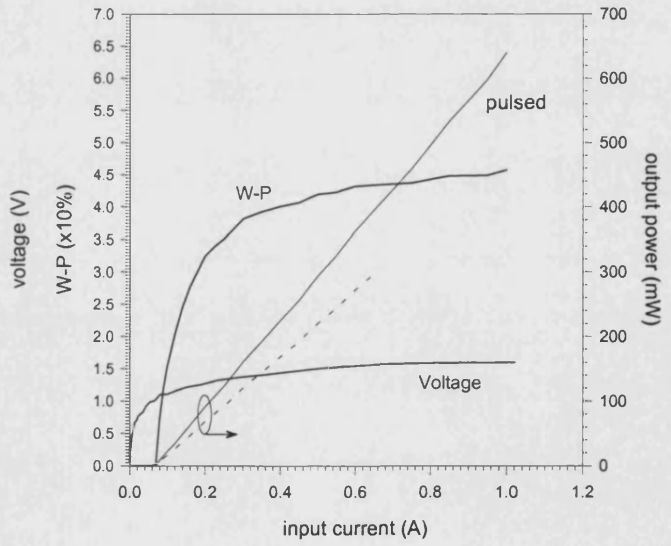


**Fig. 5.5: Experimental (pulsed) L-V-I curve and corresponding W-P efficiency measured from in-house fabricated PBTLs. [5μs pulse width, 0.1% duty cycle; Temperature: 20°C. Neutral density filters have been used to avoid the saturation of the detector]. The CW L-I characteristic (dashed line) is also shown for comparison.**

Measurements taken under Continuous Wave (CW) operation show a 30% decrease of output power: 300mW are achieved, without COD, at an injected current of 600mA, Fig. 5.5. Such 30% decrease in the achievable output power, compared to the value measured under pulsed condition for the same injected current, can be explained by the above-mentioned considerations on the present, modest heat-sinking mount, and that carrier spillage occurs when the junction temperature increases, [Chapter 2]. However, noticeably the threshold current in CW operation is almost unchanged and no thermal roll-over occurs in the current range in which the devices have been tested.

Near-field intensity measurements have been taken under pulsed operation imaging the optical field at the device output facet onto a CCD camera (magnification and numerical aperture of used objective lens used are x10 and 0.25 respectively). Comparisons of profiles measured just above threshold with those computed with the passive analytic model and the active HGCM model, [Appendix B], are shown in Fig. 5.6.

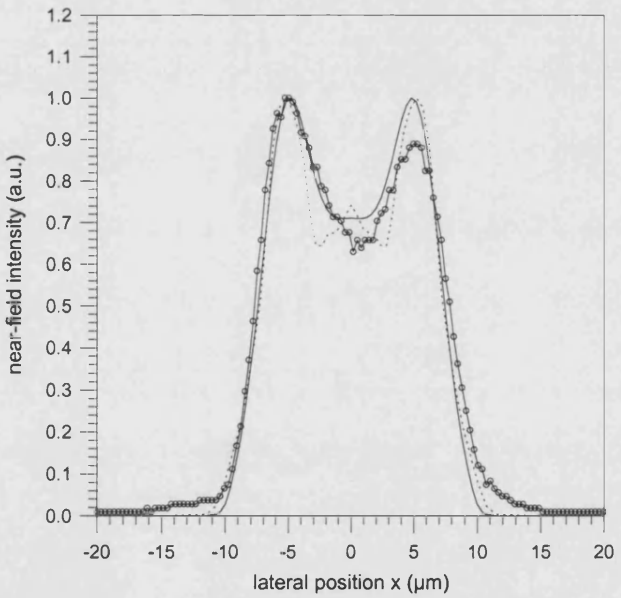


**Fig. 5.6: Comparison between measured (line with circles) and theoretical, computed with the passive analytic model (solid line) and the HGCM model (dotted line), near-field intensity profiles from PBTLs.**

The main device parameters used with the model are summarised in Tab. 5.3.

**Tab. 5.3: Parameters for modelling parabolic bow-tie lasers.**

| Parameter | Value | Parameter | Value |
|---|---|---|---|
| Diffusion constant | $D_c=8\cdot10^{8}\mu m^2s^{-1}$ | Gain coefficient | $A=1.5\cdot10^{-8}\mu m^2$ |
| Recombination coefficient | $B_r=1.4\cdot10^{2}\mu m^3s^{-1}$ | Carrier density at transparency | $N_{tr}=1\cdot10^{6}\mu m^{-3}$ |
| Active layer doping density | $N_0=1\cdot10^{4}\mu m^{-3}$ | Active region thickness | $d_{QW}=0.021\mu m$ |

The beam quality has been determined first by directly measuring the far-field pattern. The far-field intensity profiles, measured at various injection current levels are presented in Fig. 5.7. A 0.25mm slit has been placed in front of the photodetector to increase the measurement resolution ( 0.05 deg ). Details on the measurement set-up are given in Appendix E.

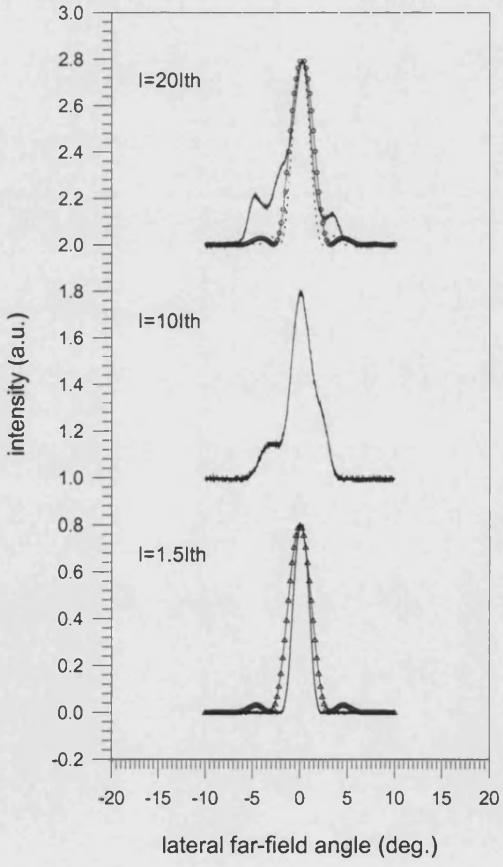


**Fig. 5.7: Far-field intensity profiles measured without the use of external optics from PBTLs at $I=1.5I_{th}$, $I=10I_{th}$ and $I=20I_{th}$.The diffraction-pattern (dotted line) from a corresponding 20µm wide uniformly illuminated aperture, and the theoretical profiles computed with the STM model (solid line with triangles) and the HGCM model (solid line with circles) are also shown.**

The measured far-field lateral width at Full Width Half Maximum (FWHM), or simply lateral divergence, for injected currents up to 20 times the threshold value, is $\theta_x = 2.8\,\text{deg}$, corresponding to the diffraction-limit angle $\theta_d = \arcsin\left(\frac{\lambda}{D}\right) = 2.8\,\text{deg}$, equation (2.16), for a D=20μm wide uniformly illuminated aperture, [5-9]. Fig. 5.7 also shows that there is good agreement between measured and predicted far-field profiles. It was not possible to observe or quantify the presence of beam steering since with present measurement apparatus the accuracy of the scale is $0.5\,\text{deg}$, [Appendix E], which is of the same order of magnitude of reported beam steering angles, [5-13], [5-14].

The narrow far-field profiles of Fig. 5.7 have been measured without the use of external lenses: this is one of the most attractive features of index-guided PBTLs, compared to MOPA-type devices, [5-15], [5-16]. The calculated brightness of such devices is $137\text{MWcm}^{-2}\text{srad}^{-1}$ at $I = 1A = 20I_{th}$.

The Strehl Ratio was estimated experimentally by measuring the power through slits placed at the far field plane and with aperture corresponding to the diffraction-limit divergence angle. The Strehl Ratio value decreases gradually from 100%, at low output powers, to 66% for $I = 1A = 20I_{th}$, corresponding to 450mW in the diffraction-limit angle. The decrease in the value of the Strehl Ratio is attributable to the broadening of the far-field pattern, Fig. 5.7, due to the simultaneous oscillation, at the highest current, of the fundamental mode and of the first higher order mode.

From the measured near- and far-field profiles it was possible to measure the $M^2$-factor, equation (2.38), found to be 1 at threshold and increasing to a maximum value $M^2 = 1.28$ at $I = 1A = 20I_{th}$.

The main operational characteristics and beam quality parameters for the optimised PBTLs, measured at injection currents just above threshold and at 20 times the threshold, are summarised in Tab. 5.4.

**Tab. 5.4: Comparison of the operational characteristics of the optimised index-guided Parabolic Bow-Tie Lasers at two different injection currents.**

| PBTL | Output Power | $\theta_x$ FWHM (deg) | $M^2$-factor | Strehl Ratio | Brightness ($MWcm^{-2}srad^{-1}$) |
|---|---|---|---|---|---|
| $I=1.5I_{th}$ | 2mW | 2.8 | 1 | 100% | 0.55 |
| $I=20I_{th}$ | 640mW | 2.8 | 1.28 | 66% | 137 |

## 5.4 Effect of the Device Geometry: Results Overview

Corresponding Linear Bow-Tie Lasers (LBTLs), Exponential Bow-Tie Lasers (EBTLs) and Stripe Lasers (SLs) with the same length and output width as the PBTLs discussed in the previous Section have been fabricated and characterised for comparison, [5-9], to verify the theoretical results obtained in stage of device design.

Representative characteristic curves of the L-I curves measured from LBTLs, PBTLs, EBTLs and SLs are presented in Fig. 5.8. LBTLs, PBTLs, and EBTLs show similar current threshold value, $I_{th} = 50mA$, as the PBTLA, corresponding to an equivalently low threshold current density, $J_{th} = 0.4kA/cm^2$. Only for the stripe lasers, whose active area is larger (almost double) than the one for the Bow-Tie lasers, the corresponding threshold current density is smaller ($J_{th} \sim 0.24kA/cm^2$). In addition, the larger active area results also in a higher output power. It can be noticed, in fact, that the achieved output power is comparable for the BTLs, with the PBTL reaching a maximum of 640mW/facet at the maximum value I=1A. Higher output powers are measured for the stripe laser, with 700mW/facet for the same injection current I=1A, [5-9].

Also the slope efficiencies are comparable for the three types of BTL, with the highest value ($\eta_e$=0.7W/A) from the PBTL. An efficiency of $\eta_e$=0.8W/A was measured from the stripe laser.

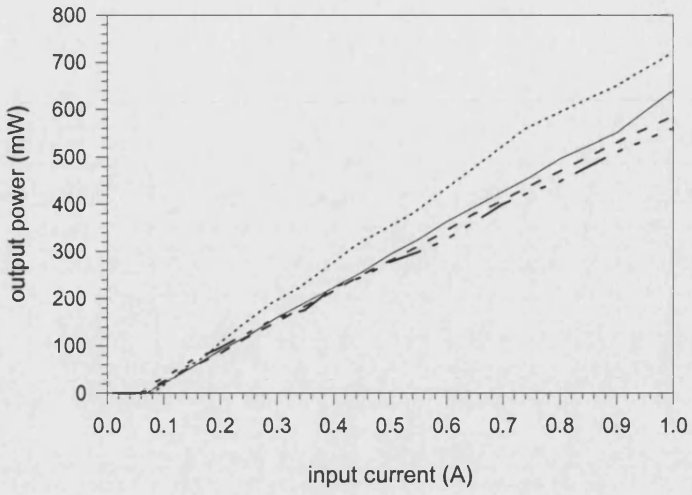


**Fig. 5.8: Optical output power versus pulsed injected current measured from PBTLs (solid line), LBTLs (dashed line), EBTLs (dash-dotted line) and SLs (dotted line). All the devices have the same length L=1050μm and same output width $w_2$=20μm.**

Near-field intensity profiles measured from all devices at an injection current $I=3I_{th}$ are presented in Fig. 5.9 and compared with the theoretical curves calculated with the active HGCM model (parameters in Tab. 5.4).

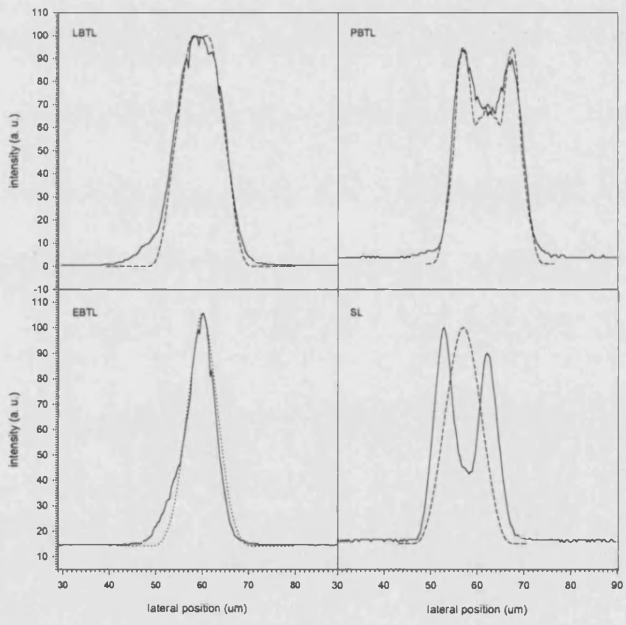


**Fig. 5.9: Measured (solid line) near-field intensity profiles for LBTLs, PBTLs, EBTLs and SLs with corresponding theoretical curves (dashed line) from the HGCM model, for comparison.**

Good agreement can be observed between experimental and computed data for all BTLs. The difference in the profiles for SLs is attributable to the fact that in the

theoretical calculations the fundamental mode only has been taken into account, whereas the measured optical field shows the contribution of all the modes supported by the structure.

The far-field profiles, measured without external optics for all devices at different values of the injected current, are plotted in Fig. 5.10 and compared with the diffraction pattern from a 20μm wide uniformly illuminated aperture and with the theoretical far-filed profile computed with the HGCM model.

The far-fields from the linear and parabolic Bow-Tie lasers show a single-lobed beam, indicating nearly single-mode operation, over a wide range of currents. A contribution of higher modes is observed only at the highest current. The measured lateral beam divergence corresponds to the theoretically estimated diffraction-limit value. On the other hand, the exponential Bow-Tie laser and the stripe laser show multi-lobed radiated beam patterns, indicating that they cannot operate, over the range of currents investigated, in a dominantly fundamental mode.

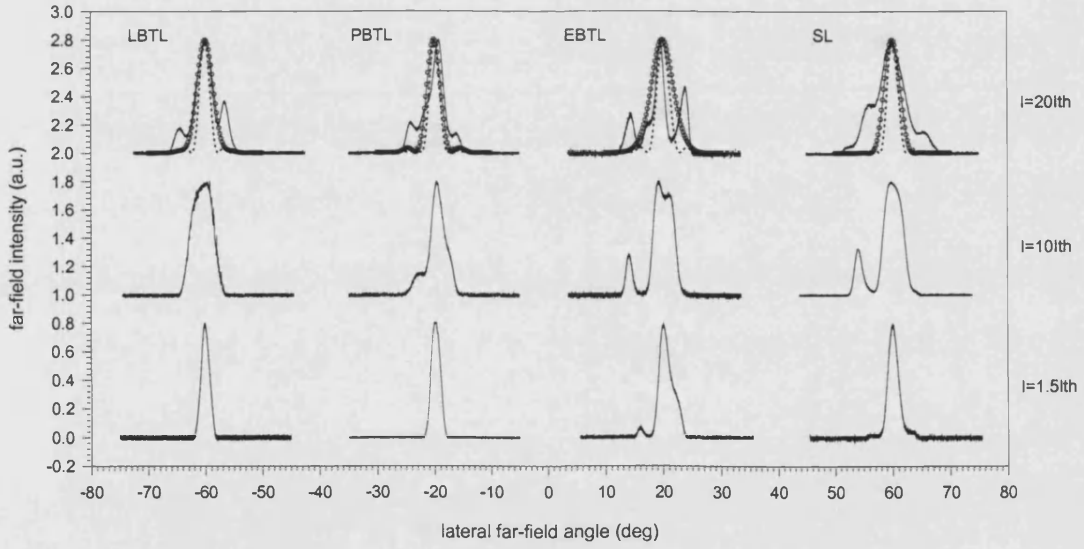


**Fig. 5.10: Far-field intensity profiles measured (solid line) without the use of external optics from LBTLs, PBTLs, EBTLs and SLs at $I=1.5I_{th}$, $I=10I_{th}$ and $I=20I_{th}$.The diffraction-pattern (dotted line) from a corresponding 20μm wide uniformly illuminated aperture and the theoretical profiles computed with the HGCM model (solid line with circles) are also shown.**

The main results from the experimental characterisation of the four types of devices, at two different operating currents ( $I = 1.5I_{th}$ and $I = 20I_{th}$ ), are summarised in Tab. 5.5 for compactness.

**Tab. 5.5: Operational characteristics of LBTLs, PBTLs, EBTLs and SLs with same output width and same length measured at two different injection currents.**

| Characteristics | Linear Bow-Tie | Parabolic Bow-Tie | Exponential Bow-Tie | Stripe |
|---|---|---|---|---|
| Threshold Current | 55mA | 50mA | 55mA | 60mA |
| Slope Efficiency (W/A) | 0.62 | 0.7 | 0.59 | 0.8 |
| **Characteristics at $I \sim 1.5I_{th}$** | | | | |
| Output Power | 1mW | 2mW | 1mW | 20mW |
| $\theta_x$ FWHM (deg) | 2.8 | 2.8 | 2.8 | 2.8 |
| $M^2$-factor | 1 | 1 | ~1 | 1 |
| Strehl Ratio (%) | 100 | 100 | 80 | 100 |
| Brightness ($MWcm^{-2}srad^{-1}$) | 0.27 | 0.55 | 0.24 | 5.5 |
| **Characteristics at $I \sim 20I_{th}$** | | | | |
| Output Power | 560mW | 640mW | 540mW | 700mW |
| $\theta_x$ FWHM (deg) | 2.9 | 2.8 | 3 | 3.2 |
| $M^2$-factor | 1.47 | 1.28 | 2.47 | 2.49 |
| Strehl Ratio (%) | 46 | 66 | 50 | <20 |
| Brightness ($MWcm^{-2}srad^{-1}$) | 107 | 137 | 65 | 62 |

## 5.5 Guiding Strength

To analyse the effect of the lateral guiding strength on the device operational characteristics, devices with identical injection metal contact area to the Index-Guided (IG-) PBTLs discussed above, but with shallower rib height $h_{RIB} = 0.45\mu m$, were fabricated. This value of $h_{RIB}$ corresponds to a lateral effective refractive index step $\Delta n_{eff} = 0.00008$, Fig. 5.2, which is negligible. Hence such devices can be considered as Gain-Guided (GG-). The shallow rib height of such GG- devices, however, is still useful for reducing current spreading, [5-17].

The increased extent of current spreading and carrier diffusion in GG- devices compared to that occurring with the deeper etched rib of IG devices can be observed in Fig. 5.11. The theoretical current density and carrier density profiles for the individual IG- and GG- PBTL element are validated by experimental near-field intensity profiles measured at low injection current ($I << I_{th}$) with low-pass optical frequency filters to highlight the presence of the carriers at the device facet.

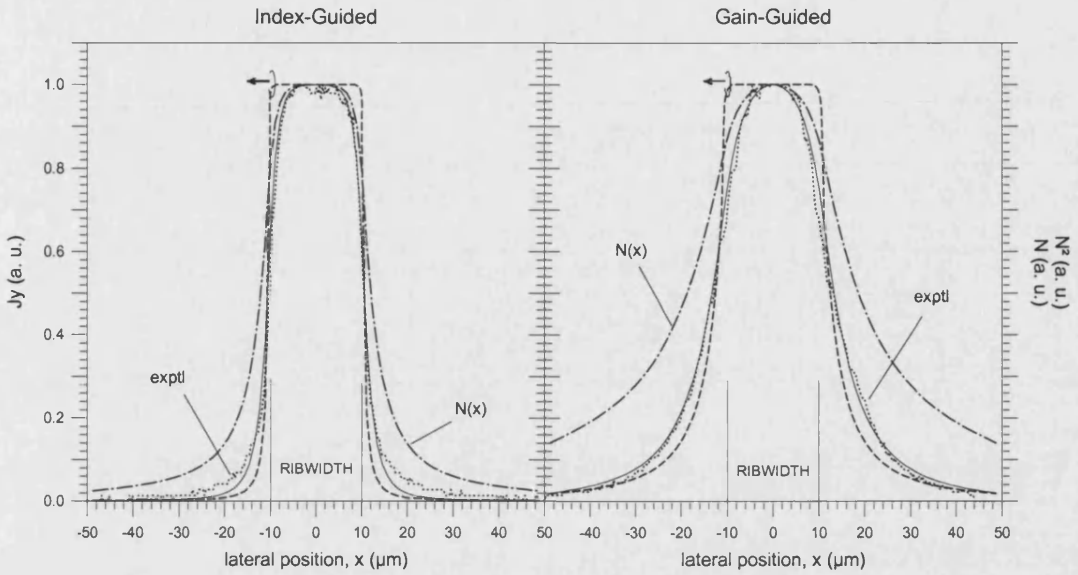


**Fig. 5.11: Experimental near-field intensity profiles (dotted line) measured at low injection current ($I<<I_{th}$) with low-pass optical frequency filters for IG- and corresponding GG-PBTLs. The theoretically estimated current density (dashed line), carrier density (dash-dot line) and carrier density squared (solid line) profiles are also shown for completeness.**

A representative comparison of the output power versus normalised current (with respect to the corresponding threshold values) for IG- and GG- PBTLs is presented in Fig. 5.12. Typical threshold currents for gain-guided PBTLs are $I_{th} = 70mA$, 30% higher compared to that of the index-guided PBTLs ($I_{th} = 50mA$), which is due to current spreading towards the edge of the device. From Fig. 5.11 it is in fact noticed that the current injection area is almost doubled in GG devices.

The series resistance for GG-PBTLs is measured to be $R_S$=0.23Ω, which is in agreement with the value for IG- devices ($R_S$=0.25Ω). The overall increase of the voltage across the diode can be attributable to the increased current spreading but also to a non-uniformity of the material wafer, [Appendix A].

However, the output optical power obtained from GG-PBTLAs per unit threshold current is almost comparable to that measured from IG-PBTLAs, which is justifiable since the active area and vertical mode characteristics are identical for the two devices. The maximum Wall-Plug efficiency (per pulse) of GG-PBTLs, 26%, is lower than that achieved with IG-PBTLs, 45%. The slope efficiency of GG- devices,

$\eta_e = 0.6AW^{-1}$. In addition the L-I curve measured from GG-PBTLs presents some pronounced kinks, attributable to filamentation. In fact, due to the absence of a defined lateral mode confinement GG- devices become sensitive to the effect of significant perturbations by injected carriers and lateral spatial hole burning, [5-18].

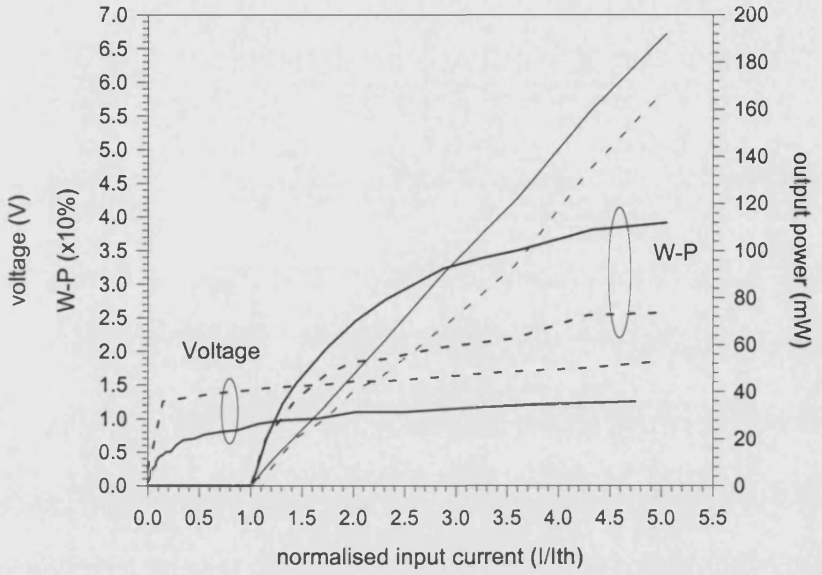


**Fig. 5.12: Pulsed optical output power versus normalised (to $I_{th}$) injected current measured from IG- (solid line) and GG-PBTLs. The corresponding voltage across the diode and the Wall-Plug efficiency curves are also shown.**

The effect of filamentation results in a dramatic degrade of the beam quality. In fact, as it can be observed in Fig. 5.13 a), the near-field intensity profiles measured from GG-PBTLs present visible irregularities.

The difference between the theoretical and the measured profiles is attributable to the fact that the effect of injected carriers on the optical field is even stronger than that theoretically calculated. The same characteristics can be observed in the corresponding far-field profiles (measured at the same currents), Fig. 5.13 b). At higher currents a multi-lobed far-field pattern is observed, with evidence of filamentation, [Chapter 2]. The asymmetry of the far-field profile can be attributed to imperfections at the device facet. Far- field profiles have been measured without the use of external optics, and with an angular resolution of 0.05deg.

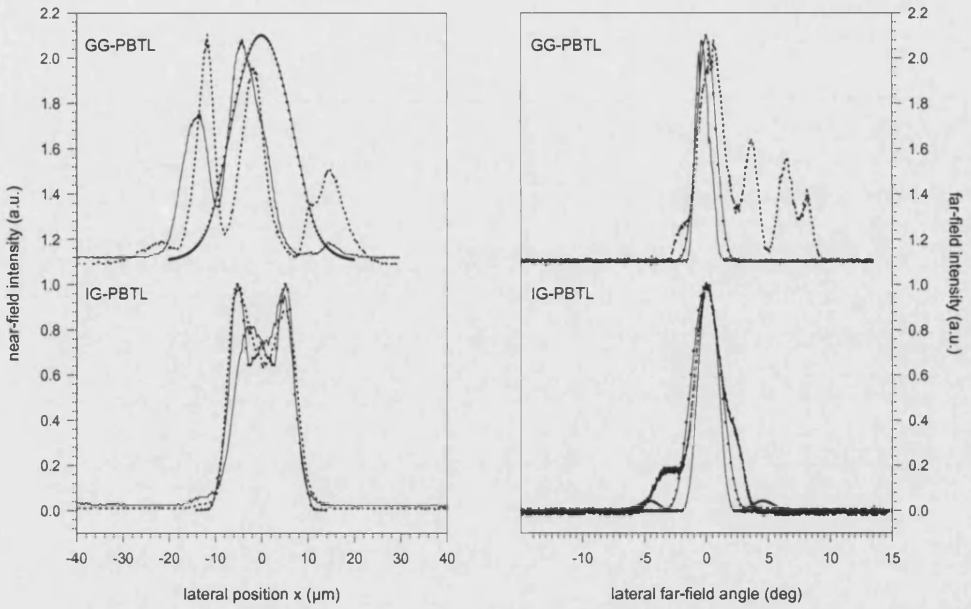


**Fig. 5.13: Representative a) near-field and b) far-field profiles from IG- and GG-PBTLs measured at injection currents $I=2I_{th}$ (solid line) and $I=5I_{th}$ (dotted line). Theoretical profiles computed with the HGCM (solid line with circles) are also shown for comparison.**

For a more detailed analysis, the near-field apparatus has been used to measure the Beam Waist (BW) of the GG-PBTL at the same injection currents as the near-field ones. By focusing the objective lens inside the resonator, the beam virtual origin has been imaged on the CCD camera. The measured profiles are presented in Fig. 5.14.

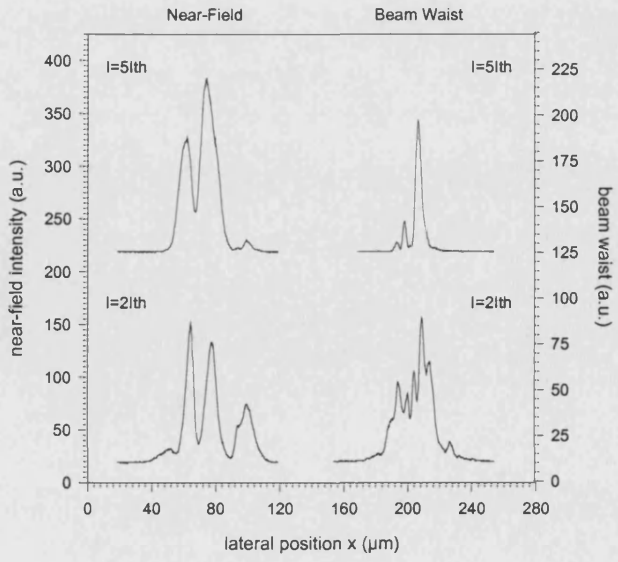


**Fig. 5.14: Near-field intensity profiles (solid line) and corresponding Beam Waists (dotted line) measured from GG-PBTLs at injection currents $I=2I_{th}$ and $I=5I_{th}$.**

Although the BW is visible over that range of currents investigated, its profile changes completely at higher injection, where filamentation becomes predominant.

A comparison of the main operational characteristics of IG- and GG- parabolic bow-tie lasers is presented in Tab. 5.6.

**Tab. 5.6: Operational characteristics measured from index-guided and gain-guided PBTLs at $I=5I_{th}$ under pulsed operation.**

| | Threshold Current (mA) | Slope efficiency (W/A) | Output Power (W/facet) | W-P (%) | $\theta_x$ FWHM (deg) |
|---|---|---|---|---|---|
| IG-PBTL | 50 | 0.7 | 0.16 | 45 | 2.8 |
| GG-PBTL | 70 | 0.6 | 0.19 | 26 | 5.2 |

## Summary

In this chapter the performance of Index-Guided Parabolic-Bow Tie Lasers (IG-PBTLs) has been described.

The systematic theoretical study necessary to optimise the device geometry has been discussed thoroughly. Details have been presented of the semiconductor material used to fabricate the tapered devices and that was specially designed to achieve high power operation.

Several Parabolic Bow-Tie lasers have been fabricated and thoroughly characterised in-house. Output powers up to 640mW facet, without COD, have been measured from PBTLs in diffraction-limited beam (2.8deg) without the use of external lenses. The corresponding maximum brightness is estimated to be ~137MW/cm$^2$-srad$^{-1}$, with beam quality $M^2$-factor=1.28 and Strehl Ratio 66%.

Near- and far-field profiles computed with the device models have been presented and shown to be in good agreement with data from the experimental characterisation of the spatial profile of the output beam.

Comparisons with measurement results from devices with different profiles (LBTLs, PBTLs, EBTLs and SLs) but same contact area confirm that the index-guided parabolic bow-tie laser constitutes a robust device design, essential to reduce mode competition and increase the brightness. Results show that although the output power levels are comparable, the output beam of Parabolic Bow-Tie Lasers seems to

be more stable and less affected by mode competition, compared to those of the other three types of devices, over the wide range of currents in which the devices have been tested.

Comparisons have been made also with Gain-Guided PBTLs. From the electrical/optical point of view the distinction between IG- and GG-PBTLs can be considered as marginal in terms of output optical power. However, the loss of lateral optical guiding is deleterious for the operation of GG-PBTLs.

# References


[5-1] D. Marcuse, *'Radiation loss of tapered dielectric slab waveguides'*, Bell Systems Technical Journal, 1970, vol. 49, pp. 273-290

[5-2] D. Marcuse, *Light Transmission Optics* (2nd Ed.), Van Nostrand Reinhold, New York, 1982

[5-3] A. F. Milton, W. K. Burns, *'Mode coupling in optical waveguide horns'*, IEEE J. Quantum Electronics, 1997, vol. Q5-173, n. 10, pp. 828-835

[5-4] T. Rozzi, M. Mongiardo, *Open Dielectric Waveguides*, IEE Electromagnetic Series, 1997

[5-5] I. Middlemast, J. Sarma, P. S. Spencer, *'Characteristics of Tapered Rib-Waveguides for High-Power Semiconductor Optical Sources'*, IEE Proc. Optoelectron., vol. 144, n. 1, 1997, pp. 8-13

[5-6] F. Causa, *'Hermite-Gauss Functions in the Analysis of a Category of Semiconductor Optical Devices'*, PhD Thesis, University of Bath, 1998.

[5-7] F. Causa, J. Sarma, *'A Quasi-Analytic Model for Longitudinally Non-Uniform Semiconductor optical Sources'*, Optics Communications, vol. 183, 2000, pp. 149-157

[5-8] F. Causa, J. Sarma, *'A Versatile method for Analysing Paraxial Optical Propagation in Dielectric Structures'*, Journal of Lightwave Technology, vol. 18, n. 10, 2000, pp. 1445-1452

[5-9] D. Masanotti, F. Causa, J. Sarma, *'High brightness, index-guided parabolic bow-tie laser diodes'*, IEE Proceedings – Optoelectronics, vol. 151, n. 2, 2004, pp.123-128

[5-10] H. Kogelnik, *'Theory of Optical Waveguides'*, in *Guided Wave-Optoelectronics*, ed. by T. Tamir, New York, Springer-Verlag (1990).

[5-11] M. Buda, T.G. van de Roer, L. M. F. Kaufmann, G. Iordache, D. Cengher, D. Diaconescu, I. B. Petrescu-Prahova, J. E. M. Haverkort, W. van der Vleuten, J. H. Wolter, *'Analysis of 6-nm AlGaAs SQW low-confinement laser structures for very high-power operation'*, IEEE J. Selected Topics Quantum Electronics, 1997, vol. 3, n.2, pp. 173-179

[5-12] D. Masanotti, F. Causa, J. Sarma, *'Design optimisation of high power high brightness parabolic bow-lie laser diodes'*, IEE Proceedings - Circuits, Devices and Systems, vol. 150, n. 6, 2003, pp. 537-541

[5-13] M. Krakowski S. C. Auzanneau, F. Berlie, M. Calligaro, Y. Robert, O. Parillaud, M. Lecomte, *'1W high brightness index guided tapered laser at 980nm using Al-free active region materials'*, Electronics Letters, vol. 39, n. 15, 2003, p. 1122

[5-14] W. D. Herzog, B. B. Goldberg, M. S. Ünlü, *'Beam steering in narrow-stripe high-power 980-nm laser diodes'*, IEEE Photon. Technol. Lett., vol. 12, n. 12, 2000, pp. 1604-1606

[5-15] E. S. Kintzer, J. N. Walpole, S. R. Chinn, C. A. Wang, L. J. Missaggia, *'High-Power Strained-Layer Amplifiers and Lasers with Tapered Gain Regions'*, IEEE Photon. Technol. Lett., vol. 5, n. 6, 1993, pp. 605-1408

[5-16] S. O'Brien, D. F. Welch, R. Parke, D. Mehuys, K. Dzurko, R. Lang, R. Waarts, D. Scifres *'Operating Characteristics of a High-Power Monolitically Integrated Flared Amplifier Master Oscillator Power Amplifier'*, IEEE Photon. Technol. Lett., vol. 29, n. 6, 1993, pp. 2052-2057

[5-17] D. Masanotti, F. Causa, *'Optical guiding properties of high brightness Parabolic Bow-Tie Laser Arrays'*, IEEE J. Quantum Electron., vol. 41, n. 7, July 2005, pp. 909-916

[5-18] D. C. Hall, M R. Surette, L .Goldberg, D. Mehuys, *'Carrier-Induced Lensing in Broad-Area and Tapered Semiconductor Amplifiers'*, IEEE Photon. Technol. Lett., vol. 6, n. 2, 1994, pp. 186-188

# Chapter 6

# *Phase-Locked Parabolic Bow-Tie Laser Arrays*

The performance of five-element index-guided Parabolic Bow-Tie Laser Arrays, development of the 'optimised' Index Guided Parabolic Bow-Tie Laser (IG-PBTL), presented in Chapter 5, is described in this chapter to show that with a careful design of the device geometry it is possible to achieve in-phase-locked operation in arrays of optically coupled positive-index lasers that do not require sophisticated fabrication hence high costs.

The operational characteristics of the laser array are compared with those from several in-house fabricated arrays differing for the number of emitters (3 and 4 elements) and profile (Linear Bow-Tie Lasers and Stripe Laser).

Theoretical calculations from models based on the Coupled-Mode Theory and on the HGCM are used to interpret the experimental results and predict the feasibility of scaling the number of array elements to achieve higher output powers and brightness.

Theoretical calculations are also presented to show the effect of the gain profile on the mode discrimination. Experimental results from arrays of 10 and 20 elements are also discussed to show that scalability to such a large number of emitters is in principle possible although spatial hole-burning can significantly influence the mode discrimination and the device beam quality.

## 6.1 Five-Element Optically Coupled Parabolic Bow-Tie Laser Arrays

The schematic of the array structure that was shown to be suitable for achieving phase-locked operation and therefore high brightness is presented in Fig. 6.1, [6-1], [6-2]. Such array is comprised of five 'optimised' IG-PBTLs, described in Chapter 5, separated from each other at a centreline spacing (inter-element spacing) S=W=20μm . For simplicity such five-element array will be referred to as 5PBTLA0 since the device facets are contiguous.

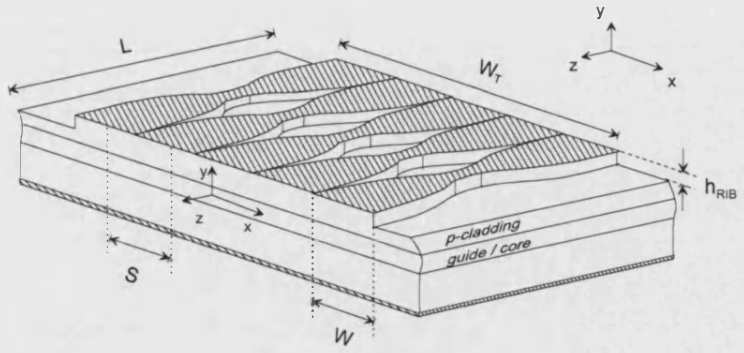


**Fig. 6.1: Schematic of the 5PBTLA0 geometry with definition of the relevant parameters.**

All device parameters are summarised in Table 6.1.

**Tab. 6.1: Relevant parameters for the parabolic bow-tie laser arrays of Fig. 6.1.**

| Parameter | Value | Parameter | Value |
|---|---|---|---|
| Individual emitter output facet | W=20μm | Array output facet width | $W_T$=100μm |
| Array total length | L=1050μm | Rib height | $h_{RIB}$=0.9μm |
| Inter-element spacing | S=20μm | Lateral effective index step | $\Delta n_{eff}$=0.007 |

All the devices have been fabricated in-house from the same material used for the individual emitters, and that was specially designed for high-power operation, as described in Chapter 5. Similarly to the individual PBTLs, the arrays were cleaved and mounted junction side down on a standard copper mounts. Uniform pumping of the laser medium was achieved by current injection on gold wire bonded contacts.

As mentioned in Chapter 5, the heat sinking properties of the mount are not optimal and the devices have not been properly packaged. Therefore the devices have been typically tested under pulsed operation (5μs pulse width, duty cycle of 0.1%) and using a Temperature Controller to stabilise the heatsink temperature (typically T=20°C).

Representative light (output) power and voltage characteristics as a function of the injection current (L-V-I curves) measured for 5PBTLA0s, and the corresponding W-P efficiency characteristic curve, are shown in Fig. 6.2.

Threshold currents $I_{th}$= 160mA are typically measured, corresponding to a threshold current density of 0.2kAcm$^{-2}$, with slope efficiency $\eta_e$=0.8W/A. Optical

output powers up to 2.8W/facet have been measured (I=3.6A=22.5$I_{th}$) without COD. Neither saturation nor thermal roll-over have been observed in the range of currents investigated (restricted because of the limitations in the thermal management of the experimental set-up, not to damage the devices).

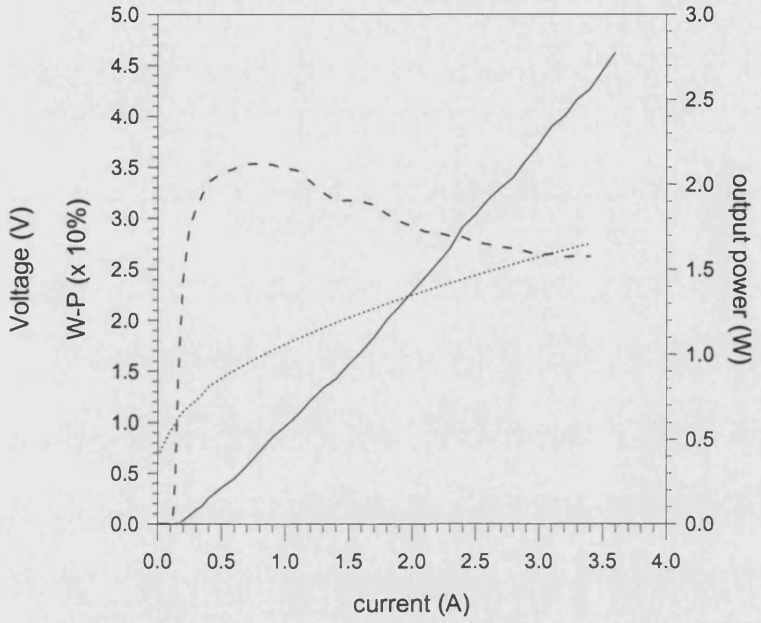


**Fig. 6.2: Experimental output power (solid line) versus injected current characteristic curve measured from in-house fabricated 5PBTLA0s. The voltage measured across the device (dotted line) and the W-P (dashed line) curves are also shown. [5μs pulse width, 0.1% duty cycle; Temperature T=20°C; neutral density filters used to avoid photodiode saturation].**

The devices series resistance has been estimated to be $R_S$=0.44Ω, higher than that measured for the individual PBTLAs ($R_S$=0.25Ω), as expected because of the increased size of the contact, [Appendix A]. As a result, the maximum Wall-Plug efficiency W-P=35% (per pulse), achieved at an output power of 0.5W/facet, is lower than that obtained for the array individual element (45%). However, the array W-P remains above 25% also for the highest output powers.

Representative near- and corresponding far-field intensity profiles measured from 5PBTLA0s for different values of the injection current are presented in Fig. 6.3.

The evolution of the (pulsed) lateral far-field intensity profile with increasing the injection current can be seen in Fig. 6.3 b). Such patterns have been measured without the use of external lenses. The angular resolution of the far-field intensity measurements is 0.05deg, [Appendix E].

At threshold the Parabolic Bow-Tie Arrays operate in the out-of-phase mode ($\pi$-phase-shift between adjacent emitters), showing the two lobes typical of this array mode. However, at higher currents the output beam becomes single-lobed and remains so over the wide range of currents investigated, indicating that the devices switch to in-phase operation (no-phase-shift between adjacent emitters), as explained in detail in the following sections.

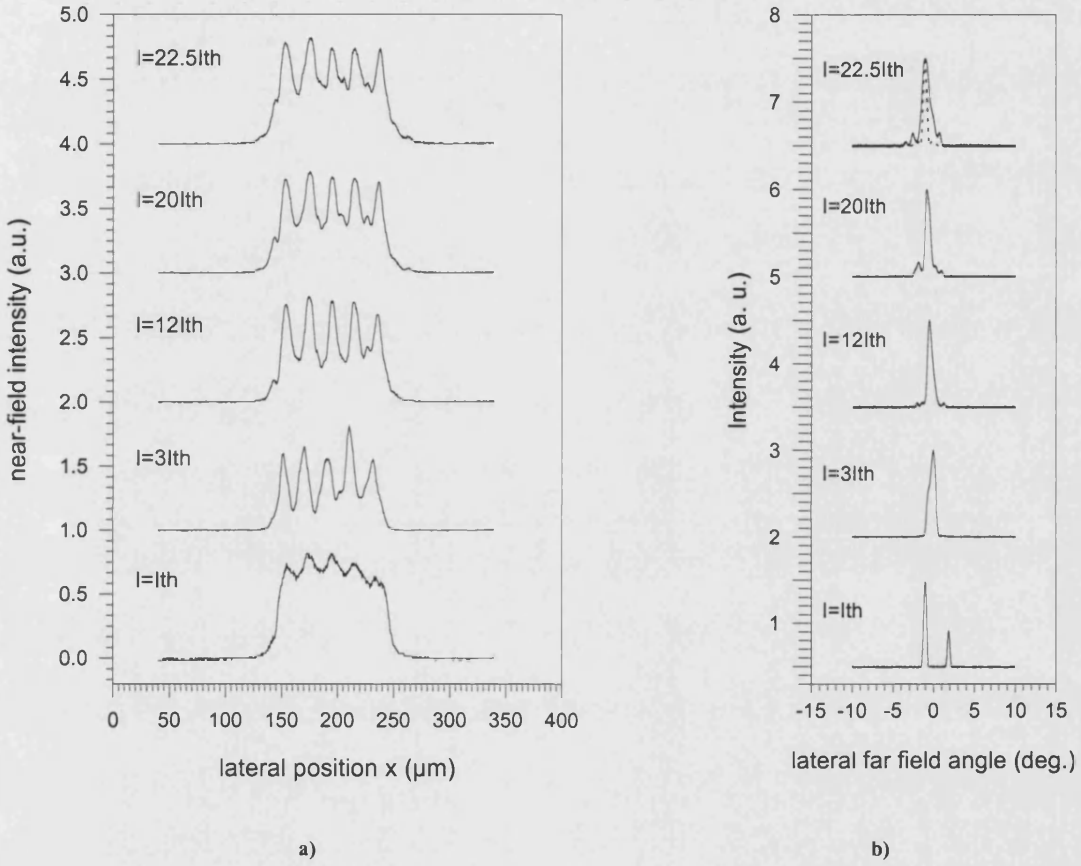


**Fig. 6.3: Pulsed a) near-field and b) far-field intensity profiles measured from 5PBTLA0s at different currents.**

Values of the far-field lateral divergence at FWHM ($\theta_x$), Strehl Ratio (SR) and brightness (B) measured from 5PBTLA0s at different injected current are plotted in Fig. 6.4.

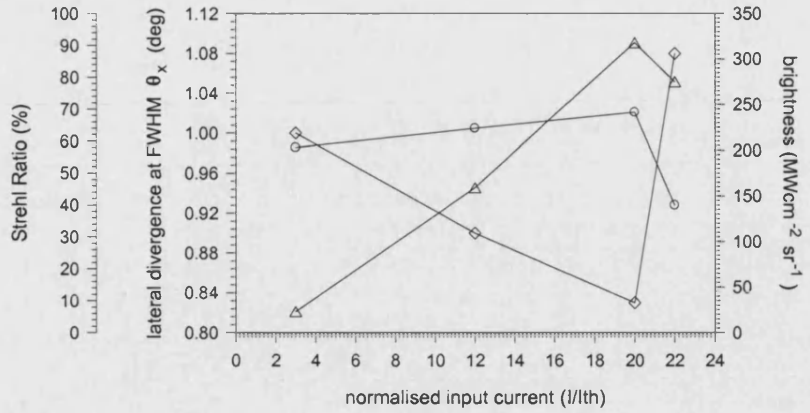


**Fig. 6.4: Measured far-field lateral divergence at FWHM (solid line with squares), Strehl Ratio (solid line with circles) and brightness (solid line with triangles) as a function of the normalised (to $I_{th}$) injected current for 5PBTLA0s.**

It can be observed that the far-field divergence for the 5PBTLA0s, for all the currents over the range of interest, is measured to be less than $0.83\,\text{deg}$, with the minimum value for the lateral divergence measured at $I=20I_{th}$. It can be also noticed that the beam divergence remains less than twice the estimated diffraction-limit angle $\theta_d = \arcsin\left(\frac{\lambda}{D}\right) = 0.56\,\text{deg}$, equation (2.16), from a corresponding D=100μm wide uniformly illuminated aperture. This confirms that at higher currents a certain degree of spatial coherence is reached, [Chapter 2]. A further important observation that supports the above statement is that the measured far-field is always considerably narrower than that measured for individual PBTLs, Chapter 5, and for which and $\theta_d = 2.8\,\text{deg}$.

The Strehl Ratio (SR) was measured experimentally by measuring the power through slits placed at the far-field plane and with aperture corresponding to the diffraction-limit divergence angle. As expected, considering the trend of $\theta_x$, the maximum value SR= 69% is obtained at at $I=20I_{th}$. SR decreases to a value of 40% for $I=22.5I_{th}$. The maximum value of brightness, $318\text{MWcm}^{-2}\text{sr}^{-1}$, is measured at $I=20I_{th}$. At the highest current the brightness for 5PBTLA0s is $275\text{Wcm}^{-2}\text{sr}^{-1}$.

Due to the accuracy of the scale of the present measurements apparatus, [Appendix E], it was not possible to establish the presence or quantify the amount of beam steering. Importantly, no astigmatism was observed in the range of currents of interest.

The characteristic operational parameters of 5PBTLA0s, including threshold current ($I_{th}$), output power (P), maximum Wall-Plug (W-P) efficiency, far-field divergence at FWHM ($\theta_x$), Strehl Ratio (SR) and corresponding Brightness (B), measured from 5PBTLA0s at different currents are summarised in Tab. 6.2.

**Tab. 6.2: Pulsed operational characteristics measured from 5PBTLA0s at different currents.**

| $I_{th}$=160mA | Max W-P (%) | P (W/facet) | $\theta_x$ FWHM (deg.) | B ($MWcm^{-2}srad^{-1}$) | SR (%) |
|---|---|---|---|---|---|
| $I=3I_{th}$ | 35 | 0.32 | 1 | 23 | 58 |
| $I=12I_{th}$ | 15 | 1.35 | 0.9 | 159 | 64 |
| $I=20I_{th}$ | 22 | 2.5 | 0.83 | 318 | 69 |
| $I=22.5I_{th}$ | 27 | 2.8 | 1.08 | 275 | 40 |

### 6.1.1 Results Interpretation

To interpret the experimental results the theoretical far-field intensity profiles of the modes supported by the 5PBTLA0s have been computed using the model based on the Coupled-Mode Theory (CMT), [Chapter 4]. The far-field profiles calculated for the five modes supported by the array are presented in Fig. 6.5 a). The far-field patterns of the in-phase ($\nu = 1$) and out-of-phase ($\nu = 5$) modes, are compared with the profiles measured above threshold and at threshold, respectively. The two main lobes of the out-of-phase far-field pattern are placed at a distance $\Delta\theta = 2.8\,\text{deg}$ from each other as predicted from the theory, [Chapter 4].

Importantly, from the presented results it is possible to deduce that the far-field broadening occurring at higher injection currents is due to the contribution of not only the fundamental but also the higher order array modes.

The grating functions for the 5PBTLA0, characterized by S=20μm, λ=0.98μm and a peak distance $\Delta\theta = 2.8\,\text{deg}$, are very similar to those computed for the array of 5 single-mode 3μm wide straight stripes, with λ=0.83μm, S=20μm and $\Delta\theta = 2.3\,\text{deg}$, plotted in Fig. 4.4. The main difference, however, is that the far-field associated to the individual PBTL ($\theta_x$=2.8deg) is narrower that that associated to the 3μm wide stripe ($\theta_x$=19deg). Thus, in the case of 5PBTLA0s, only one peak lobe of the grating function is intercepted when ν=1 and two lobes are intercepted for ν=5.

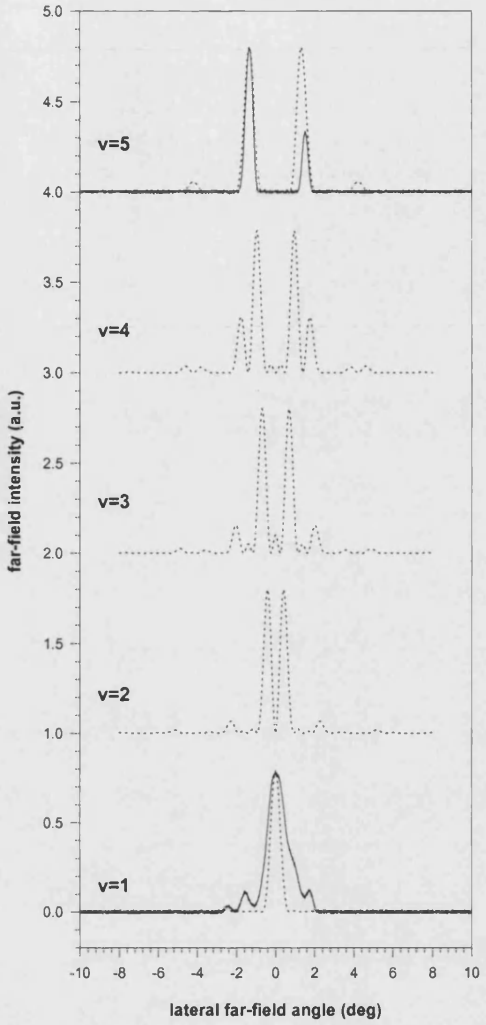


**Fig. 6.5: Computed far-field intensity profiles (dotted lines) for the 5 array modes of a 5PBTLA0; the measured profiles at $I=I_{th}$ and $I=22I_{th}$ are shown for comparison (solid line).**

For the sake of completeness, the results obtained with the models based on CMT are also compared, Fig. 6.6, with those obtained using the SDT model, [Chapter 4]. As explained in Chapter 4, comparison between the two models can be made only for the in-phase and the out-of-phase array modes. Phase-shifts of $\Delta\phi = 0$ and $\Delta\phi = \pi$, for $\nu = 1$ and $\nu = 5$ respectively, have therefore been introduced in equation (4.13) when computing the results with the SDT model.

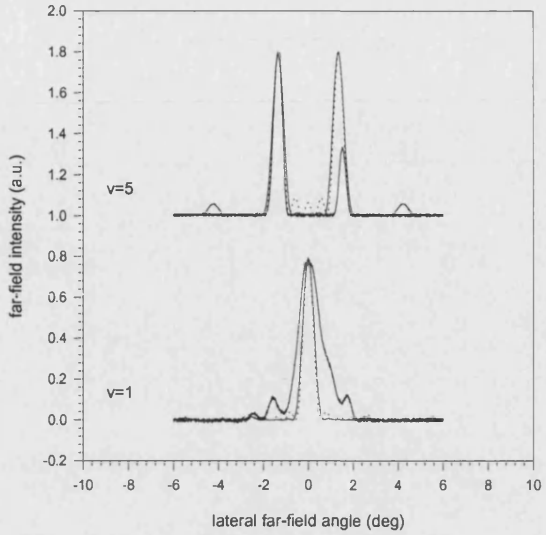


**Fig. 6.6: CMT (solid line) and SDT (dotted line) analysis for 5PBTLA0s. The experimental far-field profiles are also shown (thicker solid line).**

### 6.1.2 Modal Gain and Mode Discrimination

It is very important, at this stage, to understand the reasons behind the change in mode operation observed in 5PBTLA0s.

As seen in Chapter 4, in most index-guided arrays out-of-phase mode operation is favoured because of the better overlap of that mode with the gain distribution in the device (higher gain under the contact ridges, where also the refractive index is high and lower gain between adjacent elements, where the refractive index is lower). However it was seen that there might be some situations where, due a different gain profile, the in-phase mode can be favoured.

In the present case the change in mode operation at higher injection currents can be attributed to the effect of carriers on the refractive index and to spatial hole-burning. Near the output facets, where the elements merge in a single contact, inter-element coupling is stronger. In those regions, above threshold, on the longitudinal axis of the individual elements the refractive index is larger, but the gain is lower than that of the surrounding off-axis regions, because of spatial-hole burning. This situation (higher gain where the refractive index is lower) is conducive to quasi-in-phase operation for arrays of a small number of elements, [Chapter 4], [6-1], [6-2].

The above discussion about the array mode discrimination can be made more quantitative by referring to Fig. 6.7, which shows the computed relative modal gain,

for the five array modes supported by the structure, for the two different gain distributions (also shown on the right hand side of the picture) mentioned above. The case in which spatial hole-burning is stronger in the centre of the device facet than at the edges is also considered. The modal gains have been calculated by evaluating the overlap integral between each array mode intensity distribution and the considered lateral gain profile, [6-1]. As expected, when the gain in the region of high refractive is higher than that of the surrounding lower index regions, the modal gain of the out-of-phase ( $\nu = 5$ ) mode is the highest, Fig. 6.7 a). This is the case for 5PBTLA0s operating at threshold. However, at higher currents, when hole-burning occurs, the gain in the regions under the ridges is lower than that in the regions between adjacent elements and the modal gain of the fundamental ( $\nu = 1$ ) array mode is higher than that of the highest ( $\nu = 5$ ) order mode, Fig. 6.7 b). In the last case considered, stronger hole-burning occurs for the central elements, Fig. 6.7 c). Under these conditions, the $\nu = 2$ and the $\nu = 4$ array modes, characterised by a higher modal gain than the fundamental, in-phase ( $\nu = 1$ ) mode, are also excited. This explains the broadening of the far-field observed for the array at higher currents, Fig. 6.5.

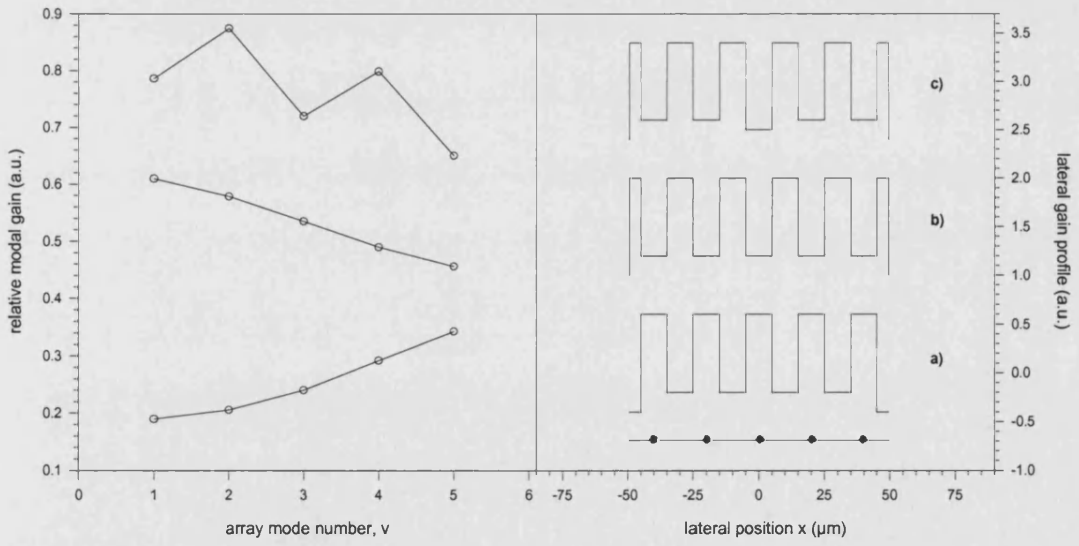


**Fig. 6.7: Modal gain as a function of the mode number computed for the 5PBTLA0 for different gain profiles: (a) high gain in high refractive index region; (b) high gain in low refractive index region; (c) high gain in low refractive index region in the presence of hole-burning at the centre of the device facet. The solid circles show the position of the elements, corresponding to the regions where the refractive index is higher.**

Importantly, the array mode selection observed in 5PBTLA0s is associated to not only the specific tapered geometry design of the laser optical cavity but also to the mode filtering effect of the device narrow central sections. In fact, as also shown later in the chapter, quasi in-phase locking is observed in other arrays of tapered bow-tie lasers but not in arrays of straight stripe lasers.

Near- and far-field profiles measured at $I=5I_{th}$ have been compared with theoretical calculations from the HGCM model, [Appendix B], where the array total optical field has been solved self-consistently with the optical gain in the device, Fig. 6.8. The modal parameters are those used for PBTLs, Tab. 5.3. The theoretical near-field relative phase profile is also plotted: no corresponding experimental profile is available, since the phase is not detected by the present near-field measurement apparatus. It is important to observe that the near-field relative phase, Fig. 6.8 c), is almost constant across the device facet, which indicates the high degree of coherence between the array emitters.

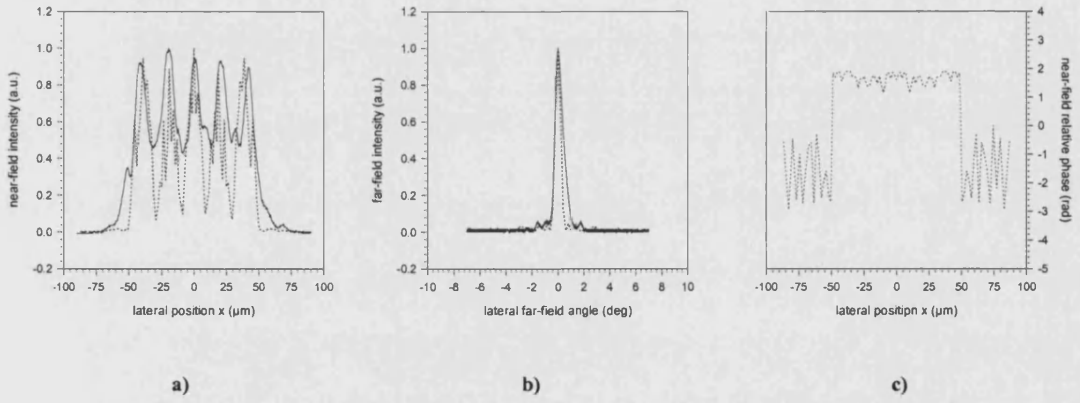


**Fig. 6.8: Comparison between measured (solid line) and HGCM computed (dotted line) profiles for the a) near-field and b) far-field distribution of 5PBTLA0s. The near-field relative phase profile, c), is also plotted. [$I=5I_{th}$].**

## 6.2 Arrays of a Small Number of Elements: Brightness

As introduced at the beginning of this chapter, the 5PBTLA0 design is the outcome of a detailed study carried out on arrays with different number of emitters and different profiles. Details of this study are given in this section.

The effect of the number of elements in the array on the output power scaling, was first studied considering arrays of 3 to 5 emitters, all characterised by inter-element spacing S=20μm (i.e., no spacing at the taper ends) and therefore (in

principle) optically coupled. Arrays of parabolic tapers, linear tapers, and straight stripe lasers, with individual emitters of the same size and the guiding properties as the optimised PBTL, [Chapter 5], were considered. All devices are of the same length, L=1050μm; the corresponding output facet widths, Fig. 6.1, are as follows: 3-element arrays: $W_T$=60μm; 4-element arrays: $W_T$=80μm; 5-element arrays: $W_T$=100μm. To be noticed that the arrays of stripe lasers correspond to broad area lasers and that their contact area is almost double that of taper arrays.

It is convenient at this stage to follow the notation used for 5PBTLA0s and label the arrays depending on the number of elements, on the profile and on the facet spacing to distinguish the different types of arrays. Following such notation, for example, arrays of 3 LBTLs with S=20μm will be referred to as 3LBTLA0s, whereas arrays of 3 PBTLs and 3 SLs with S=20μm will be referred to as 3PBTLA0s and 3SLA0s, respectively. Similarly for the arrays of 4 and 5 elements.

To show the output power scaling with increasing number of elements, the light output versus injected current density (L-J curve) characteristics for such arrays are presented in Fig. 6.9. Representative Wall-Plug efficiency curves for arrays of 3/4/5 elements are also presented, [6-2]. Importantly, it can be observed that the output power is significantly higher for arrays with a larger number of elements (N), but varies little with the geometry of the device for arrays with the same number of elements N.

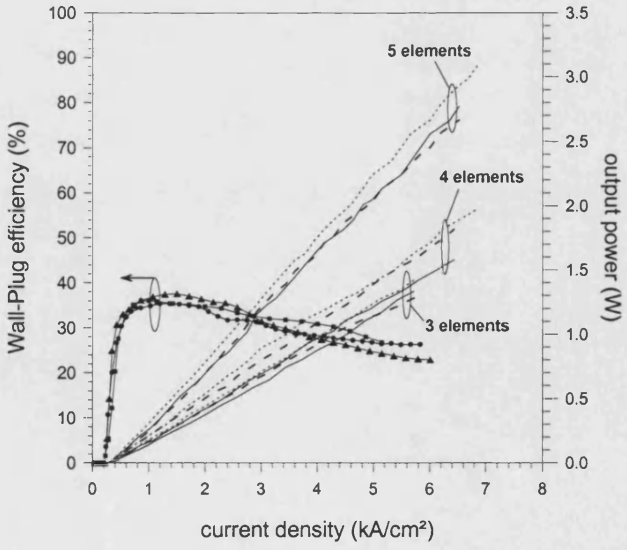


**Fig. 6.9: Optical output power and Wall-Plug efficiency versus pulsed (5μs, 200Hz) injection current density curves measured from arrays of 3 (▲), 4 (■) and 5 (●) elements of different geometries: SLs (dotted line); LBTLs (dashed line) and PBTLs (continuous line).**

The attention is now focused on arrays of N=5 elements, that achieve the highest power. For all the 5-element arrays the threshold current was measured to be typically $I_{th} = 160\,mA$ (corresponding to a threshold current density $J_{th} = 0.22\,kAcm^{-2}$); only for stripe laser arrays, because of the larger active area, the threshold current is higher ($I_{th}$=200mA) corresponding to a threshold current density $J_{th} = 0.19\,kAcm^{-2}$. The larger active area results also in a higher output power. The slope efficiency is $\eta_e = 0.8W/A$ for all the 5-element arrays. The maximum Wall-Plug efficiency, measured from 5PBTLA0s, is 35% at $I = 0.75A$ and optical output power of $0.5\,W/facet$, Fig. 6.10.

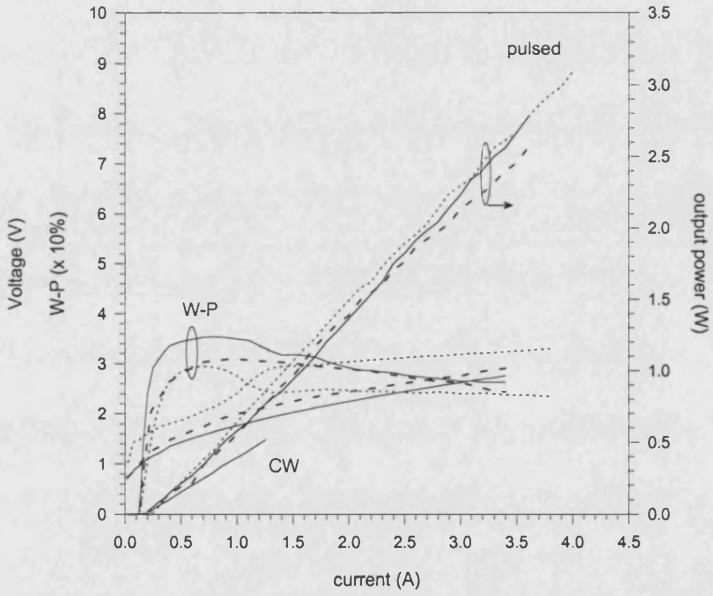


**Fig. 6.10: Pulsed (5μs, pulse width, 0.1% duty cycle) L-V-I curves and Wall-Plug efficiency measured from in-house fabricated 5SLA0s (dotted line), 5LBTLA0s (dashed line) and 5PBTLA0s (solid line). [Neutral density filters used to take readings at high power levels].**

The effect of the taper geometry on the array beam quality was investigated by comparing the far-field profiles measured from the three different types of arrays at different (pulsed) currents, Fig. 6.11. Although the output powers from all such devices are comparable, Fig.6.10, it can be noticed that the quality of the output beam varies enormously depending on the laser cavity geometry, [6-2]. The 5LBTLA0s present similar features to 5PBTLA0s, with out-of-phase operation just

around threshold and a single-lobed beam at higher currents, indicating quasi-in-phase mode operation.

By contrast, 5SLA0s are characterised by typical double-lobed far-field patterns over the wide range of currents of interest, indicating that they are always locked out-of-phase. The important, additional aspect to be considered here, and that was already mentioned in the previous Section, is that the change in mode operation in both 5PBTLA0s and 5LBTLA0s, attributable to the effect of carriers on the refractive index and to the gain distribution, is associated to the mode filtering effect of the central narrow sections, Fig. 6.1, as demonstrated by the fact that in-phase locking is not observed in 5SLA0s. Importantly, it can be observed that the narrowest lateral far-field divergence was been measured from 5PBTLA0s.

It must be mentioned that for 5LBTLA0s and 5SLA0s, similarly to 5PBTLA0s, neither astigmatism nor beam steering was observed.

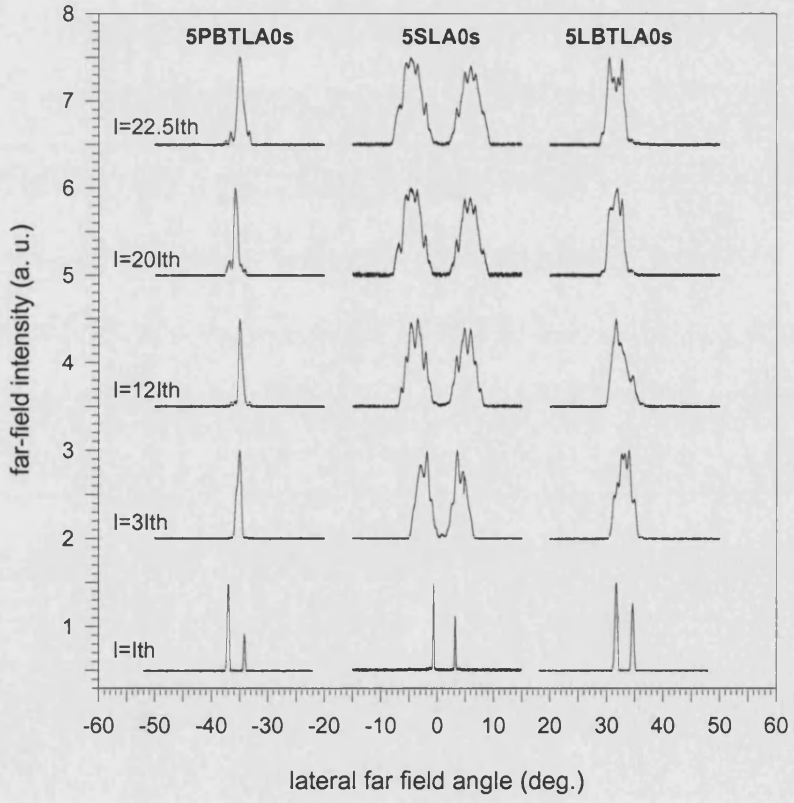


**Fig. 6.11: Pulsed (5μs, 200Hz) lateral far-field intensity profiles measured for different values of the injection current in the range from $I=I_{th}$ to $I=22.5I_{th}$ from in-house fabricated 5SLA0s, 5LBTLA0s and 5PBTLA0s without using external optics. [Angle resolution 0.05deg].**

The results presented in Fig. 6.11, indicate that, although all three categories of devices produce high power, Fig. 6.10, the corresponding brightness strongly depends on the geometry of the cavity. Values of the brightness measured for 5LBTLA0s, 5PBTLA0s and 5SLA0s, at various injected currents are plotted in Fig. 6.12. It can be observed that the brightness of 5LBTLA0s and 5PBTLA0s is typically higher than that of SLA0s, with the maximum value of $318 MWcm^{-2}sr^{-1}$ measured from 5PBTLA0s at $I=20I_{th}$. At the highest current the brightness for 5PBTLA0s is $275 Wcm^{-2}sr^{-1}$.

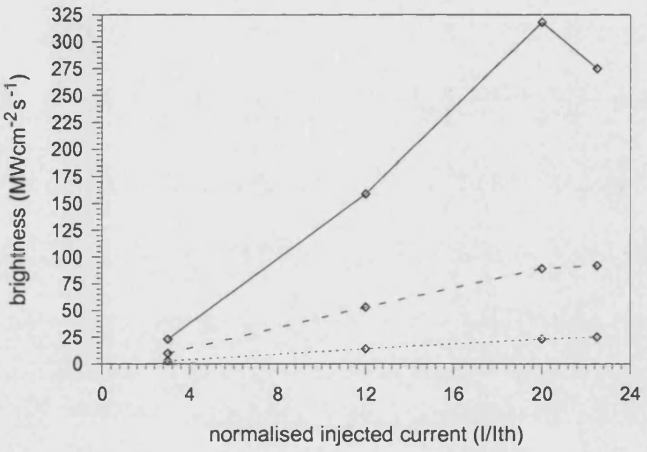


**Fig. 6.12: Values of the brightness measured for 5LBTLA0s (dashed line), 5PBTLA0s (solid line) and 5SLA0 (dotted line) as a function of the normalised (to $I_{th}$) injected current.**

The measured far-field intensity profiles at the lowest (threshold) and highest ($I=22.5I_{th}$) currents and the profiles computed using the CMT model are presented in Fig. 6.13.

As shown in Fig. 6.13, at threshold all the experimental profiles are well represented by the highest order ($\nu=N$) array mode. At higher currents only the far-field profiles from array of tapered lasers can be well described by the lowest ($\nu=1$) array mode indicating quasi-in-phase mode operation; the profile of the arrays of stripe lasers is still well represented by the out-of-phase array mode.

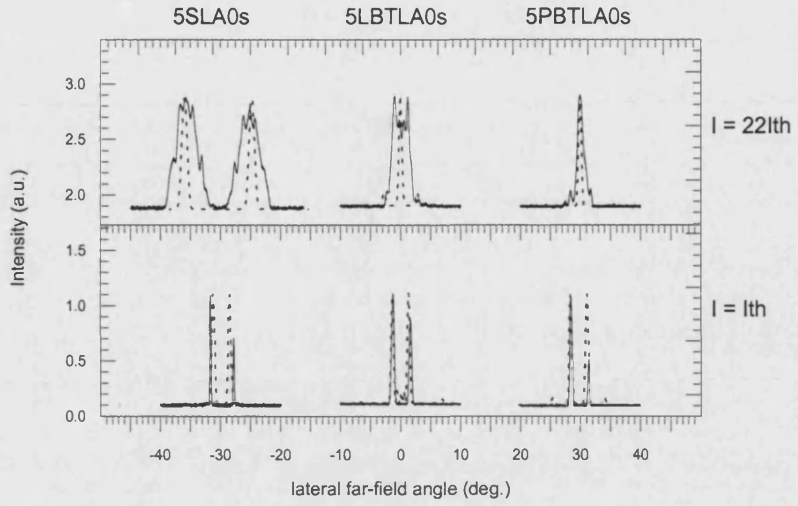


**Fig. 6.13: Far-field intensity profiles measured (solid lines) without the use of lenses from index-guided 5SLA0s, 5LBTLA0s and 5PBTLA0s at $I=I_{th}$, and $I=22.5I_{th}$ pulsed. The theoretical profiles calculated with CMT (dotted lines) are also shown. [Angle resolution 0.05deg.].**

The main characteristic parameters including threshold current ($I_{th}$), output power (P), maximum (per pulse) Wall-Plug efficiency (W-P), far-field lateral divergence at FWHM ($\theta_x$), Strehl Ratio (SR) and corresponding estimated brightness (B) measured from such devices at low ($I = 3I_{th}$) and high ($I = 22.5I_{th}$) currents are summarised for comparison in Tab. 6.3, [6-1].

**Tab. 6.3: Comparison of the operational characteristics measured from in-house fabricated 5SLA0s, 5LBTLA0s and 5PBTLA0s at $I = 3I_{th}$ and at $I = 22.5I_{th}$, pulsed (5μs, 200Hz).**

| | $I_{th}$ (mA) | Max W-P (%) | P (W/facet) | | $\theta_x$ FWHM (deg.) | | Brightness ($MWcm^{-2}srad^{-1}$) | | SR (%) | |
|---|---|---|---|---|---|---|---|---|---|---|
| | | | $I=3I_{th}$ | $I=22.5I_{th}$ | $I=3I_{th}$ | $I=22.5I_{th}$ | $I=3I_{th}$ | $I=22.5I_{th}$ | $I=3I_{th}$ | $I=22.5I_{th}$ |
| **5SLA0** | 200 | 29 | 0.17 | 3.1 | 9.1 | 13.8 | 5.0 | 25 | 0 | 0 |
| **5LBTLA0** | 160 | 31 | 0.23 | 2.6 | 2.0 | 3.1 | 8.4 | 92 | 30 | 20 |
| **5PBTLA0** | 160 | 35 | 0.32 | 2.8 | 0.8 | 1.08 | 42.4 | 275 | 65 | 40 |

To complete the characterization of the 5-element arrays with S=20μm inter-element spacing the near-field intensity profiles measured from 5LBTLA0s, 5PBTLA0s and 5SLA0s at $I=5I_{th}$, are shown in Fig. 6.14, together with the corresponding theoretical profiles calculated with the HGCM model, [Appendix B]. The computed near-field relative phase profile is also shown. The main parameters used for modelling are those used previously for 5PBTLA0s.

Important informations can be obtained by comparing the near-field relative phase profiles for the three different types of devices. The stripe laser array shows a clear change in the near-field relative phase, with almost π-shift between the value in the centre and the value at the edges of the device. This can explain the dominance of out-of-phase mode observed experimentally, Fig. 6.11.

Both tapered arrays show a higher degree of coherence. However, it can be noticed that, differently from the parabolic array, no overall coherence but only partial coherence occurs in linear taper arrays. In fact, the relative phase in 5LBTLA0s is constant over regions smaller than the individual emitter facet width (W=20μm) but it is not constant across the whole device facet. This can explain the fact that a single-lobed radiated beam is measured, but its divergence at FWHM (3.1deg) is larger than the diffraction-limit for a D=100μm uniformly illuminated aperture.

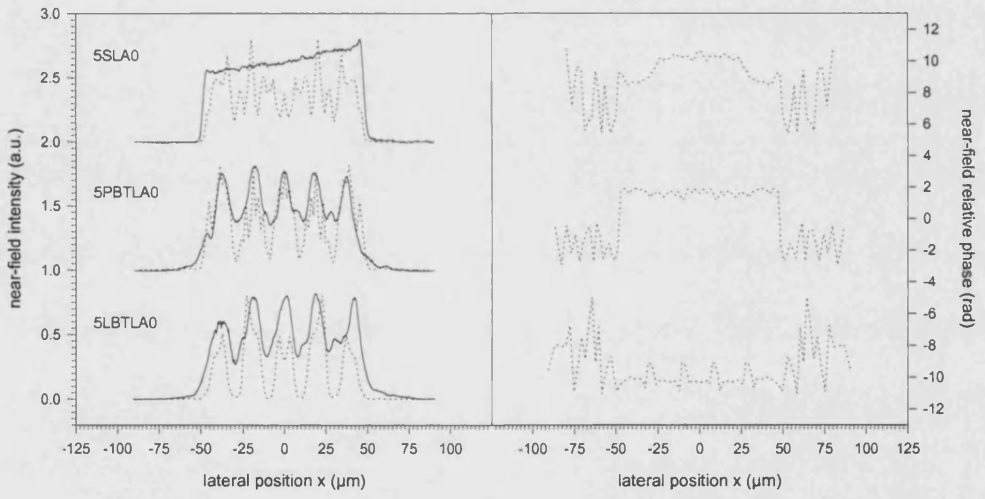


**Fig. 6.14: Comparison between measured (solid line) and HGCM computed (dotted line) near-field profiles for 5SLA0s, 5LBTLA0s and 5PBTLA0s. The corresponding computed near-field relative phase profile is also plotted on the right hand side. [$I=5I_{th}$].**

For the sake of completeness it is important to specify that similar trends to those observed for the 5-element arrays were observed also for arrays of three and four elements of all geometries. The diffraction-limit angles for the 3-element arrays (60μm wide emitting aperture) and for the 4-element arrays (80μm wide emitting aperture) are 0.93deg and 0.7deg respectively. All devices start lasing in the out-of-phase mode with only the tapered laser arrays switching to in-phase operation at

higher currents. However, the beam quality is typically lower compared to the 5-element arrays. Detailed measurements are not reported but a comparison of the main operational characteristics measured from all the different types of arrays at an injection current $I=20I_{th}$ is presented in Tab. 6.4.

**Tab. 6.4: Pulsed operational characteristics measured at $I=20I_{th}$ from of 3- 4- 5-element arrays and different profiles. Values for the individual emitters are also presented for completeness. $N_P$, $N_\theta$ and $N_B$ are the scaling factors for the emitted power, the beam divergence and the brightness, respectively.**

| | Ith (mA) | $\eta_e$ (W/A) | Output Power (W/facet) | $N_P$ | $\theta_x$ FWHM (deg.) | $N_\theta$ | B ($MWcm^{-2}srad^{-1}$) | $N_B$ |
|---|---|---|---|---|---|---|---|---|
| **SL** | 60 | 0.8 | 0.7 | 1 | 3.2 | 1 | 62 | 1 |
| **3SLA0** | 120 | 0.75 | 1.7 | 2.4 | 6 | 0.5 | 50 | 0.8 |
| **4SLA0** | 160 | 0.64 | 1.97 | 2.8 | 11 | 0.3 | 24 | 0.4 |
| **5SLA0** | 200 | 0.83 | 2.8 | 4 | 12.5 | 0.3 | 23 | 0.4 |
| **LBTL** | 55 | 0.62 | 0.56 | 1 | 2.9 | 1 | 107 | 1 |
| **3LBTLA0** | 100 | 0.7 | 1.28 | 2.2 | 2.3 | 1.2 | 95 | 0.9 |
| **4LBTLA0** | 140 | 0.63 | 1.8 | 3.2 | 2 | 1.65 | 119 | 1.1 |
| **5LBTLA0** | 160 | 0.78 | 2.1 | 3.7 | 2.8 | 1.03 | 89 | 0.8 |
| **PBTL** | 50 | 0.7 | 0.64 | 1 | 2.8 | 1 | 137 | 1 |
| **3PBTLA0** | 100 | 0.7 | 1.33 | 2 | 2.1 | 1.3 | 112 | 0.8 |
| **4PBTLA0** | 140 | 0.7 | 1.7 | 2.6 | 2.3 | 1.2 | 97 | 0.7 |
| **5PBTLA0** | 160 | 0.81 | 2.5 | 3.9 | 0.83 | 3.44 | 318 | 2.3 |

As seen in Chapter 3, ideally the total power emitted by an array of N elements is N times the power emitted from the individual element. If the array is coherently coupled and operates in the (fundamental) in-phase mode, the emitted beam is single-lobed and its lateral divergence at FWHM is N times smaller than the divergence of the individual emitter. As a consequence, since the total emitted area is N times the individual emitter area, the brightness of the array is N times the brightness of the individual emitters, [6-4]. The output power and the beam divergence from the array individual emitters are also presented in Tab. 6.4 to analyse the output scaling associated to the number of emitters and the effect of coherence on the beam quality.

Scaling factors, $N_P$ and $N_\theta$, [Chapter 3], estimated from the measured output power and beam divergence, respectively, are also reported, with the corresponding scaling factors, $N_B$, estimated for the brightness.

By comparing the data in Tab. 6.4, it can be observed that, as expected, the larger N, the larger $N_P$, although the two values never coincide, but for a fixed N, $N_P$

varies little with the geometry of the device. This was observed also in Fig. 6.9. On the other hand $N_\theta << N$ for all the devices, and, consequently, $N_B < N$. Noticeably $N_\theta < 1$ for the 3-element arrays indicating that the far-field pattern is broader than that of a single element.

However, a significant improvement in the far-field lateral beam width is observed only for 5PBTLA0s, with $N_\theta = 3.4$. This, also, was observed in Fig. 6.11, and confirms that 5PBTLA0s, with $N_B = 2.3$, are the best suited devices for high power with high brightness operation.

## 6.3 Device Scalability: Large Number of Elements

With the intention to verify if in-phase-locked operation can be achieved also with a larger number of elements (N>7-8), 10- and 20- element arrays of PBTLs were also fabricated. Following the notation introduced previously, such arrays will be referred to as 10PBTLA0s and 20PBTLA0s, respectively. The main operational characteristics measured from 10PBTLA0s and 20PBTLA0s, including threshold current ($I_{th}$), slope efficiency, maximum (per pulse) Wall-Plug (W-P) efficiency and output power (P), are summarised in Tab. 6.5.

**Tab. 6.5: Operational characteristics from 10PBTLA0s and 20PBTLA0s measured under pulsed (5μs, 200Hz) operation. The current limit is dictated by the current source. The power scaling factor $N_P$ is also reported for completeness.**

| | $I_{th}$ (mA) | $\eta_e$ (W/A) | Max W-P (%) | Output Power (W/facet) | $N_P$ |
|---|---|---|---|---|---|
| **10-el** ($I=10I_{th}$) | 300 | 0.56 | 19.7 | 1.3 | 4.3 |
| **20-el** ($I=5I_{th}$) | 600 | 0.84 | 26 | 1.8 | 11 |

Preliminary results from far-field measurements are shown in Fig. 6.15.

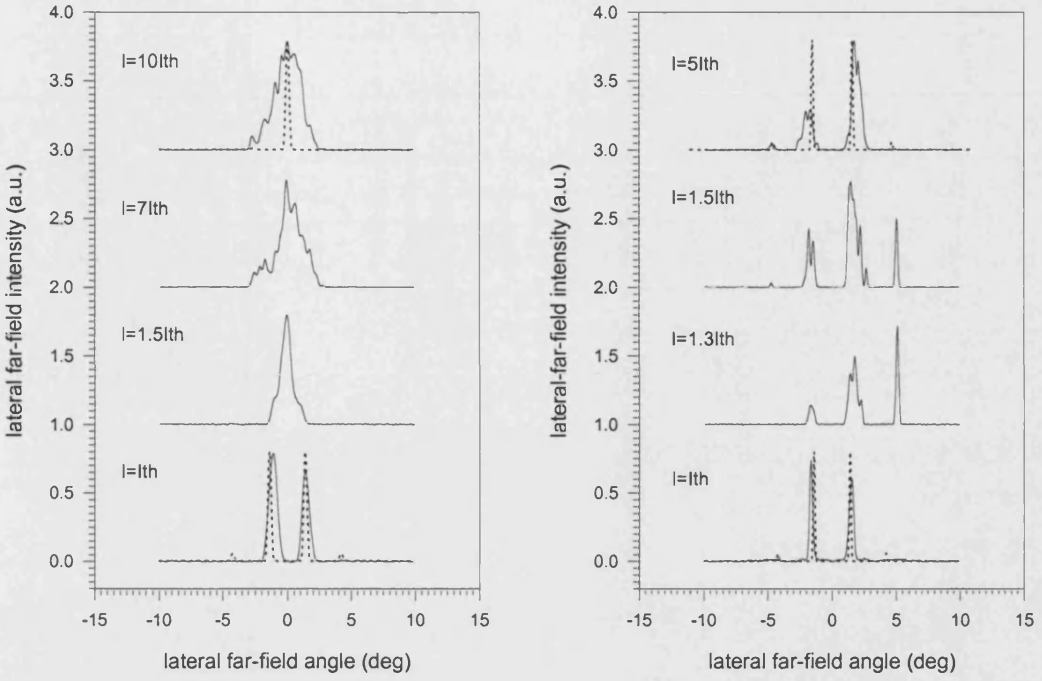


a) b)

**Fig. 6.15: Pulsed (5μs, 200Hz) lateral far-field intensity profiles measured (solid line) for different values of the injection current from in-house fabricated a) 10PBTLA0s and b) 20PBTLA0s without using external optics. The theoretical profiles calculated with the CMT model (dotted lines) are also shown. [Angle resolution 0.05deg].**

Similarly to the trend observed for the arrays of a small number of elements presented in this chapter, at threshold both 10PBTLA0 and 20PBTLA0 operate in the out-of-phase mode (π-phase-shift between adjacent emitters), showing the two lobes typical of this array mode.

At higher currents 10PBTLA0s, Fig. 6.15 a), present essentially a single-lobed output beam that is stable over the wide range of currents of interest, indicating that the device potentially switches to in-phase operation (no-phase-shift between adjacent emitters). However, a significantly broad beam is observed, indicative of the contribution of higher order modes. By contrast, at higher currents, the 20PBTLA0, Fig. 6.13 b), is characterised by multi-lobed far-field patterns, indicating that the out-of-phase mode is still favoured. This can be explained by the fact the, due to the low injection current level, the conditions for the in-phase mode to experience the highest gain, [Chapter 4], have not been reached yet.

The modal gain has been calculated to analyse the array mode discrimination in 10- and 20-element parabolic arrays. Data from calculation for the 5-elements parabolic array are shown for completeness. The obtained results, presented in Fig. 6.16, confirm that scalability is in principle possible.

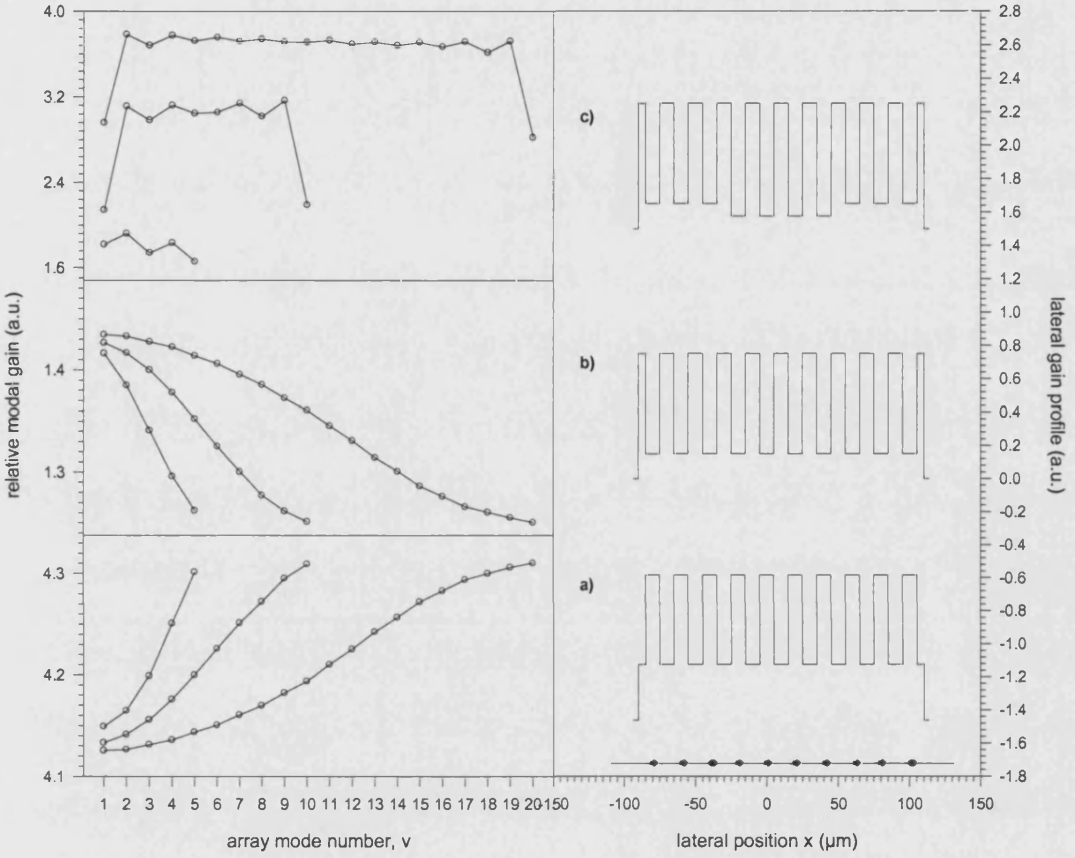


**Fig. 6.16: Modal gain as a function of the mode number computed for arrays of five, ten and twenty elements, for different gain profiles: (a) high gain in high refractive index region; (b) high gain in low refractive index region; (c) high gain in low refractive index region in the presence of hole-burning at the centre of the device. The lateral gain profiles are shown for the array of N=10 elements as an example. The solid circles show the position of the elements, corresponding to the regions where the refractive index is higher.**

As expected the modal gain of the highest order (ν=N) array mode is larger than that of the lowest (ν=1) order mode when the gain in the region of high refractive index is higher than that of the surrounding lower index regions, Fig. 6.16 a). This effect has been noticed experimentally in all PBTLA0s at threshold. On the other hand, the modal gain of the fundamental (ν=1) array mode is larger than that of the highest (ν=N) order mode when the gain in the region of high refractive index is

lower than that of the surrounding lower index regions, Fig. 6.16 b). This effect has been noticed experimentally in 5PBTLA0s and 10PBTLA0s above threshold.

However, when hole-burning becomes significant and the gain of the central elements of the array is further reduced, the modal gain of the lowest and highest order modes decreases significantly with respect to that of other modes, Fig. 6.16 c), and all modes $2 \leq v \leq N-1$ have higher modal gain. This effect is more noticeable in 10PBTLA0s and in 20PBTLA0s and has been verified also experimentally in 10PBTLA0s above threshold.

The experimental results presented in this Section show that scalability to a large number of elements with overall good spatial beam quality is in principle possible, although the changes in lateral gain profile due to hole-burning can be detrimental to the beam quality, as observed in the single-lobed but not diffraction-limited far-field is measured from 10PBTLA0s. In addition, from the data presented in Tab. 6.4, it can be gathered that the power scaling for these devices is reasonably high in the range of current investigated, indicating that these devices might be suitable for high-power high-brightness operation.

## Summary

In this chapter the operational characteristics of in-house designed phase-locked arrays of five index-guided Parabolic Bow-Tie Lasers, referred to as 5PBTLA0s, have been presented in detail to show that coherent (in-phase-locked) operation, with quasi-diffraction-limited output beam can be achieved with careful optical cavity design.

The operational characteristics of 5PBTLA0s are compared with those from corresponding arrays of Linear Bow-Tie Lasers and Stripe Lasers. Results show that, although the output powers from the three different types of devices are comparable, the tapered laser array emitted beams are of 'better quality' than those of stripe laser arrays. In fact, at threshold all the devices emit in a double-lobed beam, typical of the out-of-phase mode operation. However, at higher currents the far-fields of the arrays of tapered lasers become single-lobed while those measured from SLA0s remain double-lobed. The quasi-in-phase locking operation at higher injection currents observed in tapered laser arrays is attributed to the effect of carriers on the refractive

index and gain profiles combined with the longitudinally non-uniform coupling and the mode filtering properties of the device central section. Experimental results have been interpreted using theoretical models based on the Coupled-Mode Theory and on the Hermite-Gauss Collocation Method.

Specifically, the highest brightness ($318MWcm^{-2}sr^{-1}$) is obtained from 5PBTLA0s that emit (at $I=20I_{th}$) 2.5W/facet in a nearly-diffraction-limited beam (0.83deg) measured without the use of external lenses. At the highest current ($I=22.5I_{th}$) 5PBTLA0s show powers in excess of 2.8W/facet in a 1.08deg beam, with brightness of $275MWcm^{-2}sr^{-1}$. The corresponding estimated brightness from 5LBTLA0s is $95MWcm^{-2}sr^{-1}$, indicating that the parabolic geometry is more suited for high brightness operation.

Theoretical calculations and preliminary experimental results from arrays of 10 and 20 elements are also presented to show that scalability to a large number of elements with overall good spatial beam quality is in principle possible. The power scaling for these devices is quite high, indicating that these devices might be suitable for high-power operation. However, changes in the lateral gain profile due to hole-burning can significantly increase the modal gain of higher order modes and, therefore, strongly influence the optical output profile.

# References

[6-1] D. Masanotti, F. Causa, '*Optical guiding properties of high brightness Parabolic Bow-Tie Laser Arrays*', IEEE J. Quantum Electron., vol. 41, n. 7, July 2005, pp. 909-916

[6-2] F. Causa, D. Masanotti, '*High brightness index-guided Parabolic Bow-Tie Laser Arrays*', IEEE Photonics Technology Letters, vol. 16, n. 9, Sept 2004, pp. 2000-2002

[6-3] G. A. Evans, J. M. Hammer, *Surface Emitting Semiconductor Lasers and Arrays*, New York Academic Press (1993).

[6-4] D. Botez, D. R. Scifres, *Diode Laser Arrays*, Cambridge University Press (1994).

# Chapter 7

# *Parabolic Bow-Tie Laser Arrays: Further Discussion*

The aim of this chapter is to further discuss the performance of the five-element arrays of coherently coupled (in-phase locked) index-guided Parabolic Bow-tie Lasers described in Chapter 6 and that have been demonstrated to be an effective design to achieve high output power with high brightness, [7-1], [7-2].

To confirm the effectiveness of this optimised parabolic tapered array structure, results are presented from a study carried out to investigate the effect of inter-element spacing on the coupling between emitters and on the output beam quality. Hence, in-house fabricated arrays of mutually incoherent (otherwise identical) index-guided PBTLs are studied. The Young Two Slit experiment is also performed to measure the mutual coherence between pairs of emitters in coherent and incoherent arrays of 5-Parabolic Bow-Tie Lasers.

Theoretical calculations from the HGCM model, used to interpret most of the results from measurements of the near- and far-field profiles, are shown to be in good agreement with the data obtained from the experimental characterisation.

The results presented in the previous chapter and most of the results presented in this Chapter are obtained from devices tested typically under pulsed operation. For completeness, in this chapter preliminary results obtained for measurements from coherent and incoherent arrays of 5-Parabolic Bow-Tie Lasers under Continuous Wave (CW) operation are discussed.

The effect of the guiding strength on the coupling between emitters and on the output beam quality is also investigated. The operational characteristics measured from arrays of gain-guided 5PBTLA0s are presented and compared with those of index-guided 5PBTLA0s analysed in detail in Chapter 6.

Finally, the robustness of the design and the tolerance with respect to variations in the geometry are also discussed.

## 7.1 Arrays of Mutually Incoherent Parabolic Bow-Tie Lasers

The effect of coherent coupling between individual array elements has been further investigated by fabricating arrays of the same geometry as the index-guided 5PBTLA0s presented in Chapter 6 but with inter-element separation sufficient to ensure that no coupling occurs between adjacent PBTLs and that the array emitters are mutually incoherent, Fig. 7.1.

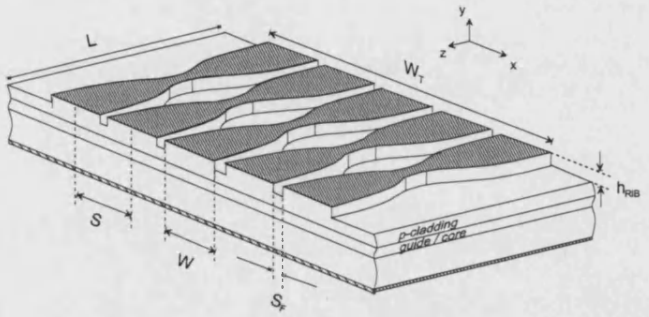


**Fig. 7.1: Schematic of a mutually incoherent Parabolic Bow-Tie Laser Array with definition of the relevant parameters.**

For the devices discussed in this chapter the device parameters are summarised in Tab. 7.1.

**Tab. 7.1: Relevant parameters for the parabolic bow-tie laser array of Fig. 7.1.**

| Parameter | Value | Parameter | Value |
|---|---|---|---|
| Individual emitter output facet | W=20μm | Facet spacing | $S_F$=10μm |
| Array output facet width | $W_T$=140μm | Inter-element spacing | S=30μm |
| Array total length | L=1050μm | Rib height | $h_{RIB}$=0.9μm |

To quantify the inter-element spacing S, or alternatively the spacing between emitters at the (wider) taper facets, here referred to as facet separation $S_F$ ($S=W+S_F$) necessary to ensure that adjacent emitters are not coupled, an estimate of the effective (lateral) carrier spreading was necessary.

Similarly to the measurements taken to characterise current spreading and carrier diffusion in index- and gain-guided PBTLs, [Chapter 5], a CCD camera combined with a short wavelength pass filter was used to image the spontaneous

emission distribution, that is the carrier distribution (squared) at very low injection currents ($I << I_{th}$ where $I_{th}$ is the threshold current) at the output facets of a ridge laser with the same aperture as the array individual emitters. The measured profile is presented in Fig. 7.2, together with the computed carrier density squared profile. The current density and carrier density profiles are also presented for completeness.

By interpreting the measurement results, Fig. 7.2, it was concluded that a distance of 10μm between array elements at the taper ends, corresponding to about 5 times the effective lateral spreading of the carriers (the maximum diffusion length $L_D$ has been estimated to be about 2μm) was sufficient to ensure that the individual elements in the array were optically uncoupled. Hence arrays characterised by an inter-element spacing S=30μm (corresponding to a facet spacing $S_F$=10μm) were fabricated. Following the same notation as for 5PBTLA0s described in Chapter 6, where $S_F$=0μm, the incoherent arrays, where $S_F$=10μm, will be then referred to as 5PBTLA10s.

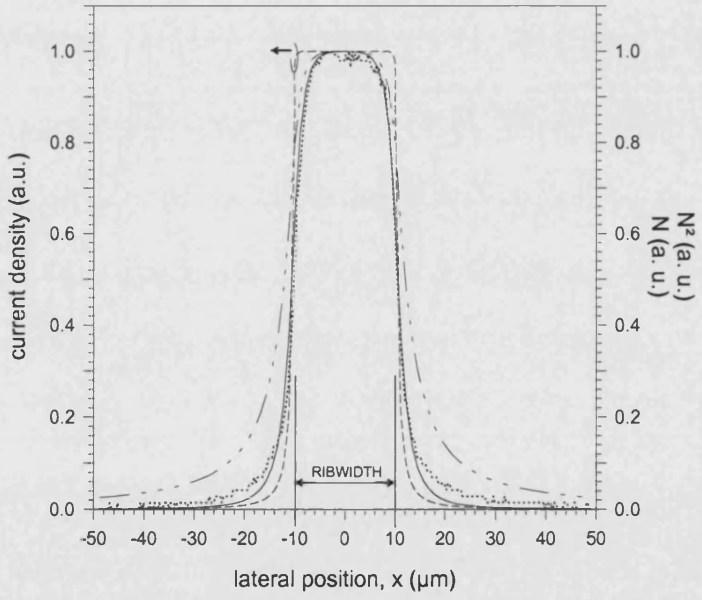


**Fig. 7.2: Experimental (dotted line) and computed (solid line) near-field intensity profile measured at low injection current ($I<<I_{th}$) with low-pass optical frequency filters for an index-guided 20μm wide ridge waveguide laser. The theoretically estimated current density (dashed line) and carrier density (dash-dot line) profiles are also shown.**

The (Pulsed) L-V-I curves measured from the two types of arrays are compared in Fig. 7.3. It can be noticed that although the threshold current remains almost constant ($I_{th}$=180mA for 5PBTLA10s compared to $I_{th}$=160ma for 5PBTLA0s), the

output power measured from 5PBTLA10s is lower than that measured from 5PBTLA0s, which is reflected in the ~30% decrease in slope efficiency. However, the series resistance remains almost constant (0.41Ω), with a decrease of 18%, on average, in the W-P efficiency.

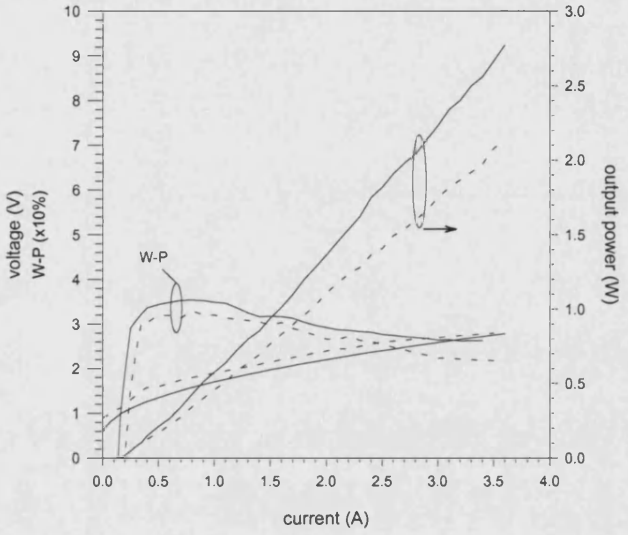


**Fig. 7.3: Pulsed (5μs pulse width, 0.1% duty cycle) L-V-I curves and Wall-Plug efficiency measured from in-house fabricated 5PBTLA0s (solid line) and 5PBTLA10s (dashed line).**

Representative near- and far-field intensity profiles measured at $I=5I_{th}$ from 5PBTLA0s and 5PBTLA10s are presented in Fig. 7.4. Theoretical profiles computed with the HGCM are also plotted for comparison.

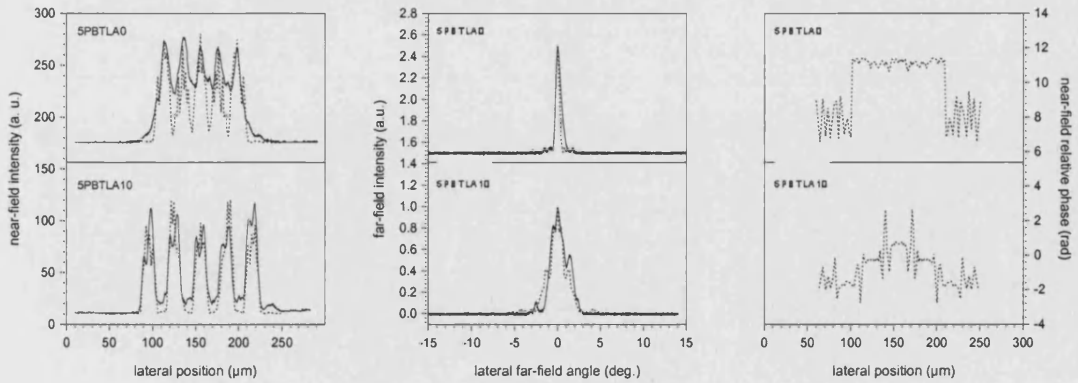


**Fig. 7.4: Comparison between measured (solid line) and HGCM computed (dotted line) data: a) near-field and b) far-field intensity profiles for 5PBTLA0s and 5PBTLA10s. The computed near-field relative phase profile is also presented, c).**

It can be noticed that the far-field lateral divergence measured from 5PBTLA10s is considerably broader (2.7deg at FWHM) than that measured from the corresponding in-phase-locked 5PBTLA0s (0.93deg FWHM). The same trend is observed also at higher currents. At $I=22.5I_{th}$ the far-field lateral divergence for 5PBTLA10s is 2.7deg at FWHM, higher than that for 5PBTLA0s, 1.08deg. This reflects the fact that, as expected from arrays of mutually incoherent (otherwise identical) emitters and confirmed by observing the computed relative phase profile, the array is coherent only over regions corresponding to the individual emitter apertures, with value varying from one emitter to the other, [7-3]. As a consequence incoherent 5PBTLA10s, with the highest brightness 84 $MWcm^{-2}sr^{-1}$, measured at I=22.5Ith, are significantly less bright than the coherent, in-phase-locked, 5PBTLA0s, for which the highest brightness, measured at $I=20I_{th}$, is 318 $MWcm^{-2}sr^{-1}$. Noticeably, the brightness from 5PBTLA10s is lower that the one of a single emitter (137$MWcm^{-2}sr^{-1}$), as expected from incoherently combined sources.

The main operational characteristics measured from the two types of in-house fabricated arrays are summarised in Tab. 7.2.

**Tab. 7.2: Operational characteristics measured from in-house fabricated 5PBTLA0s and 5PBTLA10s at an injection current of $I=20I_{th}$. Values for the individual PBTLs are also presented for comparison.**

| $I=20I_{th}$ | PBTL | 5PBTLA0 | 5PBTLA10 |
|---|---|---|---|
| Threshold current (mA) | 50 | 160 | 180 |
| Slope efficiency (W/A) | 0.7 | 0.81 | 0.62 |
| Max W-P (%) | 45 | 35 | 31 |
| Output Power (W/facet) | 0.64 | 2.5 | 2 |
| Total Area ($\mu m^2$) | 10.4 | 52 | 72.8 |
| Far-Field FWHM (deg) | 2.8 | 0.83 | 2.7 |
| Brightness ($MWcm^{-2}srad^{-1}$) | 137 | 318 | 79 |
| Strehl Ratio (%) | 66 | 57 | 19 |

Very similar trends were observed for arrays with different geometry. Representative near- and far-field intensity profiles measured at an injection current $I=5I_{th}$ for incoherent 5-element LBTLAs, PBTLAs and SLAs are presented in Fig. 7.5.

The main operational characteristics of incoherent five-element arrays of different geometries, compared to those of the optically coupled arrays, are summarized in Tab. 7.3. Corresponding values for the individual array emitters, and the estimated values for $N_P$, $N_\theta$ and $N_B$, [Chapter 6], are also reported to analyse the effect of coherence on the performance of the different types of arrays.

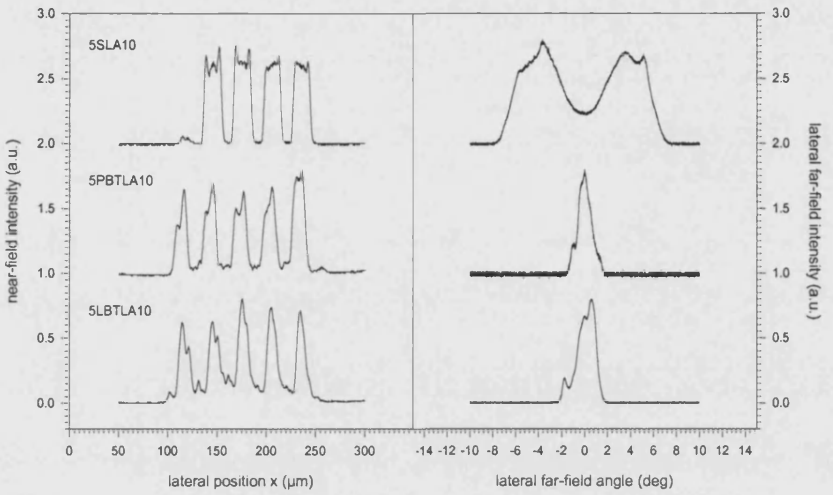


**Fig. 7.5: Measured near-field profiles and corresponding far-field profiles for 5-element incoherent arrays of LBTLs, PBTLs and SLs.**

**Tab. 7.3: Pulsed operational characteristics measured from coherent and incoherent five-element LBTLAs, PBTLAs and SLAs at $I=20I_{th}$. Values for the individual emitters are also presented for completeness.**

| | Ith (mA) | $\eta_e$ (W/A) | P (W/facet) | $N_P$ | $\theta_x$ (deg.) | $N_\theta$ | Brightness ($MWcm^{-2}srad^{-1}$) | $N_B$ |
|---|---|---|---|---|---|---|---|---|
| **SL** | 60 | 0.8 | 0.7 | 1 | 3.2 | 1 | 62 | 1 |
| **5SLA0** | 200 | 0.83 | 2.8 | 4 | 12.5 | 0.3 | 25 | 0.4 |
| **5SLA10** | 220 | 0.73 | 2.7 | 3.9 | 12.2 | 0.3 | 15.4 | 0.2 |
| **LBTL** | 55 | 0.62 | 0.56 | 1 | 2.9 | 1 | 107 | 1 |
| **5LBTLA0** | 160 | 0.78 | 2.1 | 3.7 | 2.8 | 1.3 | 89 | 0.8 |
| **5LBTLA10** | 180 | 0.65 | 1.98 | 3.5 | 2.9 | 1 | 72 | 0.7 |
| **PBTL** | 50 | 0.7 | 0.64 | 1 | 2.8 | 1 | 137 | 1 |
| **5PBTLA0** | 160 | 0.81 | 2.5 | 3.9 | 0.83 | 3.4 | 318 | 2.3 |
| **5PBTLA10** | 180 | 0.62 | 2 | 3.1 | 2.7 | 1.03 | 79 | 0.6 |

As seen in Chapter 4, ideally the total power emitted by an array of N elements is N times the power emitted from the individual element. If the array operates in the

fundamental (in-phase) mode, the emitted beam is single-lobed and its far-field lateral divergence at FWHM is N times smaller than that of the individual emitter. As a consequence, since the total emitted area is N times the individual emitter area, the brightness of the array is N times the brightness of the individual emitters, [7-3]. However, for arrays of mutually incoherent elements, the emitted beam corresponds to that of the array individual emitter. As a consequence also the maximum achievable brightness coincides with the brightness of the brightness of the individual emitter. Experimental results summarised in Tab. 7.3, show that for incoherent arrays $N_B<1$, since, as expected, $N_\theta \sim 1$ (apart from the 5SLA10s that shows a much broader far-field pattern) but $N_P$ is smaller than expected.

## 7.2 Coherence Measurements

To study more in details the occurrence of coherence in the arrays of interest in this PhD thesis, measurements of the mutual coherence between adjacent and next-nearest neighbour emitters, [7-4], have taken under pulsed condition from 5PBTLA0s and 5PBTLA10s by using the Young Two Slit experiment described in Chapter 3. The measurement set-up is described in detail in Appendix F.

Using a 0.25 Numerical Aperture (N.A) objective lens, the array near-field was imaged onto transmission slits of aperture a=100μm, and spacing $S_{sl}$=1mm. The position of the transmission slits was chosen depending on the width of the individual emitter, the inter-element spacing between the considered pairs and the lens magnification, [Appendix F], so that those two emitters only interfered. The interference pattern was detected by a CCD camera placed behind the slits.

Results from 5PBTLA0s, Fig. 7.6, show that the mutual coherence between any two adjacent elements is about $\gamma_{mn}$=V=0.5 at I=300mA (=1.875$I_{th}$). The value decreases to $\gamma_{mn}$=V=0.30 for I=800mA (=5$I_{th}$).

The relative phase between elements can be determined by the position of the fringes under the diffraction envelope. If a fringe maximum (constructive interference) occurs at the diffraction envelope maximum, the elements are in-phase. The elements are out-of-phase if a fringe minimum (destructive interference) occurs at the maximum of the envelope. It can be observed, Fig. 7.6, that the maximum of the envelope coincides with a fringe maximum for all the pairs of emitters, indicating

that, as expected, they are in-phase. However, a small displacement of maximum of the fringe can be noticed in the pattern for the III and IV elements at I=300mA. This can be explained considering that the driving current is very close to threshold value, and the considered emitters are not in-phase yet.

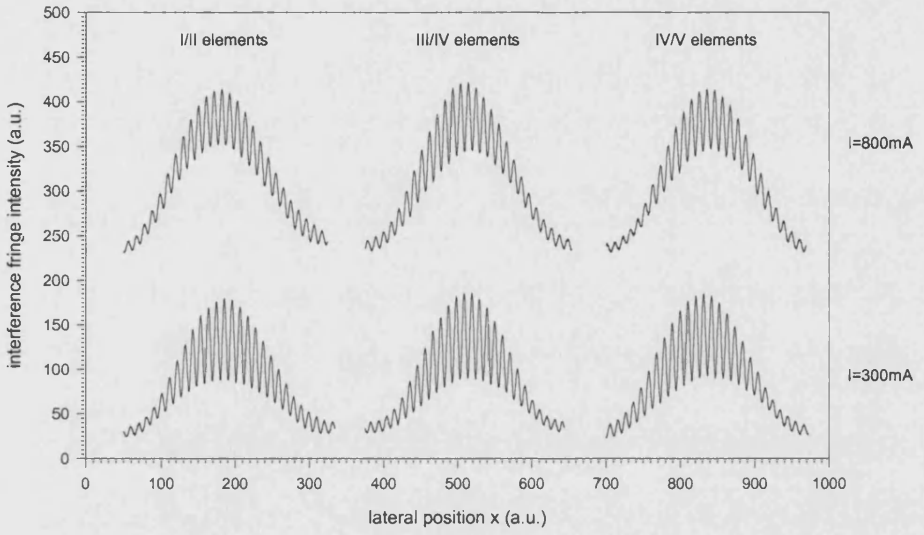


**Fig. 7.6: Interference pattern resulting from pairs of elements, corresponding to adjacent elements, of a 5PBTLA0. The intensity fringes have been measured by performing the Young Two Slit experiment.**

The interference fringe patterns for different pairs of emitters of 5PBTLA10s are presented in Fig. 7.7.

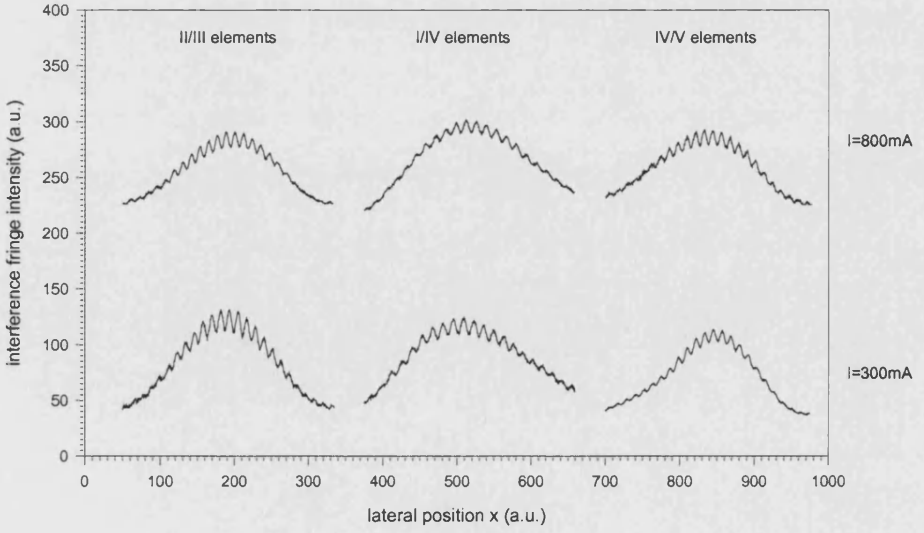


**Fig. 7.7: Interference pattern resulting from different pairs of elements of a 5PBTLA10. The intensity fringes have been measured by performing the Young Two Slit experiment.**

As expected from incoherent laser arrays, the degree of coherence between elements is almost zero and does not depend on the distance between the elements or the injected current. Its value is almost constant for the different pairs considered, and is given by $\gamma_{mn}=V=0.02$ at I=800mA. The above results confirm that coherent coupling is completely destroyed in arrays with significant inter-element spacing.

## 7.3 CW Measurements

CW measurements from 5PBTLA0s are presented and compared with those under pulsed operation discussed in the previous Chapter 6. As observed in Fig. 7.8, where the L-V-I characteristics are shown, there is no significant increase in threshold current measured under CW operation, with respect to that measured in pulsed operation. On the other hand, the slope efficiency is reduced by approximately 25% and this, combined with the significant increase of the voltage across the diode, results into a 42% decrease in W-P efficiency. The reduction in the efficiency can be attributed to the present non-optimal bonding and heat sink conditions. Due to the limitations in thermal management of the present experimental arrangement, the maximum CW driving current was restricted to $I = 1.2A = 7.5I_{th}$. However, no thermal roll-over was observed in the range of current investigated.

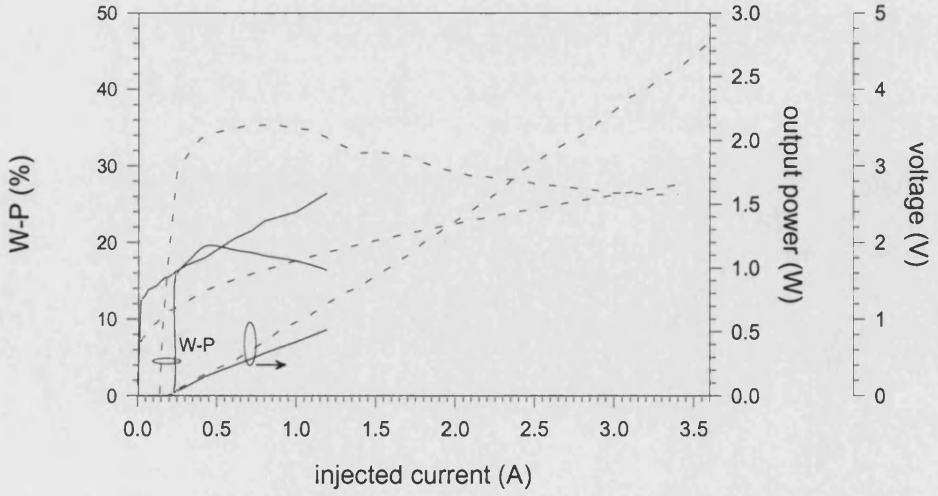


**Fig. 7.8: Comparison between CW (sold line) and pulsed (dashed line) L-V-I characteristics for a 5PBTLA0. The W-P characteristics curves are also shown. [5μs pulse width, 0.1% duty cycle; Temperature T=20°C].**

The profiles of the radiated beam pattern, Fig. 7.9, measured without the use of additional optics, confirm the trend observed under pulsed operation, [7-2].

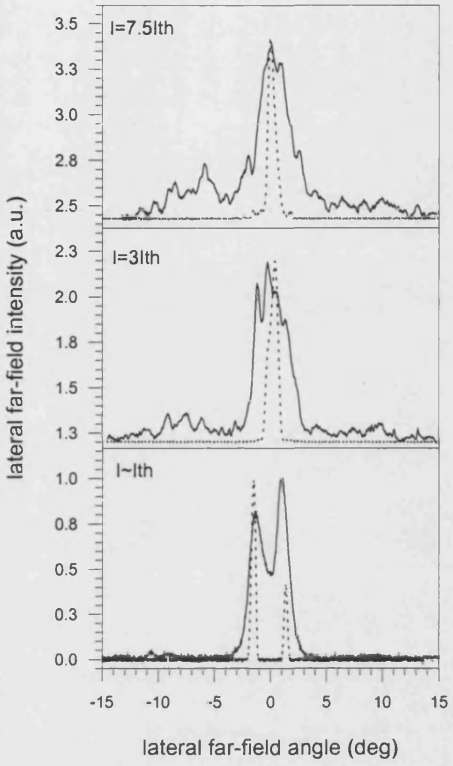


**Fig. 7.9: Comparison between CW (solid line) and pulsed (dashed line) far-field intensity profiles measured from 5PBTLA0s at different currents ($I=I_{th}$, $I=3I_{th}$ and $I=7.5I_{th}$). Measurements are taken without using external optics. [Angle resolution: 0.05deg].**

Near threshold, the out-of-phase array mode is favoured, and the radiated beam presents a double-lobed pattern typical of that mode operation. However, the peaks are broader than the corresponding peaks measured under pulsed operation. In addition, the peak separation is $\Delta\theta = 2.3\text{deg}$, which is slightly smaller than the $\Delta\theta = 2.8\text{deg}$ peak separation measured at threshold in pulsed conditions. The changes in the far-field profile can be attributed to the simultaneous oscillation of adjacent modes due to the effect of temperature on the gain profile. Broad area lasers with a 'top-hat', well confined, current profile, are characterised by a parabolic thermal profile with the heating localised in the central part of the device and resulting in a reduction of the gain in the same position, [7-5]. At threshold, because of the overlap between field intensity and gain profile, the next favourite mode is the

$\nu = 4$ mode, as explained in Chapter 4 and observed in Fig. 6.7 a), that starts oscillating simultaneously with the $\nu = 5$ mode.

The radiated beam becomes single-lobed at higher currents and output power in excess of 500mW is achieved at $I = 1.2A = 7.5I_{th}$, with a 3deg lateral beam divergence at FWHM, larger than that obtained under pulsed operation. The broadening of the far-field can also be attributed to the effect of heating that strengthens the spatial-hole burning in the central part of the device. This, as explained in Chapter 4 and observed in Fig. 6.7 c), is not conducive to out-of-phase operation but yields to the excitation of higher order modes.

As a consequence of the far-field broadening, the estimated brightness $B = 12MWcm^{-2}srad^{-1}$ (CW) at the highest current ($I=7.5I_{th}$) is reduced by an order of magnitude with respect to that obtained under pulsed conditions, $B = 128MWcm^{-2}srad^{-1}$, at the same current. The main CW results measured from 5PBTLA0s are summarised in Tab. 7.4 together with those obtained in pulsed condition, [7-2].

**Tab. 7.4: Operational characteristics measured from in-house fabricated 5PBTLA0s at $I=3I_{th}$ and $I=7.5I_{th}$ under pulsed (5μs, 200Hz) and CW operation.**

| | $I_{th}$ (mA) | Max W-P (%) | Output Power (W/facet) | | $\theta_x$ FWHM (deg) | | Brightness ($MWcm^{-2}srad^{-1}$) | |
|---|---|---|---|---|---|---|---|---|
| | | | $I=3I_{th}$ | $I=7.5I_{th}$ | $I=3I_{th}$ | $I=7.5I_{th}$ | $I=3I_{th}$ | $I=7.5I_{th}$ |
| **pulsed** | 160 | 35 | 0.320 | 0.725 | 0.8 | 0.8 | 42.4 | 128 |
| **CW** | 160 | 20 | 0.190 | 0.515 | 3.2 | 3.0 | 5.4 | 12 |

Preliminary CW measurements from 5PBTLA10s are also presented and compared with those from 5PBTLA0s discussed at above. Because of limitations in thermal management of the present experimental arrangement, as discussed before, the maximum CW driving current was restricted to $I = 1.2A = 7.5I_{th}$ also for the 5PBTLA10s.

As observed in Fig. 7.10, where the L-V-I characteristics are shown, there is no increase in threshold current measured for the incoherent array, with respect to that measured for the phase-locked one. The measured voltage across the diode also remains unchanged. However, the slope efficiency is reduced by approximately 50%, which reflects into a corresponding 50% decrease in the W-P efficiency. Such large

decrease in the efficiency of 5PBTLA10s compared to 5PBTLA0s confirms the trend observed under pulsed operation but also shows that temperature effects, combined with the present non-optimal bonding and heat sink conditions, are stronger in 5PBTLA10s, perhaps due to the bigger size.

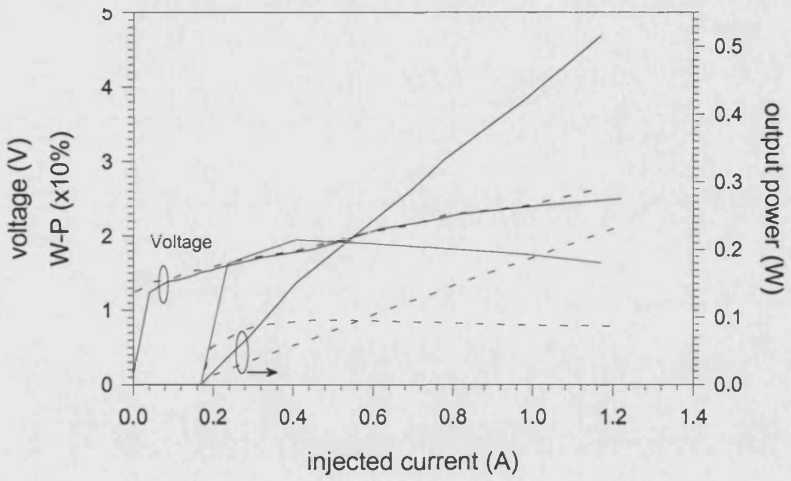


**Fig. 7.10: Comparison between CW L-V-I and W-P characteristics for 5PBTLA0s (solid line) and 5PBTLA10s (dashed line). [Temperature T=20°C].**

The profiles of the radiated beam pattern, measured without the use of external lenses, also confirm the trend observed under pulsed operation, Fig. 7.4 b), with the incoherent array radiated beam showing a stable single-lobed far-field pattern, diffraction-limited over the individual emitter aperture, for all the range of currents of interest. This shows that 5PBTLA10s are more robust than the 5PBTLA0s to changes in temperature. .

Despite the fact that the beam width for the two types of array under CW operation is comparable, the decrease in the achievable output power for 5PBTLA10s results in a further reduced brightness, estimated to be $5.88 MWcm^{-2}srad^{-1}$, half the value obtained with the coherently coupled arrays under CW operation.

The main CW measurement results from the two types of arrays are summarised in Tab. 7.5. Results obtained under pulsed operation are also presented for comparison.

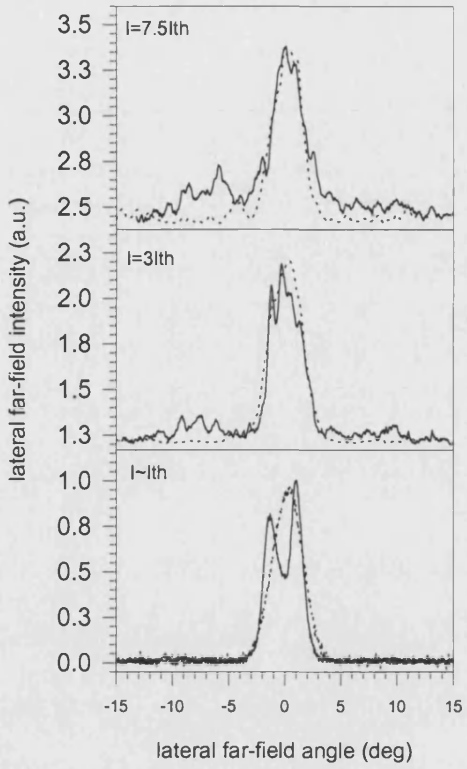


**Fig. 7.11: Comparison between CW far-field intensity profiles measured from 5PBTLA0 (solid line) and 5PBTLA10s (dashed line) at different currents ($I=I_{th}$, $I=3I_{th}$ and $I=7.5I_{th}$). Measurements are taken without using external optics. [Angle resolution: 0.05deg].**

**Tab. 7.5: Operational characteristics measured from in-house fabricated 5PBTLA0s and 5PBTLA10s at $I=3I_{th}$ and $I=7.5I_{th}$ under pulsed (5μs, 200Hz) and CW operation.**

| | $I_{th}$ (mA) | Max W-P (%) | Output Power (W/facet) | | $\theta_x$ FWHM (deg) | | Brightness ($MWcm^{-2}srad^{-1}$) | |
|---|---|---|---|---|---|---|---|---|
| | | | $I=3I_{th}$ | $I=7.5I_{th}$ | $I=3I_{th}$ | $I=7.5I_{th}$ | $I=3I_{th}$ | $I=7.5I_{th}$ |
| **5PBTLA0** | | | | | | | | |
| **pulsed** | 160 | 35 | 0.32 | 0.725 | 0.8 | 0.8 | 42.4 | 128 |
| **CW** | 160 | 20 | 0.19 | 0.5 | 3.2 | 3.0 | 5.4 | 12 |
| **5PBTLA10** | | | | | | | | |
| **pulsed** | 180 | 31 | 0.2 | 0.52 | 2.8 | 2.7 | 5.3 | 14 |
| **CW** | 180 | 8.7 | 0.1 | 0.234 | 3.2 | 3.01 | 2.3 | 5.9 |

## 7.4 Gain-Guided Parabolic Bow-Tie Laser Arrays

To investigate the effect of optical guiding strength on the device operational characteristics, the index- (weakly) guiding coupled arrays discussed in Chapter 6

have been compared to corresponding gain-guiding (diffraction-type) devices having identical injection metal contact surface area and geometry.

In particular, to follow the notation introduced in Chapter 5, the optimised 5PBTLA0s presented in Chapter 6 and characterised by a rib height $h_{RIB}$=0.9μm (with estimated lateral effective index step $\Delta n_{eff} = 0.007$) will be referred to as Index-Guided (IG-) devices. On the other hand, arrays characterised by a shallower etched rib height $h_{RIB}$=0.45μm (with negligible lateral effective refractive index step) will be referred to as Gain-Guided (GG-) devices.

As seen in Chapter 5, although the shallow rib height of GG devices is useful for reducing current spreading, there is an increase of current spreading compared to that occurring in IG- devices, Fig. 5.11. The increased extent of current spreading in GG- arrays is reflected in a 25% increase of the threshold current ($I_{th}$ = 200mA measured from GG-5PBTLA0s, compared to the $I_{th}$ = 160mA from IG-5PBTLA0s) and a 12% decrease in the device efficiency, as can be seen in Fig. 7.12, where a representative comparison of the electrical and optical characteristics from the two types of devices is presented. Noticeably, the Wall-Plug efficiency of GG- devices is lower than that of IG- devices over the range of currents investigated, [7-2].

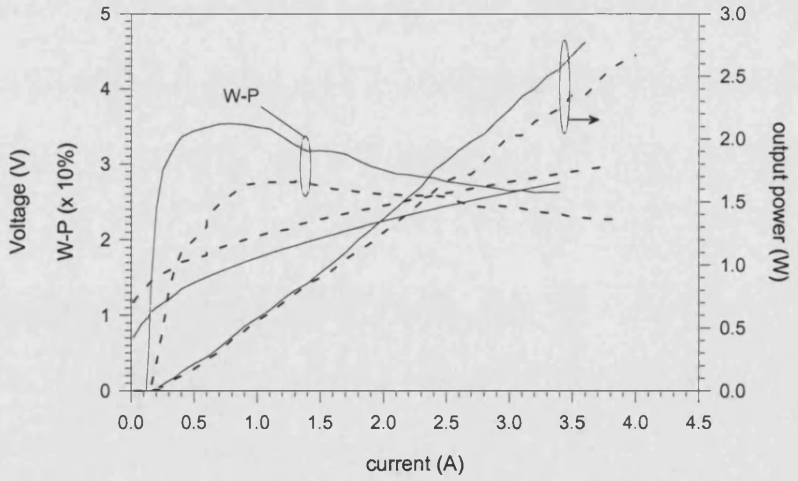


**Fig. 7.12: L-I-V and Wall-Plug efficiency curves measured from IG- (solid line) and GG- (dashed line) 5PBTLA0s. [5μs pulse width, 200*Hz*; Temperature: 20°C. Intensity filters have been used to take readings at high power levels].**

It can be noticed that, compared to IG- devices, the light current characteristic of the GG-5PBTLA0s presents pronounced kinks which can be attributed to

filamentation. In fact, the absence of a defined lateral mode confinement makes these broad area devices particularly sensitive to perturbations due to injected carriers and to spatial hole-burning, [Chapter 2]. This results in a spatial non-uniform distribution of optical power and in instabilities, [7-6]. As a consequence, the output beam quality of GG- devices dramatically degrades compared to that of IG- devices.

Typical near-field intensity profiles imaged at the facets of IG- and GG-5PBTLA0s at an injected current $I=22.5I_{th}$ are presented in Fig. 7.13, [7-2].

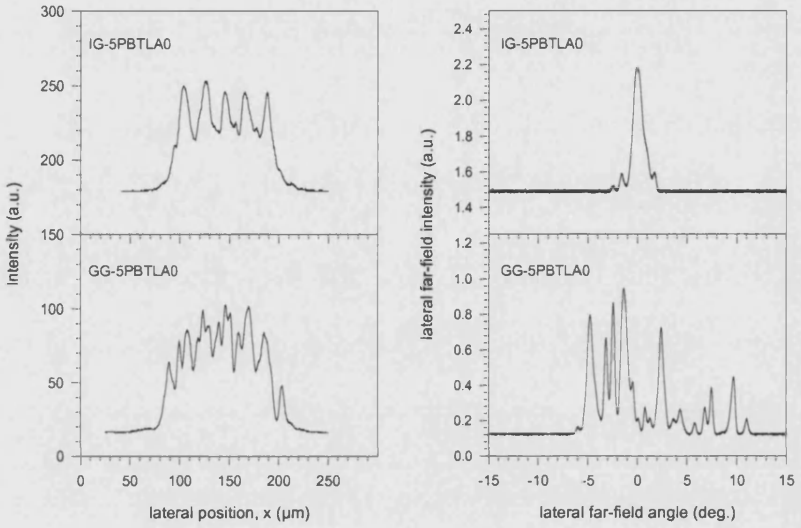


**Fig. 7.13: Near-field, a), and far-field, b), intensity profiles measured from IG- and GG-5PBTLA0s at $I=22I_{th}$.**

It can be observed that diffraction type devices are characterised by a spatial non-uniform intensity distribution: as mentioned before, the absence of a defined lateral mode confinement results in a spatial non-uniform carrier distribution with effects on the refractive index and gain profiles that yields to instabilities. This yields in turn, to poor radiated beam quality, as introduced before and as can be gathered from the corresponding far-field intensity profiles. The output beam from GG-5PBTLA0s is multi-peaked and shows evidence of filamentation, Fig. 7.13 b), thus making such devices not suitable for high brightness operation. Far-field profiles have been measured without the use of external optics, with an angular resolution of 0.05deg.

To ascertain the presence of filamentation, accurate measurements have been taken to detect the virtual Beam Waist (BW), [7-2]. The resulting BW profiles measured from GG-5PBLA0s at different currents are depicted in Fig. 7.14. The profiles of the corresponding optical near-field intensity at the device facet are also shown. It can be noticed that at low currents it is possible to distinguish five BW spots, one from each array emitter. However, as the current is increased above $I = 3I_{th}$ filamentation occurs, leading to poor beam quality.

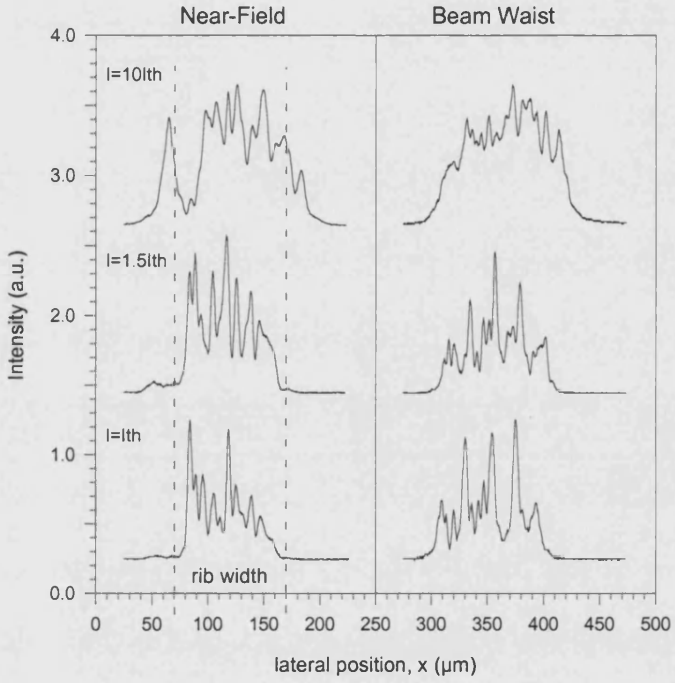


**Fig. 7. 14: Near-field intensity profiles and corresponding Beam Waists measured from GG-5PBTLA0s at different pulsed injection currents. [5μs pulse width, 200Hz].**

BW measurements are useful also to quantify the longitudinal astigmatism in GG-5PBTLA0s, that corresponds to the distance between the laser facet and the beam waist plane, i.e., the distance between the vertical and lateral waists. For the devices of interest here, the longitudinal astigmatism is estimated to be $d_A$=40μm at currents near threshold, smaller than the theoretical estimated value $d_A$=150μm, [Chapter 2]. Such difference is due to the fact that, differently from properly designed GG- devices where the optical wave freely diffracts in the active medium, here the cavity does not permit free-diffraction of the optical beam. Importantly, it

has not been possible to verify the dependence of astigmatism on injected current because at higher currents filamentation becomes the dominant feature.

Further evidence of filamentation, and confirmation of the robustness of the high power high brightness IG-5PBTLA0s, is provided by the comparison of near- and far-field intensity profiles of IG- and GG- 5PBTLA0s and 5PBTLA10s, Fig. 7.15 a), and IG- and GG- 5LBTLA0s and 5LBTLA10s, Fig. 7.15 b). The results presented in Fig.7.15 a) indicate (as expected) that the optical field is no longer affected by the device geometry. In fact, when the optical field freely propagates in the gain region, filamentation becomes a dominant feature and the optical coupling no longer affects device performance. The near- and far-field intensity profiles of GG-5LBTLA0s and GG-5LBTLA10s, Fig. 7.15 b), show similar characteristics to those of parabolic arrays, indicating that when filamentation occurs also the taper profile no longer influences the device performance

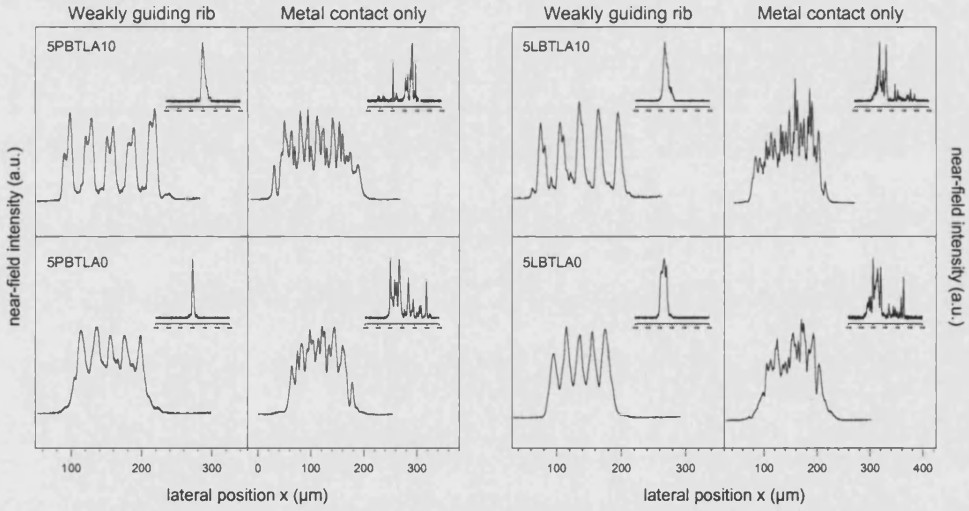


**Fig. 7.15: Near-field intensity profiles measured from a) IG- and GG- 5PBTLA0s and 5PBTLA10s and b) IG- and GG- 5LBTLA0s and 5LBTLA10 at $I=22.5I_{th}$ (pulsed). Corresponding far-field intensity profiles are presented in the insets.**

Details on the main operational characteristics measured from IG- and GG-5PBTLA0s are summarised in Tab. 7.6, [7-2].

**Tab. 7.6: Comparison of the operational characteristics measured from in-house fabricated IG- and GG- 5PBTLA0s measured under pulsed operation (5μs, 200Hz).**

| | $I_{th}$ (mA) | Max W-P (%) | $\eta_e$ (W/A) | $R_S$ (Ω) | Output Power (W/facet) | | $\theta_x$ FWHM (deg.) | | Brightness ($MWcm^{-2}srad^{-1}$) | |
|---|---|---|---|---|---|---|---|---|---|---|
| | | | | | $I=3I_{th}$ | $I=22.5I_{th}$ | $I=3I_{th}$ | $I=22.5I_{th}$ | $I=3I_{th}$ | $I=22.5I_{th}$ |
| IG | 160 | 35 | 0.8 | 0.45 | 0.32 | 2.8 | 0.8 | 1.08 | 42.4 | 275 |
| GG | 200 | 29 | 0.7 | 0.33 | 0.24 | 3.0 | filamentation | | ~0 | ~0 |

## 7.5 Tolerance: Device Length

A study on the tolerance of the individual Parabolic Bow-Tie Laser operational characteristics with respect to variations of the device dimensions (due to fabrication errors) showed that the device design is in general very robust, [7-7], [Appendix C].

However, device cleaving and therefore variations of the desired device length, have been demonstrated to have significant effect on the performance of Index-Guided Parabolic Bow-Tie Laser Arrays when designed for achieving coherent in-phase-locking operation. Considering the IG-5PBTLA0 in Fig. 7.16 a), the desired taper length is $L_t$; at the output facets the ribs merge in a single contact and the device appears to be a broad ridge laser of width $W_T$, Fig. 7.16 b).

If fabrication errors occur and the devices are cleaved with a taper length $L_S<L_t$, then the emitter facets are reduced in size ($W_S<W_{out}$) and gaps are created between adjacent elements, Fig. 7.16 c). The inter-element spacing S remains unchanged but since the facets are smaller then the device shows a facet spacing $S_F$ such that the elements could be effectively uncoupled.

The effect of wrong cleaving has been experimentally valuated by characterising devices cleaved at a (shorter) taper length $L_S$=450μm and therefore characterised by individual element facet widths $W_S$=19μm and a coupling spacing $S_F$=1μm. This could be a critical value considering that, as observed earlier in the chapter, the maximum carrier diffusion length $L_D$ is about 2μm. Such 'shorter' devices will be referred to as S-5PBTLA0s.

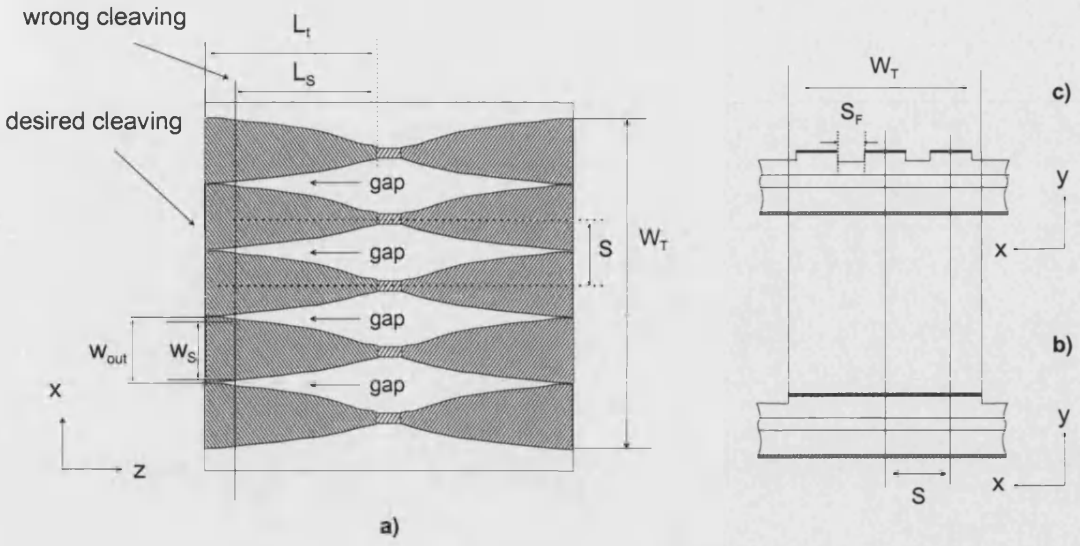


**Fig. 7.16: The effect of cleaving errors on IG-5PBTLA0s. a) top view schematic of the device with main relevant parameters: $W_T$=100μm, $w_{out}$=20μm, $L_t$=500μm, S=20μm. Front view schematics are also presented to describe the device structure when the cleaving is done at b) the desired taper length $L_t$ and c) at a wrong, shorter, taper length $L_S$.**

The optical power output versus injected current characteristics measured from IG-5PBTLA0s and S-5PBTLA0s are compared in Fig. 7.17.

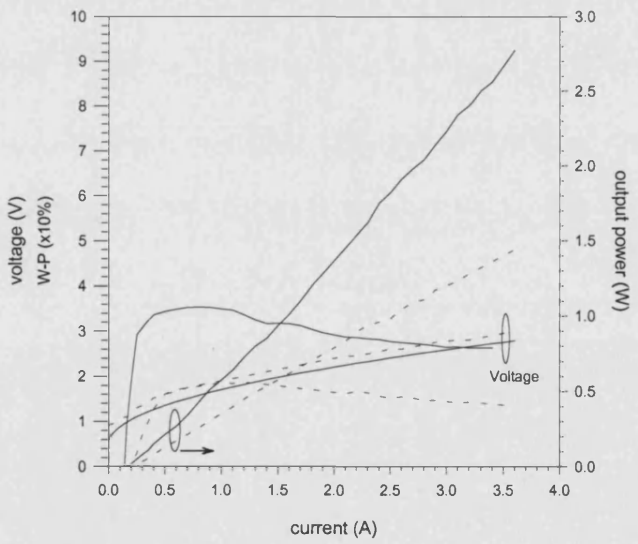


**Fig. 7.17: L-I-V and Wall-Plug efficiency curves measured from IG-5PBTLA0s (solid line) and S-5PBTLA0s (dashed line). [5μs pulse width, 200Hz; Temperature: 20°C. Intensity filters have been used to take readings at high power levels].**

The voltage across the diodes and the Wall-Plug efficiency characteristic curves are also shown. It can be observed that the 'shorter' devices are characterised

by significantly higher threshold current, measured to be $I_{th}$=250mA. In addition the output power measured from S-5PBTLA0s is lower than that measured from IG-5PBTLA0s, which is reflected in the 45% decrease in slope efficiency. The series resistance remains almost constant (0.41Ω), but the decrease in the W-P efficiency is, on average, of about 50%.

Representative far-field intensity profiles measured at different injected current from the two types of arrays are presented in Fig. 7.18. It can be noticed that, in the range of currents of interest, the far-field measured from the S-5PBTLA0s is stable and essentially single-lobed. However, its width at FWHM, 3.1deg, measured at I=15 $I_{th}$, is considerably broader than that measured from the corresponding in-phase-locked 5PBTLA0s at the corresponding current. Importantly, such divergence corresponds to the diffraction-limit angle $\theta_d = \arcsin\left(\frac{\lambda}{D}\right) = 2.95\,\text{deg}$, equation (2.16), from a D=19μm wide uniformly illuminated aperture. Hence it can be deduced that S-5PBTLAs are essentially arrays of mutually incoherent emitters.

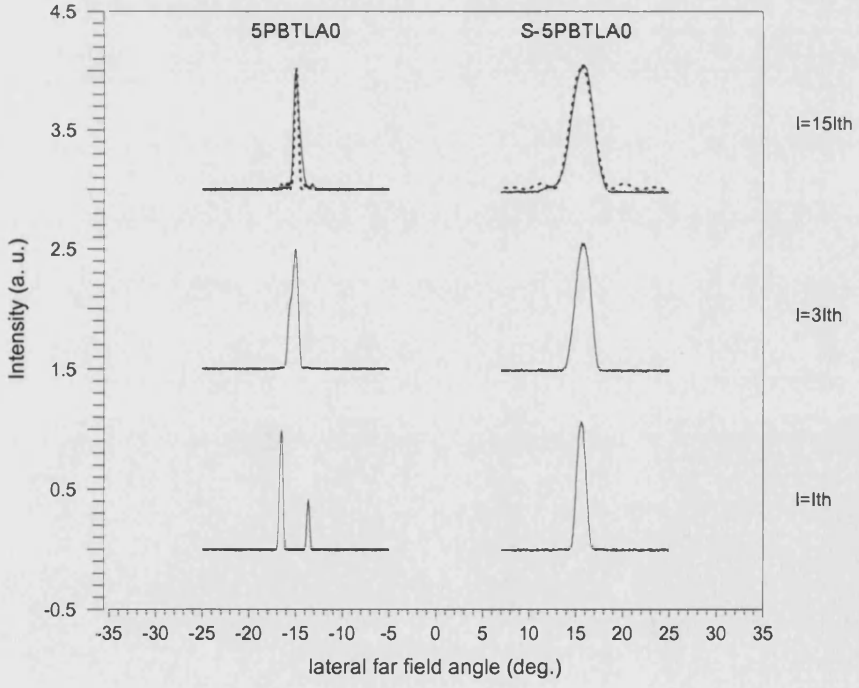


**Fig. 7.18: Pulsed (5μs, 200Hz) lateral far-field intensity profiles measured for different values of the injection from in-house fabricated IG-5PBTLA0s and S-5PBTLA0s without using external optics. The diffraction-pattern (dotted line) from corresponding 100μm and 19μm wide uniformly illuminated aperture are also shown.**

Details on the main operational characteristics measured from IG-5PBTLA0s and S-5PBTLA0s are summarised in Tab. 7.7.

**Tab. 7.7: Comparison of the operational characteristics measured from in-house fabricated IG-5PBTLA0s and S-5PBTLA0s measured at $I=15I_{th}$ pulsed (5μs, 200Hz).**

| | $I_{th}$ (mA) | Max W-P (%) | $\eta_e$ (W/A) | Output Power (W/facet) | $\theta_x$ FWHM (deg.) | Brightness ($MWcm^{-2}srad^{-1}$) |
|---|---|---|---|---|---|---|
| **IG-5PBTLA0s** | 160 | 35 | 0.8 | 1.8 | 0.9 | 212 |
| **S-5PBTLA0s** | 250 | 19 | 0.43 | 1.5 | 3.1 | 54 |

Further investigations must be carried out to study in detail the effect of a longer cleaving on 5PBTLA0 performance. Preliminary experimental results show that up to 50μm larger cleaving length seems not to affect coherent, in-phase locked, operation.

## Summary

Five-element arrays of mutually incoherent Index-Guided PBTLs, referred to as IG-5PBTLA10s, and Gain-Guided 5PBTLA0s, referred to as GG-5PBTLA0s, have been characterised to show that the coherently coupled IG-5PBTLA0 is an effective and robust design to scale up the output optical power while enhancing diffraction-limit operation and therefore brightness. In fact, it has been shown that coherent coupling is not achieved with the devices presented here, and as a consequence the beam quality is compromised.

The emitted beam from IG-5PBTLA10s is a single-lobed stable beam but, as expected in mutually incoherent arrays, is considerably broader (2.7 deg at FWHM) than that measured from the corresponding in-phase-locked IG-5PBTLA0s (0.83 deg FWHM). As a consequence the highest brightness ($98\ MWcm^{-2}sr^{-1}$) is also significantly lower than that from IG-5PBTLA0s ($318MWcm^{-2}sr^{-1}$). Noticeably, the brightness from IG-5PBTLA10s is also much lower than that of a single emitter ($137MWcm^{-2}sr^{-1}$).

The Young Two Slit experiment has been performed to measure the mutual coherence between pairs of emitters from the visibility V of the obtained interference fringe patterns. Results confirm that coherent coupling is completely destroyed in

arrays with significant inter-element spacing. The degree of coherence is, in fact is almost zero for IG-5PBTLA10s.

Results from CW measurements on IG-5PBTLA0s and on IG-5PBTLA10s confirm the trends observed with the pulsed measurements although lower efficiency and brightness are achieved in these conditions possibly due to the non-optimal bonding and heat sinking conditions of the present devices. Importantly, it has been noticed that device heating can be detrimental for mode discrimination. The brightness achieved with IG-5PBTLA0s and IG-5PBTLA10s under CW operation is, respectively, 12 $MWcm^{-2}sr^{-1}$ and 5.88 $MWcm^{-2}sr^{-1}$.

On the other hand, in GG-5PBTLA0s the absence of a defined lateral mode confinement results in a spatial non-uniform carrier distribution and a non-uniform refractive index and gain profiles that yields to instabilities. This yields in turn, to poor beam quality, the output beam being multi-peaked and showing evidence of filamentation, thus making such devices not suitable for high brightness operation.

One more aspect that has been considered is the effect of fabrication errors on the device performances. It has been noticed that IG-5PBTLA0s are very sensitive to variation in the device length, particularly to a shorter cleaving, that compromises the coherent coupling between array emitters and therefore in-phase locked operation.

# References

[7-1] F. Causa, D. Masanotti, *'High brightness index-guided Parabolic Bow-Tie Laser Arrays'*, IEEE Photonics Technology Letters, vol. 16, n. 9, Sept 2004, pp. 2000-2002

[7-2] D. Masanotti, F. Causa, *'Optical guiding properties of high brightness Parabolic Bow-Tie Laser Arrays'*, IEEE J. Quantum Electron., vol. 41, n.7, July 2005, pp. 909-916

[7-3] D. Botez, D. R. Scifres, *Diode Laser Arrays*, Cambridge University Press (1994).

[7-4] G. A. Evans, J. M. Hammer, *Surface Emitting Semiconductor Lasers and Arrays*, New York Academic Press (1993).

[7-5] E. O'Neill, P. O'Brien, J. Houlihan, J. McInerney, *'Modification of internal temperature distribution in broad area semiconductor lasers and the effect on near- and far-field distributions'*, IEE. Proc.-Optoelectron., 2000, vol. 147, n. 1, pp.31-35

[7-6] D. C. Hall, M R. Surette, L .Goldberg, D. Mehuys, *'Carrier-Induced Lensing in Broad-Area and Tapered Semiconductor Amplifiers'*, IEEE Photon. Technol. Lett., vol. 6, n. 2, 1994, pp. 186-188

[7-7] D. Masanotti, F. Causa, J. Sarma, *'Design optimisation of high power high brightness parabolic bow-tie laser diodes'*, IEE Proceedings - Circuits, Devices and Systems, vol. 150, n. 6, December 2003

# Conclusions

The objective of the research presented in this PhD thesis was to develop a novel, simple to fabricate, laser diode array to combine high power operation with high quality output beam and, therefore, achieve high brightness without the use of external lenses.

The array discussed here is a development of the index-guided Parabolic Bow-Tie Laser (PBTL) design developed in Bath and that was demonstrated to be effective for achieving relatively high output power with diffraction-limited output beam without using external optics. However, since the output power from an individual PBTL could not be increased indefinitely because the device would need to be impractically long to retain the modal properties required for high brightness, to scale up the output power and maintain the high beam quality (diffraction-limited), several PBTLs have been operated simultaneously as a coherently coupled array.

The design of Parabolic Bow-Tie Laser Arrays (PBTLAs) has been carried out in different stages focusing the attention on several aspects that are important when high power in a diffraction-limited beam is desired and that become particularly critical when the combination of multiple sources is considered.

**Beam Quality and Coherent (In-Phase Locked) Operation**

The first stage of the presented work has been to identify the key factors that limit the useful output power and that affect the quality of the laser emitted beam, such as COD, gain saturation, thermal rollover, filamentation and aging. In addition, methods and parameters to fully characterise the quality of the radiated beam have been described. Specifically, the laser beam characteristics have been compared to those of Gaussian Beams, and of the so called 'uniformly illuminated apertures', that are coherent sources.

In-phase coherence is an essential requirement for achieving high-power in a single lobe output beam which is diffraction-limited over the whole array aperture.

It was demonstrated that in general, for arrays of N identical elements each emitting a power P from an aperture W, the total emitting area is NW and the array power is NP. However, if the array is incoherent, the far-field divergence is the same as that of the individual emitter and therefore in this case the brightness of the array is the same as that of the individual emitter. On the other hand if the array is coherent the far-field divergence is N time smaller than that for the individual emitter, thus resulting in a brightness that is N times the brightness of the individual element. Therefore the advantage of achieving coherent (in-phase) coupling in array is resulting in the N-fold increase in brightness.

**In-Phase Locking in Index-Guided Parabolic Bow-Tie Laser Arrays**

In conventional arrays of index-guided stripe lasers the out-of-phase mode, characterised by a double-lobed far-field pattern, is typically favoured because of the better overlap between the optical field and the gain distribution and, therefore, because of the higher modal gain. More sophisticated array designs are, therefore, required to achieve in-phase operation and diffraction-limited output beam.

The goal of achieving high power and fundamental mode operation in index-guided arrays has been pursued here by exploiting the longitudinally non-uniform optical coupling between adjacent elements of bow-tie laser arrays.

The careful design of a Large Optical Cavity (LOC), Triple Quantum Well (TQW) semiconductor material for high power operation, used for device fabrication, was also essential, to provide simultaneously high optical output power with high COD level and the required lateral optical guiding strength.

Results from in-house fabricated laser arrays with different number of elements (N) and different geometries, namely Linear Bow-tie Laser Arrays (LBTLAs), Parabolic Bow-tie Laser Arrays (PBTLAs) and Stripe Laser Arrays (SLAs), have shown that output power significantly increase for increasing N but varies little with the geometry of the device for arrays with same N. Output powers up to of 2.8W/facet have been measured for 5-element arrays.

On the other hand, the quality of the output beam varies enormously depending on the cavity geometry. At threshold all devices operate in the out-of-phase mode; at higher currents SLAs still present a typical double-lobed far-field pattern whereas

both types of tapered laser arrays present essentially a single-lobed beam, indicating that quasi-in-phase-locking is achieved with the tapered optical cavity design.

Importantly, the narrowest far field divergence at FWHM has been measured from 5-element PBTLAs (here referred to as IG-5PBTLA0s). The measured value, 0.83deg at $I=20I_{th}$, is less than twice the estimated diffraction-limit angle, 0.56deg, and considerably narrower than that measured from an individual PBTL (2.8deg divergence at FWHM). As a consequence, the geometry of the cavity strongly influences also the achievable brightness. The highest value, $318MWcm^{-2}sr^{-1}$, achieved with PBTLAs at an injection current $I=20I_{th}$, is also higher that of the individual PBTL, for which the maximum brightness, is $137MWcm^{-2}sr^{-1}$. These results indicate that coherent coupling is significant in the operation of parabolic tapered laser arrays.

Results from CW measurements confirm the trends observed from the pulsed measurements although lower efficiency is achieved in these conditions possibly due to the non-optimal bonding and heat sinking conditions of the present measurement set up. In addition, it has been noticed that device heating can be detrimental for mode discrimination, resulting in the simultaneous oscillation of multiple array modes and, therefore, in a broadening of the far-field pattern. The maximum brightness achieved with under CW operation was an order of magnitude lower than that achieved under pulsed operation.

**Result Interpretation: Coupled-Mode Theory and Modal Gain**

Under the assumption that strong coupling occurs only at the device facets, the experimental results obtained from the arrays were interpreted using the Coupled-Mode Theory (CMT). The theoretical array mode far-field patterns were computed starting from the field of the individual emitter calculated self-consistently using the Hermite-Gauss Collocation Method (HGCM) model.

The observed change from out-of-phase to in-phase mode operation has been attributed to the effect of carriers on the refractive index and to the gain (hole-burning) distributions in the device. Near the output facets, where the elements merge in a single contact, inter-element coupling is stronger. In those regions, above threshold, the effective refractive index on the longitudinal axis of the individual

elements is larger, but the gain lower, than that of the surrounding off-axis regions. This situation (higher modal gain for lower order array modes) is conducive to fundamental (in-phase) array mode operation. However, it is important to note that in-phase operation was achieved with the combined effects of hole-burning, as discussed above, and the mode filtering effect of the central narrow stripe sections, as demonstrated by the fact that in-phase locking was never observed in SLAs.

Experimental results were confirmed by theoretical computations of the modal gain for all the array modes of PBTLAs for different gain profiles. Observing the far field intensity profiles calculated for all the array modes using the CMT, it has also been possible to explain that the PBTLAs far-field broadening at higher injection currents is due to the contribution of not only the fundamental but also the first few higher order array modes.

Scalability to a large number of elements was investigated both theoretically and experimentally reaching the conclusion that diffraction-limited operation is in principle possible in arrays of a large (N>5) number of elements. However, when hole-burning becomes significant, modal gain discrimination ceases to be effective.

**Robustness and Tolerance of the Optimised Design**

The effectiveness of the 5-element coherent coupled (in-phase locked) index-guided Parabolic Bow-Tie Laser Arrays described above was further investigated by fabricating arrays of five mutually incoherent (otherwise identical) Index-Guided PBTLs, (referred to as IG-5PBTLA10s), and Gain-Guided coupled PBTLAs (referred to as GG-5PBTLA0s). In both cases the achievable output power and the beam quality was significantly compromised.

The emitted beam from the 5PBTLA10s is a single-lobed stable beam but, as expected, is considerably broader than that measured from the corresponding in-phase-locked 5PBTLA0s. As a consequence the maximum achieved brightness, 98 $MWcm^{-2}sr^{-1}$ at $I=22I_{th}$, is also significantly lower than the one from the 5PBTLA0s.

On the other hand, in GG-5PBTLA0s the absence of a defined lateral mode confinement results in a spatial non-uniform carrier distribution and a non-uniform refractive index and gain profiles that promote unstable operation. This yields in

turn, to poor beam quality, the output beam being multi-peaked and showing evidence of filamentation, thus making such devices not suitable for high brightness operation.

One more aspect that has been considered is the effect of fabrication errors on the device performances. It has been noticed that IG-5PBTLA0s are very sensitive to variation in the device length, particularly to a shorter cleaving, that compromises the coherent coupling between array emitters and therefore in-phase locked operation.

# Future Work

The work described in this thesis has shown that Parabolic Bow-Tie Laser Arrays (PBTLAs) can produce high powers with good beam quality. However further work on tapered laser arrays is needed to investigate some important aspects that have not been considered, to improve device performances.

**Reliability and Thermal Measurements**

Thermal dissipation within high power semiconductor lasers affects output power, efficiency, reliability, spectral characteristics, near- and far-field distributions, and in commercial applications determines the extent to which that device can be utilised.

From a scientific point of view, the interest is in studying and understanding the reasons of gradual degradation of high power sources caused by longitudinal and lateral (across the facet) temperature gradient that eventually cause failure event.

The operational characteristics of the parabolic arrays presented in this PhD thesis have been measured with emphasis on the output beam quality. To have easy access to both output facets the in-house fabricated devices were mounted, also in-house, on a copper heat sink. Therefore the heat-sinking properties of the mount were not optimal and the devices were typically tested under pulsed operation, using a temperature controller.

To test the reliability of the PBTLAs, a new set of experiments would therefore include more detailed measurements at different temperatures and, for CW operation, also over a wider range of currents. Changes in the operational characteristics of high power, high brightness index-guided laser arrays due to temperature can be monitored by observing changes in the near- and far-field profiles. In addition measurement can be performed to study the spectral content of the arrays, aspect not investigated in this PhD thesis, and its changes with temperature. A comprehensive experimental study of AR and HR coatings applied to tapered lasers is also needed.

Importantly, the inherent thermal properties of the tapered arrays under high power operation can be investigated and changes in the temperature distribution at the laser facet can be monitored as the injected current is increased. This type of measurement is particularly important because variations of the thermal profile with consequent variations in the carrier distribution, results in a refractive index and gain profile that leads to early roll-over and filamentation, [1].

**Device Design**

The profile of the lateral gain is of paramount importance for selecting in-phase mode operation in index-guided laser arrays.

The parabolic laser arrays presented in this PhD thesis show high mode selectivity for a wide range of currents. However, at very high power level, due to the increase of spatial hole-burning mainly at the centre of the device facets, mode discrimination is compromised and the simultaneous oscillation of higher order modes is observed. The fabrication of individually addressable parabolic laser arrays to tailor the input current profile should be investigated to improve lateral mode control, especially at high injection current levels.

In addition, longitudinally segmented devices should be fabricated to investigate modulation properties and Q-switching. High energy Q-switch pulses are readily generated in broad are lasers, but the need of high spatial mode makes tapered lasers particularly attractive for such application. Specifically, Bow-Tie lasers showed to produce record energy pulses compared to conventional stripes, [2].

**Semiconductor Material Design**

Semiconductor lasers with small far-field divergence are of enormous importance when high brightness is desired. The array proposed in this thesis shows narrow lateral output beam obtained with careful optical cavity design, but more work is needed to further reduce the vertical beam divergence as the present elliptical far-field pattern results in low-efficiency light collection. To solve this problem a modified the laser epitaxial structure should be investigated. Some work on the semiconductor material structure can be carried out also to further increase the COD level. Adopting a large optical cavity structure was already useful to achieve a high

value for the power density before COD. However, aluminium-free materials, such as InGaAs-InGaAsP-InGaP, can be used to increase the maximum power density before failure, [3].

# References

[1] J. R. O'Callaghan, J. Houlihan, V. Voignier, G. Huyet, J. G. McInerney, B. Corbett, P. A. O'Brien, *'Focusing Properties of High Brightness Gain Tailored Broad-Area Semiconductor Lasers'*, IEEE Photon. Technol. Lett., 2002, vol. 14, n. 1, pp.9-11

[2] K. A. Williams, J. Sarma, I. H. White, R. V. Penty, I. Middlemast, T. Ryan, F. R. Laughton, J. S. Roberts, *'Q-switched bow-tie lasers for high energy picosecond pulse generation'*, Electron. Lett., 1994, vol. 30, n. 4, pp. 320-321

[3] A. Al-Muhanna, L. Mawst, D. Botez, D. Garbuzov, R. Martinelli, J. Connoly, *'High Power (>10W) continuous-wave operation from 100μm-aperture 0.97μm-emitting Al-free diode lasers'*, Appl. Phys. Lett., 1998, vol. 73, n. 9, pp.1182-1184

# Appendix A

## *Semiconductor Lasers: Operating Parameters*

A typical ridge waveguide semiconductor laser is shown in Fig. A.1. It is fabricated from a multilayer semiconductor material in which doping types and concentrations differ from layer to layer such that a p-n junction is formed at the active region, where injected free carriers recombine, [A-1]. The active region can be made either of a single layer of gain medium – this type of material is referred to as bulk material, or of a series of layers of different alloys containing one or more very thin layers of gain medium, with additional barrier layers, also of a different alloy – this type of material is referred to as Quantum Well (QW) material. Quantum Well type materials, are more often used, especially for high-power lasers, because of the advantages they offer, such as low threshold currents, small spectral linewidth or wavelength tunability, [A-1]. The particularly small size and position of the QWs layers ensures that the device has a well defined vertical profile resulting in a controlled output beam shape in the vertical direction.

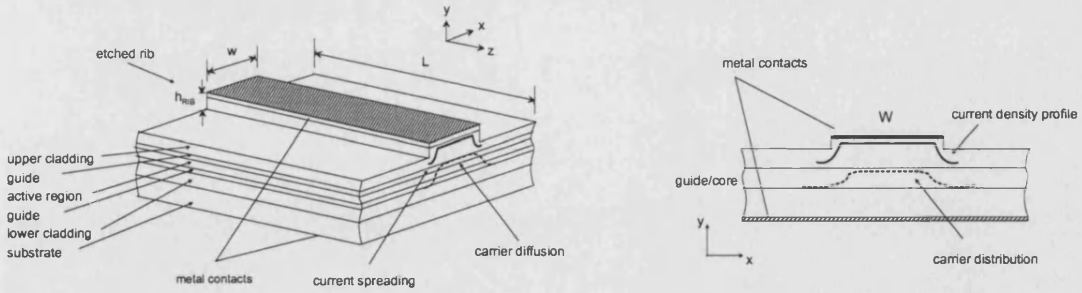


**Fig. A.1: Schematic of a ridge waveguide laser. a) 3D structure with the main parameters of interest and the multilayer structure; b) front view with details of the current density profile and the carrier distribution.**

The vertical (along y) multilayer structure is characterised by a specific refractive index profile that provides confinement of the light in the active region.

The rib etched in the cladding layer has the twofold purpose of reducing current spreading and producing a lateral effective refractive index step necessary to provide weak lateral (along x) optical guiding. The strength of the lateral optical guiding depends on the material epitaxy and on the rib height, $h_{RIB}$. The optical field produced by ridge lasers is therefore confined along both the x and y directions.

## A.1 Threshold Conditions and Lasing

When the current passes through the metal contact placed on the top of the rib, Fig. A.1, carriers are injected into the active region. All the electrons and the holes here accumulated, radiatively recombine releasing energy.

The gain $g_{mat}(x)$ in the device, the local or material gain, depends on the carrier density distribution N(x) in the active layer and on the material characteristics and is expressed as:

$$g_{mat}(x) = A(N(x) - N_{tr}) \tag{A.1}$$

where A is the gain constant and $N_{tr}$ the carrier density at transparency, which is when the gain in the laser compensates the material intrinsic loss $\alpha_i$, also called distributed losses. The gain g(x) responsible for the amplification of each optical mode along the stripe, thus called modal gain, is given by, [A-2]:

$$g(x) = \Gamma_{QW} g_{mat}(x) \tag{A.2}$$

where $\Gamma_{QW}$ is the modal confinement factor, expressing the fraction of mode intensity confined in the active layer, [A-3], [A-4]. Lasing occurs when the gain provided to the optical mode compensates the resonator losses that includes $\alpha_i$ and mirror losses $\alpha_m$, [A-3], [A-4]. In order to experience such gain, the so-called 'population inversion', corresponding to a carrier density larger than the transparency value $N_{tr}$, has to be reached, [A-1]. The minimum gain where the devices start lasing is called threshold gain, $g_{th}$, and is defined as:

$$g_{th} = \alpha_i + \alpha_m \tag{A.3}$$

The current required to increase the modal gain up to the level of the resonator losses is defined as threshold current $I_{th}$. The total distributed losses per unit length $\alpha_i$ are defined as, [A-3], [A-4]:

$$\alpha_i = \alpha_{FCc} + \alpha_S + \alpha_C \tag{A.4}$$

where $\alpha_S$ are the scattering losses and $\alpha_C$ the losses related to radiation beyond the cladding layers; the term $\alpha_{FCc}$ expresses the contribution of the free-carrier absorption losses $\alpha_{FC}$ and is defined as:

$$\alpha_{FCc} = \Gamma_{QW}\alpha_{FC} + \sum_t \Gamma_t\alpha_{FC} \tag{A.5}$$

where $\Gamma_{QW}\alpha_{FC}$ and $\Gamma_t\alpha_{FC}$ are, respectively, its ratios in the active layer and in the adjacent t-th , with $\Gamma_t$ their confinement factors, doped layers. Since the mirror losses $\alpha_m$ are given by:

$$\alpha_m = \frac{1}{2L}\ln\left(\frac{1}{R_1R_2}\right) \tag{A.6}$$

where $R_1$ and $R_2$ are the reflectivity of the two facets, then Equation A.3 becomes:

$$g_{th} = \alpha_i + \frac{1}{2L}\ln\left(\frac{1}{R_1R_2}\right) \tag{A.7}$$

By substituting equation (A.1) and equation (A.3) in equation (A.7) it follows:

$$\Gamma_{QW}A(N(x) - N_{tr}) = \alpha_i + \frac{1}{2L}\ln\left(\frac{1}{R_1R_2}\right) \tag{A.8}$$

Therefore, the threshold current is composed of two contributions: one required to pump the active region to optical transparency, and the other required to overcome the resonator losses. Below threshold, between transparency and threshold, the laser emits spontaneous emission similarly to typical Light-Emitting Diodes (LEDs). Above threshold the carrier density clamps at the threshold value $N_{th}$. Also the spontaneous emission is clamped and at any further increase of the current the charges in excess recombine radiatively. The energy released by stimulated emission coherently contributes to the optical intensity that increases proportionally to $(I-I_{th})$

Defining the differential internal quantum efficiency $\eta_i$ as the probability that an injected carrier recombines within the active region, the rate of photons $P_{stim}$ produced by stimulated emission is:

$$P_{stim} = \eta_i (I - I_{th}) \frac{h}{q\hat{\nu}} \tag{A.9}$$

where $q=1.6022 \cdot 10^{-19}$ C is the electronic charge, $h=6.626 \cdot 10^{-34}$ $Ws^2$ is Planck's constant and $\hat{\nu}$ the laser (peak) emitting frequency. Since there are losses within the cavity, only a portion of the photons generated by stimulated emission will actually contribute to the output power. Considering that the stimulated emission is expressed by the gain at threshold $g_{th}$ and assuming that the mirror losses $\alpha_m$ correspond to the photons having the chance to leave the cavity, the total emitted power P can be written as, [A-2], [A-5]:

$$P = \frac{\alpha_m}{g_{th}} P_{stim} \tag{A.10}$$

By substitution of equation (A.3) and equation (A.9) in equation (A.10) it follows:

$$P = \frac{\alpha_m}{\alpha_m + \alpha_i} \eta_i (I - I_{th}) P_{stim} \tag{A.11}$$

yielding to:

$$P = \eta_e (I - I_{th}) \frac{h}{q\hat{\nu}} \tag{A.12}$$

where:

$$\eta_e = \eta_i \frac{\alpha_m}{\alpha_m + \alpha_i} \tag{A.13}$$

is the differential external quantum efficiency and can be estimated, above threshold, from the slope of the light-current characteristic, [A-2].

Important electro-optic properties of laser diodes are determined also by measuring the so called current-voltage (I-V) characteristics of the devices. As mentioned previously, the various heterostructure layers that make up the laser are comprised of a core p-n junction diode surrounded by cladding layers to provide charge carrier confinement and optical waveguiding. The laser I-V characteristic is dominated by a p-n junction diode characteristic in series with resistors, capacitances, and inductances that model the electrical conductivities of the heterostructure and substrate layers. However, the voltage across high power lasers can be simplified to the form:

$$V = V_j + R_s I \tag{A.14}$$

where $V_j$ is the junction voltage and $R_S$ is the series resistance.

The junction voltage is usually approximated by a constant slightly larger that the energy gap $E_g$ of the active region, $E_g/q$. For the lasers of interest in this PhD thesis, $V_j \sim 0.88V$. The series resistance can be extracted from the slope of the I-V curve. Values of $R_S$ depend mainly on the material multilayer structure but also on current spreading and laser contact size, [A-2], [A-7].

# References

[A-1] E. Kapon, *Semiconductor Lasers I*, Academic Press (1999).

[A-2] E. Kapon, *Semiconductor Lasers II*, Academic Press (1999).

[A-3] H. C. Casey, Jr., M. B. Panish, *Heterostructure Lasers, Part A: Fundamental Principles*, ed. by H. C. Casey, Jr. and M. B. Panish, Academic Press, London, 1978.

[A-4] H. C. Casey, Jr., M .B. Panish, *Heterostructure Lasers, Part B: Materials and Operating Characteristics*, ed. by H. C. Casey, Jr. and M. B. Panish Academic Press, London, 1978.

[A-5] K. Petermann, *Laser Diode Modulation and Noise*, Kluwer Academic Publishers, KTK Scientific Publishers, Tokyo (1988).

[A-6] G. H. B.Thompson, *Physics of Semiconductor Laser Devices*, ed. G. H. B. Thompson, John Wiley and Sons (1980).

[A-7] R. F. Reyna, A. Marti, C. Algora, J. C. Maroto, G. L. Araujo, *'Influence of Size Factors in the Electroluminescent Emission of Large Area GaAs IRED's'*, IEEE Trans. on Electron Dev., vol. 44, n. 7, 1997, pp. 1174-1176.

# Appendix B

# *Modelling Tapered Structures*

Considerable attention has been given in literature to developing methods for the analysis of tapered laser devices, Fig. B.1: due the longitudinal (z) non-uniformity of the wave-guiding structure propagation in tapered lasers cannot, in fact, in general be solved as an eigenvalue problem, [B-1], and simple analytic solutions are not possible.

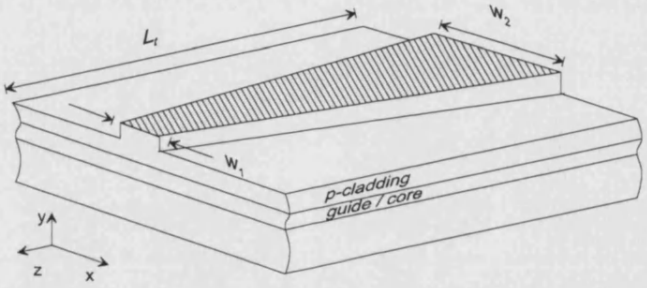


**Fig. B.1: Schematic of a taper geometry laser, with the relevant parameters of interest.**

The Beam Propagation Method (BMP), [B-2], and the Maxell-Bloch formalism, [B-3], are perhaps the most commonly used for the analysis of flared gain-guided laser amplifiers. However, another frequently used approach is represented by the function expansion method, [B-4], [B-5].

Models based on the function expansion methods have been used to analyse optical field propagation in the tapered structure lasers of interest in this work.

## B.1 Solving for the Optical Field: Function Expansion Methods

The structure considered here is assumed to have a 2D field distribution where the vertical (y) variation has separately been accounted for by using the Effective Dielectric Constant (EDC) method, [B-4]. Further, since the structure, by means of the tapered etched rib, is weakly guiding in the lateral (x) direction, the optical

propagation can be accurately solved using the scalar analysis, [B-1]. Thus, the propagating field can satisfactorily be represented by the (harmonic time-dependent) dominant field component $F(x,z)$, satisfying the Helmoltz equation:

$$\frac{\partial^2 F(x,z)}{\partial z^2} + \frac{\partial^2 F(x,z)}{\partial x^2} + k_o^2 \varepsilon(x,z,N) F(x,z) = 0 \qquad \text{(B.1)}$$

where $\varepsilon(x,z,N) = n^2(x,z,N)$ is the complex dielectric profile distribution (with $n(x,z,N)$ the corresponding refractive index profile) that takes into account the non-linear interaction between photons and injected carriers (N(x,z) is the carrier density distribution in the active layer). This is a very important complexity that needs to be addressed when modelling active semiconductor optical sources.

However, equation (B.1) must be self-consistently solved conjunction with the non-linear, diffusion-dominated equation describing the carrier diffusion, [B-6]:

$$D_c \frac{\partial^2 N(x,z)}{\partial x^2} - B_r [N(x,z) + N_o] N(x,z) - \gamma_A N^3(x,z) - g(x,z) P_d(x,z) + \frac{J(x,z)}{q d_{QW}} = 0 \qquad \text{(B.2)}$$

where $D_c$ is the (constant) diffusion coefficient, $B_r$ is the spontaneous emission recombination coefficient, $N_0$ is the doping density in the active layer and $\gamma_A$ is the auger recombination coefficient; $g(x,z) = \Gamma_{QW} A(N(x,z) - N_{tr})$ is the modal gain, with A the gain coefficient and $N_{tr}$ the transparency carrier density; $P_d(x,z) \propto |F(x,z)|^2$ is the active (average) photon density distribution in the active layer, $J(x,z)$ is the injection current density and q is the magnitude of the electronic charge.

The function expansion method is applied so that the solution to both equations (B.1) and (B.2) can be expressed in the following form:

$$F(x,z) = \sum_m a_m(z) \varphi_m(x) \qquad \text{(B.3)}$$

$$N(x,z) = \sum_n b_n(z)\phi_n(x) \qquad (B.4)$$

where $a_m(z)$ and $b_n(z)$ represents the z-dependent expansion coefficients whereas $\{\varphi_m(x)\}$ and $\{\phi_n(x)\}$ are (complete) sets of orthogonal functions, [B-7].

The choice of the basis expansion set dictated by the specific problem to be solved: an effective selection must in fact take into account the complexity of the system as well as the accuracy of the results.

## B.2 The Step Transition Method

For a fast and simple, yet quite accurate analysis of the passive tapered waveguides, a model based on the Step Transition Method (STM), [B-8], [B-9], and the Local Mode Expansion (LME) method, [B-10], was developed. Following this method the taper is representated as a series of piecewise constant unform slab waveguide sections of increasing width, Fig. B.2, and the propagating field is described by the set of (local) modes of each section.

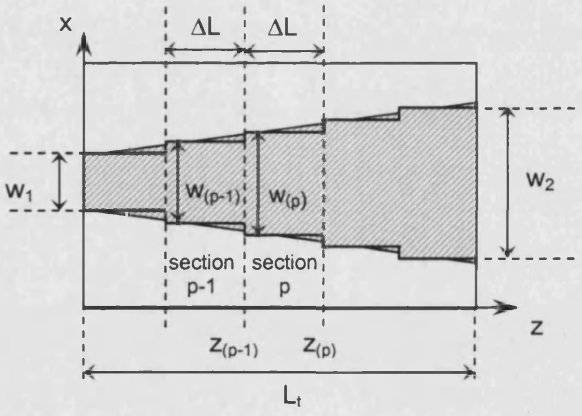


**Fig. B.2: Schematic of the step-waveguide representation of the dielectric taper following the STM. The width and length of the p-th waveguide section are $w_{(p)}$ and $\Delta L_p = z_{(p)} - z_{(p-1)}$.**

The structure is solved for an initial value problem by specifying the field profile at the narrow input waveguide section of width $w_1$. The analysis is simplified by neglecting the continuum, radiation modes, [B-11], and the reflection at the steps,

[B-9]: under the assumption of adiabatic transition its validity is not, in fact, compromised.

Following the STM, equation (B.1) is applied to each piece-wise constant region of the 'stepped' taper, Fig. 2. The total propagating field in such each section is then expanded in terms of the modes supported by that waveguide. In each section the solutions, assumed to propagate predominantly along the longitudinal (z) direction with the transverse dependence of the field invariant with z, [B-12]. The refractive index distribution n(x,z,N) in equation (B.2), now independent of z and N, is given by:

$$n(x,z,N) = n(x) = \begin{cases} n_1 & , \quad |x| \le \dfrac{w_p}{2} \\ n_2 & , \quad |x| > \dfrac{w_p}{2} \end{cases} \tag{B.5}$$

It is advantageous to write the solution as:

$$F(x.z) = F_m(x,z) = f_m(x)e^{\pm i\beta_m z} \tag{B.6}$$

with $f_m(x)$ and $\beta_m$ being the eigenmodes and the corresponding eigenvalues that occur with proper waveguides, [B-12]. Thus the mode-solutions consist of a transverse distribution of the field, $f_m(x)$, that remains unchanged along the longitudinal direction, z, and has propagation constant $\beta_m$.

The waveguide mode-functions have the mathematical property of forming a complete set of mutually orthogonal functions, [B-7], and are obtained for boundary conditions associated with the differential equation (B.3), such that the field decays to zero at infinity along the transverse (x) axis, i.e.:

$$|f_m(x)| \to 0 \text{ for } |x| \to \infty \tag{B.7}$$

### B.2.1 Propagation along the Taper

The amplitudes of the modes in each section and the propagation of the optical field along the device are analysed by using the LME method and matching the total fields at the interface between adjacent sections. The total field distribution $F_{(p)}(x,z)$ at the end of section p, superposition of the normal bound modes solutions for that section, is then written as:

$$F_{(p)}(x,z)=\sum_{m=1}^{M_{(p)}} c_{(p),m} f_{(p),m}(x)\exp\{-i\beta_{(p),m}\Delta L_p\} \tag{B.8}$$

where $\Delta L_p = z_{(p)} - z_{(p-1)}$ is the length of the p-th section and $M_{(p)}$ is the number of guided modes supported by section p, with $p = 0,1,....,M_{tot}$; $f_{(p),m}(x)$ represents the bound mode of order 1 and $\beta_{(p),m}$ the corresponding propagation constant for the section p; the (constant) coupling coefficients $c_{(p),m}$, corresponding to the expansion coefficients $a_m(z)$ in equation (B.5), are calculated as follows:

$$c_{(p),m} = \int_{-\infty}^{\infty} F_{(p-1)}(x, z_{(p-1)}) f_{(p),m}(x)dx \tag{B.9}$$

The total field at the end section corresponds to the device propagating field at the output facet, i.e. the near-field distribution.

## B.3 Hermite-Gauss Collocation Method (HGCM)

For a more rigorous analysis of semiconductor active optical sources and for the modelling of the non-linear optical field-carriers interaction, a more sophisticated quasi-analytic based on the Hermit-Gauss (HG) expansion method using the Collocation numerical Method (CM) has been used. This method, developed in the past and referred to as HGCM, [B-13]-[B-15], has been demonstrated to be suitable for the self-consistent field analysis of tapered lasers, [B-16]. In this method the basis

functions $\varphi_m(x)$ and $\phi_n(x)$ in equations (B.3) and (B.4) are the Hermite-Gauss functions $f_m(x)$ having the form:

$$f_m(x) = C_m H_m(x/w_0)e^{(-x^2/2w_0^2)} \tag{B.10}$$

where $C_m$ is a normalisation constant, $H_m(x/w)$ is the Hermite polynomial of order m, and $w_0$ is a constant parameter, referred to as width or waist parameter, [B-4]. Thus the yet unknown solutions to equations (B.1) and (B.2) can be written in the form:

$$F(x,z) = \sum_{m=0}^{M} A_m(z) f_m(x) \tag{B.11}$$

$$N(x,z) = \sum_{n=0}^{N} B_n(z) f_n(x) \tag{B.12}$$

where $A_m(z)$ and $B_m(z)$, corresponding to the expansion coefficients $a_m(z)$ and $b_m(z)$ in equation (B.3) and (B.4) respectively, are the *z*-dependent, complex expansion coefficients. The accuracy of the expansion in equations (B.11) and (B.12) is limited by the number of expansion terms, M and N. In fact, for the idealised case $M = \infty$ and $N = \infty$ provide the exact series expansion; $M < \infty$ and $N < \infty$ are used in practical situation but are an approximate representation.

To evaluate the expansion coefficients $A_m(z)$ and $B_m(z)$, equations (B.11) and (B.12) are substituted into the wave equation (B.1) and the linearised carrier diffusion equation (B.2). Using the properties of the HG basis functions, a set of ordinary differential equations in the unknown expansion coefficients, $A_m(z)$ and $B_m(z)$ is obtained. The solution to such set of equation is entirely numerical and can be obtained by using the Collocation Method (CM), [B-13]-[B-18].

# References

[B-1] A. F. Milton, W. K. Burns, *Guided Wave-Optoelectronics*, ed. by T. Tamir, Springer-Verlag, New York, 1990

[B-2] R. J. Lang, A. Hardy, R. Parke, D. Mehuys, S. O'Brien, J. Major, D. F. Welch, *'Numerical Analysis of Flared Semiconductor Laser Amplifiers'*, IEEE J. Quantum Electron., vol. 29, 1993, pp. 2244-2051

[B-3] P. K. Jacobsen, J. V. Moloney, A. C. Newell, R. A. Indik, *'Space-Time Dynamics for Wide-Gain-Section Lasers'*, Phys. Rew. A., vol. 45, n. 11, 1992, pp. 8129-8137

[B-4] D. Marcuse, *Light Transmission Optics* ($2^{nd}$ Ed.), Van Nostrand Reinhold, New York, 1982

[B-5] G. Bendelli, K. Komori, S. Arai, Y. Suematsu, *'A New Structure for High-Power TW-SLA'*, IEEE Photon. Technol. Lett., vol. 3, 1991, pp. 42-45

[B-6] G. P. Aggrawal, N. K. Dutta, *Long-Wavelength Semiconductor Lasers*, Van Nostrand Reinhold, 1986

[B-7] H. Kogelnik, *'Theory of Optical Waveguides'*, in *Guided Wave-Optoelectronics*, ed. by T. Tamir, New York, Springer-Verlag (1990).

[B-8] D. Marcuse, *Radiation loss of tapered dielectric slab waveguides*, Bell Systems Technical Journal, 1970, vol. 49, pp. 273-290

[B-9] A. F. Milton, W. K. Burns, *Mode Coupling in Optical Waveguide Horns*, IEEE J. Quantum Electronics, vol. QE-13, 1997, pp. 828-835

[B-10] T. Rozzi, M. Mongiardo, *Open Dielectric Waveguides*, IEE Electromagnetic Series, 1997

[B-11] I. Middlemast, J. Sarma, P. S. Spencer, *Characteristics of Tapered Rib-Waveguides for High-Power Semiconductor Optical Sources*, IEE Proc. Optoelectron., vol. 144, n. 1, 1997, pp. 8-13

[B-12] H. C. Casey, Jr., M. B. Panish, *Heterostructure Lasers, Part A: Materials and Operating Characteristics*, ed. by H. C. Casey, Jr. and M. B. Panish Academic Press, London, 1978.

[B-13] F. Causa, *'Hermite-Gauss Functions in the Analysis of a Category of Semiconductor Optical Devices'*, PhD Thesis, University of Bath, 1998.

[B-14] F. Causa, J. Sarma, *'A Quasi-Analytic Model for Longitudinally Non-Uniform Semiconductor Optical Sources'*, Optics Communications, vol. 183, 2000, pp. 149-157

[B-15] F. Causa, J. Sarma, *'A Versatile Method for Analysing Paraxial Optical Propagation in Dielectric Structures'*, Journal of Lightwave Technology, vol. 18, n. 10, 2000, pp. 1445-1452

[B-16] F. Causa, Model implemented in Fortran 77

[B-17] F. Causa, J. Sarma, M. Milani, 'Hermite-Gauss Function in the analysis of *Weakly Non-Uniform Semiconductor Optical Devices'*, Proceedings of the International Conference in Fibre Optics and Photonics, Madras, India, 1996, pp. 127-132

[B-18] F. Causa, J. Sarma, M. Milani, *'Hermite-Gauss Functions in the Analysis of a Category of Optical Devices'*, Il Nuovo Cimento, vol. 20, n. 3, 1998, pp. 289-320

# Appendix C

## *Optimisation of the Bow-Tie Laser Design*

This Appendix describes the detailed study carried out, and the methodology used, to optimise the geometry of the Bow-Tie Lasers (BTLs), Fig. C.1, subsequently used to develop the tapered arrays described in this PhD thesis. For the present analysis three different taper profiles (linear, parabolic and exponential) have been considered.

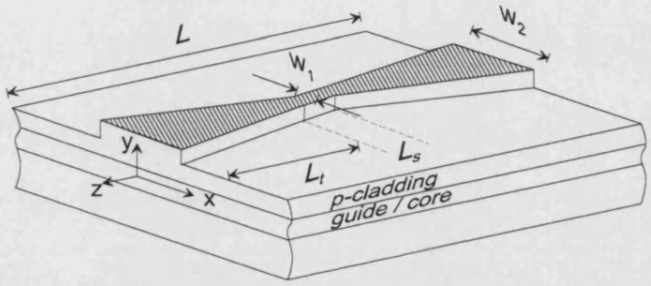


**Fig. C.1: Schematic of a linear bow-tie laser with definition of the relevant parameters.**

The passive model based on the STM and LME methods, [Appendix B], has been chosen for the optimisation, to study the optical propagation in the dielectric tapers, because it produces a fast computational procedure. As already explained the above model is valid under the assumption of passive dielectric structures; however it can be considered reasonably accurate to describe the operation of an active structure (laser) at threshold. To prove that device design optimisation computed with the passive model is reliable, the computed results have been compared with corresponding data from other available models. The accuracy of the passive model with respect to the number and/or length of the longitudinal sections chosen to approximate the taper profile, [Appendix B], has also been addressed, [C-1].

## C.1 Optimising Taper Design

In the ideal case the desired narrow output beam would be achieved by restricting the number of modes propagating in the structure to just the fundamental mode, [C-2]. However, for high-power operation the above condition is restrictive and would enhance the risk of COD. Therefore, the output width of the tapered structures of interest is broad, so that the corresponding local waveguide section is typically multimoded. The optimisation procedure was aimed to design a device geometry that could yield to the narrowest possible, single-lobed far-field intensity profile. The longitudinal variation of the taper width for the different profiles is described by:

$$w_{Lin}(z) = w_1 + z\frac{(w_2 - w_1)}{L_t} \quad \text{, linear taper} \tag{C.1}$$

$$w_{Par}(z) = \left[ w_1^2 + z\frac{(w_2^2 - w_1^2)}{L_t} \right]^{1/2} \quad \text{, parabolic taper} \tag{C.2}$$

$$w_{Exp}(z) = w_1 \exp\left[ z\frac{1}{L_t} \ln\left( \frac{w_2}{w_1} \right) \right] \quad \text{, exponential taper} \tag{C.3}$$

A set of calculations varying first the length $L_t$ and consequently the output width $w_2$ of the tapered sections has been performed to study the effect of the taper geometry on the device performance, [C-1]. The parameter of interest in this case was the lateral far-field divergence at Full Width at Half Maximum (FWHM), $\theta_x$. The vertical divergence, $\theta_y$, was not considered in the optimisation process, as it is determined by the semiconductor multilayer structure and does not depend on the device geometry. The range of variation of both, the length $L_t$ and the output width $w_2$, was dictated by the contradictory requirements to achieve high power with high brightness. The device output width had to be sufficiently wide to reduce the risk of COD, but at the same time the overall device dimensions had to be compact not only for mode discrimination, but also to favour integration, increase mechanical strength and reduce the occurrence of instability. The effective refractive index step was fixed to be, at first instance, $\Delta n_{eff} \sim 0.007$. Due to alignment errors in the ultra-violet

photolithography fabrication process, a minimum of 3μm for the rib widths is generally advisable. This value was therefore set for the input section $w_1$ of all the analysed structures. Computed results for Linear Bow-Tie Lasers (LBTLs), Parabolic Bow-Tie Lasers (PBTLs) and Exponential Bow-Tie Lasers (EBTLs) are presented in Fig. C.2.

It can be noticed, Fig. C.2 a), that for lengths above 500μm, the curves for the different profiles converge to the same value, indicating that the devices become essentially adiabatic and the performance is independent on the specific profile. However, from the trend of both, Fig. C.2 a) and Fig. C.2 b), it can be observed that the smallest values for $\theta_x$ are obtained always with the parabolic geometry, with the minimum, $\theta_x = 2.8\,\text{deg}$, for a length 500μm and an output width of approximately 20μm. This value for $\theta_x$ corresponds to the diffraction-limit angle from such aperture.

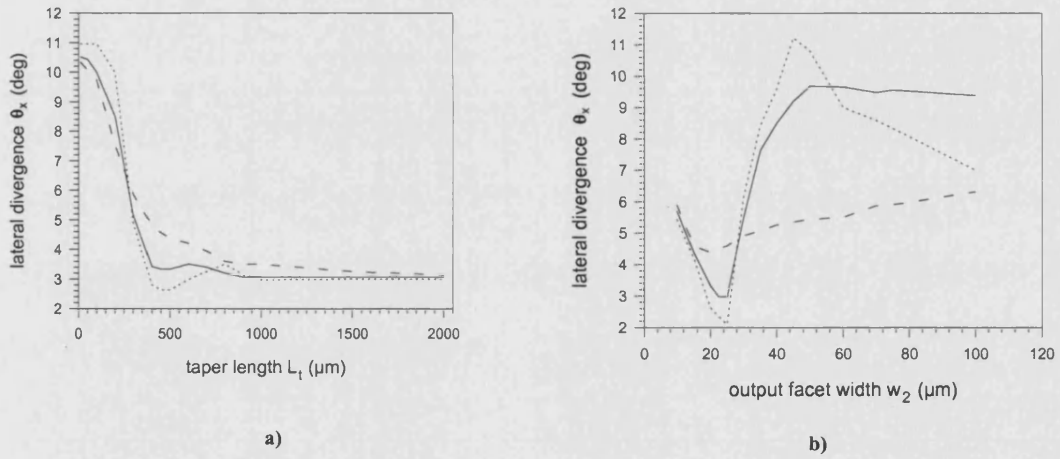


**Fig. C.2: Computed lateral far-field divergence $\theta_x$ for the LBTL (solid line), the PBTL (dotted line) and the EBTL (dash-dotted line) as a function of the a) length $L_t$ when $L_s$=50μm, $w_2$=20μm and b) output width $w_2$ when $L_t$=500μm. For all the devices $w_1$=3μm and $\Delta n_{eff}$=0.007.**

The reason for the parabolic taper to show a better performance, resides in the fact that, compared to the linear and exponential tapers, the more gradual increase of the rib width in the region closer to the output than in that close to the input, reduces the amount of coupling to higher order modes. The variation of the rib width in the region closer to the input of the tapers is, in fact, less critical because the rib width itself reduces the number of modes that the structure can support.

To complete the device optimisation the effect of lateral effective refractive index step $\Delta n_{eff}$ on the far-field divergence at FWHM was also analysed. An effective lateral index step, and therefore an explicit weak lateral guiding are, in fact, required not only to assure single-mode operation at the input section for the taper; but also to provide the devices with more robustness, i.e. lateral mode control and stability.

The computed results for the three taper profiles, Fig. C.3, confirm that the parabolic taper is best suited for high brightness applications since the FWHM of the lateral far field is always the smallest, [C-1]. The presented results also show that the far-field divergence at FWHM increases for almost negligible $\Delta n_{eff}$ (free-space diffraction) and for large $\Delta n_{eff}$ (increased coupling to higher order modes). The optimum value seems to be in the region $\Delta n_{eff} = 0.007$.

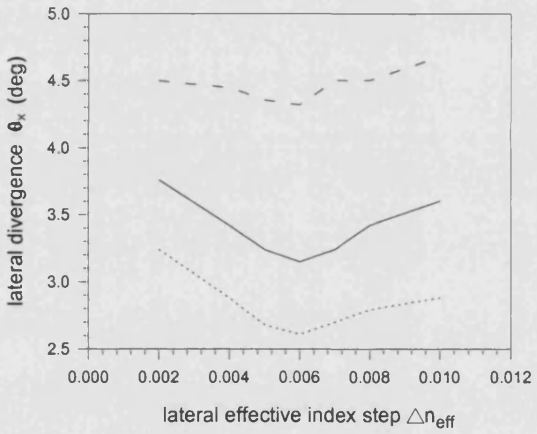


**Fig. C.3: Computed lateral far-field divergence $\theta_x$ for linear (solid line), parabolic (dotted line) and exponential (dash-dotted line) BTLs as a function of $\Delta n_{eff}$. For all the devices $L_s$=50μm, $w_1$=3μm, $w_2$=20μm and $L_t$=500μm.**

It must be specified that similar calculations to those described in this Section showed that also PBTL characterised by a taper length $L_t$=1mm and an output width $w_2$=30μm, with a 1.92deg far-field divergence at FWMH, could be suitable for high power high brightness operation. Ideally, due to the larger output width (more effective to overcome COD) and to the narrower emitted beam, such devices should also demonstrate a better performance than the 'smaller' PBTLs described before.

The choice of the latter geometry for the development of the taper arrays was dictated by the fact that lasers with bigger size would affect the compactness of the final array structure, and would make it more susceptible to mechanical stress and thermal effects.

## C.2 'Optimised' Device Geometry: Details

The theoretical results presented in the previous section indicate that the Parabolic Bow-Tie Laser with input width $w_1 = 3\mu m$, output width $w_2 = 20\mu m$, length $L_t = 500\mu m$ and effective index step $\Delta n_{eff} = 0.007$ is the 'optimum design' to achieve a diffraction-limited radiated beam. To better understand the characteristic of such device it is useful to analyse more in details its characteristics. Graphs in Fig. C.4 show the near-field intensity profiles and relative phase for a PBTL. Profiles for a LBTL and an EBTL are presented for comparison. It can be noticed that the parabolic structure shows the widest near-field intensity distribution, resulting in reduced power density at the facet, with an almost constant phase across the region where the intensity is significant, which implies nearly coherent operation. On the other hand, the linear and the exponential bow-ties present narrower near-field intensity profiles, for the exponential one even sharper, and a bigger phase variation.

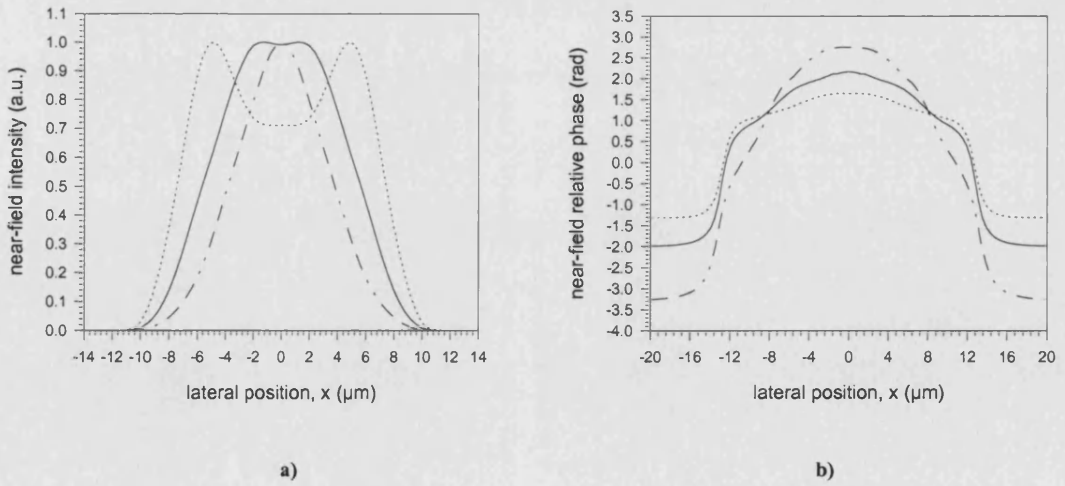


**Fig. C.4: Computed a) near-field intensity profiles and b) near-field relative phase for the 'optimised' PBTL (dotted line). Results for the linear (solid line), and exponential (dash-dotted line) BTLs are shown for comparison. For all the devices $L_s$=50μm, $w_1$=3μm, $w_2$=20μm and $L_t$=500μm and $\Delta n_{eff}$ =0.007.**

The reason of these differences can be understood observing the plots in Fig. C.5, that show, respectively, the intensity of the fundamental and of the first higher order mode along the taper cavity. The mode intensities correspond to the modulus squared of the corresponding coupling coefficients, [Appendix B], referred to as $|c_1(z)|^2$ and $|c_2(z)|^2$ respectively. The parabolic device shows an increasing proportion of the power in the fundamental mode at the end of the device, while the intensity of the first higher mode decreases. LBTLs show a quite constantly varying trend; EBTLs, on the other hand, present a decreasing proportion of the power in the fundamental mode as it propagates along the device; the intensity of the first higher mode increases.

Hence it has been explained, at least theoretically, at this point, why the parabolic profile seems to be the most suitable to achieve high power operation in a narrow far-field, and why the exponential profile seems then to be the least.

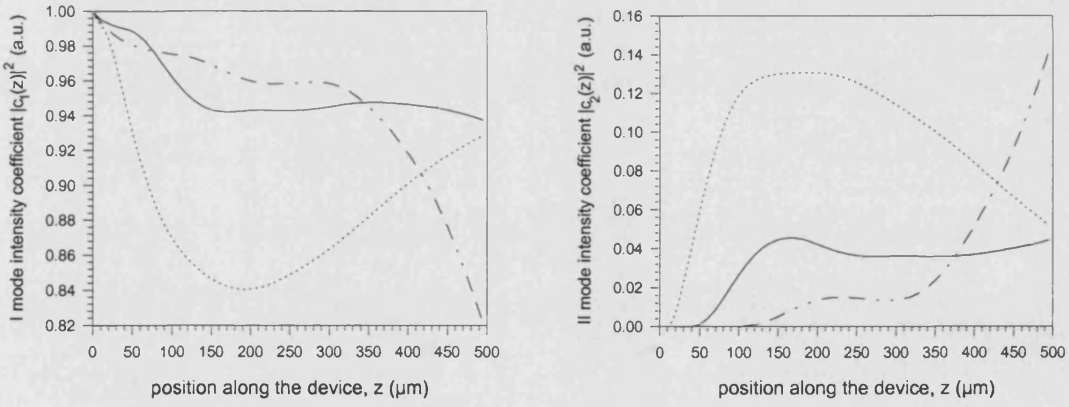


a) b)

**Fig. C.5: Computed a) fundamental and b) first higher order mode intensity along the cavity for the 'optimised' parabolic taper (dotted line). Results for the LBTL (solid line), and the EBTL (dash-dotted line) are shown for comparison. For all the devices $L_s$=50μm, $w_1$=3μm, $w_2$=20μm and $L_t$=500μm and $\Delta n_{eff}$ =0.007.**

The above statement is confirmed also by observing, in the graph of Fig. C.6, the corresponding far-field patterns: the linear and the parabolic tapers show similar profiles although the parabolic far-field is narrower with a lateral divergence, at

FWHM, $\theta_x = 2.8\,\text{deg}$; the exponential taper shows a definitely worse performance, and its lateral divergence is $\theta_x = 4.32\,\text{deg}$.

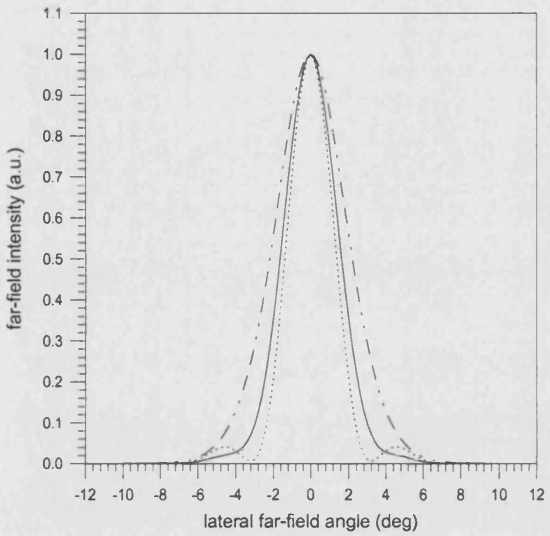


**Fig. C.6: Computed far-field intensity profiles for the 'optimised' PBTL (dotted line). Results for the linear (solid line), and exponential (dash-dotted line) BTLs are shown for comparison. For all the devices $L_s$=50μm, $w_1$=3μm, $w_2$=20μm and $L_t$=500μm and $\Delta n_{eff}$ =0.007.**

### C.2.1 Tolerance

An important aspect to be considered in stage of device design is the device 'sensitivity' to errors due to the mask resolution or those occurring during the fabrication process (etching or cleaving process). The device tolerance has therefore been studied, by analysing the effect, on the device performance, of small variations in $w_1\,(\pm 0.2\mu\text{m})$, $w_2\,(\pm 0.2\mu\text{m})$, $L_t\,(\pm 10\mu\text{m})$ and $\Delta n_{eff}\,(\pm 0.002)$.with respect to the optimised structure. The analysis of the various cases shows that the maximum increase in FWHM far field divergence is $< 0.2°$, [C-1], considered to be negligible for all practical situations. It has to be mentioned that the parabolic bow-tie geometry demonstrated to be a robust design also for larger variations of the size of the optimised structure. Up to 50μm shorter or longer cleaving (corresponding to a smaller or larger output facet width respectively) would not, in fact, compromise the adiabaticity of the structure that would still support single-mode operation and therefore emit in a diffraction-limited beam.

## C.3 Reliability of the STM Model

To test the reliability of the analytic model used for optimising the taper geometry, theoretical results have been compared with those obtained with other models previously employed for passive structures, [C-1], and with the HGCM model, [Appendix B].

The first of the above mentioned models, also, is based on the (bound) Local Mode Expansion (LME) method, [C-3], [C-4], and the Step Transition Method (STM), [C-5], [C-2]. However, the eigenvalue problem in each longitudinal section is solved numerically, using the Cascaded Matrix Method (CMM), [C-6]. This model will be referred to as CMM model. The near-field intensity profiles computed with the three different models for a linear taper, are compared in Fig. C.7.

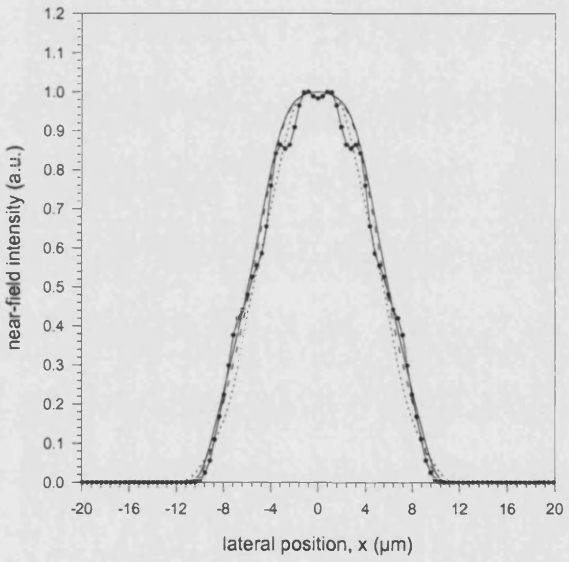


**Fig. C.7: Near-field intensity profile computed for a LBTL with the analytic model (solid line), the CMM model (dashed line), and the HGCM model for passive (dotted line) and active (solid line with circles) structures. [$L_s$=50μm, $w_1$=3μm $w_2$=20μm, $L_t$=500μm, $\Delta n_{eff}$=0.007].**

The agreement is seen to be very good. The not perfect match with the profiles from the HGCM model is attributable to the fact that both include, in the solutions, also the contributions from the continuum modes. In addition the HGCM model for active devices takes into account the interaction between carriers and propagating field.

# References

[C-1] D. Masanotti, F. Causa, J. Sarma, *'Design optimisation of high power high brightness parabolic bow-lie laser diodes'*, IEE Proceedings - Circuits, Devices and Systems, vol. 150, n. 6, December 2003

[C-2] A. F. Milton, W. K. Burns, *Guided Wave-Optoelectronics*, ed. by T. Tamir, New York, Springer-Verlag, 1990

[C-3] I. Middlemast, J. Sarma, P. S. Spencer, *'Characteristics of Tapered Rib-Waveguides for High Power Semiconductor Optical Sources'*, IEE Proceedings Optoelectronics, Part J, vol. 144, No. 1, 1997, pp. 8-13.

[C-4] T. Rozzi, M. Mongiardo, *Open Dielectric Waveguides*, IEE Electromagnetic Series, 1997

[C-5] D. Marcuse, *Light Transmission Optics* ($2^{nd}$ Ed.), Van Nostrand Reinhold, New York, 1982

[C-6] H. Kogelnik, *'Theory of Optical Waveguides'*, in *Guided Wave-Optoelectronics*, ed. by T. Tamir, New York, Springer-Verlag (1990).

# Appendix D

# *Material Design for High-Power High-Brightness*

Good semiconductor material quality is an essential prerequisite for the fabrication of high-power diode lasers. However, design considerations are very different from those related to conventional devices, [D-1]. The semiconductor material used to fabricate in house the laser structures of interest in this work was specially designed to provide simultaneously high optical output power and sufficient lateral optical guiding with the desired rib height, $h_{RIB}$, [Appendix C]. In addition a small vertical beam divergence was essential to achieve high brightness.

The thickness of the waveguide layers was the critical parameter to be adjusted to satisfy the above requirements.

## D.1 Material Requirements for High Power High Brightness

Catastrophic Optical Damage (COD) of the facets and thermal roll-over have the most predominant effects on high power devices operation, [D-2].

To estimate the on-set of COD for any given semiconductor material, it is common practice to refer to the material characteristic optical power density before failure, $P_{COD}$. Thus, for a typical stripe laser the maximum optical power output achievable before COD can be estimated by, [D-1]:

$$P_{max} = \frac{d_{QW}}{\Gamma_{QW}} w P_{COD} \qquad (D.1)$$

where w is the laser stripe width, $d_{QW}$ and $\Gamma_{QW}$ are, respectively, the thickness and the optical confinement factor of the QW region. It is common practice to define the ratio $\frac{d_{QW}}{\Gamma_{QW}}$ as the equivalent spot size S, [D-1], [D-2].

The effect of thermal rollover can be analysed considering how the thermal variations affect devices performance. The variation of the differential external quantum efficiency $\eta_e$ and the threshold current $I_{th}$ for a specific rise $\Delta T$ of the junction temperature, with respect to the temperature $T_h$ of the heatsink, are given respectively by, [D-3], [D-4]:

$$\eta_e(T_h + \Delta T) = \eta_e(T_h)\exp\left(-\frac{\Delta T}{T_1}\right) \tag{D.2}$$

and

$$I_{th}(T_h + \Delta T) = I_{th}(T_h)\exp\left(\frac{\Delta T}{T_0}\right) \tag{D.3}$$

The corresponding change in the maximum optical output power achievable, $P_{max}$, is expressed by the equation, [D-1]:

$$P(T_h + \Delta T)_{max} = \eta_e(T_h)\exp\left(-\frac{\Delta T}{T_1}\right)\left[I - I_{th}(T)\exp\left(\frac{\Delta T}{T_0}\right)\right] \tag{D.4}$$

where $T_1$ and $T_0$ are the characteristic temperature coefficients for $\eta_e$ and $I_{th}$, respectively. From the above analysis, it follows that high output power could be achieved with:

- low confinement factor to reduce the risk of COD
- a semiconductor material structure and composition that provides a large value of $P_{COD}$
- optimised device design to maximise the differential external quantum efficiency $\eta_e$ and simultaneously minimise the temperature sensitivity of $\eta_e$ and $I_{th}$;
- optimise device design to improve heat dissipation

However an optimised structure for high power operation has to deal also with other, partially conflicting, requirements such as, [D-5]:

- high confinement factor in the core to increase optical gain
- reduced overall thickness of the epitaxial layers for low thermal and series resistances
- low scattering and free-carrier absorption loss
- high doping level to reduce the series resistance
- optimum guide/barrier thickness for the carriers to improve the electrical confinement and therefore internal efficiency and thermal stability while keeping the voltage across the diode at low values

A careful design of the multilayer structure is therefore essential, with (unavoidable) trade-offs the can depend on the specific requirements. To be noticed that for high power lasers the reduction of the threshold current is not a predominant issue.

## D.2 Material Design and Characteristics

The semiconductor epitaxy, described in Tab. D.1, [D-6]-[D-8], is a Double Heterostructure (DH), Large Optical Cavity (LOC) material, based on a GaAs/AlGaAs structure and grown by low pressure Metal Organic Vapour Phase Epitaxy on n-GaAs substrate.

**Tab. D.1: The designed Semiconductor Material Structure.**

| Layer | Composition | Thickness (µm) | Doping density ($cm^{-3}$) | Dopant |
|---|---|---|---|---|
| Contact | GaAs | 0.2 | $3.0\ 10^{19}$ | Zn |
| Cladding | $Al_{0.42}$ | 0.77 | $8.0\ 10^{17}$ | C |
| Guide | $Al_{0.20}$ | 0.24 | undoped | -- |
| QW | $In_{0.2}Ga_{0.8}As$ | 7nm | undoped | -- |
| Barrier | GaAs | 10nm | undoped | -- |
| QW | $In_{0.2}Ga_{0.8}As$ | 7nm | undoped | -- |
| Barrier | GaAs | 10nm | undoped | -- |
| QW | $In_{0.2}Ga_{0.8}As$ | 7nm | undoped | -- |
| Guide | $Al_{0.20}$ | 0.24 | undoped | -- |
| Cladding | $Al_{0.42}$ | 1.77 | $1.4\ 10^{18}$ | Si |
| Buffer | GaAs | 0.5 | $1.4\ 10^{18}$ | Si |

The LOC design, [D-2], [D-9], [D-10], was chosen because it allows for a smaller confinement factor of the optical field in the active region and a

corresponding larger equivalent spot size, therefore allowing, in turn, for higher optical power density before COD, $P_{COD}$.

Oh the other hand, since the field is smoothed, the energy being transported in the cladding layers is very small, allowing for more highly doped and relatively thin cladding layers, both measures leading to small series and thermal resistances. The disadvantage of the lower modal gain is therefore compensated by the very low loss, thus allowing for longer devices to maintain high external efficiency. The number and composition of the quantum wells were chosen to provide sufficient gain to compensate the smaller confinement factor and the contribution of each layer to free-carrier absorption loss, [D-6], [D-7], [Appendix A], as well as ensuring the desired 980nm emission wavelength.

The modal properties of the semiconductor material used for device fabrication have been solved with the Effective Dielectric Constant (EDC) method, [D-11], by using the Cascaded Matrix Method (CMM), [D-12], to analyse the multi-layer structure. A detailed analysis was been carried out to study the material performance for different values for the waveguide thickness $t_w$.

Important parameters that were considered in stage of design are, importantly, the equivalent spot size $S_S$, the vertical far field divergence, $\theta_y$, at Full Width at Half Maximum (FWHM), the lateral effective refractive index step, $\Delta n_{eff}$, and the contribution of free-carrier absorption loss, $\alpha_{FCc}$.

The variation of $S_S$, $\theta_y$ and $\Delta n_{eff}$ (in this case two different value of the rib height $h_{RIB}$ have been considered) with waveguide layer thickness $t_w$, are presented in Fig. D.1 a) and Fig. D.1 b) respectively, [D-7]. These computed results indicate that a compromise can be achieved to contain the vertical beam divergence while having a sufficiently large equivalent spot size to ensure high power operation and at the same time significant lateral guiding.

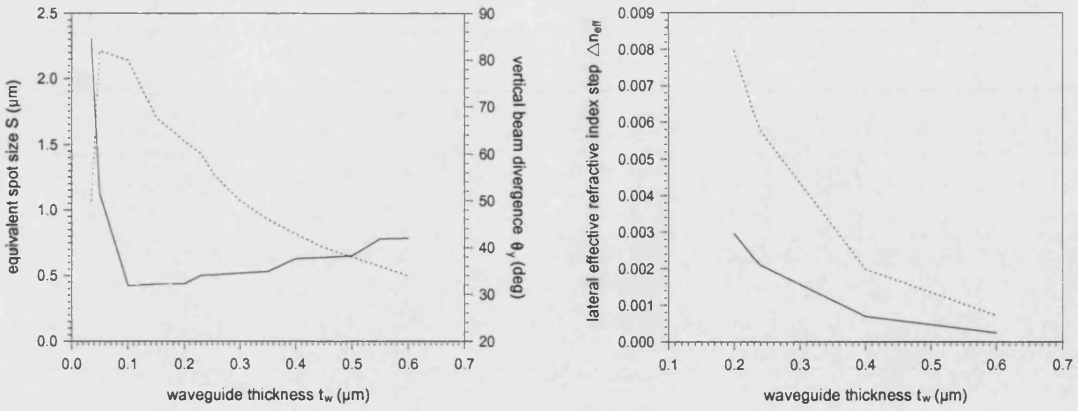


a) b)

**Fig. D.1: a) Calculated equivalent spot size $S_S$ (solid line) and vertical far-field divergence $\theta_y$ (dotted line) versus waveguide thickness $t_w$. b) Variation of the lateral effective refractive index step as a function of the waveguide thickness $t_w$, calculated for rib height $h_{RIB}$=0.8μm (solid line) and $h_{RIB}$=0.9μm (dotted line).**

The variation of the confinement factors in the active region and in the cladding layers, $\Gamma_{QW}$ and $\Gamma_{CL}$ respectively, as a function of $t_w$, has been plotted in Fig. D.2, [D-7].

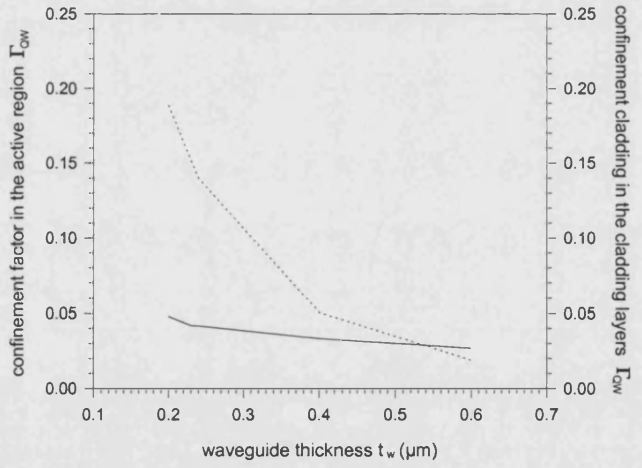


**Fig. D.2: Calculated optical confinement factor in the active region (solid line) and in the cladding layers (dotted line).**

Since the waveguide layers are not doped, the contribution to free-carrier absorption loss, $\alpha_{FCc}$, is given mainly from the active region and the cladding layers: this contribution is proportional to their confinement factors, [Appendix A].

The multi-layer structure, Tab. D.1, with the chosen $t_W = 2.4\mu m$ and $h_{RIB} = 0.9\mu m$, supports only three (bound) modes, of which the fundamental mode has the largest confinement factor in the active layer, Fig. D.3.

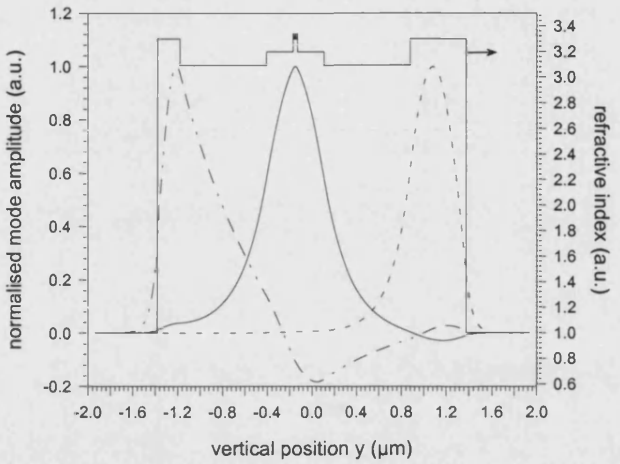


**Fig. D.3: Refractive index profile for the designed semiconductor material and calculated mode distribution for the fundamental mode (solid line) and higher order modes (dashed, dashed-dotted line).**

The confinement factor of the higher order modes in the active region is negligible; such modes also show a maximum of optical intensity exactly at the interfaces between the claddings and the outer layers; it will yields to high radiation losses (i.e. very high threshold currents) thus making them impossible to lase.

For the optimised material structure, Tab. D.1, the variation of the lateral effective index step ($\Delta n_{eff}$) and corresponding confinement factor in the active region with respect to the rib height is presented in Fig. D.4. The resulting effective refractive index step (for $h_{RIB} = 0.9\mu m$) estimated to be $\Delta n_{eff} = 0.007$, is that required by the optimised Bow-Tie geometry, [Appendix C]. It is sufficient to ensure not only (weak) lateral guiding along the device, but also single mode operation for the bow-tie central straight section. This is also in perfect accord with the minimum rib width allowed by fabrication constraints.

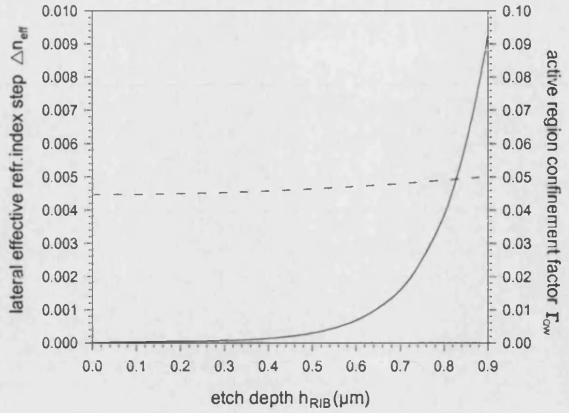


**Fig. D.4: Effective refractive index (solid line) and optical confinement factor (dashed line) in the active region as functions of the rib height ($h_{RIB}$) for the high power LOC material used for device fabrication.**

The experimental vertical far-field intensity profile, presented in Fig. D.5, matches with that predicted from the theory, giving a divergence angle, at Full Width at Half Maximum (FWHM) of $\theta_y = 58°$, [D-7].

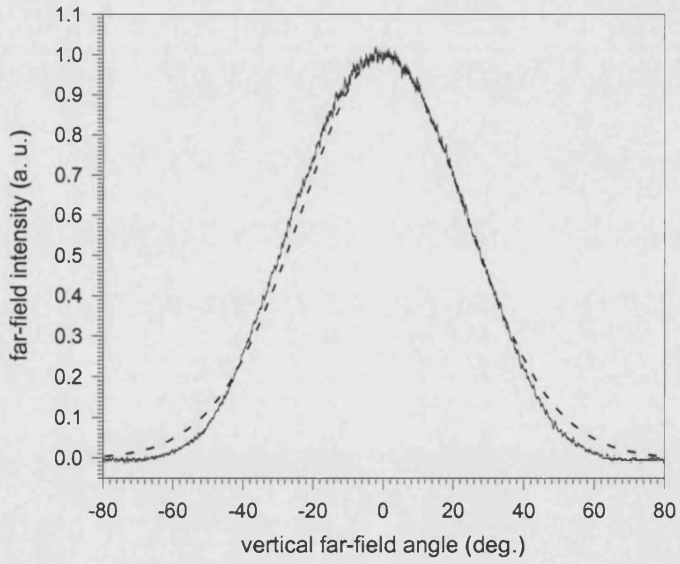


**Fig. D.5: Vertical far field intensity profile (solid line) with corresponding theoretical profile (dashed line) for comparison.**

The theoretically estimated parameters and the measured parameters for the designed material, are reported in Tab. D.2.

**Tab. D.2: Material parameters.**

| Parameter Description | Symbol | Value |
|---|---|---|
| Active Region Thickness | $d_{QW}$ (μm) | 0.021 |
| Active Region Conf.Fact. | $\Gamma_{QW}$ (%) | 0.045 |
| Equivalent Spot Size | $S_s$ (μm) | 0.458 |
| Cladding/GuideConf.Fact. | $\Gamma_{CL}$ (%) | 0.12 |
| Optical Loss | $\alpha$ ($cm^{-1}$) | 3 |
| Free Carr.Abs.Loss | $\alpha_{FCc}$ ($cm^{-1}$) | 0.6 |
| Vert. Beam Divergence | $\theta_y$ (deg) | 58 |
| $P_{COD}$ | $P_{COD}$ ($MWcm^{-2}$) | 12 |
| Characteristic temperature | $T_0$ (°C) | 218 |

The $T_0$ parameter for the material of Tab. D.2 has been extrapolated, Fig. D. 6, from CW L-I curves measured at temperatures between 15°C and 60°C; its value is found to be in agreement with expected values for semiconductor materials designed for emission in this wavelength range.

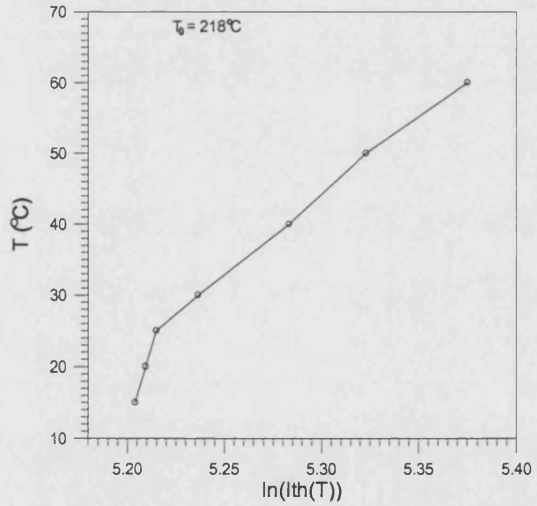


**Fig. D.6: Logarithm of the threshold current as a function of the sink temperature measured from devices under CW operation.**

# References

[D-1] G. W. Yang, R. J. Hwu, Z. T. Xu, X. Y. Ma, *'Design Consideration and Performance of High-Power and High-Brightness InGaAs-InGaAsP-AlGaAs Quantum-Well Diode Lasers ($\lambda$=0.98$\mu$m)'*, IEEE J. Selected Topics in Quantum Electronics, vol. 6, No. 4, July/Aug. 2000, pp. 577-584.

[D-2] M. Buda, T. G. Van de Roer, L. M. F. Kaufmann, G. Iordache, D. Cengher, D. Diaconescu, I. B. Petrescu-Prahova, J. E. M. Haverkort, W. Van der Vleuten, J. H. Wolter, *'Analysis of 6-nm AlGaAs SQW low-confinement laser structures for very high-power operation'*, IEEE J. Selected Topics Quantum Electronics, 1997, vol. 3, n.2, pp. 173-179

[D-3] E. Kapon, *'High-Power Semiconductor Lasers'*, in *Semiconductor Lasers II*, ed. by E. Kapon, Academic Press (1999).

[D-4] B. Mroziewicz, M. Bugajski, W. Nakwaski, *Physics of Semiconductor Lasers*, Polish Scientific Publishers (1991).

[D-5] R. Diehl, *High-Power Diode Lasers – Fundamentals, Technology, Applications*, Springer-Verlag, Berlin, 2000

[D-6] D. Masanotti, F. Causa, *'Optical guiding properties of high brightness Parabolic Bow-Tie Laser Arrays'*, IEEE J. Quantum Electron., vol. 41, n. 7, July 2005, pp. 909-916

[D-7] D. Masanotti, F. Causa, J. Sarma, *'High brightness, index-guided parabolic bow-tie laser diodes'*, IEE Proceedings – Optoelectronics, vol. 151, n. 2, April 2004

[D-8] D. Masanotti, F. Causa, J. Sarma, *'Design optimisation of high power high brightness parabolic bow-lie laser diodes'*, IEE Proceedings - Circuits, Devices and Systems, vol. 150, n. 6, December 2003

[D-9] H. C. Casey, Jr., M. B. Panish, *Heterostructure Lasers, Part A: Fundamental Principles*, ed. by H. C. Casey, Jr. and M. B. Panish, Academic Press, London, 1978.

[D-10] H. C. Casey, Jr., M. B. Panish, *Heterostructure Lasers, Part B: Materials and Operating Characteristics*, ed. by H. C. Casey, Jr. and M. B. Panish, Academic Press, London, 1978.

[D-11] D. Marcuse, *Light Transmission Optics* (2nd Ed.), Van Nostrand Reinhold, New York, 1982

[D-12] H. Kogelnik, *'Theory of Optical Waveguides'*, in *Guided Wave-Optoelectronics*, ed. by T. Tamir, New York, Springer-Verlag (1990).

# Appendix E

## *Experimental Set-Up used for Far-Field Measurements*

The apparatus employed to measure the angular far-field intensity profiles of the lasers presented in this PhD thesis is shown in Fig. E.1.

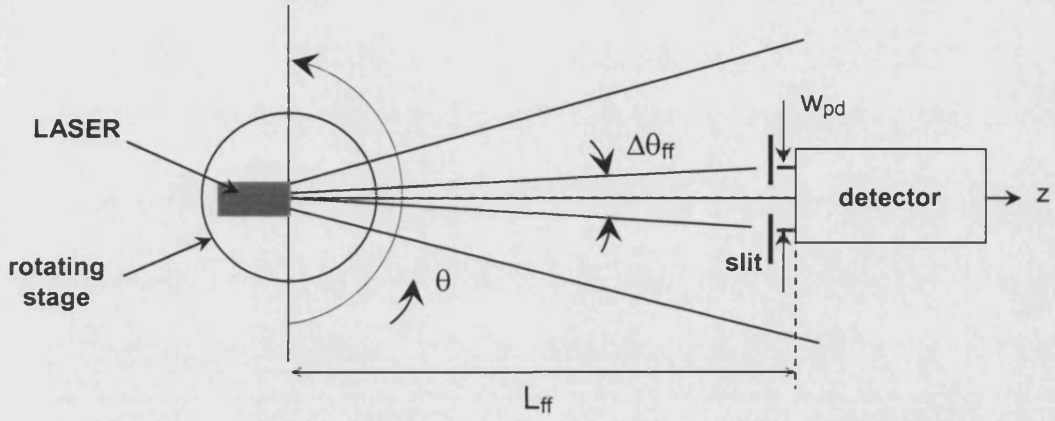


**Fig. E.1: Top view schematic of the set-up for measuring the angular far-field pattern. A slit is placed in front of the detector to increase the measurement resolution $\Delta\theta_{ff}$. The distance $L_{ff}$ between the laser and the photodetector must be fixed in order to have consistency between $\Delta\theta_{ff}$ and the resolution of the rotating stage.**

The laser is mounted on a motorised rotating stage; the centre of the laser facet is positioned in the centre of the rotation system. A photodiode is used to detect the emitted power intensity as the laser is rotated.

The signal from the photodiode is fed into a lock-in amplifier, synchronised with the laser (current) driver. The output from the lock-in amplifier is then sent to a digital oscilloscope and its intensity value is plotted versus time while the lasers is rotated, in a range of angle and with a speed specified by the operator, giving a plot of the output power versus angular position.

## E.1 Alignment and Measurement Resolution

For accurate measurements, it is very important that the device is placed exactly in the centre of rotation of the motorised stage. A CCD camera with magnification object is therefore placed on top of the laser to check its position. On the other hand, the photodetector must be on axis with the laser.

The above statement can be explained considering the important property of the angular far-field distribution of being independent from the distance at which it is measured.

This principle is followed to check the photodetector alignment: only if the photodiode is on-axis then the far-field profile measured at different distances from the laser does not change, Fig. E.2.

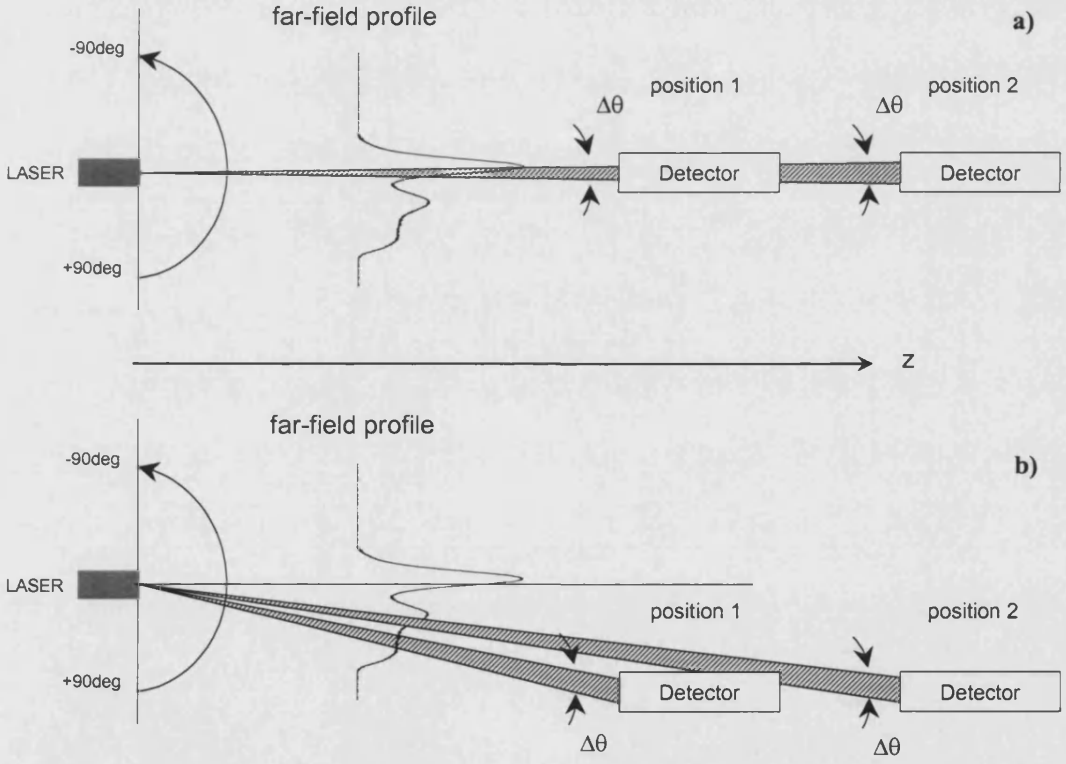


**Fig. E.2: The angular far-field profile is independent from the distance it is measured. If the photodiode is on-axis with the laser, then measurements taken at different distances give the same results, a). If the photodiode is off-axis, different distances yield to different readings, b).**

Only if the photodetector is correctly placed, then the reading taken at two different distances from the laser is, as expected, the same, Fig. E.2 a). However, if

the detector is off-axis, at two different distances from the lasers, it would read different values of intensity corresponding to two different 'sections' of the far-field pattern, Fig. E.2 b).

The distance between the photodiode and the laser is responsible for the measurement angular resolution, corresponding to the angle 'window' $\Delta\theta_{ff}$, Fig. E.1, over which the photodiode takes the reading. The value of $\Delta\theta_{ff}$ depends also on the width of the photodiode detecting area and is given by:

$$\Delta\theta_{ff} = \frac{w_{PD}}{L_{ff}} \tag{E.1}$$

where $w_{PD}$ and $L_{ff}$ have the same (length) units and $\Delta\theta_{ff}$ is expressed in radians. The smaller $\Delta\theta_{ff}$, the more accurate the measurements are, since closer peaks can be resolved. Importantly, $\Delta\theta_{ff}$ must be smaller also than the resolution of the rotating stage, to avoid taking readings of the same portion of far-field more than once.

Considering that the rotating stage resolution is 0.1deg, corresponding to 0.0017rad, and that the aperture width $w_{PD}$ of commonly used photodiodes is about less than 5mm then, from equation (E.1), it follows that to have consistency between the measurement and the rotating stage resolution, the photodiode should be placed at a minimum distance $L_{ff}$~300cm, which is not practical.

Thus, a $w_{SL}$=0.25mm wide slit, Fig. E.1, is placed in front of the photodiode detecting area. The required minimum distance, for consistency with the stage resolution, is now, with $w_{SL}$ replacing $w_{PD}$ in equation (E.1), $L_{ff}$~ 14cm. To be noticed that, with constant $L_{ff}$, placing the slit in general yields to an increase of the resolution of about 20 times.

Graphs in Fig. E.3 show the increase in resolution when the 0.25mm wide slit is placed in front of the photodiode aperture and when the distance between the photodiode and the laser is increased. The driving current is kept constant.

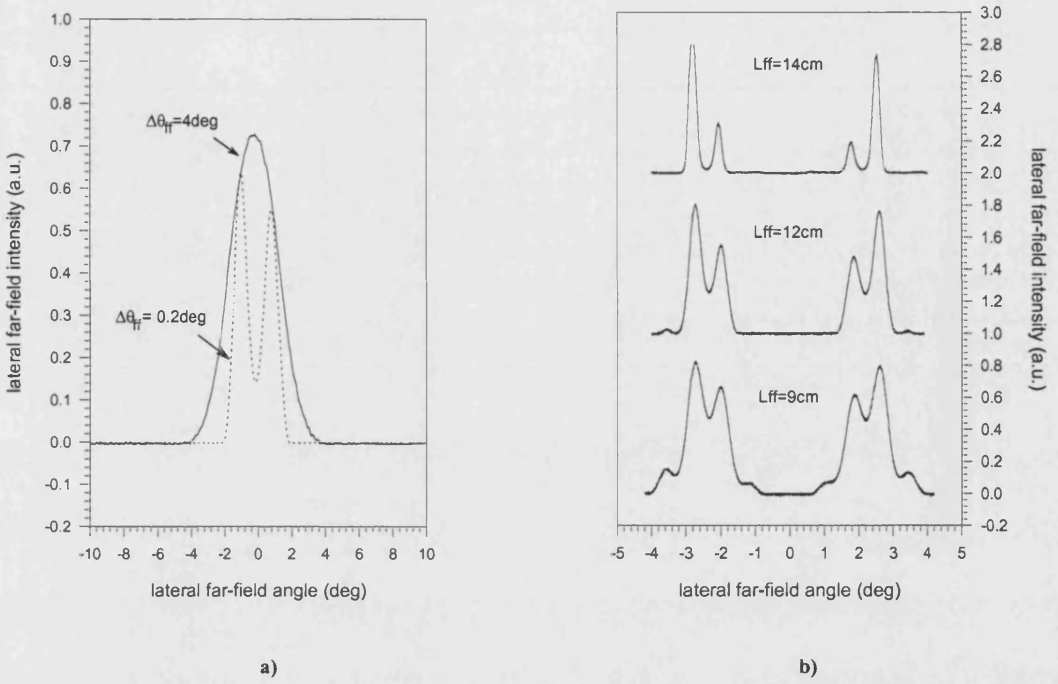


**Fig. E.3: a) At a distance $L_{ff}$=7cm the slit in front of the photodiode permits to resolve peaks (dashed line) that otherwise the photodiode would not detect (solid line). b) When using the slit, the resolution can further increase if the distance between the laser and the photodiode is increased. Consistency of the profiles also confirms that the photodiode is correctly aligned.**

## E.2 Accuracy of the Results

The accuracy of the obtained results has been tested by taking measurements for the same driving current and at the same distance from the laser but varying the stage rotating speed (by varying either the rotation range or the scanning time).

Different photodiodes have also been used to investigate the effect of their response time compared to the stage rotating speed.

The far-field intensity profiles measured at a driving current I=80mA and at a distance $L_{ff}$=15cm when the rotation angle range is 30deg and 60deg, and when the scanning time is 50sec and 100 sec, are shown in Fig. E.4. It can be noticed that there is consistency between the different patterns.

Plots in Fig. E.5 show instead measurements taken with two different photodiodes, characterised by a maximum response time of 40ns and 220ns respectively. Also in this case good consistency between the different patterns is observed.

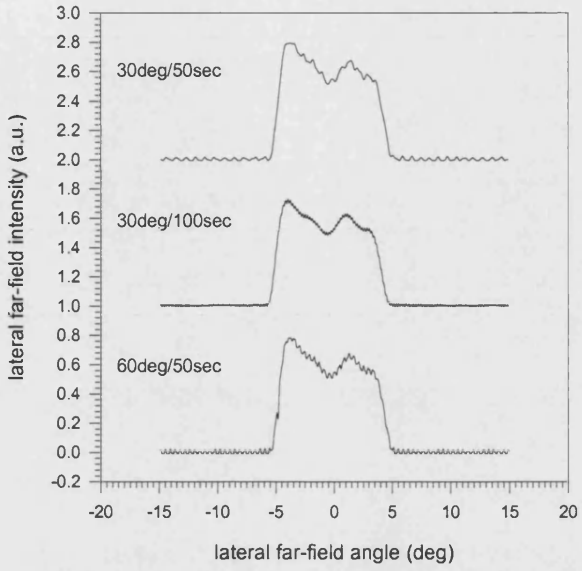


**Fig. E.4: Far-field measurement at different rotation speeds. [$L_{ff}$=15cm, 0.25mm wide slit].**

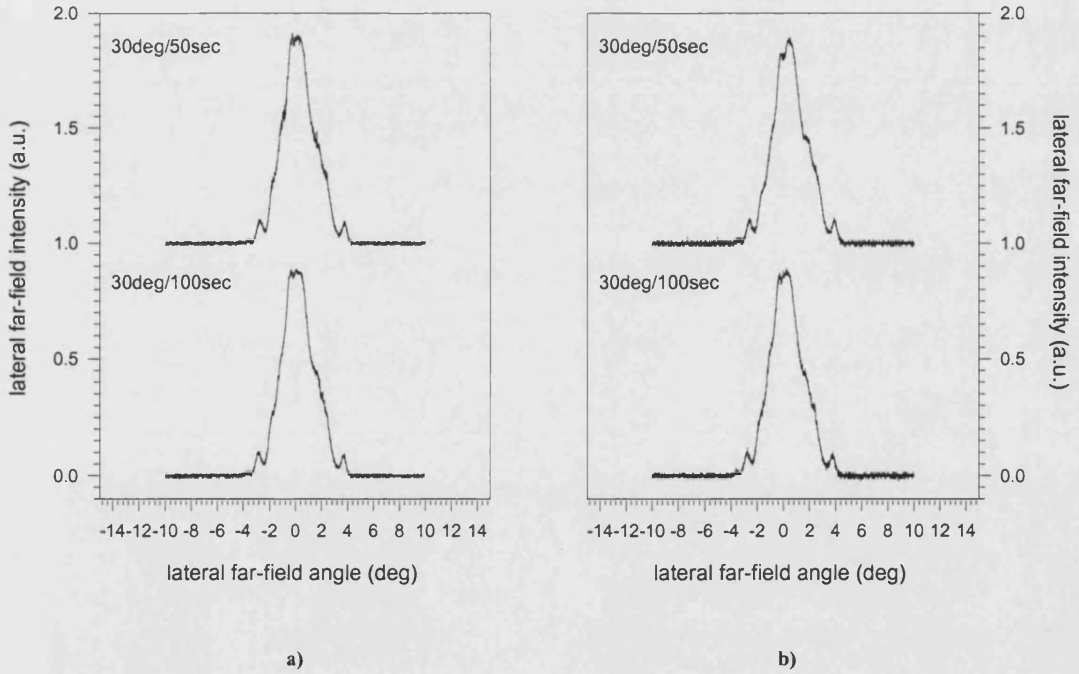


**Fig. E.5: Far-field measurements taken at a distance $L_{ff}$=50cm, for different rotation speeds and using photodiodes with maximum response time a) 40ns and b) 220ns.**

## E.3 Accuracy of the Scale

Of particular importance for far-field measurements is the error due the non-synchronisation between the rotating platform and the oscilloscope recording, which is manually operated. Thus several measurements have been taken, with the same settings, to quantify the maximum shift, in degrees, resulting from the 'human error'.

The accuracy of the scale is therefore estimated to be $\Delta\theta_S$=0.5deg, Fig. E.6.

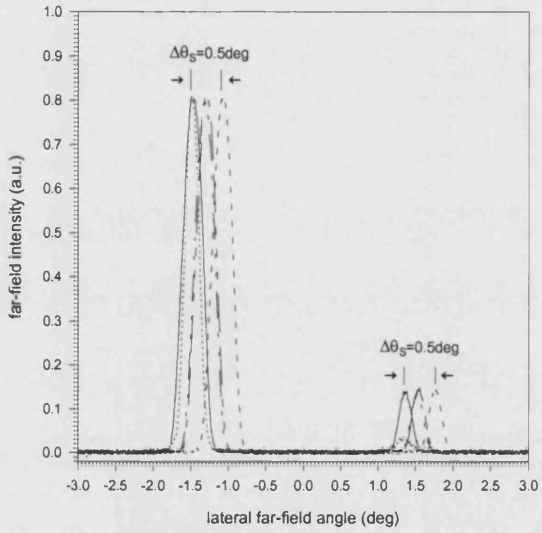


**Fig. E.6: Measurements taken to quantify the 'human error' in synchronising rotation time and recording time show that the accuracy of the scale is $\Delta\theta_S$=0.5deg.**

# Appendix F

## *Coherence Measurement Set-Up*

The most straightforward way to measure the coherence between emitters of an array of N elements, e.g., Fig. F.1 for N=4, and therefore the coherence of the array, is to measure the visibility V of the fringes produced by interfering pairs of emitters at a time, [F-1].

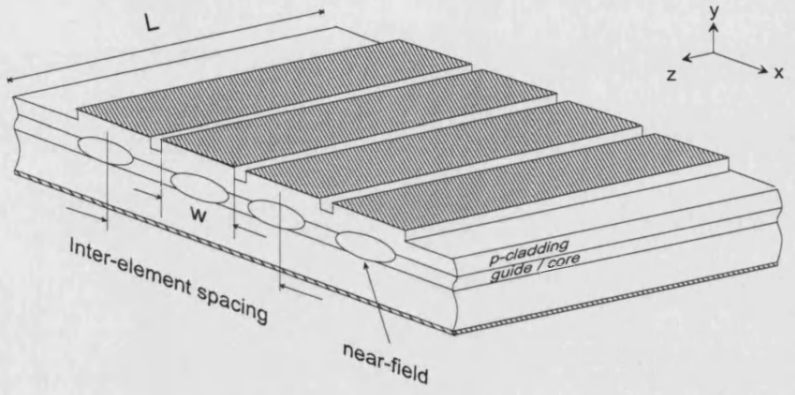


**Fig. F.1: Schematic of a stripe laser array with N=4 elements.**

The contrast or fringe visibility V, [F-1], measured by interfering the m-th and n-th array elements is given by:

$$V = \frac{I_{max} - I_{min}}{I_{max} - I_{min}} = |\gamma_{mn}| \left( \frac{2\sqrt{I_m I_n}}{I_m + I_n} \right) \qquad (F.1)$$

where $I_{max}$ is the maximum intensity of the fringe pattern, $I_{min}$ is the minimum intensity of the fringe pattern; $I_m$ and $I_n$ are the intensities of the m-th and the n-th element respectively; $\gamma_{mn}$ is the complex degree of coherence, [F-1].

To measure V and $\gamma_{mn}$ the Young Two Slit interference experiment was used, [F-1], by re-imaging the array near-field onto a pair of slits of aperture chosen so that light from only two elements is transmitted, e.g. Fig. F.2 for m=2 and n=3.

For the arrays of interest in this work, a 0.25 Numerical Aperture (N.A) objective is used to re-image (and magnify by a factor up to 15) the array near field onto transmission slits of aperture a=100μm, and spacing $S_{sl}$=1mm.

The distance between the transmission slits and the objective lens was chosen accordingly with the lens magnification, depending on the width w of the array individual emitter and the inter-element spacing $S_{mn}$ between the considered emitters so that a<w' and $S_{sl}=S_{mn}'$, where w' and $S_{mn}'$ are the 'magnified' emitter aperture and inter-element spacing, respectively. The interference fringes are detected by a CCD camera placed behind the slits.

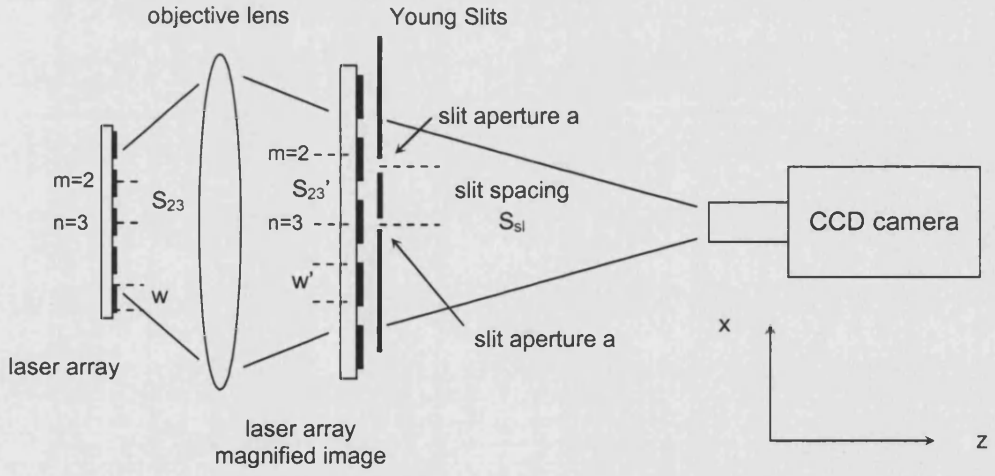


**Fig. F.2: An objective lens is used to re-image the array near-field onto a pair of slit so that only two emitters can interfere at a time. The interference fringes are detected by a CCD camera.**

If $I_m = I_n$, then equation (F.1) simplifies to $V = |\gamma_{mn}|$. Total coherence between elements will correspond to $V = 1$, partial coherence to $V < 1$ and no coherence to $V \cong 0$, Fig. F. 3.

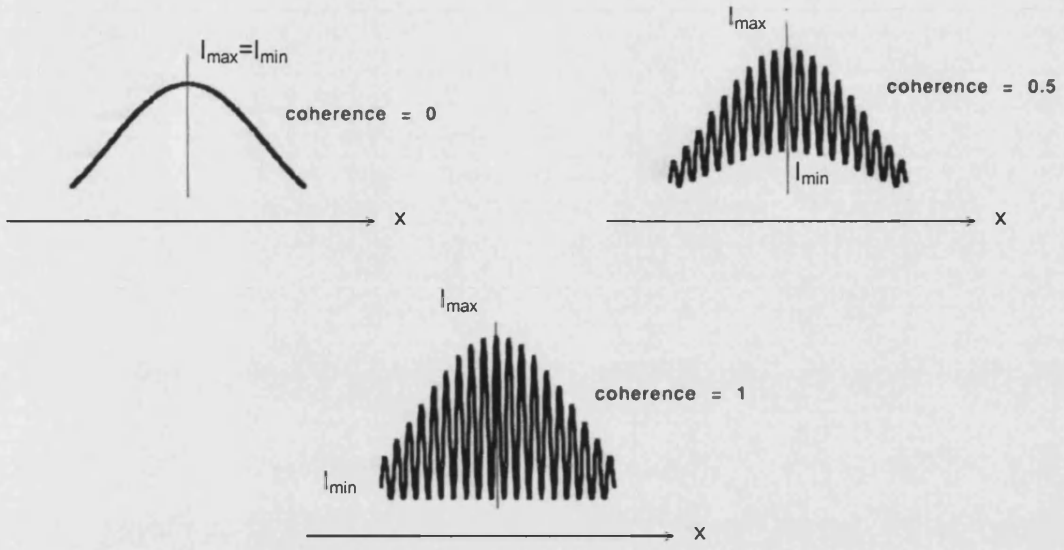


**Fig. F.3: Example of interference patterns from pairs of emitters with different degrees of coherence, to show how to measure coherence, [F-1].**

Coherence measurements are important also because it is possible to measure the relative phase between elements, determined by the position of the fringes under the diffraction envelope. If a fringe maximum (constructive interference) occurs at the diffraction envelope maximum, the elements are in-phase. On the other hand, if a fringe minimum occurs at the envelope maximum (destructive interference) the elements are out-of-phase.

# References

[F-1] G. A. Evans, J. M. Hammer, *Surface Emitting Semiconductor Lasers and Arrays*, New York Academic Press (1993).

# List of Figures

# List of Tables

# Publications from this PhD Research Work

Journals:

[1] D. Masanotti, F. Causa, *'Optical guiding properties of high brightness Parabolic Bow-Tie Laser Arrays'*, accepted for publication in IEEE J. Quantum Electron., 2005

[2] F. Causa, D. Masanotti, *'High brightness index-guided Parabolic Bow-Tie Laser Arrays'*, IEEE Photonics Technology Letters, vol. 16, n. 9, pp. 2000-2002, Sept. 2004

[3] D. Masanotti, F. Causa, J. Sarma, *'High brightness, index-guided parabolic bow-tie laser diodes'*, IEE Proceedings – Optoelectronics, vol. 151, n. 2, April 2004

[4] D. Masanotti, F. Causa, J. Sarma, *'Design optimisation of high power high brightness parabolic bow-lie laser diodes'*, IEE Proceedings - Circuits, Devices and Systems, vol. 150, n. 6, December 2003

Conferences:

[1] D. Masanotti, F. Causa, J. Sarma, *'980nm High Power Index-Guided (Phase) Coherent Parabolic Bow-Tie Laser Arrays'*, Paper CMX-5-MON, (oral presentation), CLEO/QELS2005, Baltimore, Maryland (USA), 22-27 May 2005

[2] D. Masanotti, F. Causa, J. Sarma, *'Characterisation of arrays of tapered lasers for high power operation'*, (poster presentation QEP.P2.24, * COMMENDATION PRIZE WINNER) PHOTON 04, Glasgow Caledonian University, Scotland, 6-9 September 2004

[3] D. Masanotti, F. Causa, J. Sarma, *'Study of phase-locking in arrays of index-guiding tapered lasers for high brightness applications'*, (oral presentation), ETOS 2004, University College Cork, Ireland, 26-29 July 2004

[4] D. Masanotti, F. Causa, J. Sarma, *'Index-guiding tapered laser arrays to achieve high-brightness'*, (poster presentation), Proceedings of Conference on Semiconductor and Integrated Optoelectronics, SIOE 2004, Cardiff, Wales, April 2004

[5] D. Masanotti, F. Causa, J. Sarma, *'High-power high-brightness index-guided parabolic bow-tie laser arrays'*, EUROPEAN SEMICONDUCTOR LASER WORKSHOP, (oral presentation), Turin, ITALY, 19-20 September 2003

[6] D. Masanotti, F. Causa, J. Sarma, *'Bright parabolic bow-tie laser arrays'*, Paper CC6-2-WED, (oral presentation), CLEO EUROPE EQEC 2003, Munich ICM (Germany), 22-27 June 2003

[7] D. Masanotti, F. Causa, J. Sarma, *'High brightness parabolic bow-tie lasers'*, (oral presentation), Proceedings of Conference on Semiconductor and Integrated Optoelectronics, SIOE 2003, Cardiff, Wales, April 2003

[8] D. Masanotti, F. Causa, J. Sarma, *'High power diffraction limited parabolic taper laser diode'*, (poster presentation), PREP 2003, Exeter, April 2003

[9] D. Masanotti, F. Causa, J. Sarma, *'High-power high-brightness tapered lasers'*, (oral presentation), Proceedings of Photonics 2002, Sixth International Conference on Optoelectronics, Fibre Optics & Photonics, Mumbai, India, December 2002

[10] D. Masanotti, F. Causa, J. Sarma, *'High power diffraction limited taper laser diodes'*, (oral presentation), Mini-symposium on non-linear dynamics of lasers, The Rank Prize Funds, Grasmere, UK, 19-22 August 2002

[11] D. Masanotti, F. Causa, J. Sarma, *'Tapered lasers for high brightness optical sources'*, Poster Presentation at 2002 Users Workshop-Industrial Liaison Meeting, Engineering and Physical Science Research Council, Sheffield Central Facility for III-V Semiconductors, Sheffield, U.K., 2002

# Design optimisation for high-power high-brightness parabolic bow-tie laser diodes

D. Masanotti, F. Causa and J. Sarma

**Abstract:** Optical sources that combine high power with high brightness are in great demand for various applications. Although sophisticated device designs have been demonstrated to have such desirable characteristics, to contain the device costs tapered geometry devices seem to provide attractive alternatives. Further, particularly for high-power operation, the bow-tie configuration is effective for further reducing the risk of catastrophic optical damage and for obtaining a good quality output beam. The authors present the detailed analysis that has been necessary to optimise both the material layer structure and the tapered laser geometry to achieve simultaneously high power and high brightness. Following the design guidelines, several 980 nm parabolic bow-tie lasers have been fabricated and characterised in-house, obtaining output powers in excess of 700 mW per facet in a diffraction-limited (2.7°) beam measured without the use of external lenses.

## 1 Introduction

The development of optical sources emitting high power in a diffraction-limited beam has raised increasing interest recently for various applications, including pumping erbium-doped fibre amplifiers (EDFAs) [1], free-space communications [2] and medical instrumentation [3]. To achieve simultaneously high power and high brightness both the material epitaxy and the device geometry must be carefully designed to overcome, particularly, catastrophic optical damage (COD) and optical gain saturation.

In principle, high powers can be achieved by using a broad area (BA) current injection contact [4], but it is well known that BA lasers are prone to temporal and spatial instabilities, which make the output beam difficult to predict and control [5]. Various devices have been demonstrated to enhance brightness including angled-grating distributed feedback lasers [6], antiresonant reflecting optical waveguide lasers [7] and integrated master oscillator power amplifiers [8]. However, the above devices generally require complicated fabrication techniques and the use of external optics to focus the output beam. In this respect tapered geometry laser diodes [9–12] have attracted particular attention for providing a low-cost, simple, yet effective device geometry suitable for high-power and high-brightness operation. Particularly for high-power operation, the bow-tie configuration [13] has been proved to be effective for further reducing the risk of COD of the facets and for obtaining a good quality output beam, since the central (straight) section of the device operates as a mode filter, as described in the following Sections. Most importantly, however, improved operational characteristics can be achieved by carefully designing the device geometry. In particular it is found that to optimise the output beam characteristics from a laser diode of relatively small dimensions, index-guided, nonlinearly tapered semiconductor devices are most useful [14].

This paper presents the detailed analysis that has been necessary to optimise both the material layer structure and the tapered laser geometry to achieve simultaneously high output power and a narrow output beam (high brightness).

## 2 Material and device structure

The parabolic bow-tie (PBT) laser diodes of interest in this paper are fabricated from a specially designed triple quantum well (TQW) InGaAs/GaAs/AlGaAs large optical cavity (LOC) semiconductor material grown by low pressure metal organic vapour phase epitaxy (MOVPE) on GaAs substrate [15]. The details of the multilayer epitaxy are given in Table 1.

The vertical layer structure supports three modes of which the two higher-order modes are mainly confined in the lossy cladding layers. The fundamental mode is confined to the guiding (LOC) region, with an estimated confinement

**Table 1: QW material structure used to fabricate the devices analysed in this paper**

| Layer | Composition | Thickness (μm) | Doping density ($cm^{-3}$) | Dopant |
|---|---|---|---|---|
| Contact | GaAs | 0.2 | $3.0\ 10^{19}$ | Zn |
| Cladding | $Al_{0.42}Ga_{0.58}As$ | 0.77 | $8.0\ 10^{17}$ | C |
| Guide | $Al_{0.2}Ga_{0.8}As$ | 0.24 | undoped | — |
| QW | $In_{0.172}Ga_{0.828}As$ | 70 Å | undoped | — |
| Barrier | GaAs | 100 Å | undoped | — |
| QW | $In_{0.172}Ga_{0.828}As$ | 70 Å | undoped | — |
| Barrier | GaAs | 100 Å | undoped | — |
| QW | $In_{0.172}Ga_{0.828}As$ | 70 Å | undoped | — |
| Guide | $Al_{0.2}Ga_{0.8}As$ | 0.24 | undoped | — |
| Cladding | $Al_{0.42}Ga_{0.58}As$ | 1.77 | $1.4\ 10^{18}$ | Si |
| Buffer | GaAs | 0.5 | $1.4\ 10^{18}$ | Si |



*IEE Proceedings* online no. 20030897
doi:10.1049/ip-cds:20030897
Paper first received 21st February and in final revised form 6th August 2003

The authors are with the Department of Electronic and Electrical Engineering, University of Bath, Bath BA2 7AY, UK

factor of $\Gamma_{LOC} = 0.85$. The experimental vertical far-field intensity profile measured from in-house fabricated devices matches that predicted from the theory, giving a full width at half maximum (FWHM) far-field divergence angle of $\theta_y = 58°$.

The TQW structure ensures a sufficiently high gain to overcome the small confinement of the fundamental mode in the gain layers; the estimated free carrier absorption losses are $\alpha_{FC} = 0.6\,\text{cm}^{-1}$. The equivalent spot size $d/\Gamma_{(LOC)}$ ($d$ is the active region thickness) is 0.6 μm, which is desirable for high-power operation [16].

For the devices described here a (tapered) rib waveguide is etched in the top cladding layer to provide suitable current confinement and the required explicit lateral effective index guiding. For the epitaxy of Table 1, an etch depth of $d_e = 0.9\,\mu\text{m}$ has been chosen to effectively reduce current spreading and to provide a lateral effective index step of $\Delta n_{eff} = 0.007$, which ensures that the central straight section is single-moded.

The top view schematic of the PBT device studied in this paper is presented in Fig. 1. Typical device dimensions are $w_s = 3\,\mu\text{m}$, $L_s = 50\,\mu\text{m}$, $w_o = 20\,\mu\text{m}$ $L_t = 500\,\mu\text{m}$.

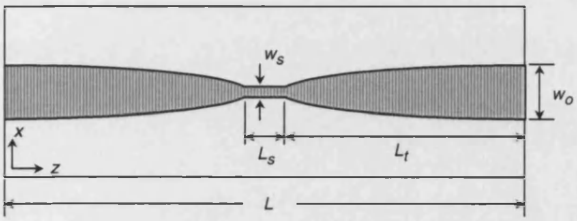


**Fig. 1** *Top view schematic of the PBT device geometry*

## 3 Device modelling

For the devices of interest here, the variation of the optical field in the vertical ($y$) direction due to the multilayer material can be removed by applying, e.g. the effective dielectric constant method [17]. Further, since the structure is weakly guiding in the lateral direction, the optical propagation is solved using a scalar analysis. Therefore, the optical field can be represented by the (harmonic time-dependent) dominant field component $F(x, z)$, satisfying the Helmoltz equation

$$\partial_z^2 F + \partial_x^2 F + k_0^2 \varepsilon F = 0 \tag{1}$$

where $k_o = 2\pi/\lambda_o$ is the free space wave number, $\lambda_o$ the free space wavelength and $\varepsilon$ the (complex) dielectric profile [18].

For the optimisation of the taper geometry, the optical propagation in the dielectric taper is solved using the step-waveguide method (SWM) [19, 20], but making use of only the bound modes to simplify the computational scheme. Therefore, the dielectric taper is represented by a sequence of slab waveguide sections of increasing width, Fig. 2. The initial field is specified as the fundamental mode of the slab of width $w_s$. The field propagating along the taper is thus represented in terms of the bound modes supported by the waveguide sections, and matched across the interface between two adjacent sections. Therefore, the field, $F_{(p)}(x, z)$, in section $p$ is written as follows:

$$F_{(p)}(x, z) = \sum_{l=1}^{M_{(p)}} a_{(p),l} f_{(p),l}(x) \exp\{-i\beta_{(p),l}(z - z_{(p-1)})\} \tag{2}$$

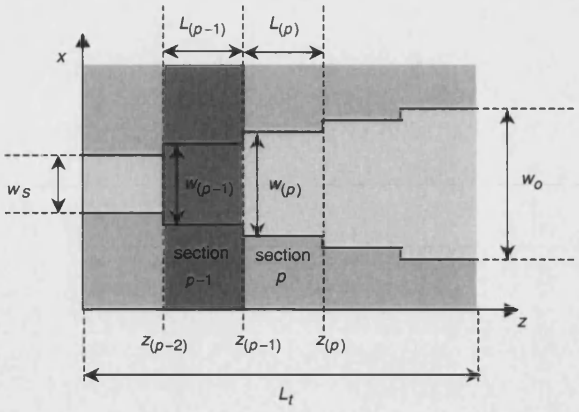


**Fig. 2** *Schematic of the step-waveguide representation of the dielectric taper*
Width and length of the $p$th waveguide section are $w_{(p)}$ and $L_{(p)} = (z_{(p)} - z_{(p-1)})$, respectively

where $M_{(p)}$ is the number of guided modes supported by section $p$, with $p = 0,1\ldots., M_{tot}$.

$$a_{(p),l} = \int_{-\infty}^{\infty} F_{(p-1)}(x, z_{(p-1)}) f_{(p),l}(x) dx$$

are the expansion coefficients (constant within section $p$)

$f_{(p),l}(x)$ represents the bound mode of order $l$ and $\beta_{(p),l}$ is the corresponding propagation constant.

Strictly, in the present formulation, the above method is valid for passive dielectric structures, but it can be considered reasonably accurate to describe the operation of the laser at threshold. The SWM has been chosen for the optimisation of the device geometry because it produces a fast computational procedure. However, the results computed with the SWM have been compared with corresponding results from other models for active devices [18, 21] to establish that device design optimisation computed with the SWM and presented in the following Section is acceptable.

## 4 Design optimisation

The SWM described above is useful to gain an insight into the optical propagation in the dielectric taper. In the ideal case the desired narrow output beam would be achieved by restricting the number of guided modes in each waveguide section to just the fundamental mode [19]. However, for high-power operation the above condition is restrictive and would enhance the risk of COD. Therefore, the output width of the tapers of interest in this paper are broad, so that the corresponding local waveguide section is generally multimoded. Having designed for the desired high-power material, the optimisation procedure nest entails designing a device geometry which yields the narrowest possible, single-lobed far-field intensity profile [14]. The parameter that is of interest in this case is the full width at half maximum (FWHM) lateral beam divergence; the vertical divergence mainly depends on the material layer structure and therefore will not be considered in this optimisation process.

For the present analysis three taper profiles have been considered:

(i) linear:

$$w_{Lin}(z) = w_s + z\frac{(w_o - w_s)}{L_t}$$

(ii) parabolic:

$$w_{Par}(z) = \left[w_s^2 + z\frac{(w_o^2 - w_s^2)}{L_t}\right]^{1/2}$$

(iii) exponential:

$$w_{Exp}(z) = w_s \exp\left[z\frac{1}{L_t}\ln\left(\frac{w_o}{w_s}\right)\right]$$

The accuracy of the SWM has been tested by changing the number $N_{tot}$ of longitudinal steps used in the calculations. The results computed by the model are presented in Fig. 3 for the near-field intensity profile for a parabolic dielectric taper. The results of Fig. 3 indicate that the SWM rapidly converges to the final profile for $N_{tot} \geq 50$, which corresponds to a step in width between adjacent sections of $\Delta w = w_{(p)} - w_{(p-1)} \leq 0.2\,\mu m$. This is consistent with the resolution (0.2 μm) for defining the fabrication mask.

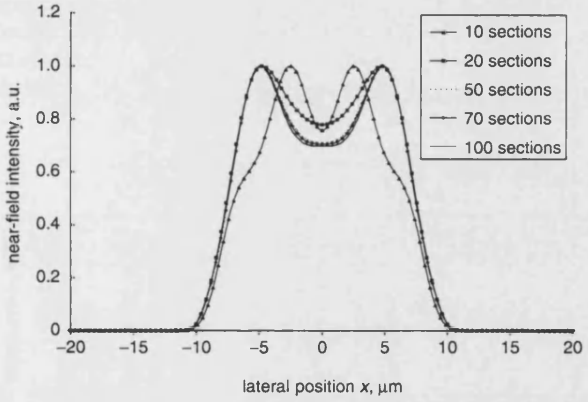


**Fig. 3** *Theoretical near-field intensity profile computed for a dielectric parabolic taper for different numbers of longitudinal steps*
$w_s = 3\,\mu m$, $w_o = 20\,\mu m$, $L_t = 500\,\mu m$

A set of calculations varying first the length $L_t$ and then the output width $w_o$ of the taper have been performed to study the effect of the taper geometry on the far-field pattern for the above taper profiles. The main results are presented in Figs. 4*a* and 4*b*. The range of variation of both parameters is wide, but that is dictated by the contradictory requirements to achieve high power and high brightness. The device output width should be sufficiently wide to reduce the risk of COD and at the same time the overall device dimensions should be compact to favour integration, increase mechanical strength and reduce the occurrence of instability. The general trend in Fig. 4*a* is that the three curves converge to the same value for very long tapers, indicating that the devices become essentially adiabatic. From Fig. 4*b* it is noticed that, compared to the results obtained from the stripe and the linear bow-tie devices, the smallest values for the FWHM of the lateral far-field intensity profile are obtained using the parabolic geometry, with the minimum for an output width of approximately 20 μm.

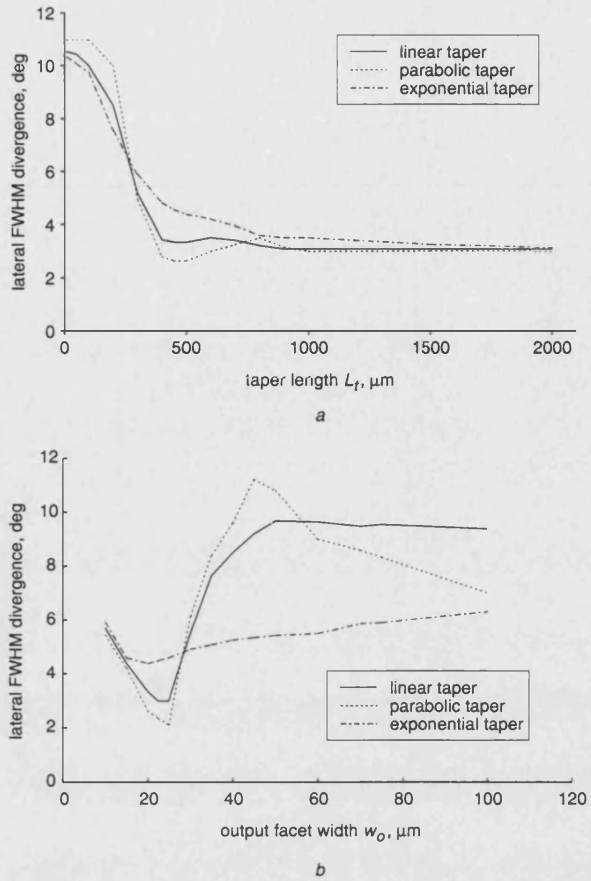


**Fig. 4** *Lateral FWHM far-field divergence computed for dielectric tapers*
For all devices: $w_s = 3\,\mu m$ and $\Delta n_{eff} = 0.007$
*a* Dependence on length $L_t$ when $w_o = 20\,\mu m$
*b* Dependence on output facet width $w_o$ when $L_t = 500\,\mu m$

To complete device optimisation, the effect of $\Delta n_{eff}$ on the FWHM far-field divergence is analysed. The SWM computed results for the three taper profiles of Fig. 5 indicate that the parabolic taper is best suited for high-brightness applications since the computed FWHM of the lateral far field for this geometry is the smallest. The results in Fig. 5 also show that the FWHM far-field divergence increases for almost negligible $\Delta n_{eff}$ (free-space diffraction) and for large $\Delta n_{eff}$ (increased coupling to higher-order modes). The optimum value seems to be in the region $\Delta n_{eff} \sim 0.007$.

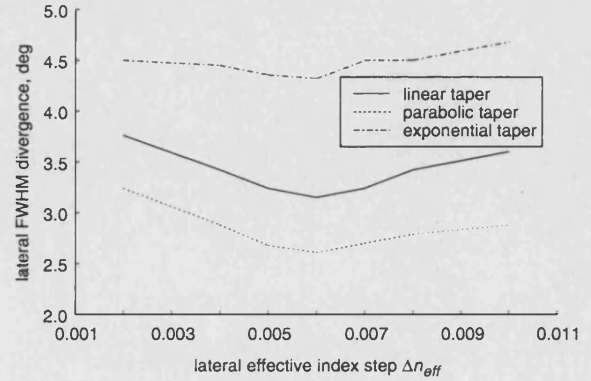


**Fig. 5** *Lateral FWHM far-field divergence computed for linear parabolic and exponential tapers for different values of $\Delta n_{eff}$*
For all devices: $w_s = 3\,\mu m$, $w_o = 20\,\mu m$, $L_t = 50\,\mu m$

The 'optimised' device dimensions have been chosen to be those indicated at the end of Section 2. The device tolerance has been studied for small variations in $w_s$ ($\pm 0.2\,\mu m$), $w_o$ ($\pm 0.2\,\mu m$), $L_t$ ($\pm 10\,\mu m$) and $\Delta n_{eff}$ ($\pm 0.002$), due to errors in the fabrication process (mask resolution, etching, cleaving). However, from the analysis of the various cases, the maximum computed error is 6% corresponding to an increase in FWHM far-field divergence $<0.2°$, considered to be negligible for all practical situations.

## 5 Experimental characterisation of in-house fabricated PBT lasers

The above design guidelines have been used to fabricate several PBT laser diodes from the specially designed high-power material, Table 1. The dimensions of the in-house fabricated devices are consistent with those of the optimised geometry, as defined in Section 2 ($w_s = 3\,\mu m$, $L_s = 50\,\mu m$, $w_o = 20\,\mu m$, $L_t = 500\,\mu m$). The devices have been systematically characterised with particular attention to the output beam spatial characteristics. A representative (light) output power as a function of the injection current characteristic (L–I curve) measured from an in-house fabricated, optimised parabolic bow-tie laser is presented in Fig. 6. Threshold currents of $\sim 50\,mA$ ($\sim 0.4\,kA\,cm^{-2}$) are typically measured with 70% slope efficiency. Output powers in excess of 700 mW per facet have been measured, corresponding to a wall-plug efficiency >40%. The maximum (output) optical power density before COD has been measured to be $P_{COD} \sim 12\,MWcm^{-2}$. Typical measured (total) optical losses are of the order of $3\,cm^{-1}$.

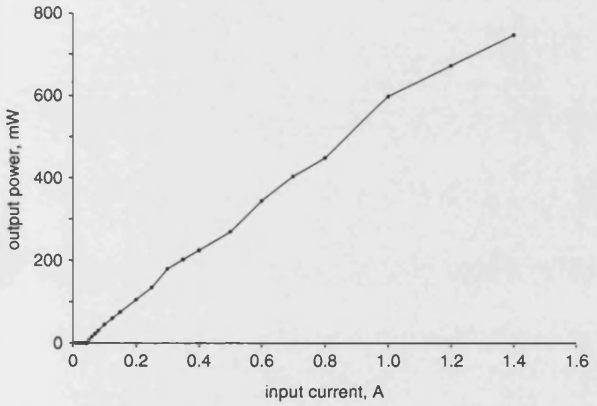


**Fig. 6** *Experimental L–I curve measured from in-house fabricated PBT laser*
0.1% duty cycle, 7 μs pulse width, temperature 20°C, neutral density filters used to avoid saturation of the detector

Near-field intensity profiles measured on several devices are in good agreement with those predicted by the SWM, Fig. 7. The far-field intensity pattern was measured without using external lenses at various injection currents, Fig. 8. The measured lateral divergence is typically $\theta_x \sim 2.7°$ (up to 20 times threshold), with Strehl ratio of ~90%, which indicates diffraction-limited operation for a wide range of output powers. The brightness has been estimated to be $\sim 150\,MWcm^{-2}\,srad^{-1}$ with beam quality $M^2$-factor <1.5.

## 6 Conclusions

A 980 nm, index-guided, parabolic bow-tie semiconductor laser has been demonstrated as an effective, low-cost, high-power optical source with high brightness.

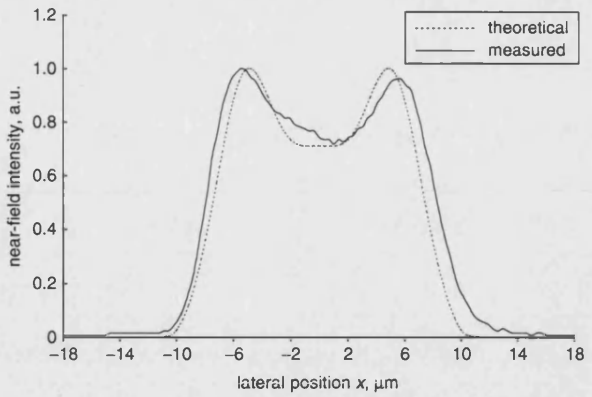


**Fig. 7** *Comparison between theoretical and measured near-field intensity profiles for optimised PBT laser*
$w_s = 3\,\mu m$, $w_o = 20\,\mu m$, $L_s = 50\,\mu m$, $L_t = 500\,\mu m$

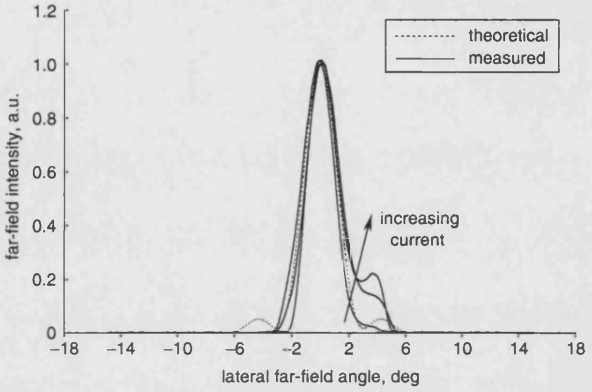


**Fig. 8** *Theoretical and experimental far-field intensity profiles measured (without lenses) from in-house fabricated optimised PBT lasers at different injection currents (200 mA, 500 mA, 1 A)*

The systematic theoretical study necessary to optimise the semiconductor material design and the device geometry has been discussed in detail. Following the design guidelines obtained from the theoretical analysis, several parabolic bow-tie lasers have been fabricated and thoroughly characterised in-house. Output powers in excess of 700 mW per facet in a diffraction-limited beam (2.7°) have been measured without the use of external lenses. The experimental characterisation of the spatial profile of the output beam has been presented and shown to be in good agreement with the theoretical profiles computed with the device model.

## 7 Acknowledgments

This work is supported by the Engineering and Physical Sciences Research Council (EPSRC), UK. Dr J. S. Roberts of the EPSRC National Centre for III-V Technologies, University of Sheffield, UK, is thanked for providing the required semiconductor material. T. J. Ryan is thanked for his expert device fabrication and for his valuable help in practical matters.

## 8 References

1 Pederson, B., Thompson, B.A., Zemon, S., Miniscalco, W.J., and Wei, T.: 'Power requirements for erbium-doped fibre amplifiers pumped in the 800, 980, 1480 nm bands', *IEEE Photonics Technol. Lett.*, 1992, **4**, (1), pp. 46–49

2 Chazan, P., Mayor, J.M., Morgott, S., Mikulla, M., Kiefer, R., Müller, S., Whalter, M., Braunstein, J., and Weimann, G.: 'High-power near-diffraction-limited tapered amplifier at 1064 nm for optical intersatellite communications', *IEEE Photonics Technol. Lett.*, 1998, **10**, (11), pp. 1542–1544
3 Williams, P.J., Lewandowski, J.J., Robbins, D.J., Wood, A.K., Robson, F.O., and Nayar, B.K.: 'Tapered laser arrays for high power operation (>1.4 W CW) at 1.59 μm for application in surgery', *Electron. Lett.*, 1998, **34**, (10), pp. 993–994
4 O'Brien, S., Zhao, H., Schoenfelder, A., and Lang, R.J.: '9.3 W CW (In)AlGaAs 100 μm wide lasers at 970 nm', *Electron. Lett.*, 1997, **33**, (22), pp. 1869–1871
5 Guthrie, J., Tan, G.L., Ohkubo, M., Fukushima, T., Ikegami, Y., Ijichi, T., Irikawa, M., Mand, R.S., and Xu, J.M.: 'Beam instability in 980 nm power lasers: experiment and analysis', *IEEE Photonics Technol. Lett.*, 1994, **6**, (12), pp. 1409–1411
6 Wong, V.V., Shoenfelder, A., O'Brien, S., De Mars, S.D., and Lang, R.: 'High-brightness α-DFB arrays at 915 nm and 1.06 μm'. IEEE CLEO Proc., Washington, DC, USA, 1999, pp. 46–47
7 Bhattacharya, A., Mawst, L.J., Nesnidal, M.P., Lopez, J., and Botez, D.: '0.4 W CW diffraction limited beam Al free 0.98 μm wavelength three core ARROW-type diode lasers', *Electron. Lett.*, 1996, **32**, (7), pp. 657–658
8 O'Brien, S., Mehuys, D., Major, J., Lang, R., Parke, R., Welch, D.F., and Scifres, D.: '1.3 W CW, diffraction-limited monolithically integrated master oscillator flared amplifier at 863 nm', *Electron. Lett.*, 1993, **29**, (24), pp. 2109–2110
9 Bendelli, G., Komori, K., Arai, S., and Suematsu, Y.: 'A new structure for high-power TW-SLA', *IEEE Photonics Technol. Lett.*, 1991, **3**, (3), pp. 42–45
10 Donnelly, J.P., Walpole, J.N., Groves, S.H., Bailey, R.J., Missaggia, L.J., and Napoleone, A.: 'High-power 1.5-μm InGaAsP/InP lasers with tapered-gain-region'. IEEE LEOS Proc., 1997, Vol. 2, paper THPi, pp. 405–406
11 Moloney, J.V., Indik, R.A., and Ning, C.Z.: 'Full space-time simulation for high-brightness semiconductor lasers', *IEEE Photonics Technol. Lett.*, 1997, **9**, (6), pp. 731–733
12 Brooks, N.S., Sarma, J., and Middlemast, I.: 'A new design for tapered-geometry high-power semiconductor optical sources'. IEEE LEOS Proc., 1996, Vol. 2, paper WZ5, pp. 207–208
13 Brooks, N.S., Causa, F., and Sarma, J.: 'An indexed guide to diverging devices: a basis for tampering with tapers'. Proc. Photonics-98, Int. Conf. on Fiber optics & photonics, Delhi, India, 1998, Vol. 1, paper TC-3, pp. 440–443
14 Masanotti, D., Causa, F., and Sarma, J.: 'High-power high-brightness tapered lasers'. Proc. Photonics 2002, 6th Int. Conf. on Optoelectronics, fiber optics & photonics, Mumbai, India, 2002, p. 237
15 Masanotti, D., Causa, F., and Sarma, J.: 'Tapered lasers for high brightness optical sources'. Users Workshop-Industrial Liaison Meeting, EPSRC, Sheffield, UK, 2002, poster presentation
16 Buda, M., van de Roer, T.G., Kaufmann, L.M.F., Iordache, Gh., Cengher, D., Diaconescu, D., Petrescu-Prahova, I.B., Haverkort, J.E.M., van der Vleuten, W., and Wolter, J.H.: 'Analysis of 6-nm AlGaAs SQW low-confinement laser structures for very high-power operation', *IEEE J. Sel. Top. Quantum Electron.*, 1997, **3**, (2), pp. 173–179
17 Kapon, E. (Ed.): 'Semiconductor lasers II' (Academic Press, 1999)
18 Causa, F., and Sarma, J.: 'A quasi-analytic model for longitudinally non-uniform semiconductor optical sources', *Opt. Commun.*, 2000, **183**, (10), pp. 149–157
19 Marcuse, D.: 'Radiation loss of tapered dielectric slab waveguides', *Bell Syst. Tech. J.*, 1970, **49**, pp. 273–290
20 Milton, A.F., and Burns, W.K.: 'Mode coupling in optical waveguide horns', *IEEE J. Quantum Electron.*, 1997, **QE-13**, (10), pp. 828–835
21 Causa, F., and Sarma, J.: 'A versatile method for analysing paraxial optical propagation in dielectric structures', *J. Lightwave Technol.*, 2000, **18**, (10), pp. 1445–1452

# High brightness, index-guided parabolic bow-tie laser diodes

D. Masanotti, F. Causa and J. Sarma

**Abstract:** The category of devices of interest in the paper is that of high power semiconductor lasers that also have high brightness. However, to achieve simultaneously high output optical power and a 'good' quality (narrow single-lobed) output beam from semiconductor lasers that can be fabricated relatively simply and cheaply, it is necessary to carefully design the cavity to control the output beam characteristics. The authors present the outcome of a systematic study on compact, index-guided semiconductor lasers of different geometry to show that with suitable design of the laser cavity it is possible to achieve the desired operational characteristics. In particular, the parabolic taper geometry has been found to be well-suited to achieve high brightness. Details of the specially designed high power semiconductor material used to fabricate the devices are also presented. The main advantage of the proposed compact devices is that the narrow output beam is achieved without the use of external lenses, thereby reducing the device cost for applications involving free-space propagation. Output powers in excess of 600 mW per facet have been measured from parabolic lasers (45% wall-plug efficiency) without catastrophic optical damage, at $I = 1\,A = 20I_{th}$, with a full width at half maximum far field intensity profile of $\sim 2.5°$.

## 1 Introduction

Recently optical sources that can deliver high power with high brightness have increasingly attracted interest for applications that require the ability to focus large optical densities to a small spot, including free-space communication [1, 2], medicine [3], second-harmonic generation [4], optical pumping of fibre amplifiers and solid state lasers [5, 6]. The challenge is now to develop optical sources with the desired characteristics, but that are compact and simple to fabricate to reduce size and costs.

Single transverse and lateral mode (high brightness) operation can be achieved by using appropriately designed narrow stripe semiconductor lasers, but the output power for such devices tends to be limited by optical gain saturation and the onset of catastrophic optical damage (COD). Larger output powers can be achieved by broadening the cross-sectional area of the active region [7], but at the expense of a poor quality output beam caused by spatial and temporal instabilities typically observed in such devices [8]. On the other hand, by using tapered-geometry semiconductor lasers, relatively large output powers can be achieved together with a good quality output beam [7, 9–12] with the added advantage of requiring relatively simple fabrication compared to other devices proposed in the literature for the same purpose, such as, for example, angle grating distributed feedback ($\alpha$-DFB) lasers [13], external cavity grating-tuned lasers [14], and anti-resonant reflecting optical waveguides [15].

Tapered devices presented in the literature can be usefully classified into two broad categories: (i) gain-guided devices, of the master oscillator power amplifier (MOPA) type [7, 10], where the diffracting optical beam is amplified in the gain region defined by the flared metal contact; and (ii) index-guided tapered devices [9, 11, 12], where an explicit lateral (effective) refractive index step weakly guides the optical field. To the authors' knowledge, most of the published literature on tapered structures is on gain-guided, linearly tapered semiconductor MOPA-type devices where the optical signal is generated by a monolithically integrated single mode stripe laser and the high power output optical beam is focused down to a diffraction limited spot using an external lens [7]. The devices described in this paper are of the second category, index-guiding devices with an etched tapered rib waveguide to produce the required weak lateral effective refractive index step. In particular the tapered devices of interest here have a characteristic 'bow-tie' shape, Fig. 1, in which a narrow central stripe acts as a mode filtering section connecting two tapered ribs designed to reduce the risk of COD at the output facets. The control of the output optical beam is then achieved by appropriately designing the device geometry, and the parabolic taper geometry has been found to be well-suited to achieve high brightness. The aim of this paper is to present the comparison of the operational characteristics of three distinct types of devices: stripe, parabolic and linear bow-tie semiconductor lasers, to show that with careful design of the laser cavity it is possible to achieve the desired high output power in a narrow output beam. The main advantage of the compact devices proposed in this paper is that the narrow output beam is achieved without the use of an external lens, thereby reducing the device cost for certain applications such as, for example, free-space interconnects and low-cost fibre links.



*IEE Proceedings* online no. 20040112

doi: 10.1049/ip-opt:20040112

Paper received 16th June 2003

The authors are with the Department of Electronic and Electrical Engineering, University of Bath, Bath BA2 7AY, UK

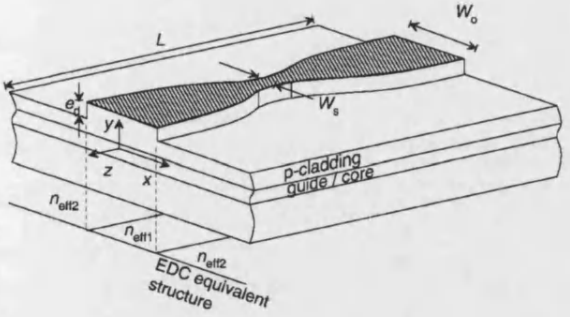


**Fig. 1** *Schematic of the parabolic bow-tie laser geometry with definition of relevant parameters*

Also indicated are the equivalent effective refractive indices that can be calculated for the etched and non-etched regions

## 2 Material design considerations

The devices of interest in this paper have been fabricated in-house from a specially designed double heterostructure (DH), triple quantum well (QW) material, [16, 17]. The semiconductor epitaxial structure, grown by low pressure metal-organic vapour phase epitaxy on a n-GaAs substrate, is based on a GaAs/AlGaAs structure with three 7-nm thick InGaAs QWs separated by two 10-nm thick GaAs barriers, Table 1. The large optical cavity active region has been designed to ensure single vertical mode operation. The guiding layer is designed to satisfy the contradictory requirements of low optical confinement to reduce the power density and therefore the risk of COD, and an adequate confinement to achieve sufficient gain. In addition it is essential to design also for a relatively small vertical beam divergence to achieve high brightness. The lasing wavelength peaks at around 980 nm.

The modal properties of the semiconductor material used for device fabrication have been solved with the effective dielectric constant (EDC) method [18] by using the cascaded matrix method [19] to analyse the multi-layer structure, Fig. 1. The multi-layer structure supports only three (bound) modes, of which the fundamental mode has the largest confinement factor in the active layer, Fig. 2. A parameter to be optimised related to the confinement factor, $\Gamma$, of the fundamental mode in the active region is the equivalent spot size $S = d/\Gamma$, where $d$ is the active layer thickness. Other important aspects that have been

**Table 1: Material structure**

| Layer | Composition | Thickness (μm) | Doping density ($cm^{-3}$) | Dopant |
|---|---|---|---|---|
| Contact | GaAs | 0.2 | $3.0 \times 10^{19}$ | Zn |
| Cladding | $Al_{0.42}$ | 0.77 | $8.0 \times 10^{17}$ | C |
| Guide ($t_W$) | $Al_{0.20}$ | 0.24 | undoped | – |
| QW | $In_{0.2}+$ | 7 nm | undoped | – |
| Barrier | GaAs | 10 nm | undoped | – |
| QW | $In_{0.2}+$ | 7 nm | undoped | – |
| Barrier | GaAs | 10 nm | undoped | – |
| QW | $In_{0.2}+$ | 7 nm | undoped | – |
| Guide ($t_W$) | $Al_{0.20}$ | 0.24 | undoped | – |
| Cladding | $Al_{0.42}$ | 1.77 | $1.4\,10^{18}$ | Si |
| Buffer | GaAs | 0.5 | $1.4\,10^{18}$ | Si |

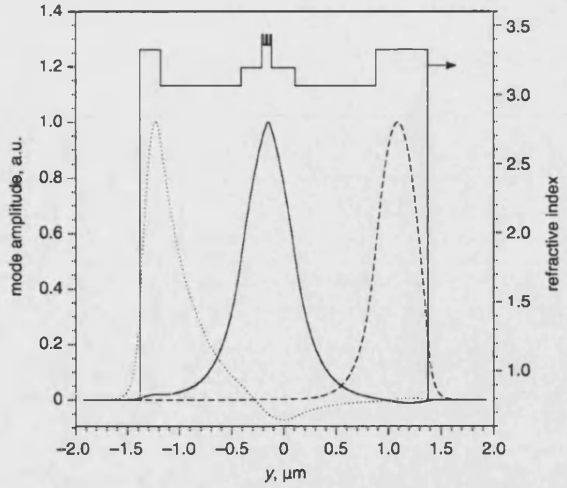


**Fig. 2** *Refractive index profile of the in-house designed multi-layer semiconductor material and amplitude profiles of the three modes supported by the structure*

considered for the design of the high power semiconductor material structure are the optimisation of the vertical beam divergence, $\theta_y$, defined as the full width at half maximum (FWHM) of the far field intensity profile, and the lateral effective refractive index step, $\Delta n_{eff} = n_{eff1} - n_{eff2}$ where $n_{eff1}$ and $n_{eff2}$ are the EDC refractive indices of the unetched and etched region, respectively, Fig. 1. The variations of $S$, $\theta_y$ and $\Delta n_{eff}$ with waveguide layer thickness are presented in Fig. 3 and Fig. 4, respectively. These computed results indicate that a compromise can be achieved to contain the vertical beam divergence while having a sufficiently large

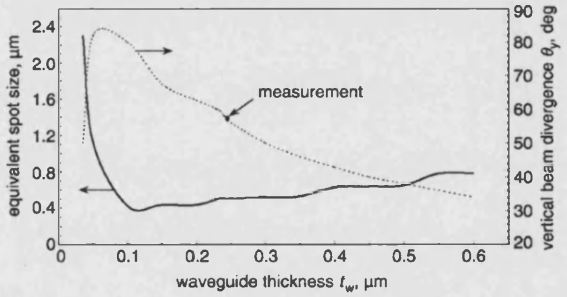


**Fig. 3** *Optimisation of the equivalent spot-size, S, and of the vertical beam divergence, $\theta_y$, with respect to waveguide layer thickness, $t_W$*

The measured $\theta_y$ value is also indicated

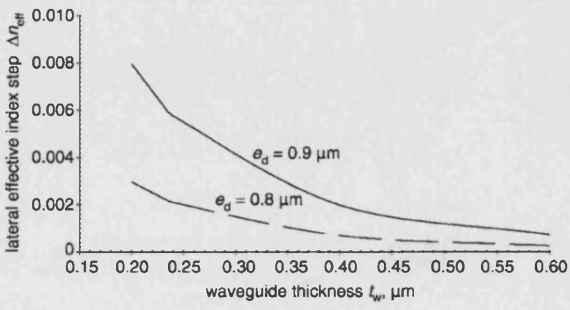


**Fig. 4** *Variation of the lateral effective refractive index step as a function of waveguide layer thickness, $t_W$, for two different etch depths*

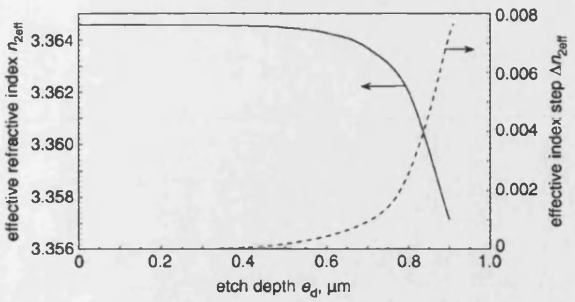


**Fig. 5** *Effective refractive index and corresponding lateral effective index step as a function of etch depth, $e_d$, for the high power semiconductor material used for the in-house fabricated devices*

equivalent spot size to ensure high power operation and at the same time significant lateral guiding. The waveguide layer thickness and the etch depth were therefore chosen to be $t_W = 2.4\,\mu m$ and $e_d = 0.9\,\mu m$, respectively.

From the specifications of the designed semiconductor material structure, Table 1, the following material parameters have been estimated theoretically: the confinement factor of the fundamental mode in the active region is $\Gamma = 0.094$; the equivalent spot size is $S = 0.43\,\mu m$; and free carrier absorption losses are $\alpha_{fc} = 0.6\,cm^{-1}$; whereas the following ones have been verified experimentally: the vertical beam divergence is $\theta_y = 58°$, Fig. 3; power density before COD is $P_{COD} = 12\,W\,cm^{-2}$; and propagation losses are $\alpha = 3\,cm^{-1}$. The variation of the effective refractive index with cladding layer thickness is explicitly shown in Fig. 5 for the designed material. With the specified material an etch depth $e_d = 0.9\,\mu m$ is suitable for current confinement to reduce current spreading. The resulting effective refractive index step estimated to be $\Delta n_{eff} = 0.007$ (at the operating wavelength of $\lambda \sim 980\,nm$) is not only sufficient to ensure (weak) lateral guiding along the device, but it also permits us to reduce on the fabrication requirements on the central straight section for single mode operation so that the necessary width is an acceptable $W_s = 3\,\mu m$.

## 3 Device geometry

The semiconductor material structure is thus optimised to achieve high power and high brightness for the vertical ($y$) field distribution. The next step is to optimise the device geometry to achieve high brightness also in the lateral ($x$) direction. The EDC method is used to reduce the analysis to two dimensions ($x$, $z$), Fig. 1, and, since the structure is weakly guiding, a scalar analysis based on a waveguide mode expansion [18, 20], is used to design the taper geometry with the lateral beam divergence, $\theta_x$, to be optimised. To simplify the design procedure the passive device is solved by expanding the propagating optical field using the (local) waveguide bound modes only [21]. Although approximate, this method yields sufficiently accurate solutions for the analysis of the device at threshold. For above threshold operation a self-consistent method based on a total field expansion method [22, 23] is used for a more accurate device analysis.

The results discussed in the next Section refer to three different device geometries: (i) linear bow-tie lasers with the width of the linear taper defined by

$$W(z) = W_s + \frac{(W_o - W_s)}{L_T} z,$$

where $L_T$ is the length of the taper; (ii) parabolic bow-tie lasers with the width of the parabolic taper defined by

$$W(z) = \sqrt{W_s^2 + \frac{(W_o^2 - W_s^2)}{L_T} z};$$

and (iii) straight stripe lasers for which $W(z) = W_o$. All the devices of interest in this paper have the same width of the output facet $W_o = 20\,\mu m$ and the same length $L = 1050\,\mu m$; for the tapered devices the straight section is characterised by $W_s = 3\,\mu m$ and length $L_s = 50\,\mu m$.

## 4 Results and discussions

The operational characteristics presented in this Section have been measured on in-house fabricated devices, with emphasis on the output beam characteristics. The devices utilised for this work have been mounted also in-house on a copper heat sink to have easy access to both output facets. Therefore, the heat-sinking properties of the mount are not optimal and the devices are typically tested using a temperature controller ($T = 20\,°C$) and a duty cycle of 0.1% (5 μs pulse width).

The output optical power against current (L–I) characteristics measured from the stripe, linear bow-tie (LBT) and parabolic bow-tie (PBT) lasers are summarised in Fig. 6 for compactness. Although the stripe active area is larger than that of the bow-tie lasers for the devices of interest in this paper, the output power from the stripe laser is only slightly higher than that measured from the bow-tie lasers at the same injection current, but clearly the corresponding current density is lower for the stripe. The slope efficiencies are comparable for the three types of devices, with the highest value (70%) from the PBT laser.

A representative detailed L–I curve for the PBT laser is shown in Fig. 7, together with corresponding voltage and wall-plug efficiency curves. Typical threshold currents are $I_{th} = 50\,mA$, corresponding to a threshold current density $J_{th} = 0.4\,kA\,cm^{-2}$, with slope efficiency of $0.7\,W\,A^{-1}$. In pulsed operation output powers in excess of 600 mW per facet have been measured from PBT lasers without COD, corresponding to a maximum wall-plug efficiency of 45%, at $I = 1\,A = 20I_{th}$. The output power significantly decreases under CW operation, reaching ~200 mW output optical power at 1 A injection current, which can also be explained by the above-mentioned consideration on the present, modest heat sinking mount. Noticeably the threshold current in CW operation is almost unchanged and thermal roll-over does not occur in the current range in which the device has been tested.

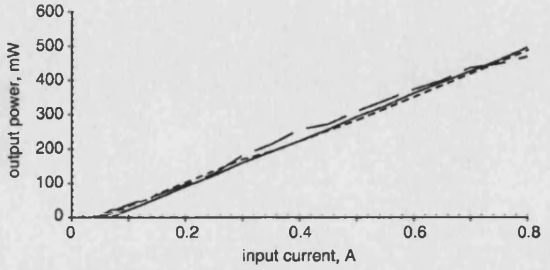


**Fig. 6** *Experimental L–I curves measured from the three categories of lasers of interest*

Solid line: PBT; dashed line: LBT; dotted line stripe laser (0.1% duty cycle, 5 μs pulse width; temperature 20 °C; neutral density filters used to avoid detector saturation)

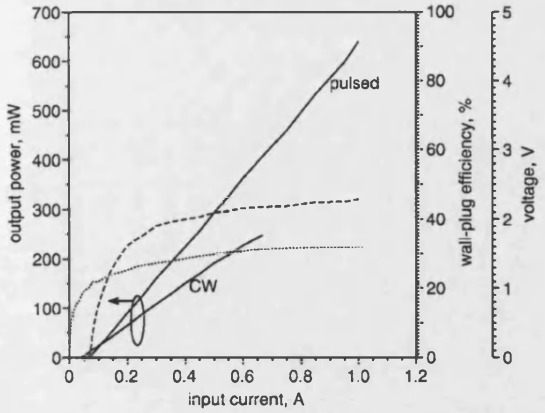


**Fig. 7** *Detailed experimental L–I curve measured from in-house fabricated PBT laser with corresponding voltage characteristics (dotted line) and wall-plug efficiency (solid line)*

(0.1% duty cycle, 5 $\mu s$ pulse width; temperature 20 °C; neutral density filters used to avoid detector saturation.) The CW L–I characteristic is also shown for comparison

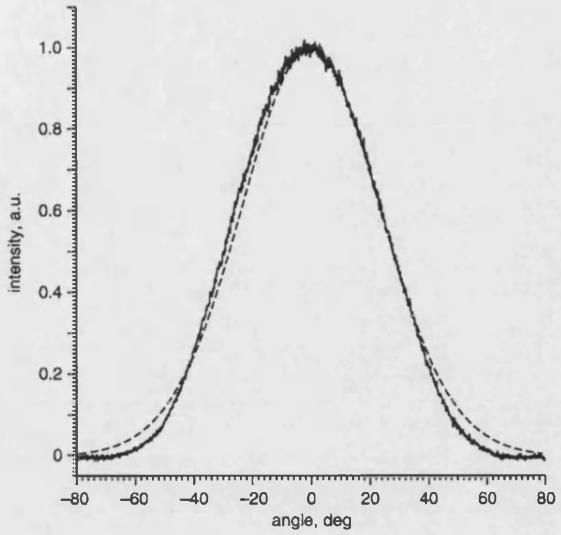


**Fig. 9** *Vertical far-field intensity profile (solid line) with corresponding theoretical profile (dashed line) for comparison*

The far-field intensity profiles, measured without external lenses, from the three types of devices at various injection current levels, at a distance of 150-450 mm from the device output facet, are presented in Fig. 8. A slit is placed in front of the photodiode to increase the measurement resolution ($<0.1°$). From Fig. 8 it is noticed that, differently from the tapered devices, the simple stripe cannot support a dominantly single-lobed far field over the range of currents investigated. In addition, although the output beam from either bow-tie lasers is of 'better' quality than that of the stripe, the far field from the parabolic taper seems to be more stable, over the current range of interest ($1 - 20I_{th}$), than that from the linear taper. The measured vertical beam divergence corresponds to the theoretical estimate, Fig. 9.

From the measurements of the near-field intensity profiles, Fig. 10, the $M^2$-factor has been estimated. The experimental results of the output power and beam characteristics for the three devices are summarised in Table 2 for compactness, at two different operating currents ($I = 1.5I_{th}$ and $I = 20I_{th}$) to show changes with current for the different types of devices. The Strehl ratio can be defined as the fraction of power within a solid angle corresponding to the diffraction limit for the device of interest and is measured using a diffraction-limited slit in front of the photodiode at a distance from the device. The brightness is calculated as the optical output power per unit emitting area and unit solid angle. From Table 2 it is noted that near threshold the operational characteristics of the three devices are comparable, all devices presenting almost ideal beam quality ($M^2$-factor $\sim$ 1 and high Strehl ratio). However, at larger injection currents ($I \sim 20I_{th}$), although the output optical power levels are comparable, the output beam quality begins to degrade significantly for the stripe, while, out of the three types of devices analysed here, the PBT seems to be giving the most desirable operational characteristics. This trend is observed over a wide range of currents.

In summary, although the output power from a stripe laser may exceed that from tapered devices at corresponding injection current levels, the beam quality in such devices

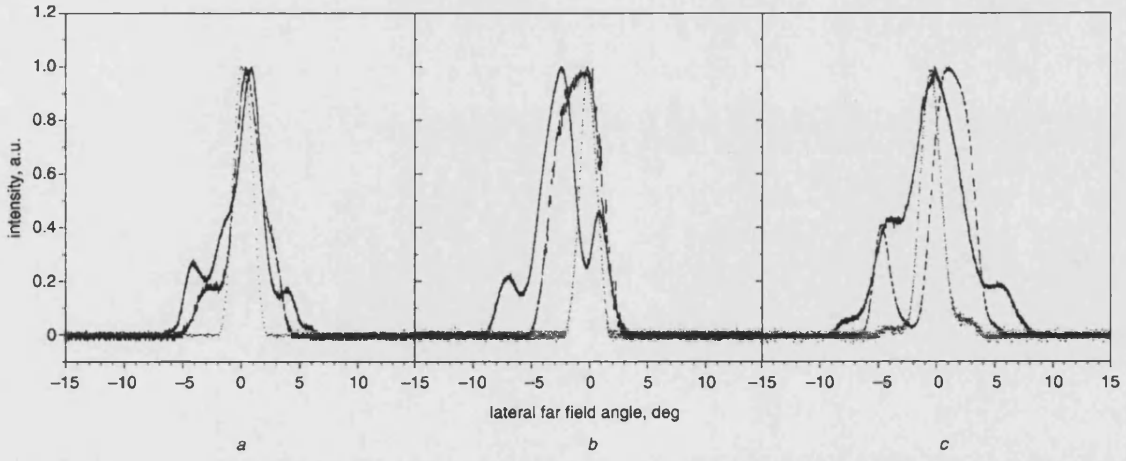


**Fig. 8** *Far-field intensity profiles measured from the three categories of devices at three different operational currents*

Dotted line $I \approx I_{th}$; dashed line $I \approx 15I_{th}$; solid line $I \approx 20I_{th}$
*a* Parabolic bow-tie
*b* Linear bow-tie
*c* Stripe

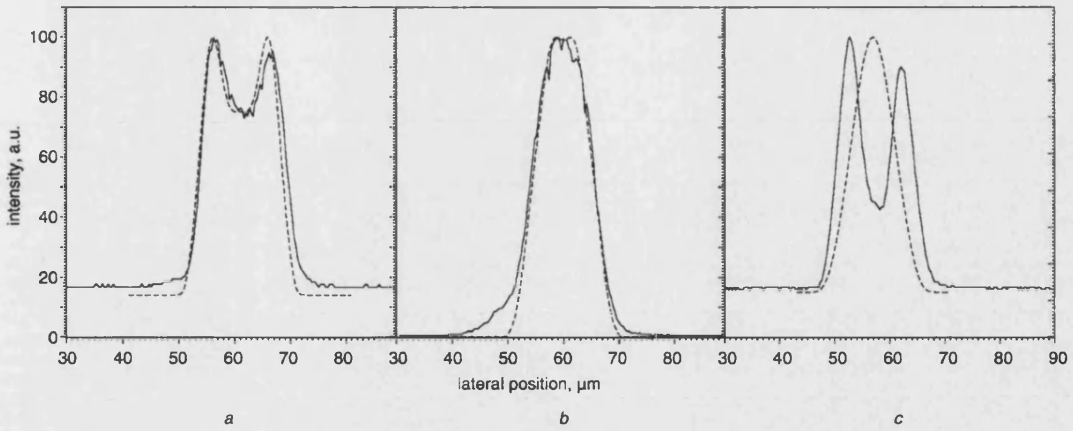


**Fig. 10** *Near-field intensity profiles (solid line) for the PBT, LBT and stripe lasers, with corresponding theoretical curves (dashed line) for comparison*

*a* Parabolic
*b* Linear
*c* Stripe

**Table 2: Comparison of the operational characteristics of stripe, linear bow-tie and parabolic bow-tie lasers with same output width and same length measured at two different injection currents**

| Characteristics | Stripe | Linear bow-tie | Parabolic bow-tie |
|---|---|---|---|
| Threshold current, mA | 60 | 45 | 50 |
| Slope efficiency, % | 57 | 62 | 70 |
| Characteristics at $I \sim 1.5I_{th}$ | | | |
| Output power, mW | ~20 | ~1 | ~2 |
| $M^2$-factor | ~1 | ~1 | ~1 |
| Strehl ratio, % | ~70 | 76 | 80 |
| Brightness, MW cm$^{-2}$ srad$^{-1}$ | 5.5 | 0.27 | 0.55 |
| Characteristics at $I \sim 20I_{th}$ | | | |
| Output power, mW | ~670 | 500 | 640 |
| $M^2$-factor | 2.49 | 1.47 | 1.28 |
| Strehl ratio, % | <20 | 45 | 66 |
| Brightness, MW cm$^{-2}$ srad$^{-1}$ | 60 | 96 | 137 |

seems to be significantly affected by mode competition, as demonstrated by the considerably lower brightness that can be achieved using stripe lasers compared to that from tapered devices.

## 5 Conclusions

To achieve simultaneously high output optical power and, 'good' quality (narrow, single-lobed) output beam from compact semiconductor lasers that can be fabricated relatively simply and cheaply, it is necessary to properly design the cavity to control the output beam characteristics. Experimental results comparing the operational characteristics of three different types of in-house fabricated semiconductor optical sources – stripe, linear and parabolic bow-tie lasers – have been presented. From these results it can be concluded that although the output power levels are comparable, the beam characteristics of the tapered bow-ties are of 'better quality' than those of stripe lasers. Further, the beam characteristics of the parabolic bow-tie laser seem to be more stable, compared to those of the other two types of devices, over the wide range of currents in which the devices have been tested.

Details of the semiconductor material specially designed for high power operation are also discussed. The devices presented in this paper are index-guided and, therefore, a robust device design is essential to reduce modal competition and increase the brightness. As many as possible material and device parameters have been quantified to achieve a realistic device design.

## 6 Acknowledgments

This work is supported by the Engineering and Physical Sciences Research Council (EPSRC), UK. Dr J.S. Roberts of the EPSRC National Centre for III–V Technologies, University of Sheffield, UK, is thanked for providing the required semiconductor material. Mr. T.J. Ryan is thanked for device fabrication and for valuable help in practical matters.

## 7 References

1 Alexander, S.B., Kintzer, E.S., Livas, J.C., Walpole, J.N., Wang, C.A., Missaggia, L.J., and Chinn, S.R.: '1 Gbit/s coherent optical communication system using a 1 W optical power amplifier', *Electron. Lett.*, 1993, **29**, pp. 114–115
2 Chazan, P., Mayor, J.M., Morgott, S., Mikulla, M., Kiefer, R., Müller, S., Whalter, M., Braunstein, J., and Weimann, G.: 'High-power near-diffraction-limited tapered amplifier at 1064 nm for optical inter-satellite communications', *IEEE Photonics Technol. Lett.*, 1998, **10**, p. 1542
3 Williams, P.J., Lewandowski, J.J., Robbins, D.J., Wood, A.K., Robson, F.O., and Nayar, B.K.: 'Tapered laser arrays for high power operation (>1.4 W CW) at 1.59 μm for application in surgery', *Electron. Lett.*, 1998, **35**, pp. 993
4 Goldberg, L., Busse, L., and Meyus, D.: 'Blue light generation by frequency doubling of AlGaAs broad area amplifier emission', *Appl. Phys. Lett.*, 1992, **60**, p. 1037
5 Botez, D., and Scifres, D.R.: 'Diode laser arrays' (Cambridge University Press, Cambridge, UK, 1994)
6 Bour, D.P., Dinkel, N.A., Gilbert, D.B., Fabian, K.B., and Harvey, M.G.: '980 nm diode laser for pumping $Er^{3+}$ -doped fibre amplifiers', *IEEE Photonics Technol. Lett.*, 1990, **2**, p. 153
7 O'Brien, S., Zhao, H., Shoenfelder, A., and Lang, R.: '1.3 W CW, diffraction-limited monolithically integrated master oscillator flared amplifier at 863 nm'. Proc. Conf. on Lasers and Electro-Optics (LEOS), Boston, USA, 1996
8 Guthre, J., Tan, G.L., Ohkubo, M., Fukushima, T., Ikegami, Y., Ijichi, T., Irikawa, M., Mand, R.S., and Xu, J.M.: 'Beam instability in

980 nm power lasers: experiment and analysis', *IEEE Photonics Technol. Lett.*, 1994, **6**, p. 1409
9 Bendelli, G., Komori, K., and Arai, S.: 'Gain saturation and propagation characteristics of index-guided tapered-waveguide travelling-wave semiconductor laser amplifiers (TTW-SLA's)', *IEEE J. Quantum Electron.*, 1992, **28**, p. 447
10 Walpole, J.N., Kintzer, E.S., Chinn, S.R., Wang, C.A., and Missaggia, L.J.: 'High-power, strained-layer InGaAs/AlGaAs tapered travelling wave amplifier', *Appl. Phys. Lett.*, 1992, **61**, pp. 740–742
11 Brooks, N.S., Sarma, J., and Middlemast, I.: 'A new design for tapered-geometry high power semiconductor optical sources'. Proc. Conf. on Lasers and Electro-Optics (LEOS), Boston, USA, 1996, vol. 2, p. 207
12 Masanotti, D., Causa, F., and Sarma, J.: 'High-power high-brightness tapered lasers'. Proc. Photonics-2002, Sixth Int. Conf. on Optoelectronics, Fiber Optics & Photonics, Mumbai, India, 2002
13 Wong, V.V., Shoenfelder, A., O'Brien, S., DeMars, S.D., and Lang, R.: 'High-brightness α-DFB arrays at 915 nm and 1.06 μm'. Proc. Conf. on Lasers and Electro-Optics (LEOS), Washington DC, USA, 1999
14 Jones, R.J., Gupta, S., Jain, R.K., and Walpole, J.N.: 'Near-diffraction-limited high power (~1 W) single longitudinal mode CW diode laser tunable from 960 to 980 nm', *Electron. Lett.*, 1995, **31**, (19), p. 1668
15 Botez, D., Napartonovich, A., and Zmudzinski, C.: 'Phase-locked arrays of antiguides: analytical theory II', *IEEE J. Quantum Electron.*, 1995, **31**, pp. 244–253
16 Masanotti, D., Causa, F., and Sarma, J.: 'Tapered lasers for high-brightness optical sources'. Poster Presentation at 2002 Users Workshop-Industrial Liaison Meeting, Engineering and Physical Science Research Council, Sheffield Central Facility for III–V Semiconductors, UK, 2002
17 Masanotti, D., Causa, F., and Sarma, J.: 'High brightness parabolic bow-tie lasers'. Proc. Conf. on Semiconductor and Integrated Optoelectronics (SIOE), Cardiff, UK, 2003
18 Marcuse, D.: 'Light transmission optics' (Van Nostrand Reinhold, New York, USA, 1982, 2nd edn.)
19 Kogelnik, H.: 'Guided wave-optoelectronics', in Tamir, T. (Ed.): (Springer-Verlag, New York, 1990)
20 Rozzi, I., and Mongiardo, M.: 'Open dielectric waveguides' (IEE Electromagnetic Series, IEE, UK, 1997)
21 Middlemast, I., Sarma, J., and Spencer, P.S.: 'Characteristics of tapered rib-waveguides for high power semiconductor optical sources', *IEE Proc., Optoelectron.*, 1997, **144**, (1), pp. 8–13
22 Causa, F., and Sarma, J.: 'A quasi-analytic model for longitudinally non-uniform semiconductor optical sources', *Opt. Commun.*, 2000, **183**, p. 149
23 Causa, F., and Sarma, J.: 'A versatile method for analysing paraxial optical propagation in dielectric structures', *J. Lightwave Technol.*, 2000, **18**, p. 1445

# High Brightness Index-Guided Parabolic Bow-Tie Laser Arrays

F. Causa, *Member, IEEE,* and D. Masanotti

***Abstract*—This letter describes a novel 980-nm parabolic bow-tie laser array (PBTLA) that is suitable for high-power and high-brightness operation. Output powers in excess of 2.5 W/facet pulsed in a 1° (lateral) beam, less than twice the diffraction limit, corresponding to 275 $MW \cdot cm^{-2} \cdot sr^{-1}$ brightness, have been measured without the use of external lenses from uncoated PBTLAs fabricated in-house (top metal contact surface area $\sim 0.1\ mm^2$). Experimental results presented in this letter indicate that coherence effects are significant in the operation of such devices. Theoretical models based on the simple diffraction theory and on the coupled-mode theory have been used to interpret the experimental results.**

***Index Terms*—High brightness lasers, high power, index-guiding, tapered geometry lasers.**

## I. Introduction

HIGH-POWER semiconductor optical sources that are characterized also by high brightness are required for various applications, including lidar, sensing, materials processing, optical pumping, medicine. The challenge in designing high-power high-brightness semiconductor sources resides in overcoming catastrophic optical damage, optical gain saturation, and filamentation. In addition, the output beam profile should be optimized to achieve the desired high brightness. Therefore, to develop semiconductor optical sources with such characteristics it is important to appropriately design both the material epitaxy and the device geometry. Effective device designs for high-power high-brightness sources can be found in the literature, including external cavity-tuned lasers [1], antiresonant reflecting optical waveguide lasers [2], and master oscillator power amplifiers [3]. However, the above designs generally require sophisticated device fabrication to sustain in-phase operation and/or the use of external optics to focus the output beam. Of interest in this letter are index-guiding tapered geometry devices [4]–[6], since they seem to provide an effective and convenient design model to combine the desirable operational characteristics of high power and narrow output beam with simple low-cost device fabrication.

## II. Parabolic Bow-Tie Laser Arrays

In the devices presented in this letter, an etched tapered rib provides (weak) lateral optical confinement. Therefore, in such devices the quality of the output beam is determined by the optical cavity design. The array discussed here is a development of a parabolic bow-tie laser (PBTL) designed in-house that was demonstrated to be well suited for high-brightness operation with moderately high-power output [4], [5]. However, the output power from a PBTL cannot be increased indefinitely because the device would need to be impractically long to retain the modal properties required for high brightness. Hence, to scale up the output optical power, a number of PBTLs are now driven simultaneously as an array. The schematic of a three-element PBTL array (PBTLA) is illustrated in Fig. 1. Different from the work presented in [7]–[9], the intention here is to achieve phase-locking between the emitters in order to obtain not only high power, but also high brightness. The PBTLAs have been designed to achieve longitudinally nonuniform coupling between the elements with weak coupling along the length of the device and strong coupling at the device facets, to sustain in-phase (array) mode operation. The experimental results, presented in Section III, have been interpreted using results computed with theoretical models based on the simple diffraction theory (SDT) [10], and on the coupled-mode theory (CMT) [11].

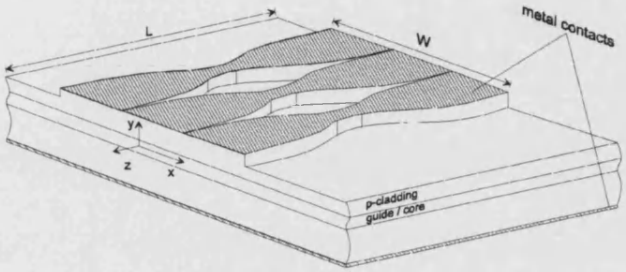


Fig. 1. Schematic of a three-element PBTLA geometry; the main parameters are also specified in the diagram.

## III. Experimental Results and Discussion

Experimental results measured from three categories of devices are considered in this letter: stripe lasers (SLs), linearly tapered bow-tie laser arrays (LBTLAs), and PBTLAs. The devices of interest here have been fabricated in-house from a specially designed 980-nm high-power double heterostructure, triple quantum-well (QW) material with three 7-nm-thick InGaAs QWs separated by two 10-nm GaAs barriers [5]. Several arrays have been fabricated with a different number of elements, but all with the same length and the same output facet width (details in figure captions), to compare performance characteristics. The devices are bonded p-side down on temperature stabilized copper mounts; however, at present, thermal management is not optimal and, therefore, the devices are tested in pulsed conditions with 0.1% duty cycle (5-$\mu$s pulsewidth).

The pulsed $L$-$J$ characteristics and wall-plug efficiency for arrays of three, four, and five elements of different geometries

Manuscript received March 26, 2004; revised May 21, 2004.

The authors are with the Department of Electronic and Electrical Engineering, University of Bath, Bath BA2 7AY, U.K. (e-mail: f.causa@bath.ac.uk).

Digital Object Identifier 10.1109/LPT.2004.833091

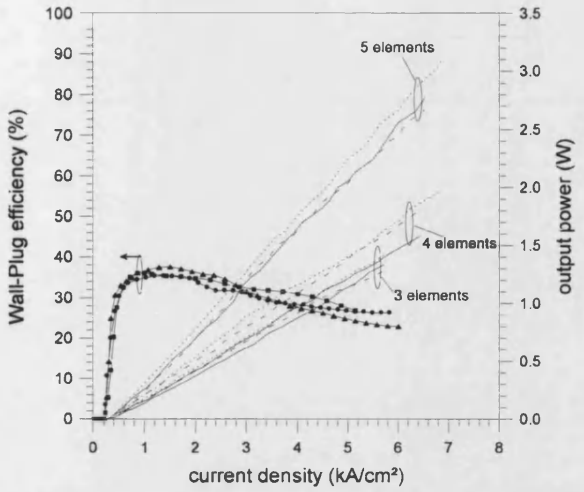


Fig. 2. Optical output power and Wall-Plug efficiency versus pulsed injection current density measured from arrays of three (▲), four (■), and five (●) elements: SL (dotted line); LBTLA (dashed line); and PBTLA (continuous line). All devices are of the same length, $L = 1.05$ mm; the output facet widths are as follows: three-element arrays: $W = 60$ $\mu$m; four-element arrays: $W = 80$ $\mu$m; five-element arrays: $W = 100$ $\mu$m. Intensity filters have been used to take readings at high power levels.

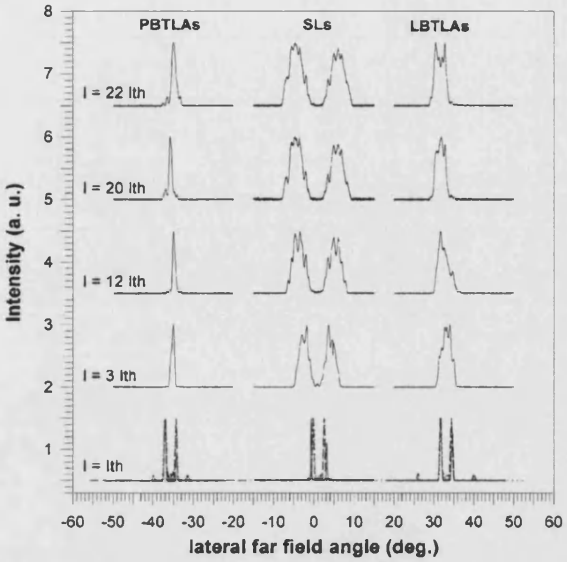


Fig. 3. Far field intensity profiles measured from SLs, LBTLAs, and PBTLAs ($L = 1.05$ mm, $W = 100$ $\mu$m) over a wide range of currents (pulsed operation). Theoretical profiles computed with the CMT (dashed line) and with the SDT (dotted line) at threshold are also included.

TABLE I
COMPARISON OF PULSED OPERATIONAL CHARACTERISTICS MEASURED FROM SLs, LBTLAs, AND PBTLAs AT LOW ($I = 3I_{th}$) AND HIGH CURRENTS ($I = 20I_{th}$)

| | Output Power ($W$/ *facet*) | | Far-Field FWHM (deg.) | | Brightness ($MWcm^{-2}sr^{-1}$) | |
|---|---|---|---|---|---|---|
| **Device** | $I=3I_{th}$ | $I=20I_{th}$ | $I=3I_{th}$ | $I=20I_{th}$ | $I=3I_{th}$ | $I=20I_{th}$ |
| SL | 0.41 | 3.1 | 9.1 | 13.8 | 5 | 25 |
| LBTLA | 0.23 | 2.6 | 2 | 3.1 | 8.4 | 92 |
| PBTLA | 0.32 | 2.8 | 0.8 | 1.08 | 42.4 | 275 |

are presented in Fig. 2. The output power is significantly higher for arrays with a larger number of elements ($N$), but varies little with the geometry of the device for arrays with the same $N$. The main operational characteristics measured from five-element arrays are summarized in Table I for low ($I = 3I_{th}$) and high current injection levels, $I = 20I_{th}$. For all such arrays, the threshold current is $I_{th} = 160$ mA (corresponding to $J_{th} = 0.2$ k Acm$^{-2}$); the slope efficiency is ~70%; the maximum wall-plug efficiency considering output power per facet is ~ 35% at $I = 0.75$ A (pulsed) and optical output power 0.6 W/facet (Fig. 2).

Representative far fields measured without the use of external lenses over a wide range of input currents from five-element arrays are presented in Fig. 3 for comparison (angle resolution of measurements ~ 0.05°). Although the output powers from all such devices are comparable, Table I, the quality of the output beam varies enormously depending on the cavity geometry. At threshold, all devices operate in the out-of-phase mode; at higher currents, SLs present a typical double-lobed pattern while both types of tapered laser arrays (LBTLAs and PBTLAs) present essentially a single-lobed beam over a wide range of currents. The latter observation is an indication of the fact that over a wide range of currents, quasi-in-phase-locking is achieved with the tapered optical cavity design. The change in mode operation can be attributed to the effect of carriers on the refractive index and gain spatial hole-burning in the device. In the region near the output facets there is no explicit lateral mode control since the elements merge in a single contact; it is in these regions that the interelement coupling is stronger. In such areas, above threshold, the modal gain in low index regions exceeds that in high index regions because of spatial hole-burning, thereby promoting in-phase operation, as discussed in [12] for arrays of a small number (3–5) of SLs. However, in the arrays of tapered lasers presented in this letter, this effect is associated to the mode filtering effect of the central region (Fig. 1), as demonstrated by the fact that in-phase locking is not observed in SLs.

The narrowest far field full-width at half-maximum (FWHM) has been measured from five-element PBTLAs (FWHM = 1.08°) which remains less than twice the estimated diffraction limit $\theta_d = \arcsin(\lambda_o/W) = 0.56°$ for a wide range of currents. Therefore, although all three categories of devices produce high power, the corresponding brightness strongly depends on the geometry of the cavity, with the highest values achieved with PBTLAs (275 MW · cm$^{-2}$ · sr$^{-1}$), Table I. A further, important observation from the measured experimental results is that the output beam from five-element PBTLAs is considerably narrower than that measured from an individual PBTL element ($\theta_d = 2.8°$) [5], indicating that coherence effects are significant in the operation of the arrays. Similar trends have been observed for arrays of three and four elements of all geometries. Preliminary continuous-wave measurements on five-element PBTLAs have shown that the far field presents two peaks at threshold, but becomes single-lobed at higher currents with FWHM = 3° at $I = 1.2$ A $= 7.5I_{th}$ and output power of 370 mW.

To interpret the above experimental results, theoretical far fields have been computed using the CMT [11], starting from the field of the individual emitters [5] under the assumption that coupling occurs only at the facets. The above results have been

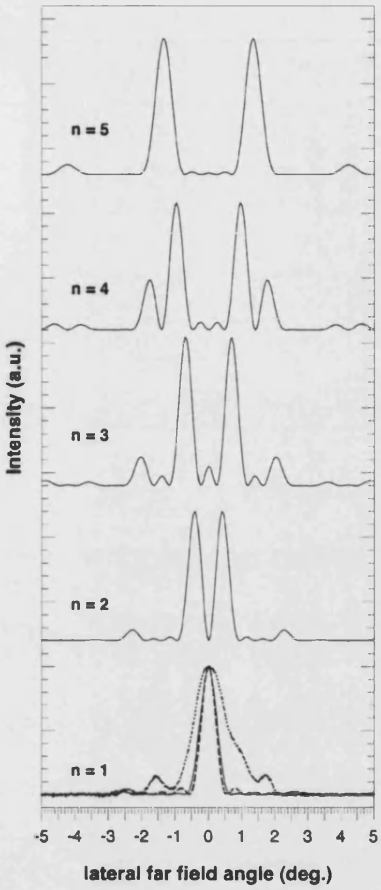


Fig. 4. Far field intensity profiles of the five modes computed with the CMT (solid line) and SDT (dashed line) for five-element PBTLA. The measured profile (at $I = 20I_{\text{th}}$) is also included (dotted line).

also compared with those obtained using the SDT [10]. Theoretical results obtained at threshold are presented in Fig. 3. To obtain good agreement between the experimental profiles and those computed with the SDT, it has been necessary to introduce a $\Delta\phi = \pi$ phase-shift between elements at threshold. At higher input currents, the phase relation between individual elements changes and it is found that PBTLAs are quasi-in-phase (fundamental mode operation) while the SLs are always locked in the out-of-phase mode. The far field intensity profiles of all the five PBTLA modes obtained using the CMT are presented in Fig. 4. From the results presented in Fig. 4, it is possible to infer that the far field broadening at higher injection currents is due to the contribution of higher order array modes. At this stage it has not been possible to quantify nor ascertain the presence of beam steering since with the present measurement apparatus the accuracy of the scale is ~0.5°, which is of the same order of magnitude of reported beam steering [6], [13]. No astigmatism was observed for any device geometry.

## IV. Conclusion

This letter presents the characterization of a category of semiconductor index-guided lasers to show that careful cavity design is essential to achieve, simultaneously, high power and high brightness. Comparisons of the operational characteristics measured from several in-house fabricated devices of different geometry have been presented and discussed in detail. Theoretical models based on the SDT and on the CMT have been used to interpret the measured far field intensity profiles. Quasi-in-phase-locking (single-lobe output beam) has been observed over a wide range of currents in tapered laser arrays which operate with longitudinally nonuniform coupling. Specifically, the brightest devices, among those considered here, are arrays of coherently coupled PBTLs (275 $\text{MW}\cdot\text{cm}^{-2}\cdot\text{sr}^{-1}$ brightness). Such devices are simple to fabricate and, thus, represent an attractive option for low-cost applications that require devices with high quality operational characteristics.

## Acknowledgment

The authors would like to thank the Engineering and Physical Sciences Research Council (EPSRC), U.K.; Dr. J. S. Roberts, University of Sheffield, U.K., for providing the required semiconductor material; T. J. Ryan (Department of Electronic and Electrical Engineering, University of Bath) for device fabrication; and the reviewers for useful comments.

## References

[1] R. J. Jones, S. Gupta, R. K. Jain, and J. N. Walpole, "Near-diffraction-limited high power (~ 1 W) single longitudinal mode CW diode laser tunable from 960 to 980 nm," *Electron. Lett.*, vol. 31, no. 19, pp. 1668–1669, 1995.

[2] A. Bhattacharya, L. J. Mawst, M. P. Nesnidal, J. Lopez, and D. Botez, "0.4 W CW diffraction limited beam Al free 0.98 $\mu$m wavelength three core ARROW-type diode lasers," *Electron. Lett.*, vol. 31, no. 7, pp. 657–658, 1996.

[3] S. O'Brien, A. Schoenfelder, and R. J. Lang, "5-W CW diffraction limited InGaAs broad-area flared amplifier at 970 nm," *IEEE Photon. Technol. Lett.*, vol. 9, pp. 1217–1219, Sept. 1997.

[4] N. S. Brooks, J. Sarma, and I. Middlemast, "A new design for tapered-geometry high-power semiconductor optical sources," in *Laser Electro-Optics Society Annu. Meeting (LEOS'96)*, vol. 2, Nov. 18–19, 1996, pp. 207–208.

[5] D. Masanotti, F. Causa, and J. Sarma, "High brightness, index-guided parabolic bow-tie laser diodes," in *Proc. Inst. Elect. Eng. Optoelectronics*, vol. 151, Apr. 2004, pp. 123–128.

[6] M. Krakowski, S. C. Auzanneau, F. Berlie, M. Calligaro, Y. Robert, O. Parillaud, and M. Lecomte, "1 W high brightness index guided tapered laser at 980 nm using Al-free active region materials," *Electron. Lett.*, vol. 39, no. 15, pp. 1122–1123, July 2003.

[7] F. J. Wilson, J. J. Lewandowski, B. K. Nayar, D. J. Robbins, P. J. Williams, N. Carr, and F. O. Robson, "9.5 W CW output power from high brightness 980 nm InGaAs/AlGaAs tapered laser arrays," *Electron. Lett.*, vol. 35, no. 1, pp. 43–44, 1999.

[8] J. S. Osinski, D. Mehuys, D. F. Welch, K. M. Dzurko, and R. J. Lang, "High-power, spectrally coherent arrays of monolithic flared amplifier-master oscillator power amplifiers (MFA-MOPAs)," *IEEE Photon. Technol. Lett.*, vol. 6, pp. 1185–1187, Oct. 1994.

[9] M. Mikulla, A. Schmitt, M. Walther, R. Kiefer, W. Pletschen, J. Braunstein, and G. Weimann, "25-W CW high-brightness tapered semiconductor laser-array," *IEEE Photon. Technol. Lett.*, vol. 11, pp. 412–414, Apr. 1999.

[10] D. R. Scifres, W. Strifer, and R. D. Burnham, "Experimental and analytical studies of coupled multiple stripe diode lasers," *IEEE J. Quantum Electron.*, vol. QE-15, pp. 917–922, Sept. 1979.

[11] D. Botez, "Array-mode far field patterns for phase-locked diode-laser arrays: Coupled-mode theory versus simple diffraction theory," *IEEE J. Quantum Electron.*, vol. QE-21, pp. 1752–1755, Nov. 1985.

[12] H. Fujii, I. Suemune, and M. Yamanishi, "Analysis of transverse modes of phased-locked multi-stripe lasers," *Electron. Lett.*, vol. 21, no. 16, pp. 713–714, Aug. 1985.

[13] W. D. Herzog, B. B. Goldberg, and M. S. Ünlü, "Beam steering in narrow-stripe high-power 980-nm laser diodes," *IEEE Photon. Technol. Lett.*, vol. 12, pp. 1604–1606, Dec. 2000.

# Optical Guiding Properties of High-Brightness Parabolic Bow-Tie Laser Arrays

D. Masanotti and F. Causa, *Member, IEEE*

***Abstract*—This paper presents the characteristics of parabolic bow-tie laser arrays (PBTLAs) which are a novel category of laser diodes specially designed to achieve high power with high brightness at 980 nm. Output powers in excess of 2.8 W/facet have been measured from five-element PBTLAs with output beam less than twice the diffraction limit, achieving high brightness of 275 $MWcm^{-2}srad^{-1}$ at 3 A (pulsed) injection current (= 22 times the threshold). Changes in the achievable brightness due to changes in the optical cavity geometry and in the lateral optical guiding strength are discussed in detail, using the coupled-mode theory to interpret the experimental results. At threshold all devices operate in the highest (double lobed) array mode. At higher currents the arrays of tapered lasers change to quasi-in-phase operation when the modal gain of the fundamental array mode dominates because of the combined effect of carrier hole burning and spatial filtering from the narrow stripe central section of the device. Similar trends have been observed under continuous-wave operation. The reduction of lateral optical guiding strength is deleterious for the operational characteristics of PBTLAs and linear bow-tie arrays, and it leads to filamentation in gain-guided devices even at low currents. Theoretical results presented in this paper show that scalability is in principle possible; however, changes in the lateral gain profile due to hole-burning can significantly increase the modal gain of higher order modes and, therefore, strongly influence the optical output profile.**

***Index Terms*—High-brightness laser arrays, high power, index- and gain-guiding, tapered geometry laser.**

## I. Introduction

HIGH-POWER semiconductor optical sources that are characterized also by high brightness are now being used in a variety of applications including, for example, fiber amplifier and solid state laser optical pumping, free space communications, second harmonic generation, medicine, laser printing, lidar. To develop such semiconductor optical sources it is important to appropriately design both the material epitaxy and the device geometry. Tapered geometry devices seem to provide an effective design to combine the desirable operational characteristics of high power and narrow output beam with simple, low cost device fabrication. A useful classification of tapered devices can be made on the basis of the guiding properties of the structure, thus distinguishing between 1) diffraction-type devices, e.g., [1]–[4], where the beam freely diffracts in the homogeneous gain medium under the flared injection metal contact—the output beam from such devices is typically astigmatic and is focused using external optics to achieve diffraction-limited operation [1] and 2) index-guided devices [5]–[10], where an etched, tapered rib provides the explicit (weak) lateral waveguiding—the output beam quality in this case depends on the optical cavity geometry.

Of interest in this paper are devices of the latter category. Specifically it was found that index-guided parabolic bow-tie lasers (PBTLs) were well suited to achieve high brightness with moderately high-power output, [5], [7], [8]. However, to scale up the optical output power achieved with PBTLs it is not practical to simply increase the device dimensions to maintain the required adiabaticity. Therefore, parabolic bow-tie laser arrays (PBTLAs) were developed [9] to attain higher power and simultaneously higher brightness with a compact and low-cost device structure. Although arrays of semiconductor lasers are not a novelty, in the PBTL Arrays described in this paper the individual elements are coherently coupled with longitudinally nonuniform inter-element coupling. Further, as described in detail in Sections II–IV, the central spatial filtering section is of paramount importance to achieve in-phase locking to attain high power in a diffraction-limited output beam. In this context, the PBTLAs are different from other, more widely known, index-guided laser diode arrays including, for example, stripe laser arrays which tend to operate in the out-of-phase mode with the characteristic, unusable two-lobed beam pattern; or the arrays of linearly tapered lasers presented in [3], [4], [10], where the individual elements were intentionally uncoupled and high output power was achieved but in a nondiffraction limited output beam.

High-power continuous waves (CW) have been achieved at 980 nm with tapered lasers and amplifiers [1], [2] by using a system of lenses to focus the beam to nearly the diffraction-limit. On the other hand, with the PBTLAs described in this paper there is no need to use external lenses to collimate the beam since the index-guided cavity geometry has been designed to achieve diffraction-limited output. As a consequence the device size is compact and the device costs are reduced. In addition, a fundamental difference with respect to previously published arrays of tapered lasers is that the physical mechanism of operation of PBTLAs is based on coherent coupling which is weak along the length of the device, but strong at the facets to ensure stability of phase-locking. As discussed in this paper, scalability is in principle possible; however, changes in the lateral gain profile due to hole-burning can significantly increase the modal gain of higher order modes and, therefore, strongly influence the optical output profile.

The semiconductor material epitaxy and main device parameters are described in Section II. The design and the operational

Manuscript received November 16, 2004; revised January 27, 2005. This work was supported in part by the Engineering and Physical Sciences Research Council U.K.

The authors are with the Department of Electronic and Electrical Engineering, University of Bath, Bath BA2 7AY, U.K. (e-mail: D.Masanotti@bath.ac.uk; f.causa@bath.ac.uk).

Digital Object Identifier 10.1109/JQE.2005.848903

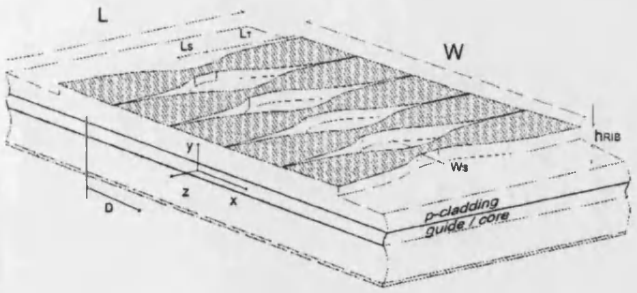


Fig. 1. Schematic of a five-element PBTLAs.

TABLE I
MATERIAL STRUCTURE

| Layer | Composition | Thickness (μm) | Doping density ($cm^{-3}$) | Dopant |
|---|---|---|---|---|
| Contact | GaAs | 0.2 | $3.0\ 10^{19}$ | Zn |
| Cladding | $Al_{0.42}$ | 0.77 | $8.0\ 10^{17}$ | C |
| Guide | $Al_{0.20}$ | 0.24 | undoped | -- |
| QW | $In_{0.2}Ga_{0.8}As$ | 7nm | undoped | -- |
| Barrier | GaAs | 10nm | undoped | -- |
| QW | $In_{0.2}Ga_{0.8}As$ | 7nm | undoped | -- |
| Barrier | GaAs | 10nm | undoped | -- |
| QW | $In_{0.2}Ga_{0.8}As$ | 7nm | undoped | -- |
| Guide | $Al_{0.20}$ | 0.24 | undoped | -- |
| Cladding | $Al_{0.42}$ | 1.77 | $1.4\ 10^{18}$ | Si |
| Buffer | GaAs | 0.5 | $1.4\ 10^{18}$ | Si |

characteristics of PBTLAs are discussed in Section III in the context of corresponding devices of different geometry to show that high-brightness operation can be achieved with a carefully designed optical cavity. Changes in the achievable brightness and filamentation characteristics due to changes in the lateral optical guiding strength are illustrated in Section IV, drawing the conclusions in Section V.

## II. Device Structure and Main Characteristic Parameters

The schematic of a five-element PBTLA is given in Fig. 1 ($W = 100\ \mu$m, $D = 20\ \mu$m, $L = 1050\ \mu$m). The laser arrays were fabricated from a double heterostructure, large optical cavity (LOC), triple quantum well (TQW) semiconductor material specially designed for high-power operation at 980 nm, [7]. The epitaxial layer structure, Table I, was grown by low-pressure metal–organic vapor phase epitaxy on n-GaAs substrate. The main material and device parameters estimated from theory or experimental characterization are the following: (vertical) optical confinement factor in the TQW $\Gamma = 0.045$; equivalent spot size $S = (d/\Gamma) = 0.458\ \mu$m where $d$ is the active region thickness; power density before COD $p_{\mathrm{COD}} = 11\ \mathrm{MWcm}^{-2}$; vertical beam divergence $\theta_y = 58°$ which is in good agreement with that estimated theoretically for the given epitaxial structure [8].

The device geometry was optimized [8] to achieve high brightness also in the lateral ($x$) direction. The effective index method, was used to reduce the analysis to two dimensions ($x, z$) and, since the structure is weakly guiding, the scalar analysis was used to study the changes in lateral beam divergence, $\theta_x$, with cavity geometry. Three different device geometries have been considered:

1) linear bow-tie laser (LBTL), for which $W(z) = W_S + ((W_o - W_S)/L_T)z$, where $W_o$ is the facet width, $Ws$ the width of the straight section and $L_T$ the taper length, Fig. 1;
2) PBTL for which
$$W(z) = \sqrt{W_S^2 + \left(\left(W_o^2 - W_S^2\right)/L_T\right)z};$$
3) straight stripe laser (SL) for which $W(z) = W_o$.

All the devices of interest in this paper have the same width of the output facet $W_o = 20\ \mu$m and the same length $L = 1050\ \mu$m; for the tapered devices the straight section is characterized by $W_S = 3\ \mu$m and length $L_S = 50\ \mu$m.

The devices discussed in this paper present (tapered) ridges, Fig. 1, with the twofold purpose of reducing current spreading and producing an effective refractive index step necessary to provide weak (lateral) optical guiding. The strength of the lateral optical guiding depends on the material epitaxy and on the rib height $h_{\mathrm{RIB}}$. The LOC material used to fabricate the arrays has been specially designed to provide simultaneously high optical output power and sufficient lateral optical guiding with the appropriate rib height. In fact, the thickness of the guide layers is the critical parameter to be adjusted to satisfy the above two contradictory requirements [7]. In particular, devices characterized by a rib height $h_{\mathrm{RIB}} = 0.9\ \mu$m will be referred to in this paper as index-guided (IG) devices since the corresponding, estimated lateral effective index step ($\Delta n_{\mathrm{eff}} = 0.009$) is sufficient to establish (weak) lateral optical waveguiding. This value of $h_{\mathrm{RIB}}$ was used to achieve diffraction limited operation from in-house fabricated PBTLs, as discussed in [7], [8]. By contrast, devices characterized by a shallower etched rib ($h_{\mathrm{RIB}} = 0.45\ \mu$m) will be referred to as gain-guided (GG) since the corresponding lateral effective refractive index step ($\Delta n \sim 0.0001$) is negligible for lateral optical guiding. The shallow rib height of GG devices, however, is useful for reducing current spreading. The increased extent of current spreading compared to that occurring in IG devices, where the etched rib is deeper, is represented in Fig. 2. The theoretical current density and carrier density profiles for the individual IG- and corresponding GG-PBTLs are validated by experimental near field intensity profiles measured at low injection current ($I \ll I_{\mathrm{th}}$) with low-pass optical frequency filters to highlight the presence of the carriers at the device facet. The increased extent of current spreading in GG devices is reflected in the increased threshold current measured from such devices, as discussed in Section IV.

The tapered ridge waveguides were fabricated by ion beam etching with p-metal deposition by Ti–Au thermal evaporation in vacuum. The devices were cleaved and bonded p-side down on temperature stabilised ($T = 20\,°$C) copper mounts. Thermal management was not optimized and, therefore, the devices were tested predominantly using pulsed current with 0.1% duty cycle (200 Hz repetition rate, 5 $\mu$s pulse duration). However, preliminary results from CW measurements are also presented for completeness in Section III.

In Section III the operational characteristics measured from PBTLAs are compared with those measured from cor-

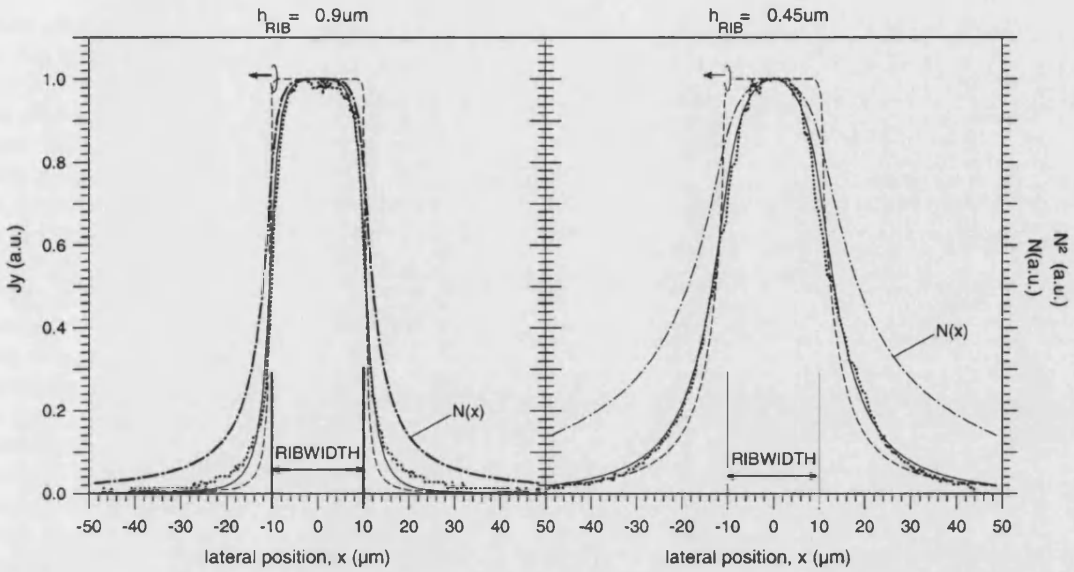


Fig. 2. Experimental near field intensity profiles (dotted line) measured at low injection current ($I \ll I_{\rm th}$) with low-pass optical frequency filters, and theoretically estimated current density (dashed line), carrier density (dash-dot line), and carrier density squared (solid line) profiles for IG and corresponding GG PBTLs.

responding arrays of five linearly tapered bow-tie lasers and SLs with same length and same output width, to show how the output beam quality is affected by the optical cavity geometry.

## III. Index-Guided Arrays: Cavity Geometry Design to Achieve High Brightness

The results discussed in this section provide the justification for the use of a parabolic geometry optical cavity to achieve high brightness. The quality of the output beam is assessed by measuring not only the full-width at half-maximum (FWHM) of the far field intensity profile, but also the Strehl ratio (SR). The SR is defined as the fraction of power contained in a solid angle corresponding to the diffraction-limit angle for that particular device, and can be estimated experimentally by measuring the power through slits placed at the far field plane with aperture corresponding to the diffraction-limited divergence angle.

Representative optical and electrical (pulsed) characteristics measured from PBTLAs, linear bow-tie laser arrays (LBTLAs) and SLs are presented in Fig. 3. For all such devices the typical threshold current is $I_{\rm th} = 160$ mA, corresponding to threshold current density $J_{\rm th} = 0.2$ kAcm$^{-2}$; the slope efficiency is $\eta_{\rm slope} = 0.8$ WA$^{-1}$. Characteristic parameters including threshold current ($I_{\rm th}$), output power at $I = 22I_{\rm th}$, maximum (per pulse) wall-plug (W-P) efficiency, FWHM of the far field intensity profile, Strehl Ratio and corresponding estimated Brightness ($B$) measured from such devices at low ($I = 3I_{\rm th}$) and high ($I = 22I_{\rm th}$) currents are summarized for comparison in Table II.

Representative far field intensity profiles measured at different (pulsed) currents from the three categories of devices, without the use of external optics, are presented in Fig. 4. The angular resolution of the far field intensity measurements is $\sim 0.05°$. It is interesting to note that at threshold all devices present a double-lobed pattern indicating out-of-phase mode operation. However, above threshold the quality of the output beam (and, therefore, the achievable brightness) changes significantly with the geometry of the optical cavity. Single-lobed

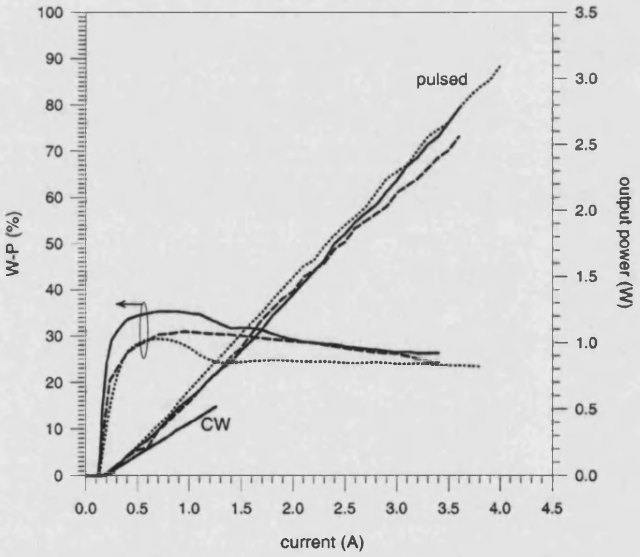


Fig. 3. Pulsed (5 $\mu$s, 200 Hz) $L$–$I$ curves and W-P efficiency measured from in-house fabricated SLs (dotted line), LBTLAs (dashed line), and PBTLAs (solid line). The CW $L$–$I$ curve from PBTLAs is also included for comparison. [Temperature: 20 °C. Neutral density filters used to take readings at high power levels].

TABLE II
Comparison of the Operational Characteristics Measured From In-House Fabricated SLs, LBTLAs, and PBTLAs Measured at $I = 3I_{\rm th}$ and at $I = 22I_{\rm th}$ Pulsed (5$\mu$s, 200 Hz)

| | $I_{\rm th}$ (mA) | Max W-P (%) | Output Power (W/facet) | | $\theta_{FWHM}$ (deg.) | | $B$ (MWcm$^{-2}$srad$^{-1}$) | | SR (%) | |
|---|---|---|---|---|---|---|---|---|---|---|
| | | | $I=3I_{\rm th}$ | $I=22I_{\rm th}$ | $I=3I_{\rm th}$ | $I=22I_{\rm th}$ | $I=3I_{\rm th}$ | $I=22I_{\rm th}$ | $I=3I_{\rm th}$ | $I=22I_{\rm th}$ |
| **SL** | 220 | 29 | 0.17 | 3.1 | 9.1 | 13.8 | 5.0 | 25 | 0 | 0 |
| **LBTLA** | 160 | 31 | 0.23 | 2.6 | 2.0 | 3.1 | 8.4 | 92 | 30 | 20 |
| **PBTLA** | 160 | 35 | 0.32 | 2.8 | 0.8 | 1.08 | 42.4 | 275 | 65 | 40 |

output beams are obtained with arrays of tapered lasers, indicating that they operate quasi-in-phase (dominant fundamental array mode). By contrast, SLs are characterized by double-lobed far fields at all currents indicating that they are always locked out-of-phase. The change in mode operation at higher injection currents in tapered laser arrays is attributed to the effect of carriers on the refractive index and to gain hole-burning. Near the output facets, where the elements merge in a single contact, inter-element coupling is stronger. In those regions, above threshold, the refractive index on the longitudinal axis of the individual elements is larger, but the gain lower, than that of the surrounding off axis regions. This situation (higher modal gain for lower order array modes) is conducive to quasi-in-phase operation for arrays of a small number of elements [11]. The important, additional aspect to be considered for the arrays of coherently coupled bow-tie lasers discussed here is that the above effect is associated to the mode filtering effect of the central narrow stripe sections (Fig. 1) as demonstrated by the fact that in-phase locking is not observed in corresponding SLs.

The experimental measurements presented in this paper have been interpreted using results computed with theoretical models based on the coupled-mode theory (CMT) [12], [13]. Assuming that significant coupling between individual emitters occurs only at the device output facets, the array far field is calculated using as a starting point the optical field of an individual emitter calculated self-consistently [8], that is, including the effects of carrier diffusion and optical gain in the cavity. According to CMT an array of $N$ weakly coupled identical elements is characterized by $N$ array modes, also referred to as "supermodes" [12]. The far field of the array mode of order $L$, $F_L(\theta)$ [13] is given by

$$F_L(\theta) = |E(\theta)|^2 I_L(\theta) \tag{1}$$

where $E(\theta)$ is the far field amplitude of the individual emitter, $I_L(\theta)$ is the "grating function" which characterizes the effect of interelement-coupling on the array far field and $L = 1, 2, \ldots, N$ is the order of the array mode. The grating function is [13]

$$I_L(\theta) = \left\{ \frac{\sin\left(\frac{(N+1)u}{2} + \frac{L\pi}{2}\right)}{\left[\sin\left(\frac{u}{2}\right)\right]^2 - \left[\sin\left(\frac{L\pi}{2(N+1)}\right)\right]^2} \right\}^2 \tag{2}$$

where $u = k_0 D \sin(\theta)$, $k_0 = (2\pi/\lambda_0)$ is the free space propagation constant, and $D$ is the (center-to-center) inter-element spacing (Fig. 1).

The array mode far field intensity profiles computed with the CMT model have been used to interpret the far fields measured from in-house fabricated arrays over a range of operating currents. As shown in Fig. 4, at threshold all experimental profiles are well represented by the highest order ($L = N$) array mode which is generally referred to as the "out-of-phase" mode indicating that adjacent elements are operating out-of-phase [12], [13]. At higher currents the far fields of the arrays of tapered lasers become single-lobed, indicating quasi-in-phase mode operation, while those measured from SLs remain double-lobed. However, as is clear from the comparison between the fundamental array mode far field and the experimental profiles at high

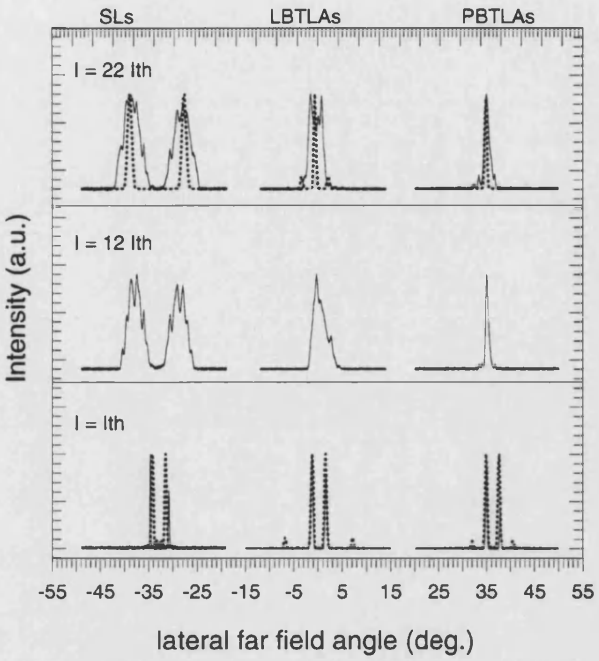


Fig. 4. Far-field intensity profiles measured (solid lines) without the use of external optics from index-guided SLs, LBTLAs, and PBTLAs at $I = I_{\rm th}$, $I = 12I_{\rm th}$ and $I = 22I_{\rm th}$ pulsed. The theoretical profiles calculated with CMT (dotted lines) are also included. [Angle resolution 0.05°].

currents (Fig. 4) although single-lobed, the far fields of both LBTLAs and PBTLAs are broader than expected revealing the contribution of higher order array modes, which explains the discrepancy between the measured far field FWHM (PBTLAs $\theta_{\rm FWHM} = 1.08°$; LBTLAs $\theta_{\rm FWHM} = 3.1°$) and the diffraction limit beam width $\theta_d = \arcsin(\lambda_o/W) = 0.56°$. In particular, although both arrays of tapered lasers, LBTLAs and PBTLAs, present essentially single-lobed far fields (i.e., quasi-in-phase mode operation) significantly higher brightness is achieved with PBTLAs ($B = 275$ MWcm$^{-2}$srad$^{-1}$) compared to LBTLAs ($B = 95$ MWcm$^{-2}$srad$^{-1}$), indicating that the parabolic geometry is more suited for high-brightness operation.

Theoretical results computed to analyze array mode discrimination in arrays as a function of the number of elements are presented in Fig. 5. As expected the modal gain of the fundamental ($L = 1$) array mode is larger than that of the highest ($L = N$) order mode when the gain in the region of higher refractive index is lower than that of the surrounding lower index region [Fig. 5(a) and (b)] [12]. This effect is noticeable experimentally in five-element PBTLAs above threshold. However, when hole-burning becomes significant and the gain of the central elements of the array is further reduced, the modal gain of the lowest and highest order modes decreases significantly with respect to that of other modes [Fig. 5(c)]. This effect is more noticeable for arrays of a large number of elements ($N > 8$), whereas for arrays of a few elements (e.g., $N = 5$) the modal gain discrimination is less pronounced. Therefore, although scalability to a large number of elements is in principle possible, the changes in lateral gain profile due to hole-burning can be detrimental for the optical output profile. Preliminary measurements on PBTLAs with $N$ up to 20 elements seem to

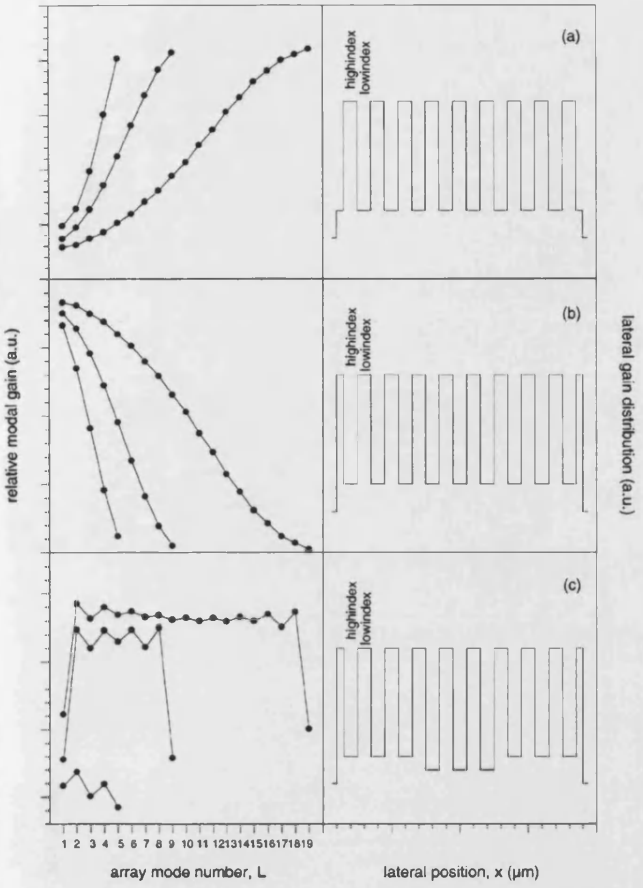


Fig. 5. Modal gain as a function of the mode number computed for arrays of five, nine, and 19 elements, for different gain profiles. (a) Highest gain in highest refractive index region. (b) Highest gain in lowest refractive index region. (c) Highest gain in lowest refractive index region in the presence of hole-burning at the center of the device. The lateral gain profiles are shown for array of $N = 9$ elements for clarity.

TABLE III
COMPARISON OF THE OPERATIONAL CHARACTERISTICS MEASURED FROM IN-HOUSE FABRICATED PBTLAS AT $I = 3I_{th}$ AND $I = 7.5I_{th}$ UNDER PULSED (5 $\mu$s, 200 Hz) AND CW OPERATION

| | $I_{th}$ (mA) | Max W-P (%) | Output Power (W/facet) | | $\theta_{FWHM}$ (deg) | | $B$ ($MWcm^{-2}srad^{-1}$) | |
|---|---|---|---|---|---|---|---|---|
| | | | $I = 3I_{th}$ | $I = 7.5I_{th}$ | $I = 3I_{th}$ | $I = 7.5I_{th}$ | $I = 3I_{th}$ | $I = 7.5I_{th}$ |
| **pulsed** | 160 | 35 | 0.320 | 0.725 | 0.8 | 0.8 | 42.4 | 128 |
| **CW** | 160 | 20 | 0.190 | 0.515 | 3.2 | 3.0 | 5.4 | 12 |

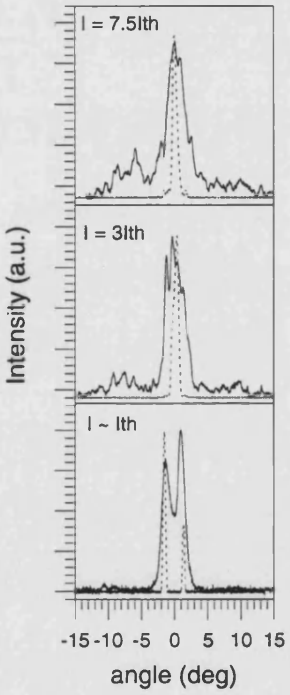


Fig. 6. Comparison of CW (solid line) and pulsed (dashed line) far-field intensity profiles measured from PBTLAs at different currents ($I \sim I_{th}$, $I = 3I_{th}$ and $I = 7.5I_{th}$). Measurements taken without using external optics. [Angle resolution: 0.05°].

validate this statement since the measured far field is not diffraction-limited, but mainly single-lobed.

With the present experimental apparatus it is not possible to establish whether the devices are affected by beam steering because the accuracy of the scale of the far field measurement apparatus is 0.5°, which is of the same order of magnitude of reported values of beam steering [6], [14].

Preliminary results from CW measurements on PBTLAs confirm the trends observed under pulsed operation discussed above. Due to limitations in thermal management of the present experimental arrangement, the maximum CW driving current was restricted to $I = 1.2A = 7.5I_{th}$. The main CW measurements results are summarized in Table III together with those obtained in pulsed conditions for PBTLAs. The threshold current is unchanged. However, the slope efficiency is reduced by approximately 25% and the W-P efficiency by 42%. This reduction in efficiency can be attributed to the present nonoptimal bonding and heat sink conditions. The $T_0$ parameter for the material of Table I used for laser fabrication has been extrapolated from CW $L$–$I$ curves measured at temperatures between 15 °C and 60 °C and found to be $T_0 = 218$ °C, in agreement with expected values for semiconductor materials designed for emission in this wavelength range. As observed previously for the results taken in pulsed conditions, near threshold the far field presents two peaks, but becomes single-lobed above threshold (Fig. 6). However, the measured far field FWHM in CW ($\theta_{FWHM} = 3°$) is broader than that obtained under pulsed conditions. As a consequence, the estimated brightness ($B = 12$ $MWcm^{-2}srad^{-1}$) is reduced by an order of magnitude with respect to that obtained under pulsed conditions, but it is still higher than that estimated for corresponding SLs ($B = 8.5$ $MWcm^{-2}srad^{-1}$) at the same CW injection current.

Compared to the more commonly used linear taper, the geometry of the parabolic taper is useful not only to achieve diffraction limited far field, but also to reduce optical feedback in the cavity at the narrow end of the tapered laser. The optical field profiles at the narrow end of an individual bow-tie laser computed for the linear and parabolic tapers [15], are compared in Fig. 7. From these results it is possible to conclude that cavity spoilers, e.g., [1], are not necessary in PBTLAs, but could be beneficial in LBTLAs.

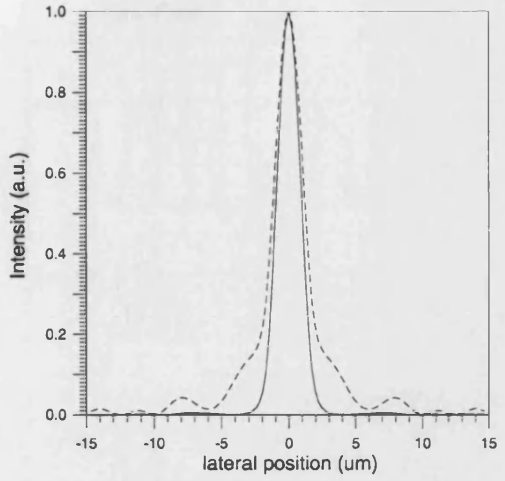


Fig. 7. Comparison of optical field intensity profile computed at the narrow end ($W = W_S$) of linear (dashed line) and parabolic (solid line) tapered lasers.

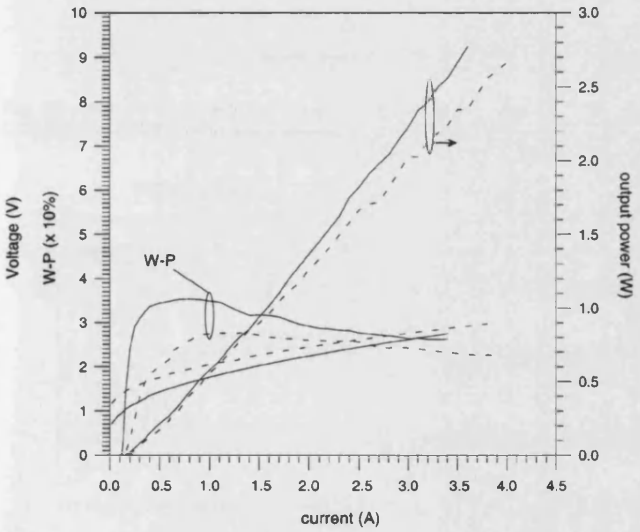


Fig. 8. $L$–$I$–$V$ and W-P efficiency curves measured from IG- (solid line) and GG- (dotted line) PBTLAs. [5 $\mu$s pulse width, 200 Hz; Temperature: 20 °C. Intensity filters have been used to take readings at high power levels].

## IV. Tapered Laser Arrays: Optical Guiding Strength

To analyze the effect of the lateral optical guiding strength on the device output power and brightness, GG devices with injection metal contact surface area identical to that of the IG devices discussed in Section III have been fabricated and characterized. Representative electrical and optical characteristics measured from IG- and GG-PBTLAs are compared in Fig. 8. As mentioned in Section II, because of the increased current spreading the threshold current of GG-PBTLAs, $(I_{\rm th})_{GG} = 200$ mA, is 25% higher than that measured for IG-PBTLAs, $(I_{\rm th})_{IG} = 160$ mA. The main operational characteristics measured from corresponding IG and GG PBTLAs are summarized in Table IV. From the opto-electrical point of view the distinction between IG- and GG-PBTLAs can be considered as marginal in terms of output optical power although GG devices are less efficient than corresponding IG arrays. The most important distinction

TABLE IV
Comparison of the Operational Characteristics Measured From In-House Fabricated IG- and GG- PBTLAs Measured at $I = 3I_{\rm th}$ and at $I = 22I_{\rm th}$ Pulsed (5 $\mu$s, 200 Hz). [$R$ = Device Resistance]

| | $I_{th}$ (mA) | Max W-P (%) | $\eta_{slope}$ (W/A) | R (Ω) | Output Power (W/facet) | | $\theta_{FWHM}$ (deg.) | | $B$ (MWcm$^{-2}$srad$^{-1}$) | |
|---|---|---|---|---|---|---|---|---|---|---|
| | | | | | $I=3I_{th}$ | $I=22I_{th}$ | $I=3I_{th}$ | $I=22I_{th}$ | $I=3I_{th}$ | $I=22I_{th}$ |
| IG | 160 | 35 | 0.8 | 0.45 | 0.32 | 2.8 | 0.8 | 1.08 | 42.4 | 275 |
| GG | 200 | 29 | 0.7 | 0.33 | 0.24 | 3.0 | filamentation | | ~0 | ~0 |

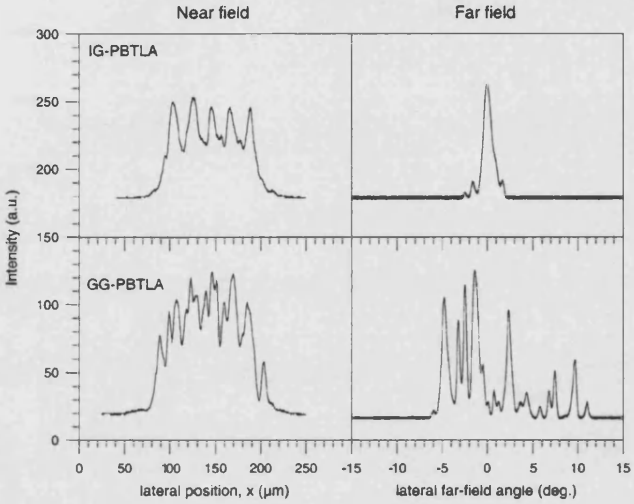


Fig. 9. Near- and far-field intensity profiles measured from IG- and GG-PBTLAs at $I = 22I_{\rm th}$ (pulsed).

between IG and GG devices in this context is that the light current characteristics of GG-PBTLAs present pronounced kinks which are associated with filamentation. In fact, filamentation is observed in both near- and far-field intensity profiles detected from GG devices. As a consequence, the output beam characteristics and, therefore, the achievable brightness from GG devices are dramatically different from those of IG devices.

Typical near field intensity profiles imaged at the facets of IG- and GG-PBTLAs above threshold ($I = 22I_{\rm th}$) are presented in the left-hand side of Fig. 9, where it is seen that the near field from GG devices presents visible irregularities. However, more significant information can be gathered from the corresponding far field intensity profiles, presented on the right-hand side of Fig. 9. Such far fields have been measured without the use of external optics, with an angular resolution of 0.05°. The output beam from GG-PBTLAs is multipeaked and shows evidence of filamentation at all currents above threshold.

To verify the presence of filamentation the following measurements have been taken on GG devices. The near field apparatus was used to detect the virtual beam waist (BW) by focusing the imaging lens inside the resonator to visualise the virtual beam origin. The resulting profiles from BW measurements are presented in Fig. 10. However, it is seen that although five BW spots (one per array element) are visible at injection currents up to about twice the threshold, the image becomes almost completely illegible at higher injection currents, as expected when filamentation occurs [16]. Further evidence of filamentation was provided by the comparison of near- and far-field intensity profiles from IG and GG PBTLAs and LBTLAs, with a view of

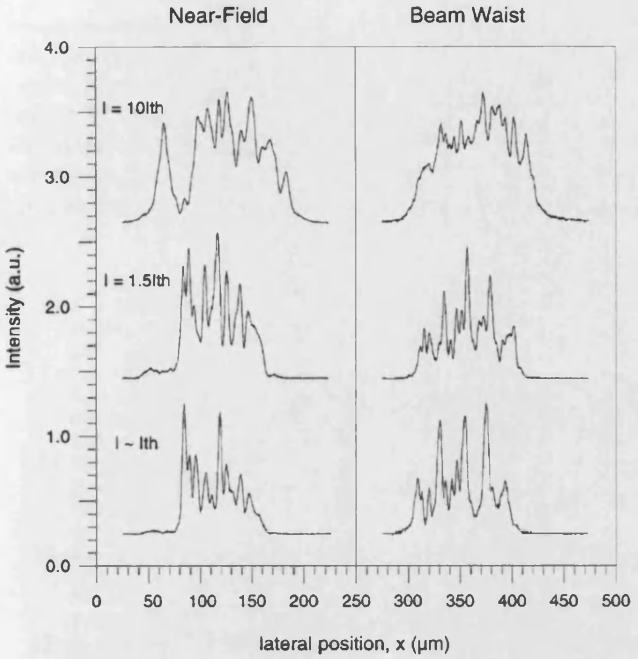


Fig. 10. Near field intensity profiles and corresponding BWs measured from GG-PBTLAs at different pulsed injection currents.

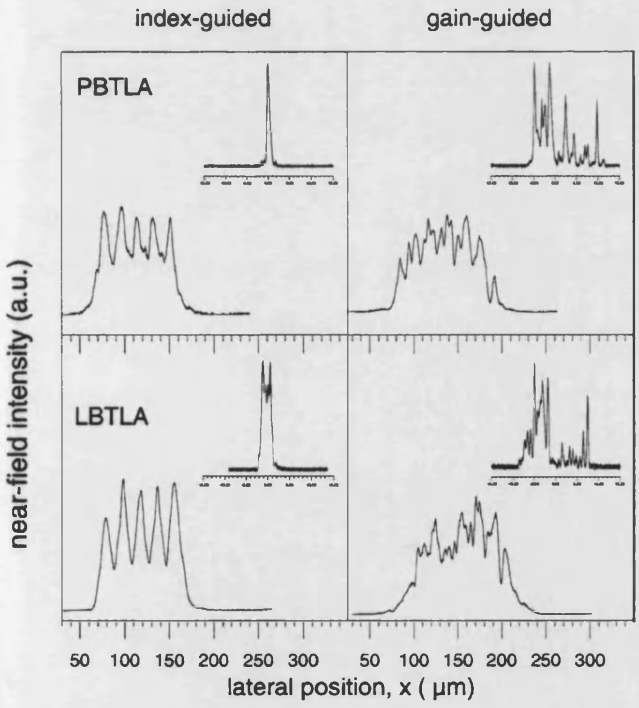


Fig. 11. Near field intensity profiles measured from IG- and GG- LBTLAs and PBTLAs at $I = 22I_{th}$ (pulsed). Corresponding far field intensity profiles are presented in the insets.

detecting beam quality changes with changes in optical cavity geometry and index guiding strength. The results are presented in Fig. 11 where it is noted that the near- and far-field intensity profiles of GG devices of both geometries display similar characteristics, indicating (as expected) that the optical field is not affected by the taper geometry and that, therefore, above threshold the optical field freely propagating in the gain region is severely affected by filamentation. By contrast, as observed in Section III, the near- and far-field intensity profiles detected from the corresponding IG devices are significantly affected by the optical cavity design.

The longitudinal astigmatism for GG-devices has been estimated to be $\sim 40$ $\mu$m near threshold. However, at higher currents the astigmatism is not clearly quantifiable because, differently from properly designed GG-devices where the optical wave freely diffracts in the active medium, here the cavity does not permit free-diffraction of the optical beam and, therefore, filamentation becomes a dominant feature. Astigmatism was not observed in IG-devices.

## V. Conclusions

The PBTLAs discussed in this paper are a novel category of high-power laser diodes with high brightness. The design and characterization of in-house designed and fabricated five-element arrays have been presented in detail to show that high-brightness operation can be achieved by careful optical cavity design. Changes in the achievable brightness due to changes in the optical cavity geometry and in the lateral optical guiding strength have been discussed. Theoretical results discussed in this paper show that scalability to a large number of elements is in principle possible; however, the changes in the lateral gain profile due to hole-burning can significantly increase the modal gain of higher order modes and, therefore, deteriorate the output beam profile.

Results computed with theoretical models based on the CMT have been used to interpret the experimental results. At threshold all experimental profiles are well represented by the highest order array mode; by contrast at higher currents, because of the effect of carriers on the refractive index and gain profiles and the mode filtering central section of the device, the far fields of the arrays of tapered lasers become single-lobed while those measured from SLs remain double-lobed. However, although single-lobed, the far fields of both LBTLAs and PBTLAs are broader than the desired diffraction-limit, revealing the contribution of higher order array modes. The estimated brightness from LBTLAs and PBTLAs is $B = 275\ \mathrm{MW \cdot cm^{-2} srad^{-1}}$ (output beam less than twice the diffraction limit), and $B = 95\ \mathrm{MW \cdot cm^{-2} srad^{-1}}$, respectively, indicating that the parabolic geometry is more suited for high-brightness operation. Preliminary results from CW measurements on PBTLAs confirm the trends observed from the pulsed measurements although lower efficiency and brightness are achieved in these conditions possibly due to the nonoptimal bonding and heat sinking conditions of the present devices. Finally, the loss of lateral optical guiding is deleterious for the operational characteristics of PBTLAs and LBTLAs. Filamentation was in fact observed in all gain-guided devices even at low currents.

## Acknowledgment

The authors would like to thank Dr. J. S. Roberts (University of Sheffield, Sheffield, U.K.) for providing the required

semiconductor material, Mr. T. J. Ryan (Department Electronic and Electrical Engineering, University of Bath, Bath, U.K.) for device fabrication, Prof. J. N. Walpole for useful discussions, and the VI European Framework Programme LASER-LAB EUROPE (ref.: mbi000430) and the Max Born Institut fur Nichtlineare Optik und Kurzzeitspectroscopie for the use of their equipment to estimate $T_0$.

## REFERENCES

[1] E. S. Kintzer, J. N. Walpole, S. R. Chinn, C. A. Wang, and L. J. Missaggia, "High power, strained-layer amplifiers and lasers with tapered gain regions," *IEEE Photon. Technol. Lett.*, vol. 5, no. 6, pp. 605–607, Jun. 1993.

[2] S. O'Brien, A. Shoenfelder, and R. J. Lang, "5-W CW diffraction-limited InGaAs broad area flared amplifier at 970 nm," *IEEE Photon. Technol. Lett.*, vol. 9, no. 9, pp. 1217–1219, Sep. 1997.

[3] M. Mikulla, A. Schmitt, M. Walther, R. Kiefer, W. Pletschen, J. Braunstein, and G. Weimann, "25-W CW high-brightness tapered semiconductor laser-array," *IEEE Photon. Technol. Lett.*, vol. 11, no. 4, pp. 412–414, Apr. 1999.

[4] J. S. Osinski, D. Mehuys, D. F. Welch, K. M. Dzurko, and R. J. Lang, "High-power, spectrally coherent arrays of monolithic flared amplifier-master oscillator power amplifiers (MFA-MOPAs)," *IEEE Photon. Technol. Lett.*, vol. 6, no. 10, pp. 1185–1187, Oct. 1994.

[5] N. S. Brooks, J. Sarma, and I. Middlemast, "A new design for tapered-geometry high-power semiconductor optical sources," in *Proc. Laser and Electro-Optics Society Annu. Meeting*, vol. 2, Nov. 1996, p. 207.

[6] M. Krakowski, S. C. Auzanneau, F. Berlie, M. Calligaro, Y. Robert, O. Parillaud, and M. Lecomte, "1 W high brightness index guided tapered laser at 980 nm using Al-free active region materials," *Electron. Lett.*, vol. 39, no. 15, pp. 1122–1122, 2003.

[7] D. Masanotti, F. Causa, and J. Sarma, "Design optimization of high power high brightness parabolic bow-lie laser diodes," *Proc. Inst. Elect. Eng. Circuits, Devices and Systems*, vol. 150, no. 6, pp. 537–561, 2003.

[8] ——, "High brightness, index-guided parabolic bow-tie laser diodes," *Proc. Inst. Elect. Eng. Optoelectronics*, vol. 151, no. 2, p. 123, 2004.

[9] F. Causa and D. Masanotti, "High brightness index-guided parabolic bow-tie laser arrays," *IEEE Photon. Technol. Lett.*, vol. 16, no. 9, pp. 2000–2002, Sep. 2004.

[10] F. J. Wilson, J. J. Lewandowski, B. K. Nayar, D. J. Robbins, P. J. Williams, N. Carr, and F. O. Robson, "9.5 W CW output power from high brightness 980 nm InGaAs/AlGaAs tapered laser arrays," *Electron. Lett.*, vol. 35, no. 1, pp. 43–44, 1999.

[11] H. Fujii, I. Suemune, and M. Yamanishi, "Analysis of transverse modes of phased-locked multistripe lasers," *Electron. Lett.*, vol. 21, no. 16, pp. 713–714, 1985.

[12] J. K. Butler, D. E. Ackley, and D. Botez, "Coupled-mode analysis of phase-locked injection laser arrays," *Appl. Phys. Lett.*, vol. 44, no. 3, pp. 293–295, Feb. 1984.

[13] D. Botez, "Array-mode far field patterns for phase-locked diode-laser arrays: Coupled-mode theory versus simple diffraction theory," *IEEE J. Quantum Electron.*, vol. QE-21, no. 11, pp. 1752–1755, Nov. 1985.

[14] W. D. Herzog, B. B. Goldberg, and M. S. Ünlü, "Beam steering in narrow-stripe high-power 980-nm laser diodes," *IEEE Photon. Technol. Lett.*, vol. 12, no. 12, pp. 1604–1606, Dec. 2000.

[15] F. Causa and J. Sarma, "A versatile method for analysing paraxial optical propagation in dielectric structures," *J. Lightw. Technol.*, vol. 18, no. 10, pp. 1445–1452, Oct. 2000.

[16] J. Guthre, G. L. Tan, M. Ohkubo, T. Fukushima, Y. Ikegami, T. Ijichi, M. Irikawa, R. S. Mand, and J. M. Xu, "Beam instability in 980 nm power lasers: Experiment and analysis," *IEEE Photon. Technol. Lett.*, vol. 6, no. 12, pp. 1409–1411, Dec. 1994.

**D. Masanotti** received the Laurea degree in electronic engineering from the University of Ancona, Ancona, Italy, in 1999. She is currently working toward the Ph.D. degree on the development of semiconductor lasers for high-power high-brightness operation at the Department of Electronic and Electrical Engineering, University of Bath, Bath, U.K.

In 1999, she joined the Department of Electronic and Electrical Engineering, University of Bath, as a Research Officer on a project for the development of Fabry–Pérot laser diodes for use in chaotic optical encryption experiments.

**F. Causa** (M'98) received the Laurea degree in physics from the University of Milan, Milan, Italy, in 1993 and the Ph.D. degree from the University of Bath, Bath, U.K., in 1998.

He joined the Department of Electronic and Electrical Engineering, University of Bath, as a Lecturer in 1999. Her research experience includes the modeling, design, and characterization of semiconductor optical devices. She has spent a period of secondment in industry sponsored by the Royal Academy of Engineering developing tapered geometry optical devices. In 2003, she visited the Tata Institute of Fundamental Research, Mumbai, India, as part of the British Council sponsored India–U.K. Young Scientist Networking Scheme. Her present research interests include the development of high-power lasers with high-brightness, high-power super-luminescent diodes, and modeling of nonlinear optical media.